High-speed optical data transmission for detector instrumentation in particle physics

Zur Erlangung des akademischen Grades eines

DOKTOR-INGENIEURS

von der KIT-Fakultät für Elektrotechnik und Informationstechnik
des Karlsruher Instituts für Technologie (KIT)

genehmigte

DISSERTATION

von

Dipl.-Ing. Djorn Karnick

geb. in Darmstadt

Tag der mündlichen Prüfung:	19.12.2019
Hauptreferent:	Prof. Dr. Marc Weber
Korreferent:	Prof. Dr. Christian Koos

Kurzdarstellung

In der vorliegenden Arbeit wird ein optisches Übertragungssystem vorgestellt, das in der Detektorinstrumentierung bei Experimenten der Hochenergiephysik, der Astroteilchenphysik oder der Photon Science zum Auslesen experimenteller Daten eingesetzt werden kann. Dabei kommt das Wellenlängen-Multiplexverfahren (Wavelength-Division Multiplexing, WDM) zum Einsatz, bei dem eine Punkt-zu-Punkt-Übertragung mit hoher Datenrate vom Detektorinneren zum Counting Room durch die parallele Kodierung mehrerer optischer Träger realisiert wird. Im speziellen wird als Kernkomponente des Systems ein optischer Mehrkanal-Sender auf Basis der Silicon-on-Insulator(SOI)-Technologie entwickelt. Diese ermöglicht es, miniaturisierte Komponenten kostengünstig und mit sehr großer Ausbeute herzustellen. Mithilfe der Erfahrungen aus der Front-End-Elektronik und den Sensorelementen können außerdem strahlenharte Bauteile hergestellt werden. Die Realisierung des Systems umfasst sowohl den Entwurf, die Simulation und die Charakterisierung opto-elektronischer Komponenten als auch die Entwicklung eines Aufbau- und Verbindungsprozesses, der die Kopplung optischer Fasern und die elektrische Kontaktierung beinhaltet. Weitere Aspekte sind die Integration des optischen Transmitters mit einer Treiberelektronik und der Aufbau eines Link-Demonstrators.

Die Hauptkomponente im Detektorinneren ist ein optischer Mehrkanal-Sender. Dieser besteht aus unabhängig angesteuerten Mach-Zehnder-Modulatoren (MZM), einem Demultiplexer (DEMUX) am optischen Eingang sowie einem Multiplexer (MUX) am optischen Ausgang. In den MZM kommen pn-Phasenmodulatoren vom Verarmungstyp zum Einsatz. Bei diesen wird eine Änderung der Phase durch das Anlegen einer Spannung in Sperrrichtung und der damit einhergehenden Ladungsträgerverarmung der aktiven Zone erreicht. Die (De-)Multiplexer sind als planare konkave Reflexionsgitter (Planar Concanve Grating, PCG) ausgeführt, bei denen das Trennen und Zusammenführen der Kanäle auf der Winkeldispersion der optischen Träger beruht. Die Laserquellen können sich außerhalb des Detektorinneren befinden. Im Unterschied zu Lösungen, welche bereits in der Fachliteratur vorgeschlagen wurden, konzentriert sich das in dieser Arbeit vorgestellte Konzept stringent auf die Anwendung unter extremen Umgebungsbedingungen und in eng begrenzten Volumina: Einerseits steigt die Anzahl erforderlicher Kabel und Durchführungen zum Detektorinneren nicht mit der Anzahl der Transmitterkanäle, da für die Hin- und Rückkanäle einer Einheit jeweils nur eine einzige optische Faser benötigt wird. Andererseits ermöglicht die Materialplattform sehr kleine Strukturgrößen und eine unerreichte Strahlenhärte. Außerdem hat selbst eine starke Änderung der Umgebungstemperatur nur einen geringen Einfluss auf die Eigenschaften sowohl der Modulatoren wie auch der (De-)Multiplexer.

Für die Vorhersage der stationären Modulationseffizienz der elektro-optischen Modulatoren wird eine Simulationsmethode entwickelt. Die Verteilungen der Ladungsträger in Anhängigkeit der Vorspannung werden mithilfe eines Finite-Elemente-Softwarepakets simuliert. Die daraus resultierende Änderung des effektiven Brechungsindexes wird in einer separaten Routine numerisch berechnet. Die Phasenmodulatoren werden durch einen pn-Übergang modelliert, welcher in einen Rippenwellenleiter integriert ist. Neben Einflüssen wie der Vorspannung, den Dotierstoffkonzentrationen oder der Ausrichtung des Übergangs kann das Modell noch erweitert werden, um auch die Auswirkungen einer Anhäufung von Oxid-Ladungen in den Mantelschichten des Wellenleiters oder einer Änderungen der Umgebungstemperatur zu berücksichtigen. Unter anderem wird dies dabei helfen, durch Strahlenbelastung verursachte Degenerationsmechanismen zu verstehen. Passive Sub-Komponenten, wie optische (De-)Multiplexer, Wellenleiter, Vielmoden-Interferometer und Gitterkoppler werden mithilfe dafür vorgesehener kommerzieller Softwarepakete simuliert.

Neben anderen photonischen Komponenten werden Modulatoren mit verschiedenen Längen und Slabhöhen im Laufe der Entwicklung eines CMOS-kompatiblen SOI-Prozesses extern gefertigt. Sie zeigen zufriedenstellende Eigenschaften, die jedoch aufgrund von Schwierigkeiten während des Fertigungsprozesses deutlich hinter den Erwartungen zurückbleiben. Beispielsweise wird ein durchschnittliches Spannungs-Längenprodukt $V_\pi L$ der pn-Verarmungsmodulatoren von 4,4 Vcm bei einer Vorspannung von 1 V festgestellt. Der Grund für diesen relativ hohen Wert ist, dass die

vorgesehenen Dotierstoffkonzentrationen während des Prozesses nicht erreicht worden sind. Andererseits ist die Grenzfrequenz der meisten Modulatortypen stark begrenzt, was höchstwahrscheinlich durch die fehlerhafte Ausführung der Vias, welche die Elektroden mit dem Modulator-Slab verbinden, begründet ist. Dennoch erreichen einige Modulatoren mit einer Länge von 3 mm eine Grenzfrequenz von etwa 30 GHz bei einer Vorspannung von 1 V. Die fehlerfreie Übertragung eines 11.3 Gbit/s NRZ-OOK-Datensignals kann sogar für jeden einzelnen Modulatortyp gezeigt werden.

Kurz vor Vollendung dieser Arbeit konnte der Fertiger eine neue Serie photonischer Chips liefern, welche einem weiteren Dotierstoff-Implantationsschritt unterzogen wurden. Damit wurde nun eine höhere Dotierstoffkonzentration erreicht. Dies äußert sich bei der statischen Charakterisierung mehrerer Modulatortypen in einer Steigerung der Modulationseffizient um 33% im Vergleich zur ursprünglichen Serie. Das Spannungs-Längenprodukt $V_\pi L$ ist um etwa 25% reduziert und beträgt 3,4 Vcm bei einer Vorspannung von 1 V. Eine weitere Untersuchung der Eigenschaften der neuen Komponenten überschreitet jedoch den Rahmen dieser Arbeit.

Auch werden thermo-optische Modulatoren getestet, bei denen die Heizelemente durch die selektive Dotierung eines Wellenleiters erzeugt werden. Dies geschieht, um die Kompatibilität zum CMOS-Prozess zu erhalten. Bei einem fortschrittlichen Design, welches lediglich 100 µm lang ist und auf verteilten lokalen Heizelementen beruht, genügen 20 mW elektrische Leistung, um eine Änderung der Phase der optischen Welle um π zu erreichen. Die Komponente wird in der nächsten Generation des Mehrkanal-Senders verwendet, um die Einstellung des Arbeitspunkts der MZM zu ermöglichen.

Passive Komponenten sind von den Schwierigkeiten während des Fertigungsprozesses offenbar nicht betroffen. Miniaturisierte fokussierende Gitterkoppler mit einem Einfügeverlust von 4,6 dB und einer 3 dB-Bandbreite von 80 nm werden für die Kopplung zwischen optischen Fasern und Wellenleitern verwendet. Leistungskoppler für die Mach-Zehnder-Modulatoren werden durch Vielmoden-Interferometer implementiert, welche einen durchschnittlichen Einfügeverlust von lediglich 0,64 dB aufweisen. PCG-(De-)Multiplexer mit unterschiedlichen Kanalzahlen werden in den Mehrkanal-Sendern verwendet. Deren gemessener Kanalabstand stimmt gut mit dem berechneten überein und die durchschnittlichen gemessenen Einfügeverluste betragen 3,6 dB.

Der wesentliche Schritt in der Aufbau- und Verbindungstechnik für opto-elektronische Bauelemente ist die permanente und stabile Faser-Chip-Kopplung. Um den Aufbau möglichst kompakt halten zu können, wird die Kopplung zwischen unter einem Winkel angeschliffenen Standard-Einmodenfasern (Single-Mode Fiber, SMF) und SOI-Wellenleitern mittels Gitterkopplern untersucht. Ein einfacher Herstellungs- und Aufbauprozess wird entwickelt, der sowohl für die Musterentwicklung als auch für die Herstellung kleiner Stückzahlen geeignet ist. Dabei wird keine spezialisierte Ausrüstung der Aufbau- und Verbindungstechnik benötigt, sondern die Präzisionsjustageelemente eines Messplatzes zur Charakterisierung photonischer Komponenten verwendet. Die SMF werden auf standardisierten V-Grubenchips befestigt und alle mechanischen Verbindungen werden durch Klebstoffe hergestellt, welche unter UV-Bestrahlung aushärten.

Die Klebeverbindung wird mithilfe eines konventionellen Kopplungsaufbaus optimiert, bei dem die Faser unter einem kleinen Winkel zur Normalen der Chipoberfläche ausgerichtet wird. Um die Justagetoleranzen zu bestimmen, werden sowohl Simulationen als auch Experimente durchgeführt. Mithilfe von Langzeitmessungen wird die Stabilität der Kopplung beurteilt. Weiterhin werden die Auswirkungen von Veränderungen der Umgebungsbedingungen wie der Temperatur oder der Luftfeuchtigkeit auf die Kopplungseffizienz untersucht. Diese haben eine Verschiebung der Fasern durch thermische Expansion der Sockel oder thermische bzw. hygroskopische Expansion der Klebstoffe zur Folge. Es wird gezeigt, dass bei einem optimiertem Aufbau weder eine starke Änderung der Temperatur noch der Luftfeuchtigkeit eine signifikante Verschlechterung der Kopplungseffizienz verursacht. Außerdem scheint der Aufbau langzeitstabil zu sein, da sich über einen Zeitraum von mehr als drei Jahren die Kopplungseffizienz nicht verringert.

Aufgrund all der Erfolge dieser Arbeit rückt die Realisierung des optischen Übertragungssystems für die Detektorinstrumentierung in greifbare Nähe. Zunächst wird ein Link-Demonstrator aufgebaut, in dem ein aus Standardkomponenten bestehender elektrischer Treiber zum Einsatz kommt. Ungeachtet offener Fragestellungen wie der Miniaturisierung der elektrischen Treiber oder einer automatischen Arbeitspunktregelung für die Modulatoren kann das Übertragungssystem in naher Zukunft in einem Detektor zum Einsatz kommen, um konventionelle Infrastrukturen zum Auslesen der Daten zu ersetzen.

Executive summary

This work addresses the realization of an optical transmission system utilizing wavelength-division multiplexing (WDM) for the read-out of experimental data in detector instrumentation in high-energy physics, astroparticle physics or photon science. The individual wavelength channels constitute a high-capacity point-to-point link from the detector front-end to the counting room. In particular, a multi-channel silicon photonic optical transmitter is developed as the core component on a silicon-on-insulator (SOI) platform. The technology enables the manufacturing of components with extremely small footprint at low costs with a very high yield. In addition, radiation-hard devices can be built based on the experience from front-end electronics and sensor elements. For one, the realization of the system comprises the design, simulation and characterization of opto-electronic link components. Next, a packaging process including the coupling of optical fibers and electrical contacts is established. Additional sub-topics are the integration of the optical transmitter with the driver electronics and the setup of a link demonstrator.

The on-detector core component is a multi-channel optical transmitter. It consists of four independently-driven Mach-Zehnder modulators (MZM), an input demultiplexer (DEMUX) and an output multiplexer (MUX). Depletion-type pn-phase shifters are utilized in the MZM, where a phase shift is induced by deliberately depleting the active zone due to applying a voltage in reverse direction. The (de-)multiplexers are implemented by planar concave gratings (PCG), where the channels are separated or merged due to the angular dispersion of the optical carriers. The laser sources can be located off-detector. In contrast to solutions proposed in the literature, the concept discussed in this thesis stringently focuses on the application in harsh environments and strong spatial confinement: for one, the number of necessary cables and feed-throughs does not increase with the number of transmitter channels, because only a single optical fiber for the unit's input and output is required. Next, the material platform offers a small foot print and unrivalled radiation-hardness. Finally, both the modulators and the (de-)multiplexers retain reliable properties even under strong changes of ambient temperature.

In order to predict the steady-state modulation efficiency of the electro-optic modulators, a simulation procedure is developed. The charge carrier distributions depending on the bias voltage are simulated using a finite-elements software package. The resulting change of the effective refractive index is calculated numerically in a separate routine. The phase modulators are modelled by a pn-junction integrated in a strip-loaded waveguide. Apart from influences such as the bias voltage, doping concentrations or junction geometry, the model can be extended to consider also the accumulation of oxide charges in the waveguide cladding or changing ambient temperature. Among other things, this will help to gain a thorough understanding of degeneration mechanisms due to radiation exposure. The passive sub-components, such as optical (de-)multiplexers, waveguides, multi-mode interferometers and grating couplers are simulated using dedicated commercial software suites.

Among other photonic components, modulators with different lengths and slab heights are fabricated by an external foundry in the course of developing a CMOS-compatible SOI process. They exhibit satisfying characteristics, although difficulties during the fabrication process yield considerable performance limitations compared to the expectations. For example, an average voltage-length product $V_\pi L$ of 4.4 Vcm is determined at 1 V bias voltage for the depletion-type pn-modulators. The reason for the relatively high value is that the nominal doping concentrations have not been achieved during the fabrication process. On the other hand, the cutoff frequency of most modulator types is limited, which is most likely due to the imperfect formation of vias connecting the electrodes with the modulator slab. Nevertheless, some of the devices with a length of 3 mm achieve a cutoff frequency in the range of 30 GHz at 1 V. The error-free data transmission of an 11.3 Gbit/s NRZ-OOK signal can even be demonstrated for every single modulator type.

Shortly before the completion of this thesis, the foundry was able to deliver a new batch of photonic chips, which have been exposed to a second dopant implantation. Consequently, a higher doping concentration has been achieved. During the steady-state characterization of several modulator types, it

manifests in an improvement of the modulation efficiency by 33% compared to the initial batch. The voltage-length product $V_\pi L$ is reduced by approximately 25% and amounts to 3.4 Vcm at a bias voltage of 1 V. A further investigation of the new devices' characteristics is nevertheless beyond the scope of this thesis.

Thermo-optic modulators, where the heaters are realized by selectively doping the waveguide to maintain conformity with the CMOS process, are tested as well. An advanced design with a length of only 100 µm relying on distributed localized heaters requires only 20 mW of electrical power to induce a π-shift of the optical wave. It will be included in the next generation of the multichannel transmitter to enable an operating point adjustment of the MZM.

Passive devices appear not to be affected from the fabrication difficulties: miniaturized focusing grating couplers with an insertion loss of 4.6 dB and a 3 dB bandwidth of 80 nm are utilized for coupling waveguides to optical fibers. Power couplers for the Mach-Zehnder modulators are implemented by multi-mode interferometers exhibiting an average insertion loss as low as 0.64 dB. PCG (de-)multiplexers with different channel numbers are used in the multi-channel transmitters. A good agreement between the measured and the calculated channel spacing is found and the measured average insertion loss is 3.6 dB.

The essential step in the packaging of opto-electronic components is establishing a permanently stable fiber-to-chip coupling. In order to maintain a compact footprint, the coupling of angle-polished standard single-mode fibers (SMF) to grating-coupled SOI waveguides is studied. A simplified fabrication and assembly process is developed, which is suitable for prototyping or the manufacturing of small quantities. Instead of requiring specialized packaging tools, the precision alignment equipment from a photonic components characterization stage is used. The SMF are mounted on standard glass v-groove chips, and all mechanical bonds are established with an UV-curing adhesive.

The joint design is optimized by reference to a conventional out-of-plane coupling assembly, where the fiber is aligned at a small angle to the chip surface normal. Both simulations and experiments are conducted in order to determine the alignment tolerances. The coupling stability over time is evaluated by long-term measurements and the impact of changes in ambient conditions such as temperature or humidity are studied. They cause fiber displacement due to thermal expansion of the sockets or thermal or hygroscopic expansion of the adhesives, respectively. It is shown that a strong variation of neither ambient temperature nor humidity causes a significant deterioration of the coupling efficiency of an optimized assembly. Furthermore, the assembly appears to be long-term stable, since no significant penalty on the coupling efficiency is observed over a period of more than three years.

With all the achievements of this work, the setup of the optical link for detector instrumentation is within reach. Using an electrical driver circuitry assembled from off-the-shelf components, a link demonstrator is assembled. Despite remaining issues, such as the miniaturization of the electrical driver or an automatic modulator operating point control, the link can be installed in a detector system in the near future to replace conventional data read-out infrastructures.

Table of contents

1 Introduction

Due to the continuously refining spatial, energy and time resolution of modern detector systems in high-energy physics (HEP), astroparticle physics or photon science, an ever-increasing number of pixels is required. Consequently, the number of electronic read-out channels increases significantly and thus the aggregated data rate easily reaches several tens of terabits per second. While massive parallelization in electronic pre- and post-processing provides the appropriate processing speed, the data link between the detector's front-end electronics and the counting room progressively becomes the bottleneck of the system. To keep the amount of aggregated data manageable, sophisticated trigger architectures reduce the data rate by online event-selection processes. For the read-out of the entire detector data, as it is required for calibration purposes, the delay results in a detector dead time of several collision event cycles. State-of-the-art read-out infrastructures, which are currently deployed in the course of the *Large Hadron Collider* (LHC) phase 1 upgrade, rely on optical links using directly modulated laser diodes as on-detector transmitter units. Each transmitter is connected to an off-detector receiver by a single optical fiber. The data rate of both up- and the downstream per link is 4.8 Gigabit per second. Similar to the detector front-end electronics, the link components are operating in harsh environment inside the detector volume. The components are exposed to a low ambient temperature, a high magnetic field and radioactive radiation close to the beam line.

In order to reduce the total number of fibers between the detector and the counting room, an optical transmission system based on wavelength-division multiplexing (WDM) can replace many single-fiber links. A schematic is presented in Figure 1.1. An on-detector multi-wavelength transmitter (Multi-λ Tx) encodes electrical data from the read-out chips (ROC) on several optical channels in parallel, which are transmitted over a single fiber. Laser sources outside the detector volume provide stabilized optical carriers. This not only reduces the on-detector power budget significantly, but also enables the utilization of standard distributed-feedback (DFB) laser diodes, as they are not exposed to harsh environment. The same considerations are valid for the receivers (Multi-λ Rx) and the data acquisition (DAQ) units. They are located in the counting room outside the radiation zone and therefore can be built from off-the-shelf equipment.

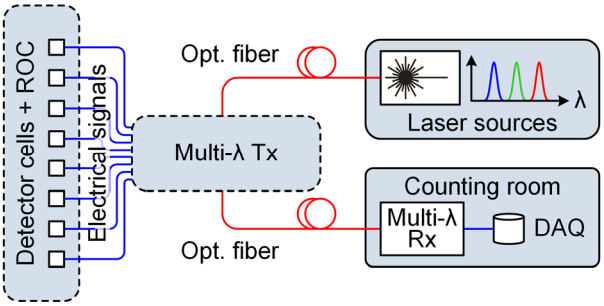

Figure 1.1: Schematic of a WDM-based optical transmission system for the detector data-readout. Off-detector laser sources generate multiple optical carriers, on which the multi-wavelength transmitter (Multi-λ Tx) encodes data from the read-out chips (ROC). The receivers (Multi-λ Rx) and data acquisition (DAQ) units reside in the counting room outside the detector cavern.

Compared to state-of-the-art read-out infrastructures, a WDM-based transmission system can increase the per-fiber data rate substantially. Assuming a moderate data rate of 10 Gbit/s per wavelength channel, the aggregated data rate of yet a four channel system exceeds the phase 1 upgrade link system by far. Moreover, the data rate can be further increased: for one, more optical channels can be used in parallel. The system is manly limited by the occupied space of the on-detector driver electronics and the total optical power that is launched into the fiber. Secondly, the data rate per channel can be increased by raising the symbol rate. However, a more efficient method is the introduction of advanced modulation formats, where more than one bit per symbol can be encoded by the modulation of both the amplitude and the phase of the optical carrier. By exploiting all the aforementioned means, the total link data rate can reach the terabit-per-second range.

The essential building block of the transmission system is the multi-wavelength transmitter. The operation principle is as follows: a demultiplexer (DEMUX) separates the incident optical channels by their wavelength. Each of them is forwarded to an electro-optic modulator, which encodes data on the respective carrier. For transporting all signals back to the counting room over a single fiber, they are merged by an optical multiplexer (MUX).

The silicon-on-insulator (SOI) technology appears to be the most feasible material platform for the fabrication of the on-detector link components, because it already enables the realization of radiation-hard front-end electronics and sensor elements. Moreover, the high contrast between the refractive indices of silicon and silicon dioxide allows for an extremely small footprint. Complementary metal-oxide semiconductor (CMOS) processes enable the manufacturing of highly integrated components at low costs with a very high yield. They encompass the structuring of passive elements such as waveguides as well as the formation of active components by means of charge carrier implantation. In addition, CMOS offers the unique possibility of the integration of photonic components and electronic circuits such as electrical drivers for the modulators in a monolithic silicon module.

On account of dopant implantation, the technology allows for the implementation of electro-optic modulators exploiting the plasma-dispersion effect. Depletion-type pn-phase shifters offer a high modulation bandwidth up to several tens of gigahertz at the expense of a comparatively small modulation efficiency. Typical values for the voltage-length product of a Mach-Zehnder modulator based on depletion-type pn-phase shifters are in the volt-per-centimeter range. Thus, an amplifying modulator driver becomes necessary. On the other hand, the advantage of the technique is its fabrication simplicity and compliance with standard CMOS processes.

In contrast, emerging modulator technologies such as the silicon-organic hybrid (SOH) platform offer substantial improvements in modulation bandwidth as well as efficiency and at the same time minimize the device footprint. However, the requirements on the fabrication are extremely demanding since the modulator relies on a well-defined slot waveguide with a slot width reaching below 100 nm. Moreover, an organic cladding material functionalizes the slot waveguide, whose deposition requires additional non-standard processing steps. The long-term stability of this material is not sufficiently investigated and the impact of radiation and low temperatures has not been studied so far. Hence, although the performance properties of the SOH platform appears superior to those of modulators based on the plasma-dispersion effect, the latter is favored for on-detector applications due to its reliability.

1.1 Development of the entire transmission system

In the framework of the research topic *Detector Technologies and Systems* (DTS), which is part of the Helmholtz-program *Matter and Technology* (MT), all required fields of expertise are concentrated at the *Institute of Data Processing and Electronics* (IPE) at the *Karlsruhe Institute of Technology* (KIT) to enable the research and development of a WDM-based data read-out system. This enterprise is divided in five sub-topics, which are briefly summarized in the following.

At first, a multi-wavelength light source is built, which consists of four DFB laser modules whose emitted optical radiation is coupled to a single optical fiber. Driver modules provide for the current supply and temperature stabilization. Next, the core component of the system, the silicon on-detector multi-wavelength transmitter unit is designed and fabricated. It implements electro-optic modulators based on Mach-Zehnder interferometers with a depletion-type pn-phase shifter in each arm. The (de-)multiplexers rely on planar concave gratings (PCG), where the optical channels are separated or merged by means of diffraction. The development of the unit encompasses the concept and design of essential photonic components including the establishment of efficient simulation methods as well as the experimental characterization. An external CMOS foundry fabricates the components on an SOI-wafer.

Thirdly, the transmitter die has to be packaged into a functional component with electrical, optical and mechanical interfaces. That includes the stable coupling of optical fibers to the chip’s waveguides

and the electrical contacting to supply the device with bias voltages and high-frequency data-signals. The latter is achieved using an RF circuit board to which the transmitter is wire-bonded. A fiber-to-chip coupling process is developed to couple angle-polished standard single-mode fibers (SMF) with sub-micrometer photonic integrated circuits. Bonding of the components is facilitated by acrylate-based UV-curing adhesives. The method enables surface-coupling with grating couplers while maintaining a planar fiber arrangement. The process provides for the coupling of photonic circuits at an early stage of development. Thus, in-situ characterization of photonic components even under a strong spatial confinement becomes feasible. At the same time, the method may be suitable for packaging photonic devices ready for production.

Furthermore, an electrical driver for the modulators is developed, which is capable to convert the data signals from the sensor electronics to appropriate driving voltages. A first version is assembled from commercially available components and is designed to provide for a large modulation voltage swing. For a second version, a driver circuit board for commercial driver integrated circuits (IC) is designed and fabricated. In the future, the driver will be integrated in an application-specific integrated circuit (ASIC).

Lastly, an off-detector receiver based on a field-programmable gate array (FPGA) is assembled mostly from off-the-shelf components, since the unit is operated within the stabilized conditions of a counting-room or data center. All the tasks contribute to the assembly of a four-channel link system demonstrator, which aims to operate at an aggregated data rate of 40 gigabit per second.

1.2 Scope of the thesis

This work attempts to push forward the realization of a novel optical data read-out system for detector instrumentation, which is scalable up to a data rate in the terabit-per-second range. Two major topics are addressed: at first, an integrated multichannel optical transmitter is developed, which begins with the design and the simulation of electro-optic modulators based on pn-phase shifters. An efficient simulation method is developed and implemented, which allows for the reliable prediction of the modulation efficiency. Furthermore, auxiliary components required to assemble the transmitter are designed. Among those are thermal modulators, (de-)multiplexers and power couplers. Based on the designs, a photonic chip is fabricated by an external foundry of which the characterization results are presented and compared to the simulations.

The second topic is the realization of a planar fiber-to-chip coupling arrangement in order to attach angle-polished SMF to grating-coupled waveguides. Together with mechanical fastening and electric contacting, it is one of the essential steps in the process of packaging opto-electronic components. The feasibility of bonding the components by acrylate-based UV-curing adhesives is investigated. A process is established, which includes the grinding and polishing of SMF, their precise alignment and bonding. In order to verify the reliability of the arrangement, the impact of strong variations in ambient conditions on the coupling efficiency is analyzed and the long-term stability is evaluated.

Finally, in order to introduce advanced optical communication systems to the benefit of detector technology, it appears necessary to bridge the gap between the two research fields. Therefore, essential conceptual and technological aspects are compiled and crucial properties of the link components are identified. In particular, it is discussed to what extent the requirements of a modern data transmission infrastructure also apply to a detector read-out system and where fundamental differences might exist.

2 Silicon-on-insulator waveguides

2.1 Silicon-on-insulator platform for photonic components

A silicon-on-insulator structure is basically a silicon-layer (Si) of a defined thickness deposited on an insulating material such as silicon dioxide (SiO_2). In the manufacturing of micro-electronics, most often the SiO_2 layer is sandwiched between a crystalline silicon surface layer and a bulk silicon substrate. That is why the SiO_2-layer is referred to as the buried oxide (BOX). The substrate thickness is typically in the range of several hundreds of micrometers, thus providing stability to allow for even large wafers up to a diameter of 300 mm. The thickness of both the crystalline silicon layer and the BOX layer is around one micrometer. The high contrast of the refractive indices of Si ($n = 3.48$) and SiO_2 ($n = 1.44$) at the telecommunication wavelength of 1550 nm facilitates a strong confinement of waveguide modes and thus small waveguides and bending radii. Ultimately, this allows for a high integration density of building blocks and thus a small footprint of devices.

2.1.1 Wafer manufacturing

The three most common methods of manufacturing SOI wafers are described in this section. The *Separation by IMplanted OXygen* (SIMOX) process relies on the implantation of oxygen-ions into a silicon wafer [1]. A schematic of the significant stages of the process is show in in Figure 2.1. At a low implantation dose, the oxygen profile resembles a nearly Gaussian shape, as depicted in Figure 2.1a). The penetration depth depends on the ions' energies. In the course of implantation, Figure 2.1b), the peak concentration saturates at the stoichiometric limit of SiO_2. Further implantation then results in broadening and flattening of the oxygen concentration profile, which is visualized in Figure 2.1c). A terminating annealing results in a uniform SiO_2 layer with distinct boundaries to the adjacent silicon layers. The penetration depth and thus the thickness of the surface Si layer is governed by the energy of the ions. If necessary, the surface silicon layer can be enhanced by subsequent epitaxial growth.

Another process to fabricate SOI wafers is the *Bond and Etch-back SOI* (BESOI) method [1]. It exploits the formation of strong chemical bonds between hydrophilic surfaces. The essential three steps as depicted in Figure 2.2 are described briefly in the following. At first, the surfaces of two silicon wafers are oxidized (Figure 2.2a)). Then, as shown in Figure 2.2b), they are brought together to form an initial bond at room temperature, which is reinforced by thermal processing. In the final step (Figure 2.2c)), the surface of the upper wafer is thinned so as the intended thickness of the Si-layer is achieved.

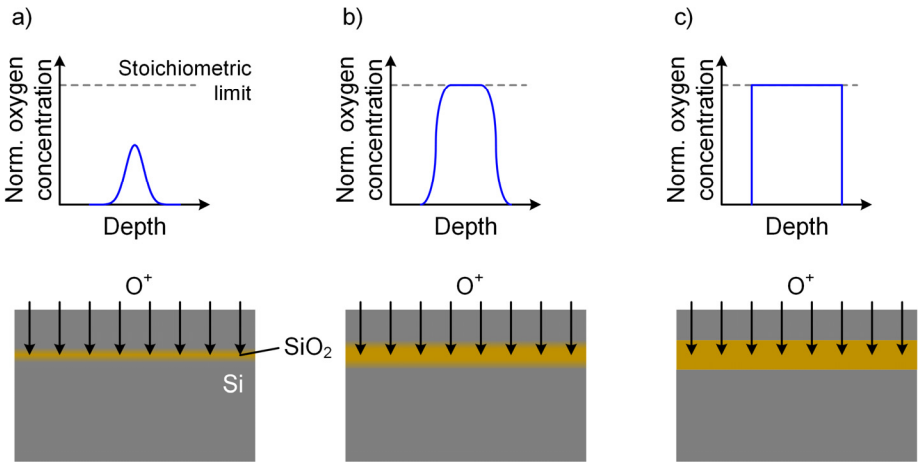

Figure 2.1: Different stages of development of the SIMOX process. a) Beginning of the process with low oxygen dose, b) peak oxygen concentration at the stoichiometric limit and c) after completed implantation and annealing.

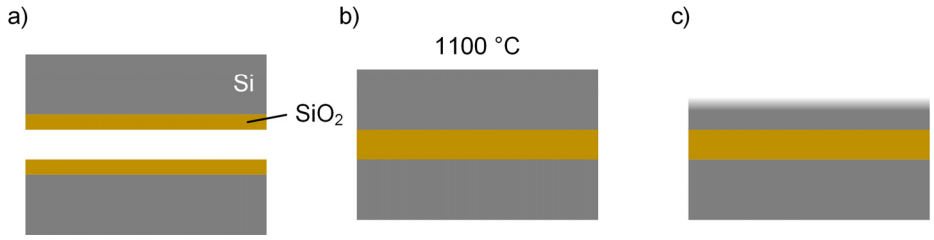

Figure 2.2: Simplified representation of the essential BESOI processing steps: a) oxidization of two separate Si-wafers, b) bonding of the oxidized surfaces, c) thinning of the upper wafer to the intended layer thickness.

In order to produce large quantities of SOI wafers that have a high quality and uniformity, the *SmartCut* process was developed. It has been proven that the produced wafers where particularly suited for photonic integrated circuits (PIC) [2]. This process, of which the steps are sketched in Figure 2.3, relies on the implantation of H^+-ions into the silicon wafer [3]. In the first step, a silicon wafer with an oxidized surface is implanted with hydrogen ions (H^+). Similar to the SIMOX process, the penetration depth is specified by the energy of the ions. The structural integrity of the silicon is locally reduced at the peak concentration of the H^+–ions. Then, a second handling wafer is hydrophilically bonded to the implanted wafer to facilitate the handling of the wafer. This process step is similar to the initial bonding step of the BESOI process. The bond is stabilized by heat treatment, which also induces the splitting of the implanted wafer at the concentration maximum of the H^+–ions. Finally, the excess part of the wafer is removed and can be recycled for the use as another handling wafer. The roughness of the surface silicon layer is reduced by subsequent polishing. If required, it may also be increased by epitaxial growth.

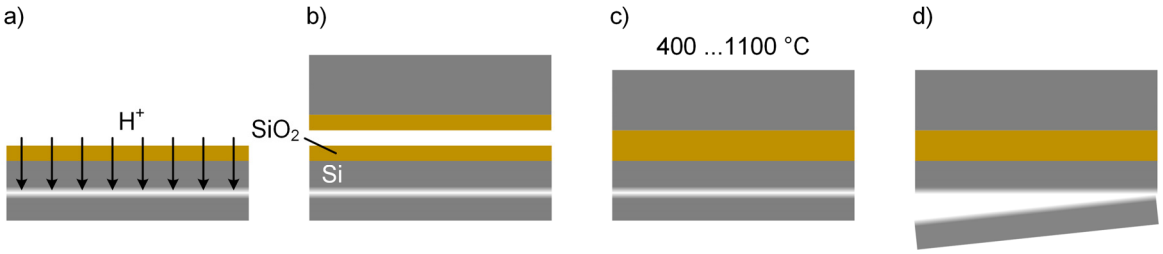

Figure 2.3: Simplified representation of the essential SmartCut processing steps. a) Implantation of H+-ions, b) bonding of a handling wafer at room temperature, c) heat treatment of bonded wafers, d) removal of excess part and subsequent polishing.

2.1.2 Wave guiding fundamentals and single-mode waveguides

A symmetric slab waveguide is the basic form of a waveguide. A core layer with refractive index n_1 is sandwiched between a cladding medium with the refractive index $n_2 < n_1$. The layers are homogeneous and infinitely extended along the x-direction. The formation of guided modes is visualized in Figure 2.4.

In Figure 2.4a), the propagation of plane waves in the semi-space $z > 0$ inside the core medium is sketched. The lines in the core layer indicate the optical path of the plane waves. They can be reflected alternately at the upper and the lower boundary of the waveguide core at $y = \pm h/2$. If the angle α is chosen as such to provide for total internal reflection at the media boundaries, the energy of the waves is confined inside the core layer. For α smaller than the critical angle, the waves are partially transmitted into the cladding layers. The wave vectors of the plane waves in the respective medium are labelled $\vec{k}_1$ and $\vec{k}_2$, respectively. If the reflected waves superimpose in-phase, standing waves in y-direction are

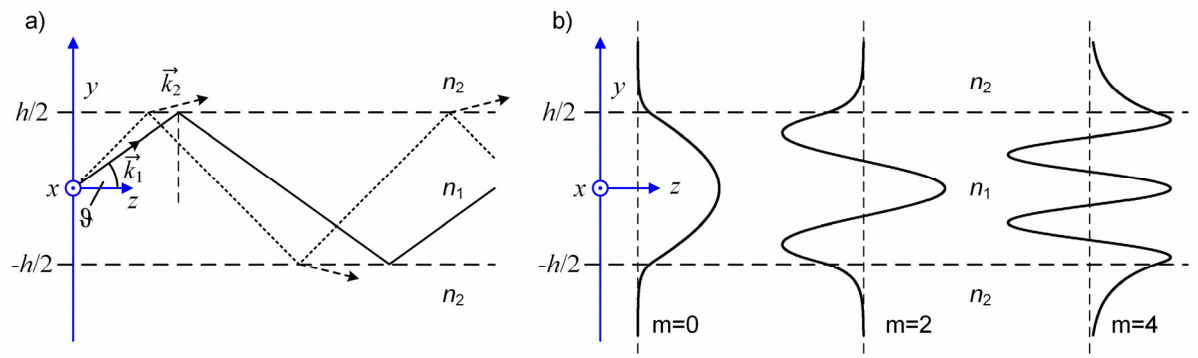

Figure 2.4: Formation of modes in a slab waveguide adopted from [5]. a) Sketch of the optical path of plane waves propagating inside the core medium by reflecting alternately at the upper and the lower boundary of the waveguide core. The solid line indicates a guided wave, while the dotted line represents a wave, which radiates partially into the cladding. b) Field distribution of the wave functions propagating in z-direction for $m = 0, 2, 4$. *The fields constitute a standing wave in y-direction inside the waveguide core* $-h/2 \leq y \leq h/2$ *and are evanescent beyond the boundaries* $|y| > h/2$.

composed, which maintain the same transverse field distribution and polarization upon the propagation along the waveguide axis [4]. These are the waveguide modes, which propagate along the z-axis.

For a transversally consistent field, the total phase difference after two consecutive reflections is

$$-2k_{1y}h + 2\varphi = -2m\pi\,, \tag{2.1}$$

where k_{1y} is the y-component of the wave vector of the plane wave, φ is the phase shift of the wave at the medium boundary. The constant m is an integer, which defines the order of the waveguide mode. Allowed modes of the slab waveguide for the mode indices $m = 0, 2, 4$ are sketched in Figure 2.4b).

The equation (2.1) yields the characteristic equation, which defines the allowed angles ϑ between the wave propagation vector and the z-axis, or in other words, the propagation constants of the waveguide mode. For TE-modes, it reads

$$w_m = \sqrt{V^2 - u_m^2} = \begin{cases} u_m \tan(u_m)\,, m = 0, 2, 4, \ldots \\ -u_m \cot(u_m)\,, m = 1, 3, 5, \ldots \end{cases} \tag{2.2}$$

with the transverse phase constant in the core u, the transverse cladding attenuation w, the normalized frequency V and the normalized propagation constant B. They are given by

$$\begin{aligned} u &= k_{1y}\frac{h}{2} & w &= |k_{2y}|\frac{h}{2} \\ V &= \frac{h}{2}k_0 A_N = \sqrt{u^2 + w^2} & B &= \frac{\beta^2 - k_2^2}{k_1^2 - k_2^2} = \frac{w^2}{V^2} = 1 - \frac{u^2}{V^2}\,. \end{aligned} \tag{2.3}$$

The value A_N is the numerical aperture. The eigenvalues of equation (2.2) are the propagation constants β of waveguide modes. Plane waves with other propagation constants cannot propagate. They are either attenuated along the z-direction or radiate into the cladding [5]. A graphical solution is given in Figure 2.5a) by the intersections of the functions on the left and right side of equation (2.2). Figure 2.5b) shows the associated normalized propagation constant as a function of the normalized frequency. It can be calculated from the characteristic equation (2.1). According to [6], it reads for the symmetric slab waveguide

$$V \cdot (1 - B) = m\pi + 2\arctan\left(\sqrt{\frac{B}{1-B}}\right). \tag{2.4}$$

The plot shows, that the increasing oscillation frequency of the incident plane wave excites an increasing number of modes, which are capable to propagate. By reference to this analysis, the waveguide geometry for a given number of modes can be derived.

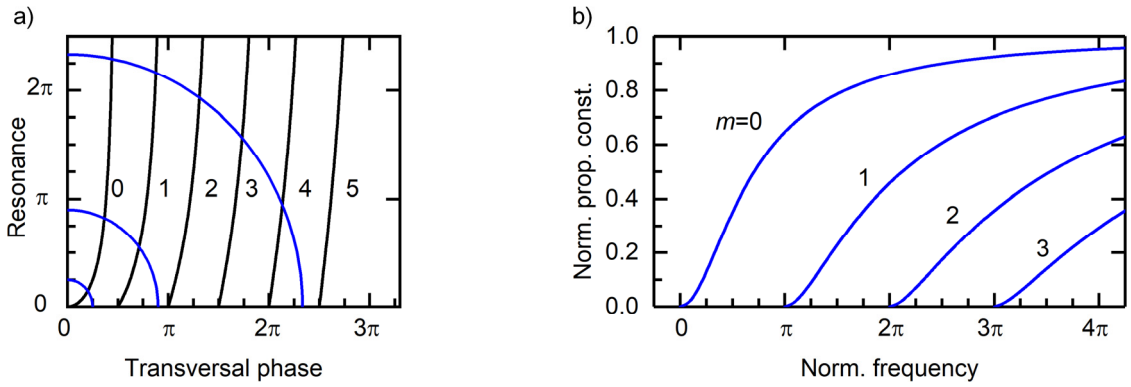

Figure 2.5: Graphical solution of the eigenvalue equation (2.2). a) The intersections represent possible propagation constants. b) Normalized propagation constant as a function of the normalized frequency of the incident plane wave according to equation (2.4).

2.1.3 Effective refractive index

The effective refractive index n_{eff} is a property, which describes the propagation of a guided mode in a waveguide. In contrast to the refractive index n, which is a material property, n_{eff} takes into account the waveguide geometry and the cladding material. The effective refractive index is larger than the refractive indices of the cladding materials and smaller than that of the waveguide core. It is given by

$$n_{\text{eff}} = \frac{\beta}{k_0}, \tag{2.5}$$

with k_0 being the vacuum wave number. The meaning of n_{eff} can be interpreted as follows: a plane wave would propagate in a medium of refractive index n_{eff} with the same phase velocity as the guided mode with the phase constant β [5].

The introduction of the effective refractive index allows for the reduction of the mathematic complexity of the waveguide analysis. Since it takes both the material and the waveguide geometry into account, a two-dimensional arrangement of refractive indices can be approximated by a one-dimensional stack [7]. This advantage of reducing complexity can be exploited for the simulation of optical waveguides, because a three-dimensional waveguide structure can be reduced to a two-dimensional problem. Thus, the requirements on memory and computation time can significantly be relaxed.

2.1.4 Multimode waveguides and self-imaging in MMI

A multi-mode interferometer (MMI) is a passive coupler that relies on the principle of self-imaging in a multi-mode waveguide. Due to the abrupt change of the waveguide width at the transition from an input single-mode waveguide to the multi-mode waveguide, higher order modes are excited and the input field is decomposed into guided modes of the multi-mode section. They co-propagate along the length of the MMI at different phase velocities and thus generate repeating interference patterns. Thus, the field is reproduced in single or multiple images at periodic intervals along the propagation direction [8].

The theory allows for the calculation of the positions, amplitudes and phases of the self-images. A schematic of the multi-mode waveguide with the essential values is sketched in Figure 2.6. The field $\Psi(x, 0)$ at the input is decomposed into the waveguide modes $\psi_i(x)$. After a distinct propagation length z_i $(i = 1 \ldots 4)$, the formation of direct or mirrored images as well as multiple images of $\Psi(x, 0)$ is observed due to the superposition of the propagating modes. Hence, the field distribution at the distance z reads

$$\Psi(x,z) = \sum_{i=0}^{m-1} c_i \psi_i(x) \exp[\mathrm{j}(\omega t - \beta_i z)]\,. \tag{2.6}$$

The integer m is the number of modes contributing to the formation of the image. The coefficient c_i is called the field excitation coefficient and is a complex normalization constant. The propagation constants β_i are associated to the respective waveguide mode $\psi_i(x)$ and ω is the angular frequency.

For the formation of a single direct image, the phase changes of all modes along z must be an even integer multiple of π. In that case, they interfere with the same relative phases as at the input ($z = 0$). Mirrored images are obtained for odd integer multiples of π. Multiple images occur for integer multiples of π/N, where N is the number of self-images. MMI can be designed to obtain various N×M-couplers. The value M is the number of occurrences of the N images at different lengths of the device. Low insertion loss and crosstalk can be achieved as well as a good balancing of the channels [9]. Hence, MMI are most successfully used as power splitters and combiners.

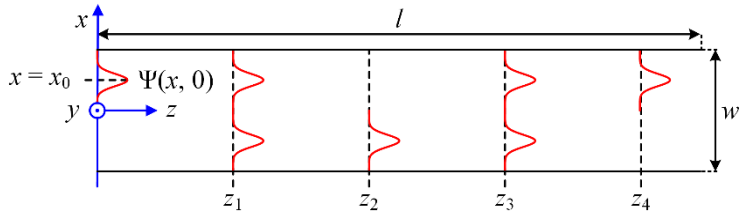

Figure 2.6: Multimode waveguide of width w and length l with an incident optical field $\Psi(x,0)$. At z_i ($i = 1 \ldots 4$), the formation of possible images are indicated. Those could be direct or mirrored single images or multiple images.

2.1.5 Diffraction-based spectrographs

In general, diffraction is the phenomenon of a wave changing its propagation direction when encountering an obstacle. For example, the obstacle could either be a reflective or a partial absorptive surface or a slit in an opaque medium. It can be understood as the forced emissions by oscillators, which are excited by an incident wave. A superposition of all emerging partial waves lead to interference patterns. The most basic approach is the description by means of the grating equation

$$\Lambda[\sin(\theta_\mathrm{i}) + \sin(\theta_m)] = m \cdot \frac{\lambda}{n}, \tag{2.7}$$

where Λ is the grating period, m the diffraction order and λ the vacuum wavelength. The refractive index n characterizes the region where the incident plane waves propagate towards the grating. A visualization is shown in Figure 2.7, taking the example of one period of a reflection grating. The solid lines may be interpreted as trajectories of the incident and reflected waves. A plane wave is incident on the grating at the angle θ_i, causing the appearance of multiple elementary waves. Their superposition composes diffraction waves in the m-th order emerging from the grating at the angle θ_m. In other words, the phase fronts of the incident wave hit the grating with a path difference $\Lambda \cdot \sin(\theta_\mathrm{i})$, while those of the emerging wave have a path difference of $\Lambda \cdot \sin(\theta_m)$. They interfere constructively, if the sum of the path

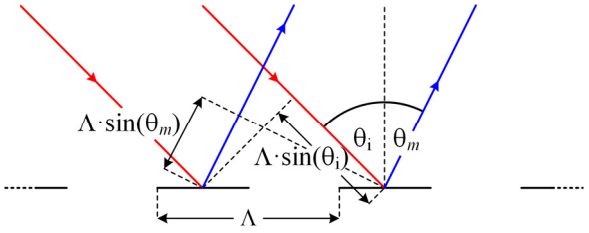

Figure 2.7: Visualization of the grating equation by reference to incident waves on a reflection grating. The solid lines may be interpreted as trajectories of the incident (red) and reflected (blue) waves.

differences equals an integer multiple of the wavelength. The phenomenon is exploited in various applications in integrated optic devices of which one is the realization of grating-based (de-)multiplexers.

The combination of a diffraction grating and a focusing element allows for building a spectrograph, which is capable of reproducing the image of an incident optical field. This has been achieved by the planar concave grating (PCG) based on a Rowland geometry [10], [11]. The schematic of a (de-)multiplexer based on a PCG spectrograph adopted from [12] is presented in Figure 2.8. The input waveguide and the output waveguides are located on a circle with the radius r, which is called the Rowland circle. The pole is the boundary point of the Rowland circle and the grating circle with the radius $2r$. The curved grating is constructed by means of projecting a virtual flat diffraction grating on the grating circle. The flat grating with the period Λ is parallel to the tangent touching the circles in the pole.

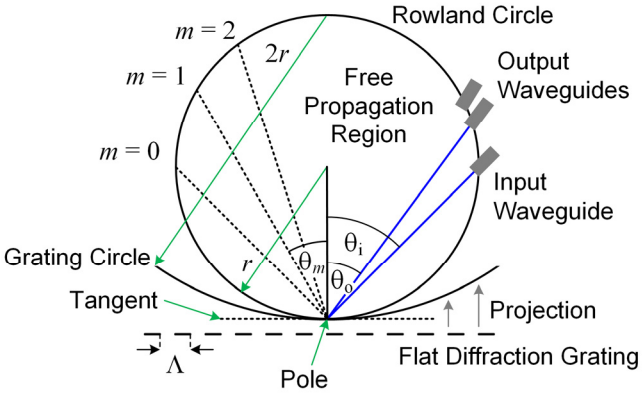

Figure 2.8: Schematic of a (de-)multiplexer based on a planar concave grating (PCG) spectrograph adapted from [12] and modified.

Using this configuration, an arbitrary point on the Rowland circle is imaged to another point on the same circle according to the diffraction order and the associated angles θ_m defined by the grating equation (2.7) for constructive interference [13]. In Figure 2.8, θ_o represents the angle, at which the array of output waveguides is aligned with respect to the grating normal. In order to achieve a compact PCG design, the diffraction order and the blaze angle are chosen as such the input waveguide and the output waveguide array are located in the same half-plane.

In a PCG, numerous reflectors assemble the curved reflector array. Given the dimensions of a photonic device, a Bragg grating can constitute a reflector very efficiently. Apart from this special application, Bragg gratings are used to build highly frequency-selective mirrors for semiconductor laser resonators or surface couplers to probe on-chip waveguides. The grating can be formed by a periodic corrugation of the waveguide or the cladding layer. The result is a weak modulation of the effective refractive index n_{eff} along the waveguide's propagation direction. The schematic is shown in Figure 2.9 [5]. The thickness of the waveguide varies with the grating period Λ. The grating teeth have the width w and the wells have the etching depth d. An incident wave, which is indicated by the blue arrows, propagates along the waveguide in z-direction. At the grating steps, a fraction of this wave is reflected.

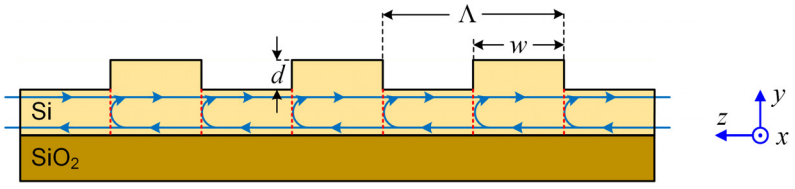

Figure 2.9: Schematic of a Bragg-reflector integrated into a silicon waveguide adapted from [5]. The grating is formed by a periodic corrugation of the waveguide, resulting in a modulation of the effective refractive index. At the grating steps, a fraction of the wave is reflected.

The phases of the reflected partial waves are shifted either by 0 or by π, according to whether n_{eff} is locally reduced or enhanced. All back-travelling partial waves are in phase, if the phase constant β complies with the Bragg condition, i.e. $\beta = \beta_{\text{B}}$. The phase of the initial wave, which continuously propagates in z-direction, remains unchanged upon traversing the grating steps.

$$\beta_{\text{B}} \cdot \Lambda = p\pi, \qquad p = 1, 2, \dots, \qquad \beta_{\text{B}} = \frac{2\pi}{\lambda_{\text{B}}} n_{\text{eff}} \tag{2.8}$$

λ_{B} is the Bragg wavelength and p is an integer which specifies the diffraction order of the grating. Hence, the relation between the grating period and the wavelength of the incident wave reads

$$2\Lambda \cdot n_{\text{eff}} = p \cdot \lambda\,. \tag{2.9}$$

2.2 Coupling of fibers and silicon-on-insulator waveguides

One of the fundamental aspects in designing integrated optical components is to provide an interface between different waveguides in order to facilitate the exchange of optical energy. In other words, the mode of a waveguide of one optical component is incident to a waveguide of another component where it excites one or more modes. For an efficient transfer of energy between the two waveguides, the largest possible overlap of the waveguide modes must be achieved.

2.2.1 Coupling efficiency and loss mechanisms

There are several mechanisms, which cause losses on the coupling between two waveguides. Except for losses due to the various misalignments, a major source for coupling loss is the mismatch of the mode-fields. It is sub-divided into the mismatch of the mode-field extent, its shape and the curvature of the phase fronts in the far-field. The possible misalignments are categorized by longitudinal, transversal and angular displacement. Longitudinal displacement is equivalent to defocusing the image along the optical axis. The transversal displacement is the areal displacement lateral to the propagation axis, while the angular misalignment describes the tilt of the optical axes of one waveguide with respect to the other.

The coupling efficiency Γ between two waveguides is calculated by solving the two-dimensional overlap integral between the optical fields $E_i(x, y)$ $(i = 1, 2)$ of the beams that are coupled from or to the respective waveguide facet. The two waveguides to be coupled are assumed to support fundamental modes with asymmetric Gaussian shapes, i.e. the mode field radii in x- and y-direction may be different [14]. The coupling is calculated by the overlap of two Gaussian beams, which enter or leave the respective waveguide. The two axes may be considered separately. The mode mismatch is essentially the mismatch of the mode-field radii $r_{s,i}$ $(s = x, y, i = 1, 2)$. A brief description of the Gaussian beam concept is summarized in Appendix A.1.

The coupling efficiencies due to the different alignment errors can be calculated separately and the x- and y-axis can be considered individually. The product of all contributions yields the total efficiency. At first, the ratio of the field radii of the two waveguide modes for each axis is defined:

$$\mu_s = \frac{r_{\text{s,2}}}{r_{\text{s,1}}}, \qquad s = x, y\,. \tag{2.10}$$

For a perfect alignment, the coupling efficiency due to the mismatch of the mode field radii is

$$\Gamma_{\text{mm},s} = 10 \cdot \log\left(\frac{2\mu_s}{1 + \mu_s^2}\right), \tag{2.11}$$

which implies that the efficiency decreases for a larger mismatch

The penalty on the coupling efficiency due to a longitudinal displacement by the length of the gap Δz between two waveguides arises from two effects. At first, the mode field radius rises with Δz. Given a perfect match at $\Delta z = 0$, this yields a mismatch of the mode field radii. On the other hand, the curvature

of the phase fronts of the incident Gaussian beam changes with Δz. Therefore, the coupling efficiency is given by

$$\Gamma_{l,s} = 10 \cdot \log\left(\frac{2\mu_s}{\sqrt{(1+\mu_s^2)^2 + (\Delta z/b_c)^2}}\right), \tag{2.12}$$

where b_c is the confocal parameter taking the curvature of the phase front into account. The impact of a longitudinal misalignment on the coupling efficiency from one waveguide to another is dependent on the coupling direction, because b is proportional to the waist of the Gaussian beam [14].

A transverse displacement Δs of the two waveguides deteriorates the coupling efficiency per axis according to

$$\Gamma_{t,s} = 10 \cdot \log\left[\exp\left(-\frac{2(\Delta s)^2}{r_1^2(1+\mu_s^2)}\right)\right]. \tag{2.13}$$

This is the case, when no defocusing or angular tilt is present, but the optical axes are not congruent. Finally, the coupling efficiency due to an angular misalignment reads

$$\Gamma_{a,s} = 10 \cdot \log\left\{\exp\left[-r_1^2\left(\frac{\pi \cdot n_{gap} \cdot \sin(\Delta\theta)}{\lambda}\right)^2 \cdot \frac{\mu_s^2}{1+\mu_s^2}\right]\right\}. \tag{2.14}$$

In this equation, n_{gap} is the refractive index of the medium between the two waveguides, $\Delta\theta$ is the angular offset of the optical axes and λ the wavelength of the coupled field. The calculated dependencies of the coupling efficiency on the different misalignments are visualized in Figure 2.10.

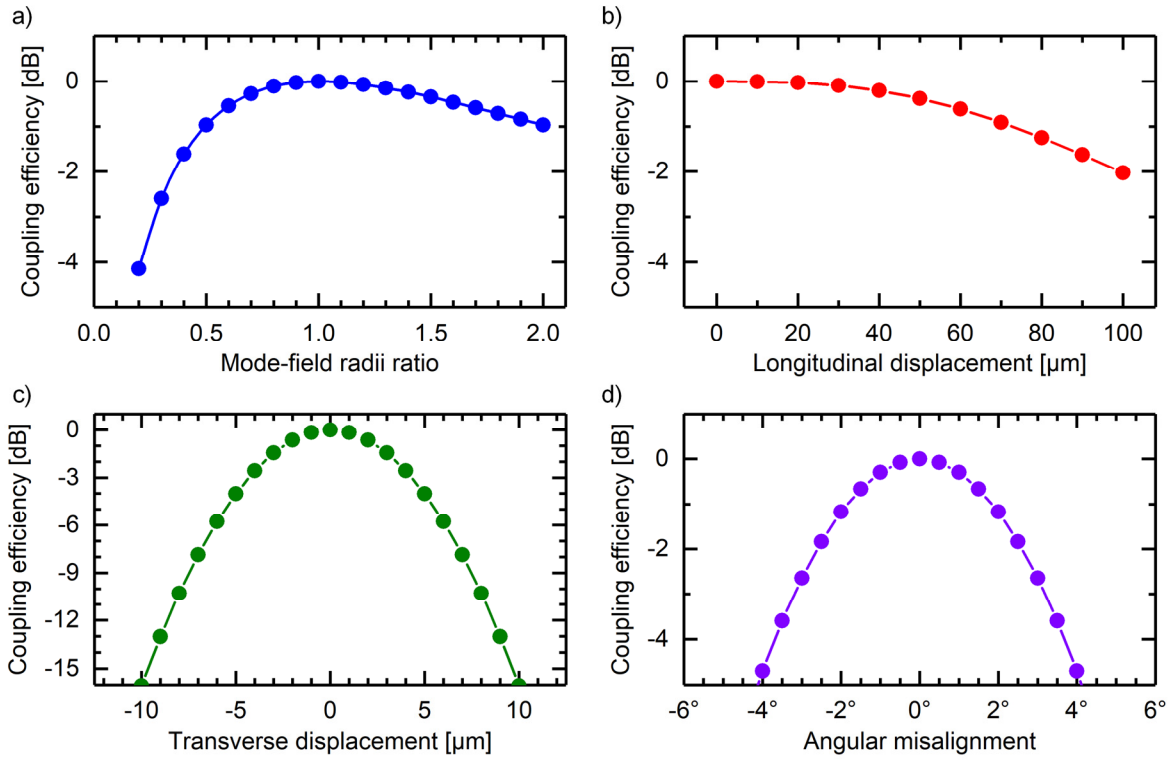

Figure 2.10: Visualization of the calculated dependencies of the coupling efficiency on the different misalignments: a) ratio between the mode-field radii of the two waveguides, b) longitudinal displacement, c) transverse displacement and d) angular misalignment. The coupling efficiencies in b) to d) are calculated for the optimum mode-field radii ratio ($\mu_s = 1$).

Since the coupling of a standard single-mode fiber (SMF) to an SOI PIC is considered, the mode-field radii differ significantly. Due to the high contrast of the refractive indices of silicon and silicon dioxide, the extent of the optical mode in the SOI waveguide is small compared to that of an SMF. Figure 2.11 shows the normalized magnitude of the electrical field in x- and y-direction of the fundamental TE-mode in a single-mode SOI strip waveguide of 0.5 µm width and 0.25 µm height. At 1/e the radii of the two half axes are 0.20 µm in x-direction and 0.14 µm in y-direction. In contrast, assuming a rotationally symmetric mode, the field radius of the SMF is 5.2 µm [15]. Considering only the extent of the waveguide mode in x-direction, the coupling loss would be 11 dB due to the mode-field mismatch according to equation (2.11) even at perfect alignment. Furthermore, due to the stronger confinement in y-direction, the loss becomes even higher. Hence, a mode-size transformation is required to adapt the mode of the SMF to that of the SOI waveguide.

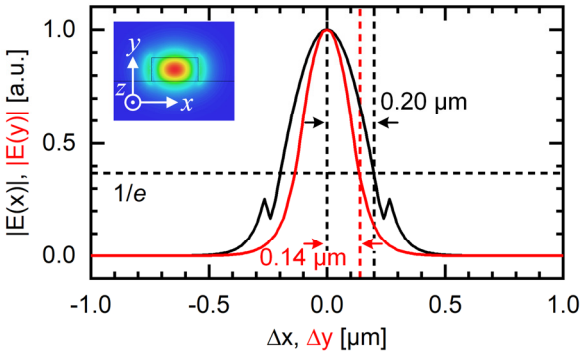

Figure 2.11: Normalized magnitude of the electrical field in x- and y-direction of the fundamental TE-mode in an SOI strip waveguide of 0.5 µm width and 0.25 µm height with a silicon dioxide cladding. The 1/e-radii of the two half-axes of the mode are highlighted. The inset shows the mode field distribution across the waveguide.

2.2.2 Mode size transformation

In order to adapt a propagating optical field in a waveguide to the confinement of another waveguide, a mode size transformation is required. The resulting insertion loss due to a mismatch of the mode-fields is discussed in the previous section. Optical tapers provide the means to adapt the extent of the mode and thus the effective refractive index along the propagation direction to another waveguide's dimensions. Possible applications are the conversion of the mode from an SMF to an integrated waveguide or from a strip waveguide to a rib waveguide. An adiabatic taper conserves the energy of the field upon the propagation along the taper by avoiding the conversion to higher-order modes or the radiation into the substrate. The transformation of the mode-field is considered adiabatic, if the variation of the taper width per unit of length is small [16].

The mode-field radius can be increased by up- and down-sizing the waveguide cross section. In an up-sizing taper, the guidance of the mode is successively improved while the mode-conversion per unit length (conversion rate) decreases. In practice, tapers with a constant conversion rate are favored which typically exhibit a horn-like shape. In a down-sizing taper, the guidance deteriorates with progressing propagation which is equivalent to an increasing conversion rate while the mode-field diameter increases. Practical taper designs employ an up-sizing structure for the lateral mode extension and a down-sizing taper for the vertical axis [14].

2.2.3 Grating couplers

Grating couplers are used in silicon photonics PIC to establish an out-of-plane coupling between an on-chip waveguide and an optical fiber. The fiber is aligned almost perpendicular to the chip's surface. In that application, the grating is used to redirect the propagation of an optical field.

The schematic is depicted in Figure 2.12a). It shows a silicon waveguide sandwiched between a silicon dioxide layer, which is suspended on a silicon substrate, and a cladding. The height of the waveguide is weakly modulated by indentations of the depth d. The result is a grating with the period Λ

and the width w of the grating teeth. The bold arrows indicate the propagation direction of the optical fields.

The mode in the waveguide with the effective refractive index n_{eff} is coupled to the cladding with the refractive index n_{c}. For the most efficient coupling, phase matching between the waveguide and the cladding is required, i.e. the propagation constants in z-direction of the field in the cladding and the mode in the waveguide core must be identical. Therefore, a Bragg-condition for the grating can be formulated. A derivation is given in Appendix A.2. For the first diffraction order the grating period Λ can be determined as a function of n_{eff}, n_{c} and the angle θ at which a monochromatic field of the wavelength λ_0 in the cladding propagates with respect to the grating normal

$$\Lambda = \frac{\lambda_0}{n_{\text{eff}} - n_{\text{c}} \sin(\theta)}. \tag{2.15}$$

However, a fraction of the optical energy is lost to the intended coupling. As indicated in Figure 2.12a), the field in the waveguide is also diffracted as such it radiates into the SiO_2-layer. Although reflection also takes place at the boundary to the silicon substrate, the optical field radiates further into the substrate. The loss due to radiation into the substrate can be reduced by tuning the duty cycle of the grating, which is the ratio w/Λ between the width of the grating teeth and the grating period. A significant improvement is achieved by selectively replacing the silicon substrate with a reflective layer, such as aluminum. This reduces the coupling losses but requires additional processing steps.

Apart from the grating, a mode-size converter is required for the efficient coupling of a standard single-mode fiber (SMF) and a silicon waveguide using a grating coupler. It is implemented by a tapered region to the waveguide, which is much longer than the grating interaction length. To maintain an adiabatic conversion and thus to obtain a high coupling efficiency, the taper length is at least 200 µm [17] but can be as long as 500 µm [18]. The mode size transformation by means of a taper is discussed briefly in the previous section. The schematic of a grating coupler with a linear taper attached is shown in Figure 2.12b). Noticeably the taper length governs the footprint of a coupling structure. To reduce spatial requirements, focusing grating couplers have been proposed [19], where focusing is achieved by curving the grating lines as shown in Figure 2.12c). Thus, they are ellipses with a common focal point, which coincides with the input of the silicon waveguide at $z = 0$. The device length reduces significantly by approximately one order of magnitude without a significant coupling penalty.

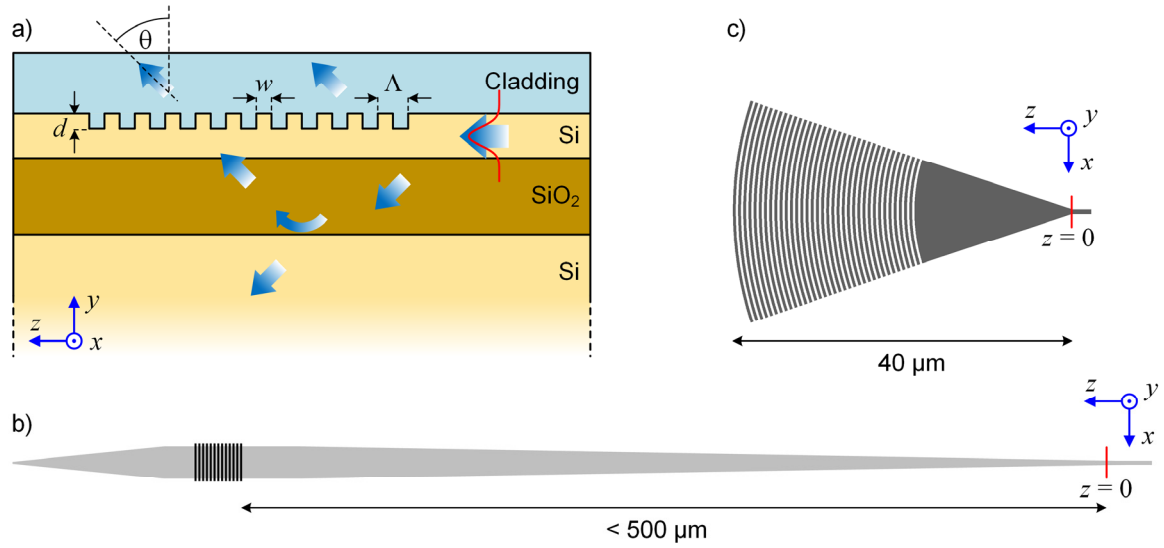

Figure 2.12: Operating principle and 1D schematics of grating couplers. a) The formation of the grating is achieved by selectively etching wells of depth d into the silicon waveguide. b) Conventional grating coupler with a linear adiabatic taper. c) Focusing grating coupler with curved grating lines. Schematics are not to scale.

The most prominent advantage of using grating couplers compared to edge couplers is that the coupler does not necessarily have to be located at the photonic chip's edge. Therefore, dicing and polishing the edges to access the couplers can be omitted. On the other hand, the disadvantage is the spectral dependence of the coupling efficiency, which originates from the dispersive nature of diffraction. Optimum coupling for a field at a given wavelength λ_0 is only achieved at the coupling angle θ. For the same reason, the grating coupler has a finite bandwidth.

Grating couplers can be manufactured in many ways. They are classified by the uniformity of the grating and by the required etch-steps. The most basic design is a coupler with a uniform grating, which is fully etched into the waveguide. In a uniform grating, the grating period and the duty cycle are constant throughout the entire coupler. However, the approximately exponential shape of the mode diffracted by a uniform grating does not match the Gaussian profile of an optical fiber and therefore results in a coupling loss of more than 1 dB [20]. A fully-etched grating coupler can reach a coupling efficiency in the range from -4 dB to -5 dB [21], [22].

A spatial variation of the grating's geometry can optimize the shape of the diffracted field and thereby reduce the coupling loss due to mode mismatch. This non-uniformity is most often achieved by ramping the period and/or the duty cycle of the grating in the propagation direction of the waveguide mode [23]. The challenge in designing non-uniform gratings is to find an optimized design, which does not require a feature size exceeding the resolution of standard CMOS processes using deep-UV lithography. Taking this into account, an insertion loss of approximately 3 dB can be achieved [20].

Another measure to influence the coupling efficiency of a grating coupler is the etch depth of the gratings trenches. As opposed to the fully-etched gratings, the couplers have shallowly-etched trenches to form the grating. This increases the coupling loss because the perturbation of the refractive index is reduced. On the other hand, it reduces scattering of the optical field at the grating steps and thereby the back reflections into the waveguide [1], [24]. Moreover, the loss due to the penetration of the optical field into the substrate is reduced [25].

3 Optical communication systems

In an optical communication system information is modulated on an electromagnetic carrier wave at a frequency in the optical spectrum. The carrier can be emitted by incoherent light sources such as light-emitting diodes or by coherent light sources such as lasers. The transmission medium can either be air, or a waveguide, which is most often an optical fiber. In that case, one speaks of a fiber-optic communication system. In the early 1980s first commercially available systems with multi-mode fibers running at a bit rate up to 100 Mbit/s where deployed [26]. In 1986 single-mode optical fibers were demonstrated with a transmission loss of 0.35 dB/km at a wavelength of 1310 nm and 0.21 dB/km at 1550 nm, respectively [27]. Together with the invention of dispersion-compensating fibers and the advent of optical amplifiers in the early 1990s, this paved the way for long-haul transport networks. Transmission systems operating at a bit rate up to 10 Gbit/s became available at that time. From 1992 on, the WDM-technique was applied in fiber-optic systems, doubling the data rate approximately every half year. Already in 2001, a record per-fiber bit rate of 10 Tbit/s was achieved. In this chapter, the fundamentals of modulating optical signals are presented and the effects that are exploited to realize electro-optic modulators on the SOI platform are explained. Furthermore, the integration and packaging of photonic components are addressed. In particular, the coupling of optical fibers to sub-micrometer waveguides are discussed and prerequisites for a permanent fiber-to-chip coupling assembly are presented.

3.1 Modulation of optical signals

The simplest way to generate an optical data signal is the switching between two levels of optical intensity and thus encoding binary zeros and ones. This scheme is referred to as two-level amplitude shift keying (2ASK). The basic form is the nonreturn-to-zero on/off keying (NRZ-OOK), where the signal level remains at the same level if two consecutive symbols are equal. The corresponding constellation diagram is shown in Figure 3.1a). The most basic receiver is a photodiode, which detects the intensity modulation of the incident signal and converts it to modulated electrical current.

By introducing a coherent receiver to an intensity-modulation transmission system, its sensitivity improves compared to a direct-detection scheme. At a coherent receiver, the incident signal is superimposed with a local oscillator and a photodetector detects the beating signal. That also allows for extracting data encoded by manipulating the frequency, the phase or the polarization of the carrier. For example, binary symbols can be defined not by different intensity levels, but by a phase shift of π as depicted in Figure 3.1b). This modulation format is referred to as binary phase shift keying (BPSK). Assuming a fixed average power, the symbol spacing is enhanced compared to that of 2ASK, which yields an improved receiver sensitivity [28]. Modulating the amplitude and the phase also enables to encode more than one bit per symbol. This either increases the data rate of the channel or improves its spectral efficiency. The constellation scheme of *quadrature phase shift keying* (QPSK) is depicted in Figure 3.1c). Two bits per symbol are encoded with four constellation points in the complex plane, each differing by a phase shift of $\pi/2$. If the phase shift is halved further, the 8-*level phase shift keying* (8PSK) in Figure 3.1d) is obtained, resulting in three bits per symbol. Furthermore, information can be encoded on both the amplitude and the phase of the carrier to increase the number of bits per symbol.

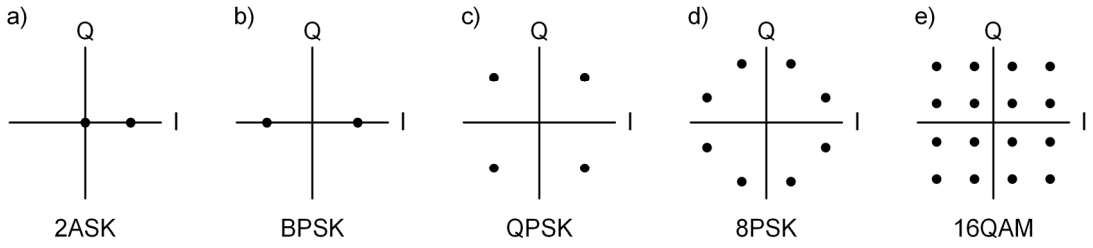

Figure 3.1: Constellation diagrams in the complex plane for different modulation formats. a) 2ASK (1 bit/symbol) b) BPSK, (1 bit/symbol), c) QPSK (2 bits/symbol), d) 8PSK (3 bits/symbol) and e) 16 QAM (4 bits/symbol)

Generally, these schemes are referred to as multilevel *quadrature amplitude modulation* (m-QAM). The square 16QAM scheme is sketched in Figure 3.1e). It encodes 4 bits per symbol at 3 amplitude and 12 phase levels. The exact mapping of constellation points can be chosen according to the dominating channel impairment.

The modulation of both amplitude and phase is state-of-the-art in coherent optical transmission systems. Advances in digital signal processing (DSP) allow for highly efficient forward error correction (FEC) techniques and digital pre-equalization that mitigates the impact of chromatic dispersion. The applied modulation formats in commercial systems are BPSK in submarine links, QPSK in long-haul terrestrial systems and 16QAM in metropolitan and regional networks, achieving a data rate per fiber of up to 200 Gbit/s [29]. Indeed, the continuous growth of internet traffic constantly demands a growth in intercontinental transmission capacity. Recently, a single-fiber transmission capacity of 65 Tbit/s over 6600 km using 64QAM modulation achieving 6 bits per symbols was demonstrated. Moreover, a record spectral efficiency was achieved at a data rate of 34.9 Tbit/s over the distance of 6375 km by also encoding 6 bits per symbol using amplitude and phase shift keying (APSK) on two polarizations [30]–[32].

In contrast to long-haul and intercontinental networks, the constraints on the expenses for installation and operation of short-range infrastructures are much more stringent. The most prominent example is the access network, which connects network subscribers to the central office. The infrastructure is most often a point-to-multipoint architecture in a passive optical network (PON) and covers a distance of less than 20 km. The requirements for future access networks are a bi-directional transmission capacity of 1 Gbit/s per user and low-cost subscriber equipment [29].

A quite similar situation is found in the infrastructure of today's and future data centers. Those are required for modern high-performance computing and big-data analysis as well as media streaming and cloud computing services. A data center consists of thousands of computing nodes including processors, memory sub-systems and mass storage devices. Apart from the power consumption of such multi-node systems, a major challenge is to establish an interconnection network [29]. The high number of computing nodes or servers demands for low-cost interconnects providing a sufficiently high data rate while consuming only a small amount of energy. The transmission distance is typically in the range of a few hundred meters, which is why intensity modulation and direct detection (IM-DD) is favored. Deployed optical links operate at a data rate of up to 14 Gbit/s while components for standardized 28 Gbit/s architectures are ready for commercialization [33]. Already at the present day, active optical cables with transceivers operating at a data rate of 100 Gbit/s for short-range interconnects are commercially available [34].

Even on the smallest scale, optical data transmission is replacing high-speed electronic links. For example, optical short-range interconnects allow for inter-chip communication without soldered wires or capacitive connections. Several architectures have been proposed, which are capable to integrate multi- and many-core computer systems along with the required periphery on a common photonic interposer board. Compared to electrical connections, this is beneficial for the system's latency as well as the energy consumption. Moreover, neither the density of electronic pins nor the distance between the system components pose a limit to integration [35], [36].

3.2 Modulation techniques

The most basic method of encoding data on an optical carrier is switching the intensity of a light source such as a laser diode by changing the injection current. Due to the coupling of the amplitude and the phase, a broadening of the emission spectrum accompanies the intensity modulation. This may limit the length of the transmission link due to increased fiber dispersion. To prevent spectral broadening, an external modulator can switch the optical carrier's intensity. Most often, this is achieved by using a Mach-Zehnder modulator (MZM), where a phase shifter is inserted in each of the arms of an interferometer. A schematic is sketched in Figure 3.2a). An incident optical field E_{in} splits into the two

arms of the interferometer ($i = 1, 2$). The phase shifter in each arm changes the phase of the respective field by φ_i according to the applied voltage V_{Bi}. The amplitude of the output field E_{out} is the superposition of the fields from the two arms. For an input optical field E_{in}, it is given by

$$E_{out} = \exp\left[\mathrm{j}\frac{1}{2}(\varphi_1 + \varphi_2)\right]\cos\left[\frac{1}{2}(\varphi_1 - \varphi_2)\right]E_{in}. \tag{3.1}$$

The intensity is given by the square of the absolute value of the amplitude $|E_{out}|^2$. The transfer functions of the amplitude and the intensity are sketched in Figure 3.2b). Despite the cosine and squared cosine shape, a linear operating range can be chosen for both functions. The amplitude can be approximated by a linear function in the proximity of zero. For the intensity, a similar approximation is legitimate at the quadrature point. If the phase shifts of the upper and the lower arm are chosen to have opposite signs, i.e. $\varphi_2 = -\varphi_1$, then E_{out} is purely amplitude-modulated. This is called the push-pull operation of the modulator [37].

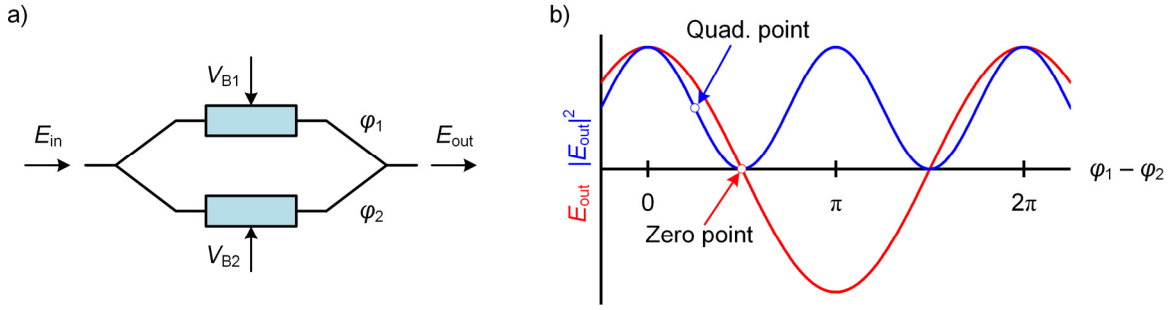

Figure 3.2: a) Schematic of a Mach-Zehnder modulator with a phase shifter in each of the interferometer arms. b) MZM transfer function of the field amplitude and intensity in push-pull operation. In the proximity of the marked operating points the respective transfer function can be approximated linearly.

Phase shifting is achieved by changing the real refractive index and thus the propagation velocity of an optical wave in a medium. The implementation is dependent on the material platform. A most effective way is exploiting the linear electro-optic effect, which is also known as the Pockels effect. It is a second-order non-linear effect, that is, the refractive index changes proportional to the applied electric field. It is only present in materials without inversion symmetry, i.e. where the second-order component of the susceptibility is non-zero [38]. This effect is used in commercially available electro-optic modulators based on lithium niobate. In some materials with non-vanishing third-order susceptibility, also the quadratic electro-optic effect (Kerr-effect) is available. In that case, the refractive index changes proportionally to the square of the applied electric field.

In contrast to the modulation of the real part of the refractive index, electro-absorption modulators (EAM) manipulate an optical carrier's intensity by means of changing the absorption coefficient of the material in response to an applied electrical field. The underlying mechanism is described by the Franz-Keldysh effect. Applying an electrical field to a bulk semiconductor allows for the tunneling of charge carriers and the bandgap energy is therefore reduced. Thus, the absorption spectrum is extended towards a photon energy which is lower compared to that without an applied voltage. In quantum-well structures, the most prominent mechanism in the presence of an electric field is the quantum-confined Stark effect (QCSE). Similar to the Franz-Keldysh effect, the electric field induces a shift of the energy levels of the conduction band and the valence band. The result is a change of the absorption coefficient, which is accompanied by a change of the real refractive index [39].

Another device with the potential to modulate the intensity of an optical field is the ring resonator. In principle, it is a waveguide loop with a defined geometry. Resonances occur due to constructive interference, if the optical path length of the ring equals integer multiples of the wavelength. The coupling to adjacent waveguides can be achieved by the overlap of the evanescent fields in a directional coupler or by a multi-mode interferometer (see section 2.1.4). The most basic functional device consists of a resonator ring and one bus waveguide. The incident field from a bus waveguide is coupled to the

ring and from there back via the same coupler. The result is an all-pass filter, with spectral notches evenly separated by the free spectral range [40]. By tuning the effective refractive index in the ring, the spectral location of the notch can be manipulated. Thus, the device can act as an intensity modulator.

3.3 Quality measures of communication channels

To enable retrieving the electrical data from an optical signal, a photo receiver is used. Regardless of the detection method, the essential component is a photodetector, which typically is a semiconductor photodiode. It converts the incident optical power P_{opt} to a photocurrent I_{p} by the absorption of photons. However, several noise mechanisms lead to the fluctuation of the electrical signal, which eventually yields a degradation of the signal quality. The fundamental noise mechanisms in the receiver are shot noise and thermal noise. Additional contributions may stem from intensity fluctuations of the laser, the spontaneous emission in active media of optical amplifiers or the fluctuations of the number of charge carriers in avalanche photodiodes. Shot noise occurs due to the fact, that an electric current is a stream of electrons that are generated at random times. It can be attributed neither to the light source nor to the detector, because the fluctuation manifest only upon the interaction between the photons and the detector. In contrast, thermal noise occurs in any resistor due to thermal motion of charge carriers [5], [26].

Signal degradation due to noise occurs, because the fluctuations result in a distribution of the signal levels around their mean values. Thus, an optimum decision threshold has to be found to distinguish between the logical levels with as few detection errors as possible. The signal degradation is quantified by the signal-to-noise ratio (SNR) given by the ratio of the average signal power and the noise power. Given a Gaussian distribution of the signal levels associated to the respective logical values and an optimum decision threshold, the SNR relates to the bit error ratio (BER). The BER is defined by the ratio of the number of bits that are identified incorrectly by the decision circuit and the total number of received bits. It can be determined experimentally by comparing a received bit stream with a reference or, with restrictions, by extracting the bit error parameter (Q-parameter) from a measured eye diagram.

In practice, a receiver sensitivity is determined to achieve an error-free transmission. Given a fixed extinction ratio of the signal source, the sensitivity is defined by the minimum average optical input power, which is required to maintain a given target BER. Apart from noise, other sources of impairments are the non-linear behavior of active components such as optical amplifiers in the transmission link or timing errors such as digital jitter. While the former manifests as non-linear signal distortions, the jitter reduces the SNR due to fluctuations in the sampling time.

3.4 Electro-optic modulators on a silicon-on-insulator platform

Building photonic components from a silicon-based technology platform is considered a key contribution to dealing with the continuously growing data traffic worldwide. Highly integrated components can be manufactured at low costs with a very high yield in complementary metal-oxide semiconductor (CMOS) processes [41]. Hence, photonic transceivers become attractive for cost- and power-efficient mass-market applications such as optical network units (ONU) at communication network subscriber's premises, enabling fiber-to-the-home (FTTH) services. In addition, large-scale data centers, where thousands of servers operate in parallel, will profit from utilizing silicon-based optical links as energy-efficient, high-speed and low-cost interconnects.

However, in contrast to many semiconductor materials, silicon does not exhibit the linear electro-optic effect due to the inversion symmetry of the crystal. Moreover, the Kerr effect and the electro-absorption effects are weak at the targeted operation wavelengths of 1310 nm or 1550 nm, respectively. Possible alternatives to achieve modulation in silicon are exploiting the plasma-dispersion effect or the thermo-optic effect.

Recently, also other methods to achieve modulation in silicon have been demonstrated. In the silicon-organic hybrid (SOH) technology, a conventional slot waveguide is filled and functionalized with an organic cladding material exhibiting a strong linear electro-optic effect. The optical field and the electric field of the modulation signal are strongly confined in the slot waveguide and a high modulation efficiency can be achieved due to the strong overlap of both fields [42]. However, this technology requires fabrication steps beyond CMOS processing and the long-term stability of the cladding material is yet to be shown. Moreover, in the plasmonics technology, very compact phase modulators based on metal-dielectric-metal waveguides can be built. A surface plasmon polariton (SPP) is an electromagnetic surface wave, which propagates along a dielectric-metal interface. The refractive index of the dielectric can be manipulated by applying a voltage and thus, the phase of the SPP is changed. The technology exploits the optical properties of metallic nano-structures in order to route and manipulate optical fields. Therefore, it offers many applications beyond the modulation of optical signals, such as sensors or switches as well as compact photodetectors [43].

Within the scope of this work, modulator technologies that can be realized with standard CMOS processes are considered. Those are depletion-type pn-modulators relying on the plasma-dispersion effect and modulators exploiting the thermo-optic effect. They are of particular interest for data transmission systems for detector read-out applications due to the maturity of the technology, their durability and their potential to be optimized for the operation in harsh environments. The operation principles are discussed in the following sections.

3.4.1 Plasma-dispersion effect

The plasma-dispersion effect describes the dependency of the complex refractive index on the concentration of free carriers in the material. The mechanisms to manipulate the carrier concentration can be carrier injection, accumulation or depletion. Devices based on carrier-injection are implemented by a pin-junction across a waveguide and are considered to have the highest efficiency. However, this is at the expense of the modulation bandwidth, which is governed by the lifetime of the minority carriers. In contrast, a modulator based on carrier-depletion employs a pn-junction across the waveguide, which is operated at a reverse bias. The carrier density is manipulated by varying the width of the depletion region. The modulation bandwidth is not limited by the lifetime of the charge carriers. However, it yields only a low efficiency compared to carrier injection, because of the small change of the carrier density with varying voltage. Still, it is the preferred mechanism for building a high-speed modulator. The challenge is to find an optimum geometry, which combines a high bandwidth, an adequate modulation efficiency, a small footprint and an acceptable loss of the device. Optimized devices have been demonstrated: an MZM with 3.5 mm phase shifters operating at a data rate of 10 Gbit/s exhibits an extinction ratio of 18 dB [44]. With a similar device, a data rate of up to 40 Gbit/s has also been achieved at a significantly reduced extinction ratio of 6.5 dB. Moreover, in [45] an MZM with 0.5 mm phase shifters is presented, which operates at 52 Gbit/s. However, the resulting extinction ratio is only 2 dB. Typical values for the voltage-length product $V_\pi L$ at low bias voltages are between 1.5 Vcm and 2.5 Vcm.

Figure 3.3 represents the schematics of two different phase modulator designs in areal and cross-sectional view. Both variants are implemented in a strip-loaded waveguide. The optical mode is concentrated in the strip region. The edges of the slab are highly p- or n-doped, respectively to provide for a high conductivity, where the metal (Al) contacts are attached. In the carrier-injection phase-modulator shown in Figure 3.3a), the region between the doped regions remains intrinsic silicon. Upon applying a forward voltage, free charge carriers are injected into the strip region and thus change the refractive index. In the depletion-type phase modulator in Figure 3.3b), the strip region includes a pn-junction. The p- and the n-region are lightly doped compared to the slab sections and a depletion region develops across the junction. When a reverse bias is applied, its width increases and the refractive index is changed. Both modulator geometries can be fabricated in standard CMOS processes.

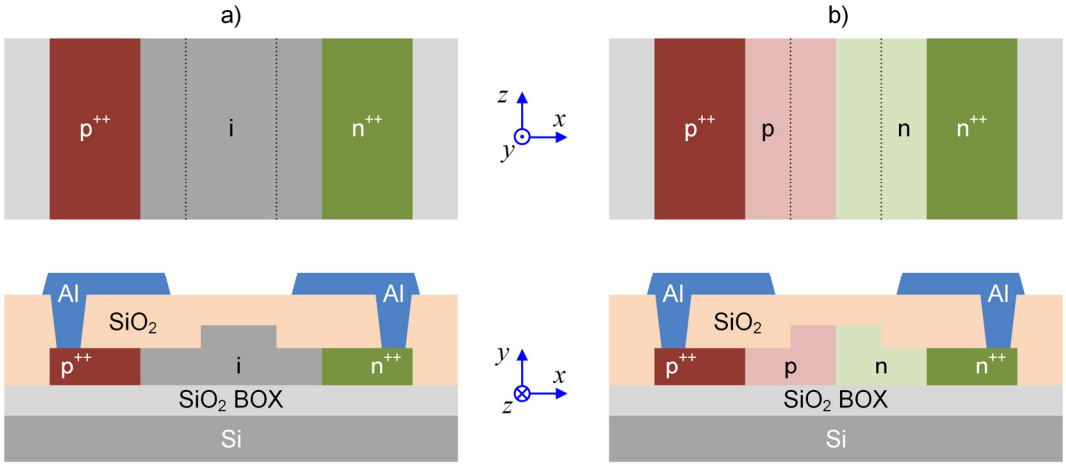

Figure 3.3: Areal view (top) and cross section (bottom) of possible phase modulator designs on the SOI platform based on the plasma-dispersion effect. a) Carrier injection modulator and b) carrier-depletion modulator.

In order to achieve a modulation bandwidth up to the Gigahertz range, the metal electrodes are implemented as transmission lines along the strip-loaded waveguide. Thus, the capacitance is distributed and therefore minimized, which allows for very long electrodes. The electrical wave of the driving signal propagates in the same direction as the optical wave. Provided a matching of the propagation velocities, this allows for interaction over the entire length. Consequently, long modulators can be designed, of which the small change of the refractive index per unit length accumulates to a sufficient total phase change [46].

The plasma-dispersion effect has been studied extensively by Soref and Benett [47]. They compared data for the change of the refractive index from the literature with their own results of absorption experiments. For electrons, their results were in good agreement with the Drude-model, while a correction was required for the holes. The investigation led to simplified expressions to predict the change of both the refractive index and the absorption with changing carrier density. At a wavelength of 1550 nm, the relations for the change of the refractive index Δn and the change of the absorption $\Delta\alpha$ are as follows:

$$\Delta n = \Delta n_\mathrm{e} + \Delta n_\mathrm{h} = -[8.8 \times 10^{-22} \times \Delta N_\mathrm{e} + 8.5 \times 10^{-18} \times (\Delta N_\mathrm{h})^{0.8}] \tag{3.2}$$

$$\Delta\alpha = \Delta\alpha_\mathrm{e} + \Delta\alpha_\mathrm{h} = 8.5 \times 10^{-18} \times \Delta N_\mathrm{e} + 6.0 \times 10^{-18} \times \Delta N_\mathrm{h}. \tag{3.3}$$

$\Delta n_{\mathrm{e,h}}$ is the change of the refractive index resulting from a change of the concentration of the free electrons or holes, respectively while $\Delta\alpha_{\mathrm{e,h}}$ is the contribution to the absorption due to the change of electron or hole density $\Delta N_{\mathrm{e,h}}$, respectively. Similar expressions hold for the wavelength of 1310 nm.

The charge carrier distribution $\Delta N_{\mathrm{e,h}}$ is dependent on the applied bias voltage V, because it is equivalently described at the pn-junction by the width w_dep of the depletion region. The relation reads [48]

$$w_\mathrm{dep} = \sqrt{2\frac{\epsilon_0\epsilon_\mathrm{r}}{q}(V_0 - V)\left(\frac{1}{N_\mathrm{A}} + \frac{1}{N_\mathrm{D}}\right)}, \tag{3.4}$$

where ϵ_0 is the vacuum permittivity, ϵ_r is the relative permittivity and q the elementary charge. $N_{\mathrm{A,D}}$ is the concentration of the respective dopant species and V_0 is the built-in potential of the junction. The bias voltage V is applied by an external source. Equation (3.4) shows that w is inversely proportional to the square root of carrier concentrations, which are dominated by the respective ionized doping species. On the other hand, w also relates proportionally to the square root of V. According to the Drude model (despite the constraints described above), the change of the refractive index Δn and the change of the absorption $\Delta\alpha$ are therefore likewise proportional to the square root of V. Although the extent of the

depletion zone dominates the effective refractive index in the waveguide, equation (3.4) is not sufficient for a complete analytical description. In order to quantify the change of the effective refractive index with the bias voltage, the overlap of the depletion zone with the guided mode has to be taken into account.

The modulation bandwidth of a depletion-type pn-modulator is dominated by the junction capacity and the resistances of the neutral regions between the highly-doped regions and the depletion zone. Therefore, the device can be modelled by a series circuit of the resistances R_{sn} and R_{sp} representing the p-doped or the n-doped region, respectively and the depletion region capacity C_{dep}. Further influences stem from the capacity of the transmission line and the resistance and inductance of the deposited metal. According to these considerations, the cutoff frequency for the reverse-biased diode is given by

$$f_{\mathrm{c}} = \frac{1}{2\pi\left(R_{\mathrm{sn}} + R_{\mathrm{sp}}\right)C_{\mathrm{dep}}}. \tag{3.5}$$

Each of the resistances R_{sn} and R_{sp} is the sum of the resistances in the slab and in the strip region. The particular resistances can be calculated from the geometry and the conductivity σ of the majority charge carriers in the respective region

$$R = \frac{1}{\sigma}\frac{w_{\mathrm{r}}}{h_{\mathrm{r}}L}. \tag{3.6}$$

w_{r} is the width and h_{r} the height of the respective region. The total length of the phase shifter is L. Due to the reduced height, the resistance in the slab is typically higher than in the strip region and thus has the stronger influence on the total resistance [49]. Although the depletion region's capacity is composed of several contributions, it can be approximated by the capacity of a plate capacitor as a function of the plate dimensions

$$C_{\mathrm{dep}} = \epsilon_0\epsilon_{\mathrm{r}}\frac{hL}{w_{\mathrm{dep}}}, \tag{3.7}$$

where h is the height of the waveguide strip.

3.4.2 Thermo-optic effect

The thermo-optic effect describes the variation of the refractive index upon a change of the temperature of a material. In silicon, this property is exploited to construct opto-electronic sensors or devices such as optical switches, tunable filters or electro-optic modulators [50]. At a wavelength of 1550 nm and an ambient temperature of 300 K, silicon exhibits a thermo-optic coefficient $\mathrm{d}n/\mathrm{d}T$ of 1.86×10^{-4} K^{-1}. In contrast, the coefficient of thermal expansion (CTE) is smaller by two orders of magnitude [51].

Although quite limited in their bandwidth, thermo-optic modulators achieve a high modulation efficiency on an extremely small footprint. They can be used quite efficiently whenever a high bandwidth is of minor importance. Typically, they can be deployed as supplementary phase shifters in Mach-Zehnder modulators for the operating point adjustment. Devices with different geometries and heater architectures have been demonstrated. Provided that the fabrication relies on standard CMOS processes, the required electrical power to achieve a full π-shift is typically in the range between 10 mW to 25 mW [52].

However, a high thermo-optic coefficient may also prove to be a drawback. In wavelength-selective devices such as Fabry-Perot cavities or diffraction gratings, the change of the refractive index due to the thermo-optic effect may yield a deviation of device characteristics upon a change of the ambient temperature [50]. For example, a change of the effective refractive index in a diffraction-based spectrograph results in a shift of the diffraction angle associated to a given wavelength. Taking the example of a grating-based (de-)multiplexer, this manifests in a spectral shift of the transmission windows. Even in material systems where the thermo-optic coefficient is significantly smaller, the

impact of the ambient temperature on device characteristics is not negligible. In the case of semiconductor laser diodes utilizing a distributed-feedback (DFB) resonator, the emission wavelength is dependent on the grating period, which in turn is temperature-dependent via both the thermal expansion and the thermo-optic effect [53].

3.4.3 Silicon photonics for next-generation communication systems

The silicon-on-insulator (SOI) technology platform is most promising for telecommunication applications. The high contrast of the refractive indices of silicon (Si) and silicon dioxide (SiO_2) enables the miniaturization of opto-electronic components to the range of a few hundred nanometers. That allows for the dense integration and thus a small footprint of photonic integrated circuits (PIC). Additionally, silicon photonic components can be fabricated in CMOS processes and high-quality SOI-wafers are widely available [54]. Both reasons allow for a very high reproducibility and low-cost products. Moreover, many foundries offer multi-project wafer runs, where different PIC designs can be combined on a single wafer. This helps to reduce costs during PIC development, where only a small number of prototypes for testing and validation are required. Finally, CMOS-based photonic components offer the unique possibility to integrate electro-optic components monolithically with electronic circuits on the same wafer. At present, this is, however, only feasible for special applications, where short electrical connections are of utmost importance. In most cases, the area occupied by the photonic circuit is much larger than the electronic circuitry. Additionally, the latter requires an advanced CMOS process due to smaller feature sizes compared to the former. Therefore, the production costs of the PIC become excessively higher compared to separate fabrication using the appropriate processes [37].

Various components can be included in a PIC. For one, there are numerous passive elements such as waveguides, (de-)multiplexers, mode-size converters and grating couplers. On the other hand, waveguides can be functionalized by doping, enabling the construction of modulators and photodetectors. However, there are still some challenges on the path to a complete set of photonic components: Due to the indirect bandgap, there is no way to build efficient electrically pumped lasers. Therefore, the hybrid integration of III-V semiconductor components either by flip-chip bonding or epitaxial growth is required [55]–[57]. As discussed in the previous section, silicon does not have a linear electro-optic effect due to the inversion symmetry of the crystal. A significant modulation effect can only be achieved by exploiting either the plasma-dispersion effect or the thermo-optic effect.

3.4.4 Complementary technologies to silicon photonics

Apart from silicon, modulators for optical communication systems can be fabricated on various material platforms. Lithium niobate ($LiNbO_3$) and gallium arsenide (GaAs) exploit the linear electro-optic effect (Pockels-effect) to modulate optical carriers while indium phosphide (InP) uses primarily the quantum-confined Stark effect (QCSE). Numerous devices based on those material systems are commercially available. $LiNbO_3$ modulators are widely used in long-haul terrestrial and submarine optical links, where fiber dispersion limits the system performance. Offering a high modulation bandwidth and excellent signal quality, they have proven their reliability in deployed telecommunication systems over decades [58]. However, with a length of several centimeters, the devices have a large footprint, which makes scaling for short-range applications difficult and opposes a dense integration. Only of late, the development of nano-photonic electro-optic modulators on the $LiNbO_3$ material platform has been endeavored [59].

Due to the high electron mobility and low-loss substrate, GaAs is a material system well-known for ultra-fast electronic components. Using appropriate compounds, also waveguides for telecommunication wavelengths can be fabricated. Moreover, active devices such as lasers, photodetectors and modulators can be built. The electro-optic performance is similar compared to $LiNbO_3$ while the insertion loss is slightly higher [60]. However, the device footprint can be reduced significantly by applying a slow-wave electrode structure. As a result, the phase velocity of the electrical

signal matches that of the optical wave. Several designs have been proposed, which yield a device length of one centimeter [61]–[63].

The InP material platform is perhaps the strongest competitor to silicon photonics, since it provides an almost equally dense integration. A distinct advantage of the material system is the direct band gap, which allows for the fabrication of efficient laser diodes and semiconductor optical amplifiers [64]. Hence, complete transmitters consisting of a semiconductor continuous-wave (cw) laser and an external modulator can be monolithically integrated on a single photonic chip [65]. However, the material is more expensive and only available on small wafers. Moreover, the fabrication relies exclusively on epitaxy which lessens the yield [66].

3.5 Wavelength-division multiplexing

In an optical transmission system using wavelength-division multiplexing (WDM), multiple optical carriers at different wavelengths are modulated independently and are transmitted over the same optical fiber. The topology may provide an individual point-to-point link for numerous network subscribers. On the other hand, the individual channels can compile a single high-capacity point-to-point link. The latter is typically used for long-haul telecommunication networks [26]. In Figure 3.4, a schematic of a WDM optical transmission system is depicted.

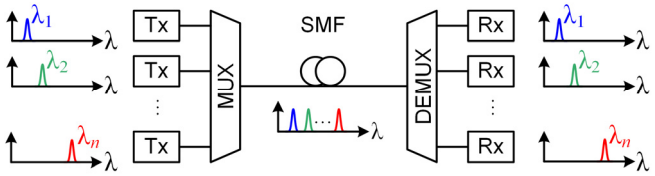

Figure 3.4: Schematic of an optical transmission system with wavelength-division multiplexing (WDM) operating n parallel wavelength channels.

Each transmitter (Tx) encodes its data stream on an optical carrier at the wavelength λ_i $(i = 1,2, \dots, n)$. All signals are combined by an optical multiplexer (MUX) and are transmitted typically over a standard single-mode fiber (SMF). On the receiver side, an optical demultiplexer (DEMUX) separates the optical carriers and routes them to individual receivers (Rx). The data signals from the transmitters are decorrelated and may overlap in the time domain. However, an overlap in the frequency (or wavelength) domain is not tolerable. Due to the phase noise of the laser sources, a guard band between the carriers is compulsory to provide for a spacing between the channels and thus to prevent crosstalk. State-of-the-art WDM systems have a channel spacing of 50 GHz. Those are referred to as dense WDM (DWDM) systems. The individual optical channels operate at a bitrate up to 100 Gbit/s using QPSK modulation, polarization multiplexing and coherent detection [29].

3.6 System integration and packaging

In order to construct a functional module from a microsystem component, a reliable set of interfaces to its surroundings has to be established. In the course of doing so, the application of the component is strongly governing the requirements on the package. The electrical, thermal, mechanical and the optical interface are the most important when considering packaging of opto-electronic components [67]. In an optimum package, as many interfaces as possible are optimized simultaneously, thereby achieving the highest possible reliability. At the same time, the requirements on the cost are quite stringent, since the packaging is the largest portion of the cost of a device.

The intended application of the module has a significant influence on the package design. For example, when designing a transceiver module for an optical communication system, the most important aspects are high-frequency electrical connections, temperature stabilization and a small footprint. In contrast, the primary concern in designing an FTTH ONU is obtaining a high-speed component at the lowest possible cost, which at the same time must operate reliably in non-stabilized environment. Short-

range interconnects for automotive or industrial applications must be extremely robust while those for data center applications must be small and energy-efficient. In detector instrumentation, the primary concern is that any on-detector equipment must not obstruct the measurement accuracy. Thus, the footprint, the mass and the energy consumption are of capital importance. Next, long-term reliability is important because detector facilities typically are not accessible for maintenance purposes over a longer period of time. Furthermore, on-detector link components may have to endure harsh conditions, which will be elaborated in chapter 4.

The optical interface is essentially the coupling of one or more optical fibers to the opto-electronic component in order to transfer the optical energy with the largest possible efficiency. The important design aspects are the direction of the coupling and the adaption of the mode sizes of the on-chip waveguide and the optical fiber. The direction could either be in-plane, i.e. the on-chip waveguide and the fiber are aligned in the same plane and their cores are parallel. This is the case, where the coupling spot is located at the chip's edges. In an out-of-plane arrangement, the optical fiber is aligned at an elevation angle to the on-chip waveguide. Hence, the coupler does not need to be at the chip's edges.

The electrical interface encompasses the power supply of a device as well as the provision of data or control signals. In most cases, the contact pins of an external connector are connected to metal pads on the chip by bond wires. When considering a high-frequency electrical signal, the connection must be regarded as a transmission line whose properties are dependent on the used material, the geometry and the load it is connected to. If necessary, the electrical connection can include a circuitry for impedance matching.

The operation characteristics of most electro-optic components are dependent on the ambient temperature. Therefore, an active temperature control is necessary. In addition, for amplifiers or light sources, a constant active heat removal might also be required. In both cases, the thermal interface of the package has to provide an optimized heat transfer between the component and the module's environment. The design aspects to consider are the thermal conductivity, the deflection temperature, the glass transition temperature and the coefficient of thermal expansion (CTE) of materials used in the package. The heat transfer can be accomplished for example by air or liquid cooling, heat pipes, or microchannel cooling. The active temperature control is typically implemented by thermo-electric cooling or heating with Peltier elements.

Finally, the mechanical interface is always considered in close connection to the thermal interface. It considers the variety of materials compiling the connection between the component and the package and thus the resulting reliability of the entire module. The characterizing properties are tensile and shear strength, fatigue endurance or different CTE of the materials. In the special case of packaging an opto-electronic component, the design of the mechanical interface has to take into account the very stringent tolerances of a fiber-to-chip coupling arrangement. This clearly puts a constraint on the available materials, since they need to be rigid and should have a small coefficient of thermal expansion. On the other hand, rigid material joints tend to induce strain on the material joints and thus might bring forward an early wear-out failure.

3.7 Fiber-to-chip coupling

The coupling of optical fibers to opto-electronic components is one of the major contributions to the cost of commercial devices for telecommunication applications [67]. Both the device and the material system of the photonic chip decide on the method of attaching an optical fiber to the photonic chip. In general, the adaption of the mode sizes of the fiber and the device is required. For example, the coupling of a laser diode to an SMF is typically achieved using a micro-lens at the fiber tip. A micro-lens is generally fabricated by a drawn-taper technique or by chemical etching processes. Other methods use ball or cylindrical lenses, which are mounted between the facet of the laser diode and the butt-fiber. However, due to a simplified fabrication and alignment, the micro-lenses are usually preferred [68].

Due to the rather large mismatch of the mode sizes of SMF and SOI PIC, a mode-size transformation is vital for a sufficient coupling efficiency. The issues of coupling loss due to mismatch of the modes of two waveguides and the conversion of the mode-sizes is discussed in section 2.2. Several methods of coupling have been proposed. They are predominantly distinguished between the orientations of the fiber axes of the coupling waveguides with respect to each other.

3.7.1 Fiber-to-chip coupling using edge-couplers

In a coupling arrangement with edge couplers, the fiber axis is aligned in parallel to that of the chip waveguide, which is why the arrangement is called in-plane coupling. Either tapers or lenses can be used for the mode-size transformation. In-plane coupling arrangements are mostly polarization-independent and pose no limitation on the optical signal's bandwidth.

A most common approach is using down-sizing adiabatic tapers. A large input waveguide supports a mode with dimensions similar to that of the fiber. By gradually decreasing the size in the vertical and the lateral direction, the taper approaches the size of the on-chip waveguide. This method often requires a three-dimensional transformation to achieve maximum efficiency [69]. However, the variation of the waveguide height requires complex fabrication techniques, which are not necessarily compatible with CMOS fabrication. Another approach achieves the mode-size adaption with a two-stage arrangement, where the first stage incorporates a rib waveguide taper and second stage can be an inverse taper. This requires supplemental materials and processing steps as well, but the coupler can be fabricated as a post-processing step [70]. In order to reduce the device size, coupler designs with three tapering stages have been proposed as well [71]. For a reduced fabrication complexity, a two-dimensional coupler design can be utilized, which uses a transformation optics design [72]. The coupler is designed as such that the mode-field is adapted only in the lateral direction with respect to the chip plane. Its functionality has been demonstrated, but the device shows a low coupling efficiency compared to three-dimensional designs.

In contrast to down-sizing tapers, up-sizing or inverted tapers have been proposed for the mode-size conversion for the coupling of optical fibers to photonic components. Compact nanotapers have been proposed, which can be structured directly on the SOI wafer. Other layouts employ an additional overlayer on the tapered waveguide [73], [74]. The operating principle relies on the delocalization of the waveguide mode at the narrow end of the taper. This delocalization yields an increased overlap with the larger mode of the optical fiber. Since the mode field extents deeply into the buried silicon dioxide and cladding, the effective refractive index approaches that of the fiber. This can suppress back reflections effectively. However, a fraction of the mode also extends into the silicon substrate and therefore is lost for the coupling. This is the main reason for a limited mode-size at the narrow end. This issue can be mitigated by adding layers with high refractive index to the waveguide cladding. A carefully designed inverted taper can achieve a butt-coupling efficiency of 0.6 dB at a wavelength of 1550 nm [73], [75].

Since both edge-coupling arrangements have only a small alignment tolerance of about ±300 nm, optimum coupling efficiency can only be achieved with a very precise fiber-to-chip alignment (see section 2.2). Therefore, additional measures such as v-groove integration are required for fast and cost-effective assembly techniques [76].

3.7.2 Fiber-to-chip coupling using grating couplers

In a surface-coupling arrangement with grating couplers, the axis of the optical fiber is aligned at a small angle with respect to the photonic chip's surface normal. The operation principle is discussed in section 2.1.5. In contrast to any etch-coupling arrangement, no dicing or polishing of the chip edges is required to access the on-chip waveguides. Hence, the complexity of the subsequent packaging process is reduced. Moreover, individual components on a wafer can be optically probed before separation, which enables wafer-scale tests [77].

Apart from the diffraction grating, the couplers incorporate an adiabatic taper or focusing element. That is why the grating section of the waveguide can be designed so as to approach the dimensions of the core of the optical fiber. The consequence is an improved alignment tolerance of almost an order of magnitude compared to inverted tapers. However, since grating couplers rely on diffraction of the optical field, they have intrinsically a limited bandwidth. Moreover, the central wavelength of the coupler becomes a function of the fiber alignment angle.

State-of-the-art grating couplers achieve a coupling efficiency up to -3 dB. Typically, a grating bandwidth (1 dB) in the range of 40 nm is achieved. A non-uniform grating design results typically in the lowest coupling losses. In [21], uniform, non-uniform and broadband gratings have been fabricated in the same process and compared with each other. The non-uniform grating coupler shows a coupling efficiency of -3.2 dB at a wavelength around 1580 nm, followed by the uniform grating coupler at -3.8 dB. Both devices have a bandwidth (1 dB) of 36 nm. In contrast, a broadband grating coupler with a lower coupling efficiency has a bandwidth (1 dB) of 90 nm. Other non-uniform grating coupler designs achieve an average coupling efficiency of -3.1 dB at 1550 nm with a bandwidth of 41 nm [20]. Further improvement of the coupling efficiency can be achieved by introducing a reflective layer to the waveguide. This is usually sandwiched between two layers of BOX or located at the backside of the waveguide [78], [79]. The coupling efficiency of the gratings, which explicitly exclude the losses of the waveguide tapers are reported to be as low as -1.6 dB at 1530 nm for uniform gratings with a bandwidth (1 dB) of 44 nm [80] and even -0.36 dB at 1200 nm for non-uniform gratings [81]. The latter was demonstrated to have a bandwidth (3 dB) of 100 nm.

The coupling efficiency of a focusing grating coupler appears to be slightly less compared to adiabatically tapered designs in favor of a significantly reduced footprint. Uniform grating couplers have been fabricated on a CMOS-compatible SOI platform, achieving a coupling efficiency of -5.2 dB at a wavelength around 1540 nm and a bandwidth (1 dB) of 41 nm [19]. In [25], a focusing design is presented, which relies on an intermediate silicon nitride layer sandwiched between two silicon slabs. The insertion loss at a wavelength of 1480 nm is 4.4 dB and a bandwidth (3 dB) of 38 nm is obtained.

Finally, grating couplers can be used not only for the coupling of optical fibers to PIC. They also facilitate the hybrid integration of discrete opto-electronic components such as laser diodes and SOI waveguides. This has been demonstrated for example in [82], where a laser diode is integrated with an SOI waveguide using a micro-optical bench.

3.7.3 In-plane coupling using angle-polished fibers

Although an out-of-plane coupling scheme has many advantages such as high coupling efficiency and alignment tolerance, the major drawback is the space requirement of the attachment mechanics in a conventional packaging process. At first, the optical fiber’s bending radius determines the minimum height required for a coupling arrangement. Even the latest fiber technology only specifies a minimum radius of 10 mm [83]. Secondly, since the fiber is aligned at a small angled with respect to the chip surface normal, a mounting structure such as a socket or block is oriented in the same direction. This usually results in large and bulky mechanics, which may also involve the obstruction of a significant fraction of the chip surface [84]. Therefore, a planar arrangement with a small footprint in the chip plane is favored for the out-of-plane coupling technique.

A low profile of the package can be maintained, if the field from the optical fiber can be redirected to the grating coupler. This can either be achieved by discrete imaging elements such as lenses or prisms, or by grinding and polishing the fiber facet. In the latter case, the fiber is polished at an angle smaller than 45° and its axis is aligned parallel to the chip surface. By means of total internal reflection at the polished fiber facet, the optical field can couple radially from the fiber to the grating coupler. The advantage of this method compared to using discrete elements is the simplified alignment for optimum coupling. On the other hand, it requires additional processing of the optical fibers. The schematic of the coupling arrangement is presented in Figure 3.5.

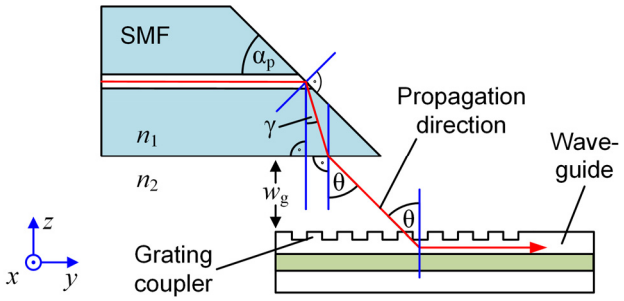

Figure 3.5: Schematic of an out-of-plane coupling arrangement, where the axis of the optical fiber remains in the plane of the chip surface.

The polishing angle α_p is dependent on grating coupler's incident angle θ and is calculated from Snell's law

$$n_1 \sin(\gamma) = n_2 \sin(\theta) \tag{3.8}$$

and the geometric relations in Figure 3.5

$$\gamma + 2 \cdot \alpha_p = 90°, \tag{3.9}$$

where n_i $(i = 1, 2)$ are the refractive indices of the fiber cladding and the surrounding medium. The angles γ and θ are the angles of refraction in the respective medium. The relation holds as long as the condition for total internal reflection is satisfied. Due to the small difference of the refractive indices between the fiber core and the cladding, a change of the refraction angle at that boundary is neglected. The gap size w_g quantifies the clearance between the fiber cladding and the waveguide grating's surface.

The concept has been invented quite some time ago for the coupling of multi-mode fibers to laser diodes and photodetectors, in order to construct optical transmitters and receivers with a small footprint, so as to be integrated in micro-electronic environments [85], [86]. In the course of developing novel transmitter and receiver modules for long-haul applications, this special fiber-to-chip coupling technique was also applied successfully to single-mode fibers (SMF) [87], [88]. Only recently, it has been re-discovered and introduced for the surface-coupling of SOI waveguides. The application of angle-polished fibers does not impose a significant penalty on the coupling efficiency compared to a conventional out-of-plane alignment [84], [89].

3.7.4 Alignment techniques

In order to obtain the optimum efficiency of a fiber-to-chip coupling, the stable mounting of the photonic chip on the substrate is required as well as a careful alignment of the fiber prior to fixation. To obtain the best possible coupling efficiency, up to six axes are optimized independently [90]. The x-, y- and z-direction are linear translations in space, while the rotation by the angle θ_{rot}, the elevation by θ_{elev} and the azimuthal alignment θ_{azim} are angular tilts. The six degrees of freedom of the alignment of a fiber with respect to the coupler of a photonic chip are indicated in Figure 3.6.

For prototype assemblies or small quantities, the alignment is accomplished actively. In a common procedure, the fiber is positioned with respect to the coupler on the chip while monitoring the coupling efficiency. The optimum position is achieved, when the coupling efficiency is highest. The alignment is performed using micro-mechanical stages in combination with piezo-driven positioners. The process can be automatized to some extent, that is, a controller unit manipulates the fiber alignment using a dedicated algorithm until the optimum coupling efficiency is achieved.

In contrast, passive alignment techniques rely on placing optical fibers in pre-fabricated structures. Those can be grooves integrated on the chip, which can be fabricated by anisotropic etching processes [76]. Structures to guide a fiber into the position can also be fabricated with the LIGA lithography [91], [92].

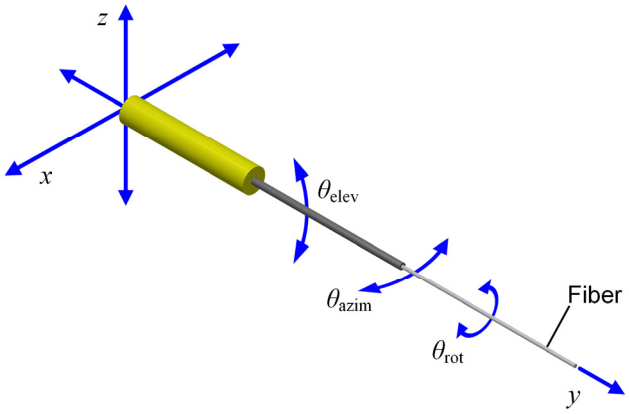

Figure 3.6: The six degrees of freedom to align an optical fiber. The y-axis equals the optical axis. The sketch is adopted from [90] and modified.

Flip-chip bonding is a viable solution for hybrid integration concepts. For example, a semiconductor laser diode can be passively aligned on top of a passive PIC by an appropriate bump-design. Moreover, entire packaging concepts for on-chip or on-board optical interconnects make use of passive alignment with flip-chip bonding [93], [94].

Although the aforementioned techniques provide a sufficient alignment precision, they rely on customization and multiple processing steps. Therefore, novel approaches aim for a simplified procedure enabling high throughput and yield of the packaging process. For example, in [95] a fiber-to-chip coupling process for fiber arrays is demonstrated, which relies on standard microelectronics tools and off-the-shelf fiber components. The position of the fibers are specified by v-grooves in the silicon photonic chip.

3.7.5 Fixation techniques

Many fixation techniques have been proposed for the packaging of micro-electronic and opto-electronic systems, such as optical contacting, hydroxide bonding or diffusive bonding [96]. However, the most prominent are laser welding and adhesive bonding. In the past, only laser welding has been considered to provide sufficient accuracy and long-term stability of the package. The biggest obstacle to achieve the required accuracy with adhesives were the shrinkage during the curing process as well as post curing shrinkage.

Adhesive bonding in packaging mostly relies on using epoxy resins, room-temperature vulcanizing adhesives and adhesives that cure in the presence of ultra-violet (UV) radiation. The latter is usually preferred, because UV radiation can cure a bond instantly and on-demand after alignment. At the same time, the performance properties such as the strength and durability equal or even exceed those of epoxies [97]. As with all adhesives, the bond quality depends on various influences: for one, the design of the bond and the selection of the involved materials decides about the system stability. Furthermore, material stress and different CTE between mounted devices and the substrate have to be considered. Stability issues related only to the adhesive materials are primarily an incomplete cure and hygroscopic expansion, i.e. an irreversible dimensional displacement due to temperature and humidity change. Also degradation due to the exposure to acid or alkali as well as visible and non-visible optical radiation have to be taken into account [96].

Over the course of time, UV-curable acrylate-based adhesives have been developed, which are composed of oligomers, monomers, additives and a photo-initiator. The formulations can be adjusted to achieve optically clear resins, with a set of specific properties, such as refractive index, adhesion or resistance to optical radiation. In particular, a careful selection of additives can provide for a low shrinkage rate and minimization of hygroscopic expansion [98]. Hence, the stability of an adhesive-

bonded joint is mostly subject to the bond design and its uniformity, the selection of the appropriate adhesive for the given materials and the complete curing of the bonding layer.

In fiber-to-chip coupling arrangements, the adhesive forms the bond between an optical fiber fixed on a sub-mount and a substrate. After optimization of the fiber alignment for maximum coupling efficiency, the fiber and the sub-mount are fixed on the substrate. A displacement of the bonded components results in a misalignment of the fiber with respect to the optimum position. In turn, this directly translates to a deterioration of the coupling efficiency. Therefore, the joint-design aims for maintaining the coupling efficiency during the curing procedure as well as during the component's usage under various environmental conditions.

4 Optical links in detector instrumentation

4.1 The large hadron collider and the CMS experiment

The *Large Hadron Collider* (LHC) at the *European Organization for Nuclear Research* (*Organisation européenne pour la recherche nucléaire*, CERN) is the largest and most powerful particle accelerator in the world. It accelerates either protons or lead ions counter-rotating in two separate rings with a circumference of 27 km. Bunches of accelerated particles can be brought to collision at four different crossing points of the ring at an event rate of up to 40 MHz. This rate is referred to as the bunch crossing rate. The design center-of-mass energy of colliding protons is 14 TeV and a luminosity of 10^{34} $cm^{-2}s^{-1}$. The lead ions can collide with 2.8 TeV per nucleon at a peak luminosity of 10^{27} $cm^{-2}s^{-1}$ [99].

With its commissioning in 2010, the LHC was capable of colliding protons with a center-of-mass energy of 7 TeV at a luminosity two orders of magnitude less than the nominal value [100], [101]. Up to 2015, it has been increased continuously to 14 TeV. Since then, LHC is operating at nominal luminosity of 10^{34} $cm^{-2}s^{-1}$. Before acceleration to the maximum energy, the LHC ring is provided with particles pre-accelerated in the injector chain. This is a succession of a linear accelerator (Linac2), the Proton Synchrotron Booster (PSB), the Proton Synchrotron (PS), and the Super Proton Synchrotron (SPS). The protons are injected in the LHC at an energy of 450 GeV.

At each crossing point, one or more particle detectors are located. The *Compact Muon Solenoid* (CMS) and the ATLAS (*A Toroidal LHC ApparatuS*) detector are both general-purpose detectors, suitable for investigating a wide range of physical phenomena [102], [103]. They share the interaction point with the smaller experiments TOTEM (*TOTal Elastic and diffractive cross section Measurement*) and LHCf (*Large Hadron Collider forward*), respectively. The TOTEM experiment investigates the scattering effects of proton-proton collisions [104] while LHCf measures the number and the energy of neutral pions [105].

In contrast, ALICE (*A Large Ion Collider Experiment*) is a detector for heavy ions and designed to study the properties of the quark-gluon plasma at extreme values of energy density and temperature in nucleus-nucleus collisions [106]. The *Large Hadron Collider beauty* (LHCb) experiment is dedicated to the research of the relations and differences between matter and antimatter [107]. The latest experiment at LHC is called *Monopole and Exotics Detector at the Large Hadron Collider* (MoEDAL) and is located in the same cavern as LHCb. It is designed to expand and to complement the research activities of ATLAS and CMS by searching for ionizing avatars of new physics such as magnetic monopoles or massive (pseudo-)stable charged particles [108].

The detector systems of all experiments deploy different sub-detectors, which are sensitive to one particular particle property. For example, a tracking system analyzes the trajectory of charged particles while a calorimeter measures their energy. The sub-detectors consist of numerous detector cells, which in turn are assembled to detector arrays. The analysis of the measurement data of all detector sub-systems compile a unique signature of the particles which enable research groups around the world to study the events in detail.

The main purpose of CMS is to identify the tracks of charged particles generated by collision events and to measure their energy. A perspective schematic is shown in Figure 4.1 [109]. The central component is a superconducting solenoid. It provides a magnetic field of 4 T to bend the path of the particles. The charge of the particles can be obtained by observing the direction towards which the particles are bent while the momentum is deduced from how much they are deflected from their original trajectory. Both properties are measured with the tracking system, which is located inside the bore of the solenoid. It is divided into an inner and an outer tracker sub-system. The inner tracker is located closest to the interaction region. It consists of 66 million silicon pixel-detectors on three cylindrical

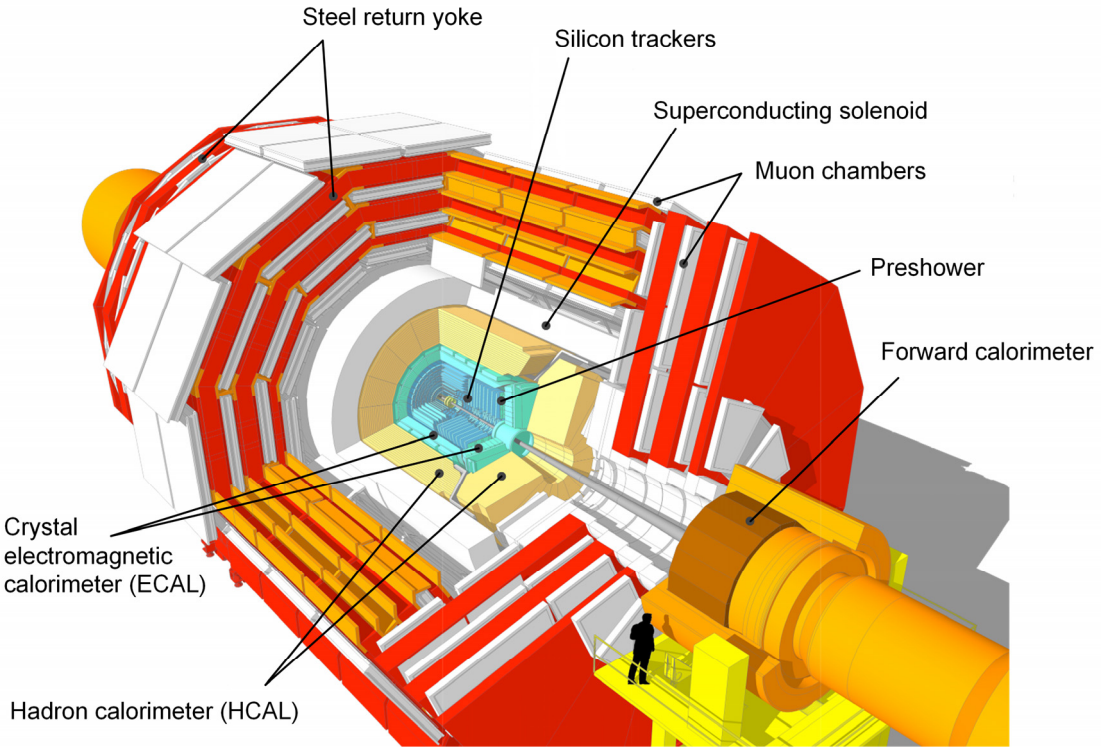

Figure 4.1: Schematic of the CMS detector showing the individual sub-detector systems [109].

layers providing a three-dimensional vertex reconstruction. It is enveloped by 10 layers of almost 10 million silicon microstrip-detectors which constitute the outer tracker.

The silicon trackers are girdled by the electromagnetic calorimeter (ECAL), which is constructed of approximately 70.000 lead tungstate ($PbWO_4$) scintillating crystals and photodetectors in the barrel and the endcaps. It is designed to measure the energy of electrons and photons, the energy of jets and missing transverse energy [110]. It also contains preshower-detectors in front of the endcaps to identify neutral pions and to improve angular resolution at high-luminosity operation. Its sensor modules produce 137.000 individual electronic signals.

The outermost detector inside the solenoid is the hadronic calorimeter (HCAL). In contrast to the ECAL, its purpose is to measure hadron jets, neutrinos or exotic particles by means of analyzing missing transverse energy [111]. Due to the proximity to the solenoid, materials in the barrel and the endcap section are chosen to be non-ferromagnetic, such as copper alloys and stainless steel. Parts of the HCAL also extend outside the solenoid. The outer calorimeter is inserted between the solenoid and the muon system while the forward calorimeter is a cylindrical structure located in front of the outermost steel yoke. The total number of electronic channels of HCAL is in the range of 10.000.

To identify interesting processes despite the background noise, muon detection is an essential capability of the CMS-detector. Three different measurement methods are used in the muon sub-system. Those are drift tubes in the barrel region, cathode strip chambers in the endcap region, and resistive plate chambers in both the barrel and endcap [112].

Using all sub-detector systems, many particles can be identified. A detector cross-section along with the schematic of the detection of muons, electrons, charged hadrons and neutral hadrons is given in Figure 4.2 [113]. Muons emerging from the interaction region (blue solid line) are bent in the magnetic field and induce hits in the silicon tracker. They pass the calorimeters and the solenoid and are detected in the muon sub-system before they escape the detector barrel. Electrons (red solid line) and charged hadrons, such as pions (green solid line) are also bent in the magnetic field. Similar to the muons, their traces are registered by the silicon tracker. The electrons then deposit all their energy in the

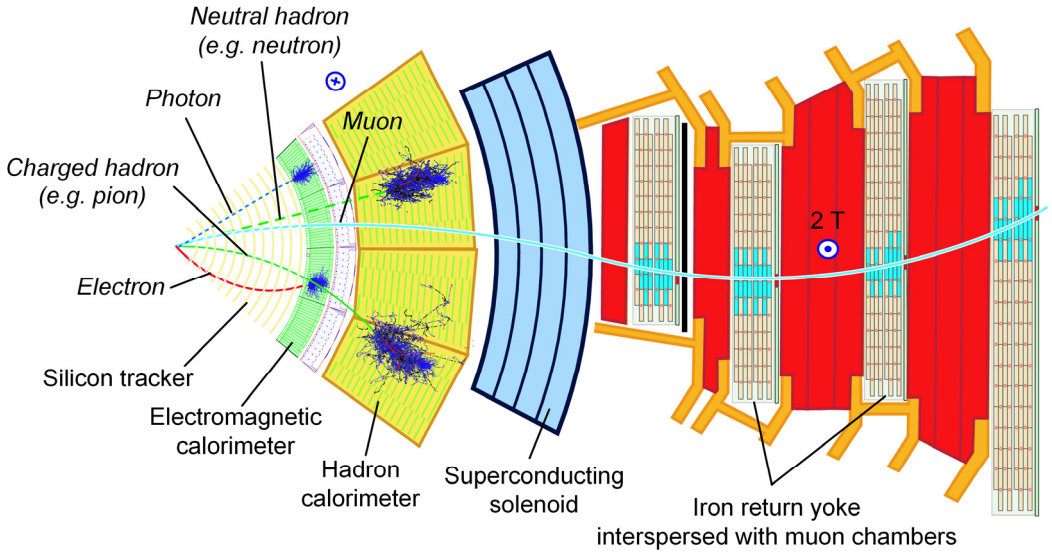

Figure 4.2: Cross section of the CMS-detector with the different detector sub-systems and the schematic of the detection processes [113]. Colored traces indicate the trajectories of different particles.

electromagnetic calorimeter and thus do not continue to propagate. In contrast, the charged hadrons pass the electromagnetic calorimeter and are only absorbed in the hadronic calorimeter. The trajectories of uncharged particles such as neutrons (green dashed line) or photons (blue dashed lines) are not perturbed by the magnetic field. The photons are absorbed in the electromagnetic calorimeter. The neutrons continue to propagate through the detector and are absorbed in the hadronic calorimeter.

At the initial design luminosity of 10^{34} $cm^{-2}s^{-1}$, 17 collision events per bunch-crossing in average occur [114]. That implies a rate of particle interactions around 10^{9} s^{-1} at the bunch-crossing rate of 40 MHz. The amount of aggregated data per bunch-crossing is approximately 1 Mbyte [103], which yields a net data rate of 320 Tbit/s.

For the data read-out, storage and analysis to become manageable, that rate must be reduced using an online event-selection process, a two-stage hierarchical trigger system consisting of the *Level-1 Trigger* (L1) and the *High Level Trigger* (HLT). The reduction is achieved by means of selecting potentially interesting events to retain for further analysis and discarding all the others. For a trigger decision of L1, only a fraction of the acquired detector data from the calorimeters, the preshower-detectors and the tracker is used to identify an event. The total raw data is pipelined in the detector front-end electronics for 3.2 µs after the bunch crossing. Hence, the trigger data must be collected and a decision must be made which has to be received by the front-end electronics within that period [114]. The event rate after the L1 trigger stage is reduced to 75 kHz. At the HLT stage, analysis and filtering of the events take place. In particular, event-filter units aggregate the event data from the different front-end buffers. The event rate after processing is 100 Hz, which is compatible to mass-storage devices.

Motivated by the discoveries achieved during the first years of LHC operation, the accelerator will undergo several technical upgrades targeting at a peak luminosity of 5×10^{34} $cm^{-2}s^{-1}$ in 2025. These upgrades are summarized in the *High-Luminosity LHC Project* (HL-LHC). Since the increased luminosity poses new challenges to the detectors of the experiments located at the beam crossing points, they are also subject to major transformations [115]. As shown in Figure 4.3, the upgrade is divided into three phases, each containing a shutdown and run period. The diagram also includes the projected peak luminosities during the respective periods as well as the time-integrated luminosity.

After the long shutdown 1 (LS1) from February 2013 to March 2015, LHC was operating at the nominal luminosity of 10^{34} $cm^{-2}s^{-1}$ at a bunch-crossing rate of 40 MHz. Since then, the center-of-mass energy of proton-proton collisions has been 14 TeV. During Phase-1, which began with the long

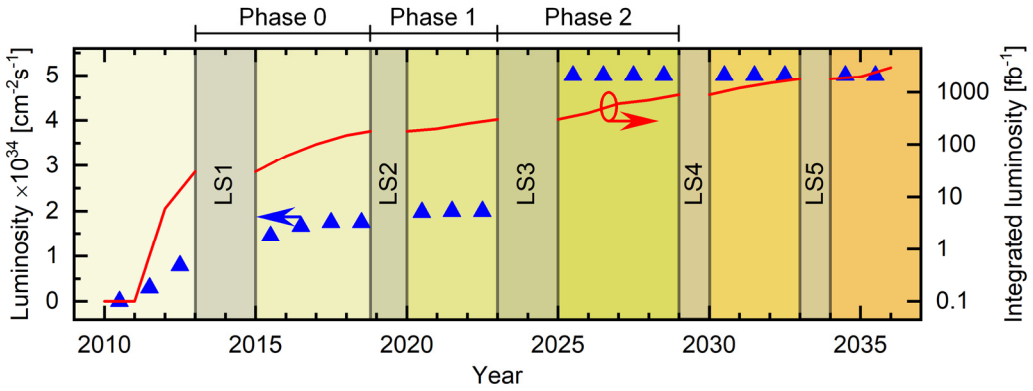

Figure 4.3: Schedule of the High-Luminosity LHC-Project through 2035, showing the operational phases until the peak luminosity is reached, dates for long shutdowns (LS1…5) of LHC and projected luminosities [115], [117].

shutdown 2 (LS2) at the end of 2018, particularly the injector chain is upgraded which yields a peak luminosity of 2×10^{34} $cm^{-2}s^{-1}$.

At the CMS experiment, revisions of all detector sub-systems will be carried out. To some extent, repairs are required due to damage imposed by radiation. On the other hand, improvements and upgrades will enable CMS to operate successfully under the new conditions. The major changes involve upgrades of the muon system, the hadronic calorimeters, and the tracker as well as the DAQ and monitoring systems [116].

With the Phase-2 upgrade, the peak luminosity of LHC is increased to 5×10^{34} $cm^{-2}s^{-1}$. This is achieved by inserting new magnets into the accelerator ring and placing more powerful focusing magnets in front of the experiments. Similar to Phase-1, also the experimental detectors will undergo significant upgrades. Apart from replacing aged components, the upgrade of CMS encompasses an increased granularity of most sub-detector systems. Additionally, the latency of the L1 trigger is increased to the target of 12.5 µs. This provides for a sufficient amount of time for track reconstruction and the matching of the tracks to the muon system and the calorimeters. However, this change requires subsequent upgrades of the sub-detector read-out electronics [117].

4.2 Data read-out of a detector system

The efficient data read-out is most crucial, where the amount of aggregated electronic data per bunch crossing is highest. For example, this is the case for the CMS silicon tracker, where several 10 million silicon sensors produce signals to reconstruct a particle's trajectory. An optical data transmission system is utilized for both the detector data read-out (uplink) and the timing, trigger and control (TTC) data (downlink). Compared to a purely electronic transmission relying on coaxial cabling, data transmission with optical carriers has several advantages: due to the high carrier frequency and the strong field confinement in a glass fiber, the link is immune to electromagnetic interference. Additionally, the non-conductive transmission medium offers a galvanic insulation between the transmitter and the receiver. Furthermore, the energy consumption and heat dissipation of the system can be kept low. Since the read-out system requires a large number of independent channels, a lower mass and spatial requirement of the fibers compared to cables become significant.

4.2.1 Optical read-out and control systems

A schematic of the *CMS Tracker Readout and Control System* [118] is shown in Figure 4.4. Signals from the silicon sensors are amplified and sampled by a dedicated front-end ASIC. They are stored in a pipeline until the ASIC receives the acceptance from the L1-trigger. Then, multiple data signals are time-multiplexed and transmitted to the counting room over an analog optical link using a pulse-amplitude modulation scheme. The front-end driver (FED) converts the data to a digital signal and forwards it to the data acquisition system (DAQ). The front-end controller (FEC) transmits digital clock

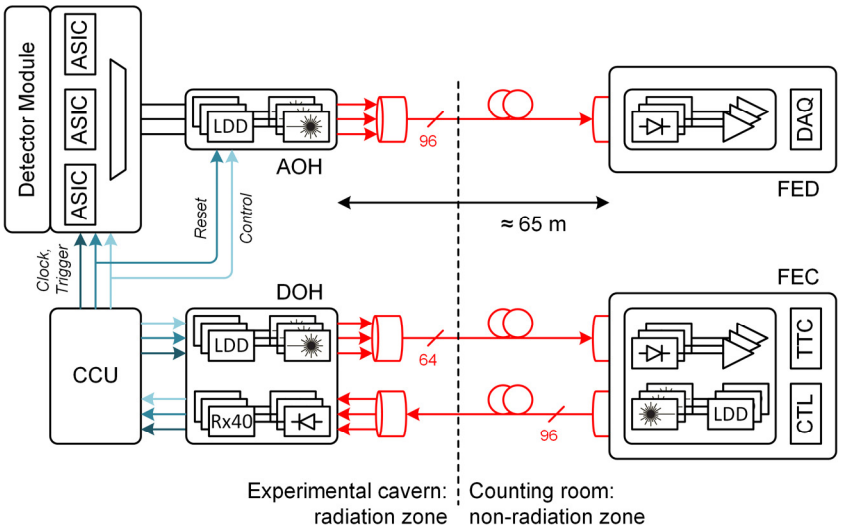

Figure 4.4: Schematic of the CMS tracker data readout (top) and control (bottom) systems optical links [118]. The connections between the experimental cavern and the counting room are multi-fiber ribbons with up to 96 individual fibers.

and control data to the digital opto-hybrid (DOH). A custom-designed receiver ASIC (Rx40) converts the signals and forwards them to the communication and control units (CCU) at the detector front-end. Control data resulting from CCU processing is transmitted back to the FEC by the DOH.

The optical transmitter (Tx) is implemented by a directly intensity-modulated laser diode operating at a wavelength around 1310 nm. Each Tx is connected with an individual single-mode fiber. Bunches of fibers are merged to a multi-fiber ribbon (8×12 fibers), which is connected to a multi-channel analog receiver at the counting room. The on-detector receiver uses an InGaAs photodiode and a custom digital receiver ASIC. In most cases, commercially available components cannot be used on-detector due to the heavy constraints on available space. Hence, a semi-custom package has been developed for housing off-the-shelf components.

As in all experimental detectors at LHC, the silicon tracker is the detector sub-system closest to the interaction point. Hence, not only the sensor elements but also the DAQ units and the read-out interface are subject to a significant radiation dose. That is why the radiation hardness of both the opto-electronic components and the driver and controller electronics has been extensively studied. In order to validate transceiver components, numerous specimens of semiconductor lasers and photodiodes have been irradiated in many experiments in the past [119]–[121]. At high particle fluence, the leakage current of photodiodes increases and even exceeds the signal level. Thus, the responsivity decreases significantly. Post-irradiation annealing is almost negligible. In laser diodes, the threshold current rises upon increasing fluence, while the slope efficiency becomes continuously smaller. Some devices only maintain spontaneous emission after irradiation. With the upgrades to the High-Luminosity LHC in mind, research is still ongoing to develop system components that are capable of withstanding the expected doses.

4.2.2 Optical links for CMS upgrades

In the past, the collaborations of each experiment at LHC have independently developed data transmission links for detector control, DAQ and TTC data. As part of the LHC upgrade schedule, the *Versatile Link* (VL) project was established. It is a joint ATLAS-CMS project developing a general-purpose optical link for detector instrumentation [122]. The data transmission is based on the intensity modulation of laser diodes and the direct detection using photo diodes. Different topologies can be implemented, such as a point-to-point link as well as a point-to-multipoint link in a passive optical network (PON). The on-detector transceiver should be a low-mass and low-volume module, with only small power consumption and heat dissipation.

The link operates either at a carrier wavelength of 850 nm using multi-mode fibers or at 1310 nm using single-mode fibers. The reason behind is to keep the compatibility to existing installations in the different experiments. A data rate of 4.8 Gbit/s is provided bi-directionally and the system is transparent at the serial interfaces. A schematic of a bi-directional link is sketched in Figure 4.5. The *GigaBit Transceiver* (GBT) project addresses the development of a customized transceiver module, which is qualified to operate under the harsh conditions at the detector front-end. The *GigaBit Transceiver* (GBTx) module incorporates a serializer/de-serializer, which acts as the interface between serial data from the front-end electronics and the GBT protocol. The interface to the optical signal is provided by the *Versatile Transceiver* (VTRx) module, which consists of a custom-designed laser diode driver (LDD) ASIC and a transimpedance amplifier (TIA) ASIC. An optional feature is the implementation of a slow-control adapter (SCA). The components are manufactured in CMOS technology with a feature size of 130 nm to ensure resilience to ionizing radiation and single-event upsets [123], [124]. At the back-end in the counting room, the transceivers are implemented by off-the-shelf components, since none of the on-detector environmental restrictions apply.

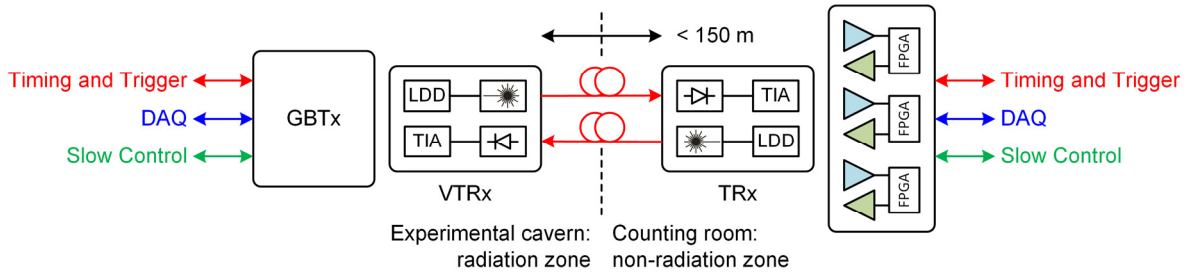

Figure 4.5: Implementation of bi-directional VL architecture for the detector data read-out and timing trigger and control signal transmission. At the back-end in the counting room, the transceivers are implemented by off-the-shelf components. Schematic adopted from [126] and [127].

In the course of the VL project, optic and opto-electronic components, such as optical fibers, laser diodes and photo diodes have been validated for the use in a radiation-hard optical link. A prototype VL transceiver based upon the standardized SFP+ module has been demonstrated successfully in a feasibility study [125]. The performance of commercially available opto-electronic components has been studied in more detail and environmental specifications where determined [126]. The calorimeter systems have to withstand a total dose of 10 kGy (5×10^{14} neutrons/cm^2) while components in the inner detector and close to the interaction region must withstand 500 kGy (5×10^{14} neutrons/cm^2 and 1×10^{15} hadrons/cm^2) up to the year 2030. Hence, two levels of radiation tolerance are categorized by calorimeter-grade and tracker-grade. The temperature range for the VL components is specified to be between -30 °C and +60 °C. The low value specifies to operate silicon sensors in the experimental cavern while the high boundary takes operation in the back-end into account. The magnetic field of the solenoid can reach 4 T, which therefore becomes the magnetic field tolerance requirement. Several suitable devices have been identified and methods to mitigate the deterioration of components due to radiation exposure have been suggested. All components in the VL system have to be tolerant to calorimeter-grade radiation levels [127].

For the phase-2 upgrades of ATLAS and CMS, the *Versatile Link PLUS* (VL$^+$) project pursues the development of a bi-directional data link supporting data rates of up to 10 Gbit/s upstream and 5 Gbit/s downstream. Together with the *Low-Power GBT* (LpGBT) project [128], it is devoted mostly to the further development of the on-detector transceiver [129]. Apart from the development of tracker-grade radiation-hard LDD, commercially available vertical-cavity surface-emitting laser diodes (VCSEL) and photo diodes have been qualified. The VL$^+$ transceiver can be configured with different counts of up- and downstream channels. One up to four transmitters and one receiver can be accommodated in the same form factor. At the same time, the LDD of the transmitter channels can either be implemented discretely [130] or array-based [131], [132], of which the latter would reduce the required space in the detector barrel significantly.

4.3 Short-range interconnects for detector instrumentation

As mentioned in the previous sections, efficient and low-cost optical interconnects are a vital element in future data centers and high-performance computers. Apart from the performance, reliability and energy efficiency, the expenses for installation and operation of the links are of supreme interest. Novel technologies like SOI-based optical network components are promising to meet those requirements. The goal is a high-performance network architecture with a transceiver cost of a few US-cent per gigabit per second [133]. Considering an experimental setup in high-energy physics (HEP), the requirements on the data communication equipment are quite similar, albeit the emphasis of the attributes is slightly different. Just like interconnects in a data center, the transmission distance of a data read-out link is a few hundred meters at maximum. That relaxes the requirements on link performance compared to long-haul systems and allows for IM-DD schemes. In addition, the requirements on the data rate and the energy consumption are applicable for both scenarios.

Of course, components of a HEP data read-out link are subject to special requirements. Commercial optical interconnects have to fulfil Telcordia requirements on ambient conditions. The most important are the temperature range of 5 °C to 40 °C and the relative humidity range of 5% to 85%. Any component, which complies the specifications, shall not sustain any damage or deterioration of functional performance during its operating life, if it is operated within these conditions [134]. As already introduced in section 4.2.2, the temperature range required for optical link components is -30 °C to +60 °C. However, Telcordia environmental requirements do not consider magnetic fields. Yet, on-detector components operate in proximity to the detector's magnet, which requires a tolerance to magnetic fields up to 4 T.

In contrast to the facility of a data center, the cavern of a HEP experiment is not freely accessible for maintenance. Therefore, rigorous requirements on the expectancy of any on-detector components apply. Nevertheless, the most stringent constraints on interconnects in detector instrumentation are radiation tolerance, which is entirely of no relevance in data centers, and space requirements. Although scientific experiments may become as large as CMS, the available space for the front-end and DAQ electronic is very limited, because every volume element not covered by a sensor is diminishing the detector's resolution. Therefore, this application is one of the very special cases, where the high effort of monolithic integration yields a significant benefit. The integrated front-end component, including sensor, trigger, slow-control and data-readout would consume less space compared to discreet components.

4.4 A novel multi-channel optical detector read-out system

Based on experience, the spatial resolution of an experiment such as CMS will increase continuously to maintain the required measurement accuracy upon higher luminosities in the future of LHC. The growing complexity of the detectors will inevitably yield an ever-increasing number of electronic channels and thus a higher demand on bandwidth for both the data read-out and the control infrastructure. At the same time, volume and mass of the cables and energy consumption of the front-end electronics should be low to minimize multiple scattering [135]. Similar requirements apply for other scientific research fields such as astroparticle physics or photon science. A descriptive example is the *Adaptive Gain Integrated Pixel Detector* (AGIPD), which is developed at the *European X-Ray Free Electron Laser* (Eu-XFEL) facility at *Deutsches Elektronen-Synchrotron* (DESY). Among other techniques, the detector is used for coherent diffraction imaging (CDI), a technique to reconstruct images of an object from its measured diffracted intensity [136]. At a repetition rate of 10 Hz, bunches of 2700 X-Ray laser pulses are delivered to the detectors with a separation of 220 ns. AGIPD is a two-dimensional sensor array consisting of 16 modules with 512×128 pixels each, which operates under vacuum conditions. The current read-out infrastructure uses 16 10GbE links delivering a data rate of up to 80 Gbit/s. Additionally, an external control system communicates with the detector via three 100MbE lines [137]. In contrast to CMS, AGIPD is a much smaller detector system and the spatial requirements are therefore more stringent.

An increased bandwidth of the read-out channels offers a reduction of the number of cables that connect the detector to the DAQ system. That improves the sealing of the experimental chamber, because the number of cables in the vacuum-air feed-through reduces significantly. Furthermore, complexity and energy consumption of the front-end electronics can be reduced due to the smaller number of transmitters.

4.4.1 Detector data read-out system based on WDM

A promising solution is an optical data transmission system based on wavelength-division multiplexing (WDM), where data is encoded on numerous optical carriers, which are conveyed over a single optical fiber. This technique is quite common in optical transport networks to achieve highest per-fiber data rates (see section 3.5). The technique may as well facilitate the read-out of detectors in scientific experiments [135], [138]: it significantly reduces the number of optical connections between the detector and the counting room, which facilitates the sealing of the detector. Next, the laser sources can be located off-detector, or even outside the experimental cavern. Thus, they are not contributing to the energy budget inside the detector volume and are not subject to performance degradation due to radiation impact. Moreover, the infrastructure is highly scalable, because the number of channels can be selected according to the total amount of data produced by the detector module and the requirements on read-out latency.

A schematic of the transmission system is presented in Figure 4.6. A multi-wavelength-channel laser generates stabilized optical carriers at wavelengths λ_i, which are multiplexed and conveyed over a single optical fiber to a multi-wavelength transmitter module (multi-λ Tx) inside the detector volume. An optical demultiplexer (DEMUX) separates the incident carriers λ_i. Each is forwarded to a Mach-Zehnder modulator (MZM), which encodes electrical data from the front-end electronics. The signals from multiple sensors in the detector module are multiplexed in a front-end ASIC and amplified to obtain a driving signal with an aggregated data rate in the range of 10 Gbit/s. Each driving signal feeds an electro-optic modulator associated to one specific wavelength channel. The data-carrying optical channels are re-multiplexed and guided back in a single optical fiber to the counting room. There, the channels are demultiplexed again and routed to individual receivers (Rx), which convert the optical signals to electrical data for further processing in the data acquisition infrastructure (DAQ).

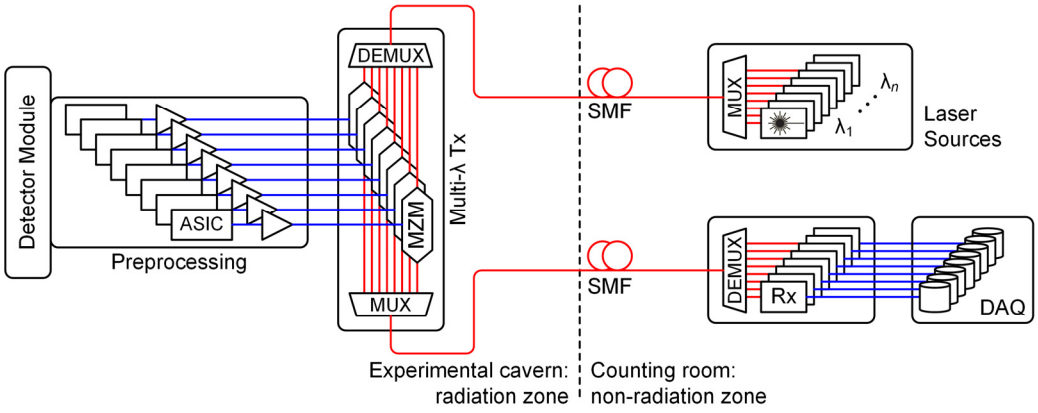

Figure 4.6: Schematic of a novel optical transmission system based on wavelength-division multiplexing (WDM) for detector instrumentation. In contrast to most telecommunication systems, the multi-wavelength laser is located remotely from the transmitter.

As already discussed in the introduction, the SOI technology appears to be the ideal platform for the realization of the on-detector transmitter for the WDM-based data read-out link. All essential components can be realized on the platform. For example, electro-optic modulators based on the plasma-dispersion effect provide the required bandwidth and maintain a reliable operation even under harsh conditions. Power couplers and (de-)multiplexers can be reproducibly realized, because the mature CMOS fabrication easily sustains the required fabrication accuracy. To date, this allows for a feature

size well below the operating wavelength and thus the monolithic integration of entire photonic circuits consisting of various building blocks. Hence, a miniaturized integrated multi-wavelength transmitter as presented above can be fabricated very cost-efficiently even in quantity.

4.4.2 Telecommunication WDM transmitters

Multiple concepts of WDM transmission links based on integrated components have been proposed and demonstrated during the recent years. They can be mainly categorized by the material system and the modulator technology. In [139], a four-channel silicon photonic WDM link is proposed, which is based on MZM with depletion-type pn-phase shifters. The modulators operate at 12.5 Gbit/s, yielding an aggregated data rate of 50 Gbit/s. The transmitter incorporates a single-wavelength laser source for each channel, which is realized by bonding active gain material into the silicon structures. The modulated optical carriers are concentrated on a single output by an optical multiplexer.

Due to the small footprint and energy efficiency, many research groups pursue the utilization of resonant ring modulators. Their wavelength selectivity facilitates cascading the devices, which is why a separate multiplexer at the transmitter output can be omitted. A descriptive example is given in [140], which discusses a transmitter design as part of a transceiver for an on-board optical interconnect. It consists of 8 cascaded ring modulators operating at 10 Gbit/s each, thus achieving a total data rate of 80 Gbit/s. The required optical carriers are provided by an external laser source. The receiver is implemented by 8 photodiodes, which are accessed by individual waveguides. A similar device with four channels is proposed in [141]. The utilized modulators achieve error-free transmission at 40 Gbit/s.

In order to realize short-range interconnects for chip-to-chip communication, solid-state links have been proposed. The transmission medium typically is a silicon waveguide integrated in an optical routing layer on a carrier substrate. The transmitter and receiver presented in [142] utilize electro-absorption modulators, photodetectors and Echelle (PCG) (de-)multiplexers to assemble an 8-channel link. CMOS driver and receiver electronics are flip-chip bonded to the photonic components. Each channel requires an external laser source which is coupled to the respective modulator input. Error-free transmission at 10 Gbit/s over the entire link is achieved for individual channels.

Another approach is the hybrid integration of electro-optic modulators based on III/V material systems in silicon waveguides. In [143] a four-channel transmitter with integrated lasers and electro-absorption modulators is presented. MMI combiners multiplex the modulator output signals to a single waveguide. The packaged module also contains a CMOS driver. Running each channel at 28 Gbit/s, the transmitter achieves an aggregated data rate of 112 Gbit/s.

In order to maximize the total transmission capacity, also electronic multiplexing techniques are utilized in the context of multichannel optical transmission systems. The link presented in [144] utilizes the discrete multi-tone (DMT) multiplexing technique with QAM-modulated subcarriers while maintaining intensity modulation and direct detection (IM-DD). The transmitter consists of four MZM with silicon depletion-type pn-phase shifters. The multiplexing of the modulator output signal is achieved by ring-based WDM filters. Each channel includes a photodiode for power monitoring. The optical carriers have to be provided individually to the modulator inputs. Counting on a hard-decision forward error correction (HD-FEC), the achieved net data rate of a single channel reaches 100 Gbit/s.

Most recently a research group proposed four-channel optical transmitters on different material systems which are claimed to achieve an aggregated data rate of 400 Gbit/s using pulse-amplitude modulation (PAM). In [145], the transmitter relies on externally modulated lasers and a CWDM multiplexer. In contrast, [146] demonstrates a transmitter with four parallel silicon photonic travelling-wave MZM. An optical carrier from an external laser source is distributed via cascaded couplers to the MZM. Thus, no wavelength discrimination for the individual channels is considered. Furthermore, the modulator outputs are not multiplexed and must be probed via individual couplers.

All devices and systems proposed to the present day are primarily intended for the use in short-range interconnects in data centers or in chip-to-chip communication links. Practical implementations eventually will have to comply with Telcordia standards. However, it appears that especially the transmitter designs are not fully suitable for on-detector applications. For example, the strong temperature sensitivity of resonant ring modulators requires a temperature stabilization. On the other hand, active components such as laser diodes and EAM based on a III/V material system are subject to performance degradation due to radiation impact. Furthermore, the simultaneous usage of both a demultiplexer for the cw optical carriers and a multiplexer for the output signals in order to reduce the total number of optical fibers has not been considered. Hence, detector instrumentation will benefit substantially from an optimized solution for an optical transmission system for the data read-out as proposed in this thesis.

4.4.3 The multichannel optical transmitter

The fundamental building blocks to assemble the envisioned on-detector transmitter are electro-optic modulators and (de-)multiplexers. Two depletion-type pn-phase shifters with a length of 3 mm in a Mach-Zehnder interferometer (MZI) configuration constitute a modulator. The (de-)multiplexers are planar concave gratings (PCG), as introduced in section 2.1.5. 2×2-MMI are used as power splitters and combiners and grating couplers are utilized to probe the sub-micrometer silicon waveguides with standard single-mode fibers.

In Figure 4.7a) an excerpt of the transmitter's process layout is presented. The four Mach-Zehnder modulators (MZM) are aligned in a column and are discernible by the metal electrodes and the contact pads at each side. The overall footprint of the unit is 3.8 mm × 1.7 mm. At both the input and the output, 2×2-MMI are used as power splitters and combiners. Therefore, each modulator has two ports at both the input and output. The electrodes are coplanar waveguides (CPW). The phase shifters of the MZM are located in the gaps between the signal and the respective ground electrode.

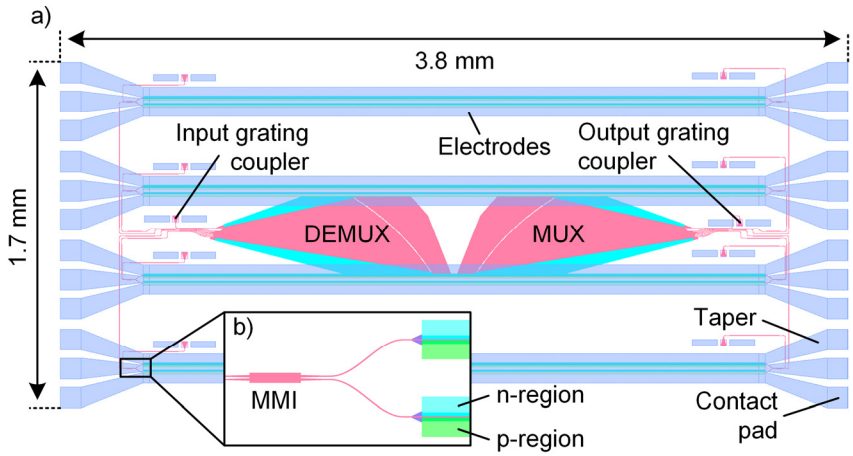

Figure 4.7: Excerpt of the process layout to illustrate the design of the integrated four-channel transmitter unit. a) Alignment of four Mach-Zehnder modulators and a demultiplexer (DEMUX) and multiplexer (MUX). b) Close-up of one of the modulators beneath the metal electrodes, which shows two waveguides emerging from the MMI. Each ends in a depletion-type phase shifter composed of a p- and n-doped strip-loaded waveguide.

The demultiplexer and the multiplexer are nested in the free space between the two inner modulators to minimize the unit's footprint. Thus, restrictions especially on the device width apply. They have an identical geometry and are aligned inversely. Two variants of the transmitter are implemented on the photonic test chip. Both employ four identical modulators but differ in the utilized (de-)multiplexer design. The variant Tx1 is equipped with a 7-channel (de-)multiplexer. The four modulators are connected to the ports with odd index starting from one. Using only every second channel introduces a larger spacing of adjacent channels, which is advantageous to avoid device crosstalk. A 9-channel (de-)multiplexer is utilized in Tx2, which has the same central wavelength and channel spacing as the

7-channel design. In order to accommodate the two additional channels, the angles θ_i and θ_o determining the position of the input and output waveguides on the Rowland circle are increased. That way, the spacing between adjacent channels does not reduce significantly. Consequently, the device width remains unchanged, although the reflector array becomes longer.

The common ports of the (de-)multiplexers are probed by dedicated grating couplers. One of the input ports of each MZM is connected to the demultiplexer output associated to the respective channel. The second port can directly be fiber-probed via an auxiliary grating coupler. The MZM output is realized similarly to the input configuration: one port is routed to the multiplexer while the other one is terminated by a grating coupler. Hence, each modulator can be tested and characterized both individually and as part of the system. Figure 4.7b) presents a close-up of the area, where the two waveguides associated to the respective MZI arm emerge from the MMI. Each connects to a depletion-type pn-phase shifter. The metal electrodes are not shown for clarity.

A photonic chip hosting the multi-wavelength transmitter is fabricated at the foundry of *IMS-CHIPS* in Stuttgart, Germany on a silicon-on-insulator (SOI) platform with a 250 nm silicon layer. The process is outlined in section 5.2. Alongside four transmitter units, the chip contains numerous active and passive components for characterization purposes. Among others, those are depletion-type pn-modulators, thermal modulators designed to provide for an operating point adjustment, (de-)multiplexers and power couplers.

4.5 Radiation effects in MOS devices

Apart from a wide temperature range and high magnetic fields at which on-detector equipment has to operate reliably, it is perpetually exposed to ionizing and X-ray radiation. In particular, radiation-hardness is all the more crucial, the closer detector modules or link components are deployed to the beam line. The impact of radiation on on-detector components is clearly beyond the scope of this thesis. Nevertheless, it is discussed briefly in this section, because the demand for radiation tolerance does affect the design of the link components.

In principle, two effects are observed when radiation interacts with a solid [147], [148]: firstly, incident particles can cause lattice defects, which yield a change of the energy bands. Secondly, positive charges accumulate in the oxide close to the interface between silicon and silicon dioxide in metal-oxide semiconductor (MOS) structures. They stem from the radiation-induced generation of electron-hole pairs. A fraction of holes fills oxygen vacancies, which exist in the oxide due to excess non-passivated silicon and remain there as positive charges. On the other hand, they may induce breaking the bonds of silicon atoms to their neighbors, and thereby produce interface traps within the silicon bandgap.

In an active component such as a MOS field-effect transistor, particularly the accumulation of charges in the oxide directly affects the device properties. Positive oxide charges attract electrons in the silicon layer, which results in the formation of a conducting inversion channel between source and drain of the transistor. Thus, the threshold voltage can shift severely even to the point of device failure. A similar consequence is observed in SOI-based electro-optic modulators relying on the plasma-dispersion effect as presented in section 3.4.1. A doped silicon waveguide sits on a silicon dioxide layer (SiO_2 BOX) and is optionally surrounded by a silicon dioxide cladding. Similar to a MOS device, the accumulation of localized charges in the oxide affects the charge carrier distribution in the active region. A schematic of the changing charge carrier distribution is sketched in Figure 4.8.

Figure 4.8a) shows the silicon waveguide hosting the pre-irradiated pn-junction. The grey section between the p- and the n-region represents the depleted region at thermal equilibrium. The post-irradiated state is depicted in Figure 4.8b), where positive charges accumulate in the oxide surrounding the waveguide. In the p-doped region, the oxide charges repel the free holes, which effectively narrows the conducting channel. In contrast, free electrons are attracted towards the boundary between the n-doped silicon waveguide and the oxide and the region becomes largely depleted. Both effects eventually

reduce the conductivity of the respective region, which in turn decreases the device's modulation efficiency. To date, the impact of radiation on the device performance is investigated at CERN, and the principal suitability of depletion-type pn-modulators for radiation environments has already been verified. [149]–[151].

In order to improve the radiation hardness of the depletion-type pn-modulator, two design parameters can be optimized. At first, the dopant concentrations can be raised. That increases the average density of free charge carriers in the modulator's slab region. Secondly, the height of the slab h_s itself can be increased, which lessens the impact of the carrier constriction in the slabs. However, both measures are also limited: a high doping concentration induces additional loss due to free carrier absorption. On the other hand, increasing the slab height reduces the confinement of the optical mode in the waveguide.

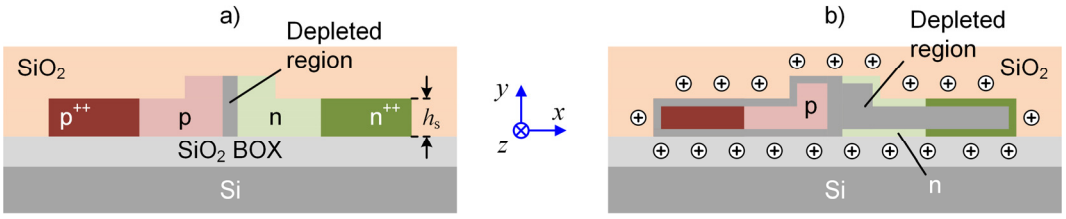

Figure 4.8: Schematic change of the charge carrier distribution in a depletion-type pn-modulator upon the exposition to radiation. a) Pre-irradiated pn-junction. b) Post-irradiated pn-junction with accumulated positive charges in the oxide layers. h_s expresses the slab height of the waveguide.

Other approaches to mitigate the impact of oxide charges on the modulator performance are the removal of the surrounding oxide regions to the greatest possible extent. For one, an organic material, such as a polymer, can replace the SiO_2 cladding. In contrast, the buried oxide cannot be replaced without a significant modification of the fabrication process, which then no longer complies with CMOS standards. However, although being a challenging process, it is possible to remove most of the BOX under the modulator and let it rest on periodic supporting structures. Due to the significant reduction of SiO_2 in the proximity of the waveguide, the accumulation of positive charges is obstructed without compromising the modulator performance or the structural integrity. The oxide removal is illustrated in Figure 4.9.

Figure 4.9a) shows a standard strip-loaded SOI waveguide with a SiO_2 cladding. Figure 4.9b) illustrates the same waveguide after opening the cladding oxide over the waveguide and partly removing the buried oxide. The resulting supporting structures are bars of SiO_2, which are periodically aligned crossways to the waveguide. First experiments of the selective removal of SiO_2 by a wet-etching process have been made at the *IMS-CHIPS* facilities. An SEM picture of a test structure is presented in Figure 4.9c). In contrast to the schematic shown in Figure 4.9b), the waveguide is supported by sockets instead of bars, because the parts protruding from below the waveguide have been removed by the wet etching as well. The development of an oxide removal process is still at an early stage. Likewise, the

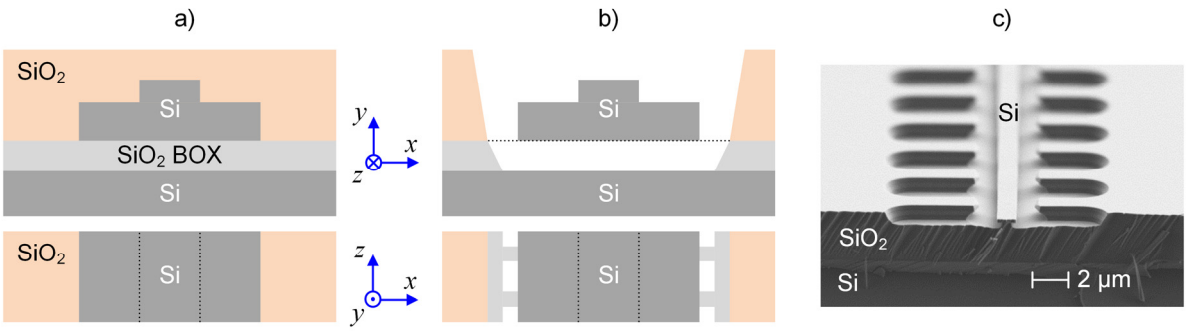

Figure 4.9: Illustration of the removal of oxide layers, which surround a strip-loaded silicon waveguide. a) Standard SOI waveguide with a SiO_2 cladding, b) SOI waveguide with the buried oxide partly removed, c) SEM image made by IMS-CHIPS of a test structure with periodically removed oxide.

investigation of the impact of oxide removal on the modulator performance and radiation hardness is still pending and clearly a subject of future work.

5 Silicon photonic devices and electro-optic modulators

In this chapter, the concept and the design as well as the simulation and the experimental characterization of silicon-based photonic components are discussed. The focus lies on the development of Mach-Zehnder modulators incorporating depletion-type phase shifters. Yet, among supplemental components such as grating-based (de-)multiplexers, multi-mode interferometers and grating couplers, thermo-optic phase shifters are considered as well.

The components are building blocks to assemble the integrated on-detector transmitter unit as presented in section 4.4. The devices are available for characterization on a photonic chip, which is fabricated on an SOI substrate according to the process described in section 5.2. It also includes variants of the transmitter unit, which are the essential element to construct a link system demonstrator.

5.1 Simulation methods

The work flow for the calculation of the modulation efficiency of the depletion-type phase shifters consists of two stages. At first, the change of the charge carrier concentration in the strip-loaded waveguide upon applying a reverse voltage is analyzed. In the second step, the resulting change of the refractive index and the induced phase change of the propagating mode are calculated. The first task is accomplished using the *Technology Computer Aided Design* (TCAD) tool *Synopsis Sentaurus*. A two-dimensional model of the strip-loaded waveguide containing the pn-junction is generated. The model is described in section 5.4. *Sentaurus Device* (sdevice) using the finite-elements method is utilized to simulate the charge carrier distributions. The change of the refractive index is subsequently calculated numerically according to equation (3.2). The effective refractive index is obtained by solving the integral between the electrical field vector $\vec{E}(x,y)$ and the location-dependent change of the refractive index $\Delta n(x,y)$

$$\Delta n_{\text{eff}} = \frac{\iint \Delta n(x,y) \cdot \left|\vec{E}(x,y)\right|^2 \mathrm{d}x\mathrm{d}y}{\iint \left|\vec{E}(x,y)\right|^2 \mathrm{d}x\mathrm{d}y}. \tag{5.1}$$

The expression evaluates the overlap between the optical mode and the refractive index change by means of building the product of the spatial refractive index distribution and the absolute square value of the field amplitude. The denominator provides for normalization. Assuming a homogeneous refractive index profile along the mode's propagation direction, $\Delta n_{\text{eff}}(z) = \text{const.}$, the accumulated phase shift of the optical field after the propagation length L is given by the integral along the z-axis

$$\Delta\varphi = \frac{2\pi}{\lambda_0} \int_{z=0}^{L} \Delta n_{\text{eff}} \, \mathrm{d}z = \frac{2\pi}{\lambda_0} \Delta n_{\text{eff}} \cdot L \tag{5.2}$$

with λ_0 as the free-space optical wavelength.

The calculation of the effective refractive index is verified by means of a complementary method, which involves the numerical simulation of the mode using *COMSOL Multiphysics*. In the following, it is referred to as "mode simulation method". As before, the change of the refractive index $\Delta n(x,y)$ is calculated from the charge carrier distribution. The resulting absolute refractive index profile is then applied to a strip-loaded waveguide model defined in *COMSOL*. The profile is given by

$$n(x,y) = n_{\text{Si}} + \Delta n(x,y), \tag{5.3}$$

where n_{Si} is the refractive index of intrinsic crystalline silicon at the considered wavelength. The change of the effective refractive index Δn_{eff} then is obtained in the course of conducting the simulation.

In Figure 5.1, examples of the simulated cross-sectional refractive index profile (a)) and the fundamental TE-mode of the waveguide (b)) are shown. The simulation is conducted for a phase shifter in a strip-loaded silicon waveguide with a height h of 220 nm and a width w of 500 nm. Figure 5.1c)

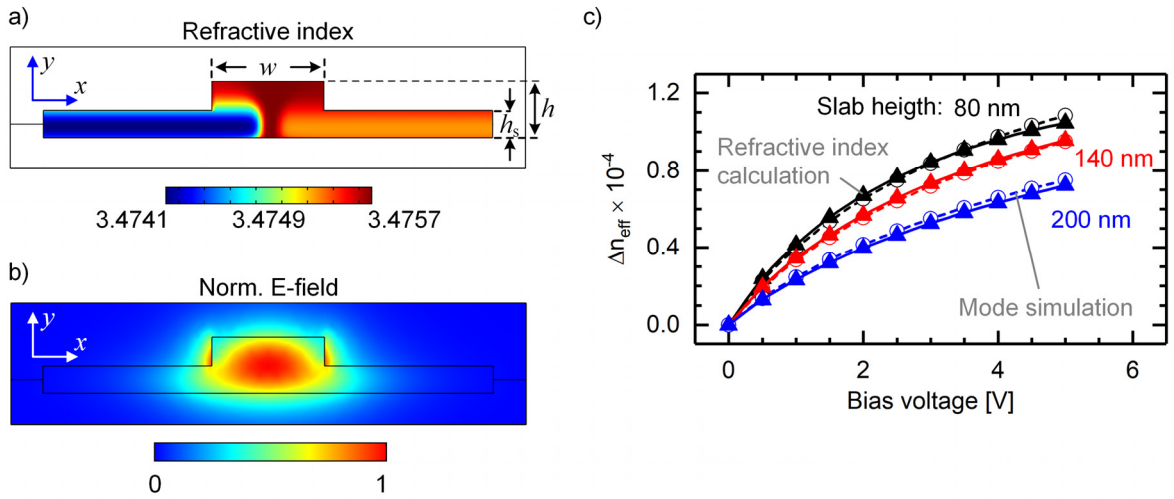

Figure 5.1: Intermediate results and comparison of two workflows to obtain the effective refractive index change of a strip-loaded silicon waveguide, which incorporates a pn-junction for phase modulation. a) Refractive index distribution $n(x, y)$ and b) normalized electric field distribution from the numerical calculation of the fundamental TE-mode. c) Calculated change of the effective refractive index as a function of the bias voltage for different slab heights h_s. The triangular symbols connected with solid lines and the open circles connected with dashed lines represent results, which stem from the two different simulation workflows.

shows the calculated change of the effective refractive index Δn_{eff} in the waveguide as a function of the bias voltage for different heights h_s of the slab. In particular, the results of both methods described above are compared in the diagram. The triangular symbols connected with solid lines represent the results of the refractive index calculation method while the open circles connected with dashed lines represent those from the method utilizing the mode simulation. Recognizably, the results are in excellent agreement, which is also confirmed in several other studies. Therefore, both methods are considered equivalent. In favor of a reduced complexity and a simplified workflow, the refractive index calculation method is chosen for the subsequent studies.

For the simulation of most of the sub-components such as MMI, grating couplers or waveguide tapers, the transient solver of *CST MICROWAVE STUDIO* is used. It relies on the finite integration technique, which solves discretized Maxwell equations in the integral form [152]. The refractive indices of materials are taken from the software's database as well as publicly available databases [153].

Compared to the operation wavelength, the required simulation area for the PCG multiplexers is relatively large. In favor of computation time, they are reduced to two-dimensional structures by means of calculating the effective refractive index for the slab waveguide region. The simulations are then conducted using *COMSOL Multiphysics*. The numerical calculations are performed in the frequency domain with the finite-elements method.

5.2 Fabrication technology

The photonic chip, which hosts all components discussed in this chapter, is fabricated at the CMOS line of the *IMS-CHIPS* foundry. The substrate is an SOI wafer with a silicon thickness of 250 nm on 3 µm buried oxide (BOX). The dimensions and required feature sizes vary considerably across the included components. This becomes most apparent taking the example of PCG (de-)multiplexers. While the slab waveguide covers an area of up to several square millimeters, the dimensions of the Bragg reflectors are in the sub-micrometer to micrometer range. Therefore, both optical lithography and electron beam lithography are used.

Apart from fully etching the silicon down to the BOX, the process includes two different shallow etching depths. The 130 nm etch depth defines the slab height of the strip-loaded waveguides. In addition, a second depth of 70 nm is available for etching the trenches of the grating couplers. Utilizing an oxide mask facilitates the realization of the varying feature sizes and different etching depths.

The dopants are injected by the implantation of arsenic ions as donors and boron ions as acceptors. Two different concentrations are available for each dopant species. The targeted concentrations of donors and acceptors to define pn-junctions is N_D=2.5×10^{17} cm^{-3} and N_A=3.5×10^{17} cm^{-3}, respectively. In the highly-doped zones, where vias connect the slab of a strip-loaded waveguide with the electrodes, the concentration of both species is 10^{19} cm^{-3}. 1 µm of thermally oxidized silicon (TEOS) is deposited as cladding material. Contact windows for the vias are formed by selectively removing the TEOS. Then, an aluminum alloy is deposited using a titanium compound as adhesion promoter. The resulting metal layer covering the TEOS is structured to form the electrodes and contact pads. The essential parts of a similar process at *IMS-CHIPS* are described in detail in [154]. However, it differs in that at the time of publishing, a p-doping was not available.

The photonic chip layout is assembled using the framework of *Mentor Graphics Pyxis Custom IC Layout Platform*. The PCG multiplexer geometries are generated by a custom implementation in MATLAB. All other involved devices and components are generated by making use of the *Pyxis Advanced Multi-Purpose Language* (AMPLE) programming language.

5.3 Experimental setups and measurement methods

In this section, the characterization methods for the relevant device properties are described and the generic experimental setups are presented.

5.3.1 Steady-state modulation efficiency

To facilitate the analysis of the modulation efficiency, an MZM can be designed asymmetrically, i.e. the optical path lengths of both arms differ intentionally. This is achieved by elongating the waveguide of one of the interferometer arms. Due to the optical path difference, the phase relation between the fields from the two arms varies with the wavelength. Hence, the output intensity changes with the wavelength and the transmission spectrum of the MZI resembles a cosine according to

$$|E|^2 = A \cdot \cos^2(a\lambda - \phi) = \frac{1}{2} A \cdot \left[1 + \cos\left(2 \cdot (a\lambda - \phi)\right)\right], \tag{5.4}$$

where A is the amplitude, a an arbitrary real constant and ϕ the phase of the cosine. Figure 5.2a) sketches a typical measured transmission spectrum normalized to maximum intensity. Once a bias voltage is applied to one of the phase modulators, the propagation velocity of the optical field in the respective interferometer arm changes globally and a uniform change of the MZI output intensity is observed. In an asymmetric MZI, the change of the phase relation manifests as a shift of the transmission spectrum by the interval $\Delta\lambda$. Figure 5.2b) illustrates the shift taking the example of normalized transmission

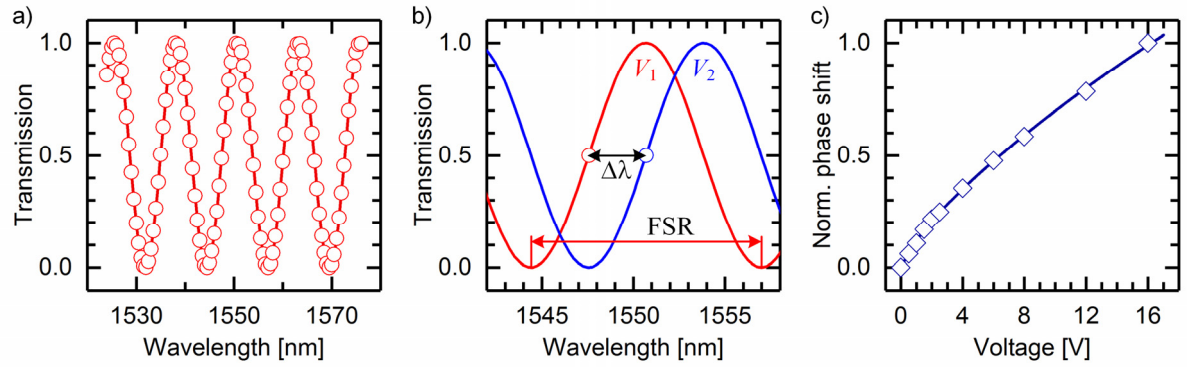

Figure 5.2: Relevant steps of calculating the steady-state modulation efficiency of phase shifters in MZM configuration. . a) Normalized measured spectrum (symbols) and the associated fit curve (line), b) close-up of the spectra at two different operating points for bias voltages V_i $(i = 1, 2)$. The spectrum shifts by $\Delta\lambda$. The free spectral range (FSR) is given by the path difference between both interferometer arms. c) Normalized phase shift as a function of the bias voltage deduced from the wavelength shifts obtained from b).

spectra at two bias voltages V_i $(i = 1, 2)$. For clarification, the transmission of 0.5 is denoted. $\Delta\lambda$ is the interval by which this point shifts upon switching from the voltage V_1 to V_2.

The MZI arm where the additional phase shift is induced in determines the sign of $\Delta\lambda$. Depending on which phase shifter in the MZI is biased, $\Delta\lambda$ is greater or less than zero for bias voltages in reverse direction. If the voltage is applied to the phase shifter in the interferometer arm including the optical path elongation, the transmission spectrum is red-shifted. In contrast, biasing the phase shifter in the arm without elongation yields a blue shift.

The phase change $\Delta\varphi$ at the bias voltage V_{i+1} in relation to V_i is proportional to the ratio of $\Delta\lambda$ and the free spectral range (FSR) of the interferometer. It reads

$$\Delta\varphi = 2\pi \cdot \frac{\Delta\lambda}{\mathrm{FSR}}. \tag{5.5}$$

The FSR is given by the period of the cosine and reflects the path difference of the interferometer arms. It can be obtained by the wavelength interval between two transmission minima. This is also indicated in Figure 5.2b). Finally, the progress of the phase as a function of the bias voltage is plotted. Typically, all values are normalized to the phase at 0 V. Thus, the result represents a relative phase shift. An example is shown in Figure 5.2c), where a normalized relative phase shift is plotted as a function of the applied bias voltage. The steady-state figure of merit is the voltage-length product $V_\pi L$. It quantifies the voltage V_π that is required to achieve a phase shift of π with a phase shifter of the length L. It can be derived from $\Delta\varphi$ according to

$$V_\pi L = V_\mathrm{B} \frac{\pi}{\Delta\varphi} L\,, \tag{5.6}$$

where V_B is the bias voltage, at which the value is calculated. The equation is based on expressing V_B as the fraction $\Delta\varphi/\pi$ of V_π that results in a phase shift $\Delta\varphi$. The formalism to calculate the relative phase change as well as the definition of the voltage-length product are commonly used in literature and can be found for example in [155].

The modulation efficiency is analyzed experimentally by means of measuring the steady-state output spectrum of the modulator within the boundaries of the C-band for different bias voltages. The transmission setup is sketched in Figure 5.3. It consists of an *Agilent* 81689A tunable laser source (TLS), a manual polarization controller (MPC), and an optical head and interface (*Agilent* 81623B and 81618A) as a power meter (PM). Red connections represent optical paths while the blue connections are electrical conduits. The bias voltage from a *Keithley* 2400 source measure unit (SMU) is applied to the device under test (DUT) using a *Picoprobe* SG microwave probe.

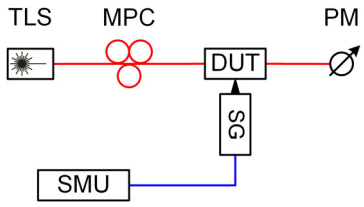

Figure 5.3: Sketch of the steady-state characterization setup of electro-optic components. The device under test (DUT) is optically probed with cleaved SMF. A bias voltage is applied with a source measure unit (SMU). The polarization of the optical field from the tunable laser source (TLS) is adjusted using a manual polarization controller (MPC) to match that of the photonic chip's input grating couplers. The intensity of the DUT optical output is measured with a power meter (PM).

The transmission spectrum for every bias voltage is obtained by consecutively measuring the optical power at discrete wavelengths in uniform intervals. The significant parameters are extracted by fitting equation (5.4) to the measured values. The transfer function $T(\lambda)$ compensates for the Gaussian-shaped filter characteristic of the grating couplers

$$T(\lambda) = \exp\left[-\frac{(\lambda - \lambda_c)^2}{b}\right], \tag{5.7}$$

where λ_c is the transmission peak of the grating couplers at a fixed coupling angle and b an arbitrary real constant. According to the same method, other active and passive devices, such as thermal modulators, (de-)multiplexers or multi-mode interferometers are experimentally characterized.

Another method of characterizing an electro-optic modulator is to measure the steady-state transmission at a specific wavelength as a function of the bias voltage or bias current. This is useful for the characterization of devices with a flat spectral response, such as electro-absorption modulators (EAM) or symmetric Mach-Zehnder modulators, where the spectral analysis is not possible. The experimental setup is identical to that presented in Figure 5.3. In contrast to the evaluation presented above, the method quantifies the modulator's transfer function including the interferometer characteristic. Thus, the analysis is also useful to identify adequate operating points of the Mach-Zehnder modulator (see Figure 3.2).

5.3.2 Small-signal characterization

The electro-optic modulation bandwidth is an important characteristic of a device, because it gives a measure of the data modulation performance. The characterization is performed by exciting the device under test (DUT) with a sinusoidal signal whose frequency is ramped up and measuring the optical signal with a wideband photodetector. The result is a spectral response of the electrical signal after the conversion to the optical domain in the DUT and the re-conversion at the photodetector.

Typically, the characterization can be accomplished by measuring the scattering parameters using a vector network analyzer (VNA). On the other hand, an RF signal generator can be used for the electrical excitation of the DUT. In this case, the spectral response is obtained by measuring the electrical signal from the photodetector with an electrical spectrum analyzer (ESA). The latter method has the advantage of a high resolution, while only the magnitude of the DUT transfer function can be measured. Using a VNA also allows for the measurement of the device's return loss and its input wave impedance.

In Figure 5.4, the experimental setups for the characterization of the frequency response are sketched. An *Agilent* 81950A TLS generates the optical carrier of which the polarization is manipulated by an MPC to match that of the DUT input grating coupler. A *Newport* 1014 wideband photodetector (PD) is used to detect the output signal.

In Figure 5.4a), the setup for the characterization of a single phase shifter is shown. In the following, this configuration is referred to as "single-ended" due to the similarity of the wiring. The electrical

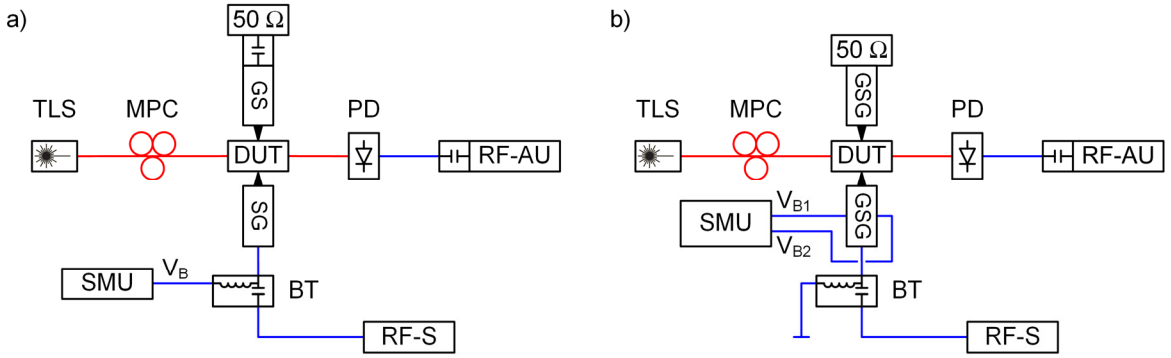

Figure 5.4: Sketches of the dynamic electro-optic characterization setups for single-ended and push-pull operation. Generally, the device under test (DUT) is optically probed with cleaved SMF. a) In single-ended operation, an RF source (RF-S) drives the DUT via a bias-tee (BT) and a bias voltage is applied with a source measure unit (SMU). The DUT is electrically terminated with a 50 Ω resistance. The modulated optical signal is detected by a photodetector (PD) which is connected to an RF analyzer unit (RF-AU). b) To achieve push-pull operation, the GS/SG probes are replaced by customized GSG probes, which have individual bias feeds and decoupling capacitors in both ground lines. A dual-channel SMU enables independent biasing of both MZM arms.

driving signal is applied via an *SHF* BT45 D bias-tee, where a bias voltage provided by a *Keithley* 2400 SMU is superimposed. A 50 Ω resistance terminates the DUT transmission line via a DC block. *Picoprobe* GS/SG microwave probes are used for contacting. In this specific characterization procedure, the RF source (RF-S) is port 1 of a *Rohde&Schwarz* ZVA24 VNA, while the RF analyzer unit (RF-AU) represents port 2.

In order to operate the phase shifters in both arms of the MZM simultaneously, it is electrically probed in GSG configuration. Due to the common signal electrode, the phase shifters have to be biased with voltages of opposite polarity, while the signal electrode hosts the bias voltage's ground potential. On the other hand, the ground electrodes are in contact with the ground potential of the RF source. To resolve this contradiction, customized *Picoprobe* RF probes are used, which have decoupling capacitors and individual bias feeds integrated in each of the ground lines. Hence, a separate bias-tee for the bias supply or a DC block for the terminating resistor are not needed. However, to avoid a floating DC ground potential between both phase shifters, it is pulled to the common ground via the DC port of the bias-tee at the source probe.

The sketch of the altered setup is shown in Figure 5.4b). In this configuration, the independent biasing of both MZM arms is facilitated using an *Agilent* B2912A dual-channel SMU. A detailed sketch of the resulting circuitry is given in Figure 5.6 on page 49.

Prior to the characterization of the EOE response, the calibration of the measurement system is performed and the electrical scattering parameters of the DUT are determined according to the experimental setup presented in Figure 5.5. The system is through-open-short-matched (TOSM) calibrated to the reference plane of the microwave probe tips.

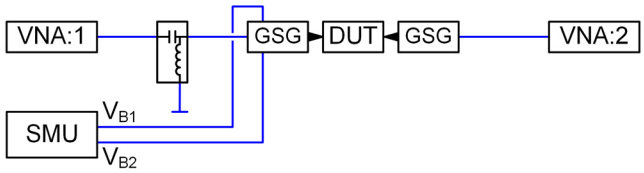

Figure 5.5: Setup sketch for the experimental determination of the scattering parameters of a DUT using a network analyzer and GSG microwave probes for contacting.

The EOE characterization is performed by changing the setup while maintaining the VNA calibration state. The photodetector is connected to the VNA port 2 and in return the respective microwave probe is terminated by a 50 Ω resistance. The approach does not affect the port 1 return loss characteristics but introduces an uncertainty to the transmission characteristics from port 1 to port 2 of the DUT, which have to be taken into account in the evaluation.

Nevertheless, the method is applied, since no calibration data or transfer characteristic is available for the photodetector. Accepting this as a prerequisite, the results of the EOE characterization and the scattering parameters may be directly compared to assess the modulator performance.

An important figure of merit of the both the electro-optic conversion and the S_{21} parameter is the 3 dB bandwidth. Since the electro-optic bandwidth can only be determined by measuring the electrical signal at the output of the photodetector, the quadratic dependency of the electrical power P_{el} on the photocurrent I_{p} has to be taken into account. The photocurrent depends linearly on the incident optical power P_{opt} and the detector responsivity R_{d}. Thus, the relation between the electrical power at the load resistance R_{L} and the optical power is likewise quadratic

$$\begin{aligned} I_{\mathrm{p}} &= R_{\mathrm{d}} \cdot P_{\mathrm{opt}}, \quad P_{\mathrm{el}} = R_{\mathrm{L}} \cdot I_{\mathrm{p}}^2 \\ \Rightarrow P_{\mathrm{el}} &= R_{\mathrm{L}} \cdot \left(R_{\mathrm{d}} \cdot P_{\mathrm{opt}}\right)^2. \end{aligned} \tag{5.8}$$

In the logarithmic notation, the exponent is represented by a factor of 2. Hence, to identify the optical 3 dB bandwidth of an electro-optic modulator, the electrical 6 dB bandwidth has to be determined. The

relation (5.8) also has to be considered when comparing the electro-optic response and the S_{21} parameter of a modulator.

5.3.3 RF characterization circuitry

Figure 5.6 shows the schematic of contacting both phase shifters of an MZM DUT in GSG configuration. The phase shifters share the DC ground potential on the signal electrode, which is equalized with the RF ground potential. The necessary connection is established exclusively for the DC bias by a short circuit between the signal pin and the RF ground potential at the DC port of the bias-tee. Due to the alignment of the pn-junctions, the bias voltages have opposite polarity.

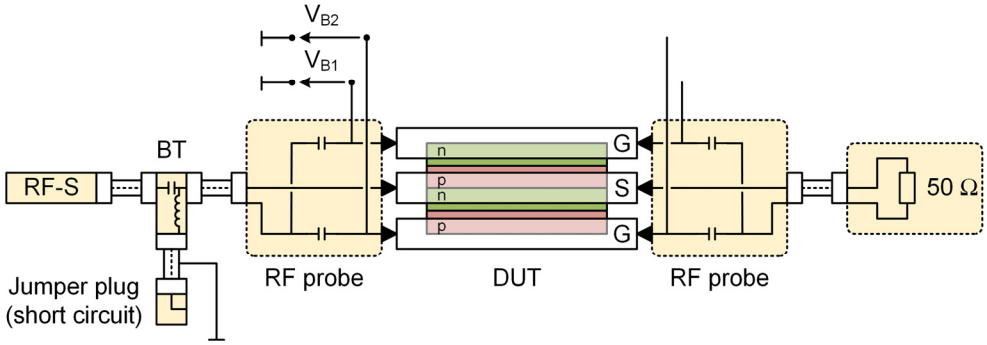

Figure 5.6: Schematic of the modulator contacting configuration using customized microwave probes, which contain capacitors in the ground lines for the isolation of the bias voltage.

In contrast, the RF signal is coupled to the modulator in a standard GSG configuration, where the modulator electrodes act as a coplanar waveguide. Thus, an isolation between the RF and the DC ground potentials is required. It is achieved by the insertion of DC blocks in the ground lines. The circuitry is implemented by customized microwave probes, of which the schematic is included in Figure 5.6. Arbitrarily, the bias voltages V_{B1} and V_{B2} are applied via the source probe depicted on the left side.

The equivalent circuit of the situation is given in Figure 5.7a). The RF source is modelled by an ideal RF voltage source V_{RF} with the internal resistance R_{L}. The bias-tee is represented by the blocking capacity C_{BT} and the inductivity L_{BT}. The capacities C_{P} model the blocking capacities integrated in the microwave probes. The ideal bias voltage sources $\tilde{V}_{\mathrm{B}i}$ $(i = 1{,}2)$ are included along with their internal resistances $R_{\mathrm{I}i}$. The pn-junctions of the phase modulators are modelled by the diodes M_i. The termination resistance R_{L} is identical to the internal resistance of the RF generator. Further resistances of the cables, feed lines or contacts are neglected.

Figure 5.7b) shows the equivalent circuit that is relevant for the bias voltage supplies. Only the DC-coupled elements remain and the common ground potential between the diodes becomes apparent.

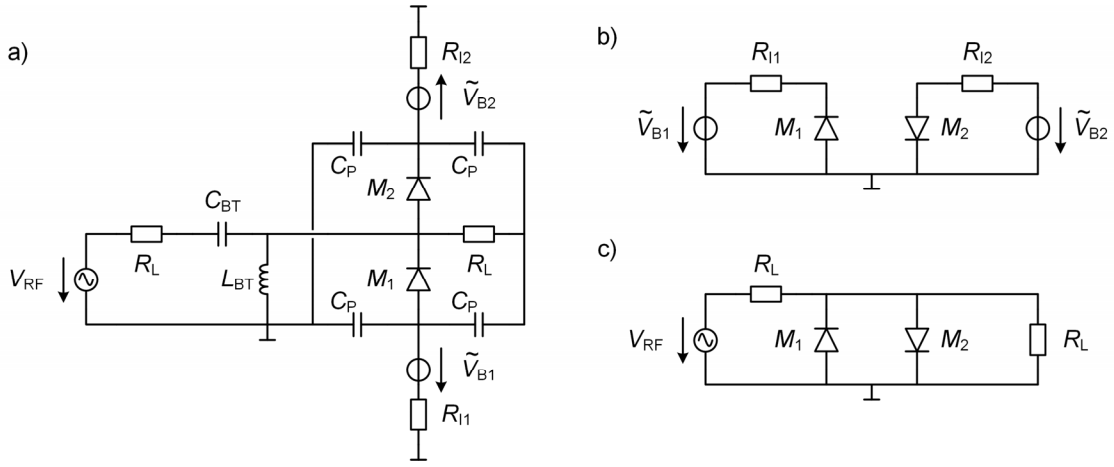

Figure 5.7: Equivalent circuits of the modulator driving circuitry. a) Complete circuit, b) DC circuit, c) RF circuit.

Furthermore, the alignment of the modulator pn-junctions requires opposite polarities of the bias voltages to operate both in reverse direction.

The equivalent circuit in Figure 5.7c) shows the situation for the RF signal. Both modulators are connected in a parallel circuit to the RF source and are terminated by the load resistance R_L. Due to the opposite alignment of the pn-junctions, a voltage swing reduces the phase in M_1 and simultaneously enhances the phase in M_2, or vice versa. Thus, this alignment allows for push-pull operation of the MZM with a single RF source.

5.3.4 Data transmission experiment

In order to evaluate the signal quality the electro-optic modulators are capable to generate from an electrical signal, the transmission and reception of a bit stream encoded on an optical carrier is required. The experimental setup is a bit error ratio tester (BERT), which is based on an *Altera* Stratix V GX FPGA running on a *Transceiver Signal Integrity Development Board*. Depending on the requirements, the modulator DUT can be driven single-ended or in GSG configuration. A schematic of the setup is presented in Figure 5.8, where a GSG contacting of the modulator DUT is assumed. Therefore, two bias voltages are required and the wiring is identical to the frequency response characterization setup depicted in Figure 5.4b).

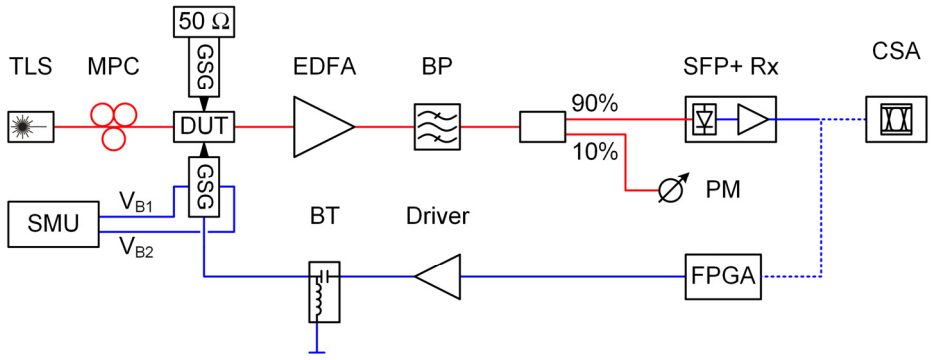

Figure 5.8: Sketch of the experimental setup to evaluate the signal integrity of an optically transmitted PRBS.

The FPGA generates a pseudo-random bit sequence (PRBS), which is amplified by an electrical driver circuit to a level appropriate to obtain an adequate modulation depth. The driver is part of a customized four-channel amplifier circuitry designed and assembled from discrete components.

The optical carrier from an *Agilent* 81689A TLS is coupled to the DUT using cleaved SMF. An MPC manipulates the polarization alignment. Customized *Picoprobe* GSG microwave probes similar to the small-signal characterization setup are used for contacting the source signal as well as the termination resistor. The receiver for direct detection is implemented by the optical receiver of a *Fiberstore* SFP-10GER-55 SFP+ module (SFP+ Rx). It consists of a photodiode, a transimpedance amplifier and a limiting amplifier. The electrical output signal of the receiver is fed back to the FPGA board, where the BER is estimated by means of comparing the source signal with the received signal. Alternatively, the received signal can be forwarded to a *Tektronix* CSA8200 communication signal analyzer (CSA) to visualize the eye pattern. The CSA uses a *Tektronix* 80E04 sampling module with an analogue bandwidth of 20 GHz for the data acquisition. The limiting amplifier provides for stable logical signal levels, which is beneficial for the BER evaluation. At the same time, however, it obstructs an analysis of the signal extinction ratio.

In a practical transmission system, the average power of the optical signal at the receiver is determined by the optical power of the laser source and the accumulated attenuations along the signal path. Among others, these are the insertion loss of the transmitter components, fiber attenuation or coupling losses. In order to avoid the receiver being limited by thermal noise, an *IPG Photonics EAD Series* erbium-doped fiber amplifier (EDFA) amplifies the output signal of the DUT. A *TECOS* tunable

bandpass filter (BP) suppresses the spectral noise components flanking the optical carrier on which the payload is encoded. The optical input power to the receiver is measured using a 90:10 optical power splitter and power meter (PM) comprising of an optical head and interface (*Agilent* 81623B and 81618A).

Both the driver unit and the FPGA board in combination with the SFP+ transceivers are also utilized in the transmission system demonstrator described in chapter 7. The topology of the demonstrator is derived from this experimental setup. A description of the operating principle and more detailed schematics are given chapter 7 as well.

5.4 Depletion-type pn-modulators

Given the spatial resolution requirements on current and future LHC experiments, the number of electronic sensor channels will increase strongly. Consequently, this puts a keen demand on the data read-out bandwidth. As already discussed in section 4.4, an optical transmission systems with a silicon-based on-detector transmitter unit offers a large data rate and satisfies the requirements on low energy consumption, volume and mass.

In this section, the requirements on the essential system components are discussed. Furthermore, design rules are specified in order to define a modulator design optimized for the application in a harsh environment. A simulation model of a depletion-type pn-phase shifter as a core component of an integrated transmitter is developed. The influences of the fabrication process tolerances on the device performance are explored by comparing simulation results to experimental data of an existing device. Based on specifications of the fabrication process outlined in section 5.2, the model is used for projecting the performance of devices designed in this work. Furthermore, the model provides the opportunity to consider the accumulation of oxide charges. Thus, performance degradation due to radiation exposure can be taken into account in future studies. In the course of the device characterization, the simulation results are compared to experimental data. Furthermore, the small signal characteristics are analyzed and the back-to-back data transmission at a rate of 11.3 Gbit/s is demonstrated. Finally, the influence of environmental conditions on the steady-state and small-signal performance is evaluated.

5.4.1 Boundary conditions and design rules

Taking again the example of the CMS detector, the silicon tracker is the sub-system with the highest number of detector channels and therefore the most demanding on the read-out bandwidth. Consequently, it clearly benefits from the high data transmission bandwidth of an optical transmission system. At the same time, the sensors and pre-processing units are located closest to the beam line and therefore are exposed to high radiation doses. Furthermore, according to the *Versatile Link* specifications (see section 4.2.2), the expected operating temperature range is between -30 °C to +60 °C and the magnetic field can reach 4 T. Finally, the energy input of any on-detector component must be low, to avoid excess effort of cooling the detector.

Based on the boundary conditions, the following set of requirements are defined: most importantly, like any on-detector equipment, especially the active components such as electro-optic modulators have to be radiation-hard. Additionally, the on-detector processing and transmitter units have to have a small footprint and mass, so that they do not block sensor cells and thereby impair the detector accuracy. Moreover, the energy consumption must be low so that the read-out sub-system does not add to the detector's total energy input compared to state-of-the art solutions. Ideally, the optical components are athermal. Since this goal is not easily achieved, the performance should at least be stable at constant ambient conditions.

As described in section 5.2, the devices are fabricated on an SOI substrate with a silicon thickness of 250 nm on 3 µm of buried oxide. The top cladding is a 1 µm silicon dioxide layer. The basic waveguide width is 500 nm. A fabrication process is readily available at *IMS-CHIPS* foundry [156]. The depletion-type phase modulators are implemented as strip-loaded waveguides, which comprise a pn-junction. The

basic property, which is subject to optimization, is the location of the pn-junction, in order to maximize the overlap of the optical mode and depletion region. It is predominantly dependent on the concentrations of n- and p-dopants. The selection of the slab height and the doping concentration has an effect on the radiation hardness, which is accompanied by a change of the modulation efficiency. While this optimization is clearly beyond the scope of this thesis, some design rules extracted from previous work are adapted and examined. Further, the length of the device governs the modulation efficiency. According to equation (5.2), a longer device yields a smaller $V_\pi L$. At the same time, the capacitive load scales with the device length, which limits the modulation bandwidth. Hence, any modulator design is a trade-off between the modulation efficiency and the modulation bandwidth.

Finally, the total energy consumption has to be considered. This includes thermal stabilization using local heaters, because the operating point of an MZI-based modulator may shift with changing ambient temperature. In non-standard modulator designs, the impact of ambient temperature can be reduced either by special athermal designs or by adding a polymer cladding with a negative thermo-optic coefficient to the phase shifters [157].

5.4.2 Phase shifter geometry

The modulator design considered in this thesis relies on a horizontal pn-junction, which is embedded in a strip-loaded waveguide. A schematic of the cross section including the relevant dimensions is shown in Figure 5.9. The strip has the height h and the width w. Typically, h is specified by the silicon layer thickness of the wafer. The total extent of the slab is w_s and the height is h_s. The waveguide is p- and n-doped, respectively. The actual pn-junction is located in the strip section, resulting in the formation of a depletion region with the width w_{dep}. At the far end of each side of the waveguide, a heavily doped region is included, which provides the interface to the metal contacts. The width of the p- and the n-region between the heavily doped corners and the strip is given by $w_{s,p}$ or $w_{s,n}$, respectively. The net widths of the doped regions within the strip boundaries are w_p and w_n. Similar to w_{dep}, they are governed by the doping concentrations.

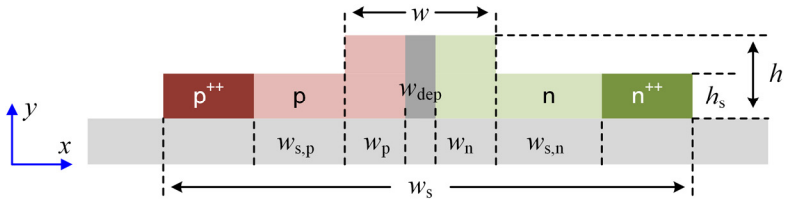

Figure 5.9: Schematic of a depletion-type pn-modulator, which is based on a doped strip-loaded waveguide. The structure is defined by height h and width w of the strip waveguide as well as height h_s and width w_s of the slab. $w_{s,p}$ and $w_{s,n}$ are the extents of the lightly doped regions in the slab between the heavily doped contacts and the strip waveguide. w_{dep} is the width of the depletion region and w_p and w_n are the widths of the respective neutral regions in the strip waveguide.

A tuning of the strip-loaded waveguide geometry affects both the modulation efficiency and the small-signal frequency response. For one, the waveguide geometry governs the grade of the confinement of the optical mode and its overlap with the depletion region. If required, the overlap can be optimized by adjusting the doping profile [158], which however is limited by the loss due to the free charge carriers. On the other hand, the geometry affects the electrical properties, because the doped waveguide promotes the interaction of the optical wave and the electrical signal. In particular, the dimensions of the strip region has an impact on both the junction capacity and the resistance in the neutral zones. The resistance in the slab is likewise dependent on the slab dimensions. The relations are described by the equations (3.6) and (3.7). Again it is emphasized, that the resistance in the slab region is typically higher compared to the strip, and thus dominates the total resistances. Table 1 summarizes the dimensions of the modulators.

Table 1: Summary of the relevant dimensions defining depletion-type pn-modulators based on a strip-loaded waveguide as depicted in Figure 5.9.

h	w	h_s	w_s	$w_{s,p}$	$w_{s,n}$
250 nm	500 nm	120 nm	18.0 µm	1.75 µm	1.75 µm

In addition, as discussed in section 4.5, the waveguide geometry can have an influence on the radiation hardness of the device. Apart from the 130 nm etch depth resulting in a slab height of 120 nm, the fabrication process presented in section 5.2 offers a second depth of 70 nm that is natively used for etching the trenches of the grating couplers. In the present study, it is used for the realization of an alternative modulator design. Except for the resulting slab height of 180 nm, it is identical to the design based on the dimensions given in Table 1. Although the analysis of device performance degradation due to radiation exposure is clearly beyond the scope of this work, non-irradiated devices with different slab heights are compared in both simulations and experimental characterizations. The study may be restricted to the experimental comparison of only two waveguide geometries, but advantageously, no additional processing steps are required.

5.4.3 Phase shifter simulation model

The simulation model is assembled using *Sentaurus Structure Editor* as part of the TCAD suite. The phase shifter is modelled by the cross section of a strip-loaded waveguide according to Figure 5.9. The pn-junction interface is located within the boundaries of the strip waveguide section. A bias voltage can be applied to the heavily-doped regions via electrical contacts, which are dedicated interface regions from the structure to the simulation environment. A Delaunay mesh is used yielding triangular mesh cells that discretize the model in two dimensions [159]. Two levels of refinement are distinguished: in the proximity of the strip waveguide, the minimum edge length is set to 5 nm, while it is 10 nm in the periphery. At the model boundaries, the edge length is adjusted automatically by the mesh generator. A further manual mesh refinement does not have an impact on the simulation results.

In order to define the characteristics of the simulation model, experimental results of a real device are used. In particular, the steady-state modulation efficiency of a Mach-Zehnder modulator with depletion-type pn-phase shifters is taken as reference. It is based on the design provided by the *OpSIS* project and is presented in [160]. With the same modulator, the temperature studies described in section 5.4.7 are carried out. The thickness of the silicon layer is 220 nm, the waveguides have a width of 500 nm and the phase shifters have a length of 3 mm. The peak doping concentrations in the active region around the rib waveguide are specified by 5×10^{17} cm^{-3} of donors in the n-region and 7×10^{17} cm^{-3} of acceptors in the p-region. The highly-doped regions for the electrical contacts have the concentrations 5×10^{20} cm^{-3} (n^{++}) and 1.7×10^{20} cm^{-3} (p^{++}).

The modulation efficiency is dependent on many properties of the modulator design. At first, the geometry of the strip-loaded waveguide has a strong influence because it governs the mode confinement in the waveguide. That includes the thickness of the silicon layer, the width of the strip section or the etch depth to form the slab region. Secondly, the design and the doping concentrations of the pn-junction affects the modulator's performance profoundly. For example, a pn-junction can be aligned either vertically or horizontally across the waveguide or the donor-layer partly encloses the acceptor-layer in a u- or s-shape [161]–[163]. Moreover, the doping profile can be modulated in the propagation direction. Zig-zag and periodically interleaved rectangular junction designs have been demonstrated to improve the interaction between the optical field and the depletion region [155], [164]–[166]. However, especially the periodically modulated doping profiles are extremely demanding on the process accuracy while the formation of a vertical junction requires additional processing steps compared to conventional designs.

Yet in a modulator based on a standard horizontal pn-junction, the accuracy of the dopant implantation is vital to the device performance. For one, the implantation depth and concentration as well as the position and extent have to be well defined. The former is governed by the implantation

energy and duration. The latter is predominantly dependent on the mask alignment accuracy, which is subject to alignment tolerances in the range of 50 nm. Furthermore, an incomplete activation of the dopants may change the regions' dimensions and the resulting concentrations [167]. Finally, the actual location of the pn-junction boundary may deviate from the intended due to diffusion of charge carriers.

For one, this can result in a deviation of the junction interface from the intended location. On the other hand, the boundaries of the p- and n-doped region do not converge at the intended position, but are separated by an intrinsic region of with w_i. Beyond that, the pn-junction can be deliberately displaced from the waveguide center in order to optimize the overlap between the active region and the optical field. Figure 5.10 shows both situations schematically. A positive sign of the offset d_m in Figure 5.10a) indicates an offset towards the n-region while the junction is shifted towards the p-side for a negative sign. In Figure 5.10b) w_i is the width of the intrinsic region.

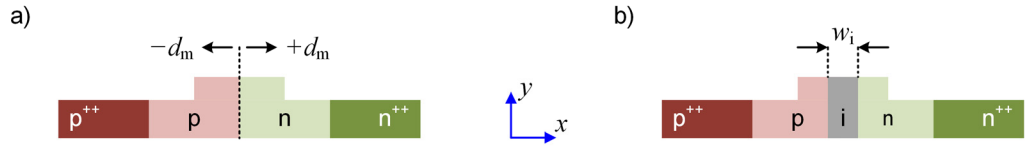

Figure 5.10: Schematic representations of possible pn-junction alignments. a) Displacement of the junction interface by an offset $\pm d_m$ from the waveguide center. b) Separation of the p- and n-doped region by an intrinsic region of with w_i.

The model of the simulated modulator is shown in Figure 5.11a) along with the distribution of the doping concentrations. The intended location of the junction is at $x = 0$, which is the center of the waveguide. The doping profile is considered uniform in the slab region, which is a common assumption for state-of-the-art implantation processes [168]. At the pn-junction boundary, the concentrations do not decrease abruptly in x-direction but decay also according to the shape of a Gaussian function.

That way, the finite penetration depth of the implants towards the interface and the subsequent diffusion is taken into account. In the vertical direction, the doping concentration is assumed to have a Gaussian shape with the peak concentration at a penetration depth at half the height of the silicon layer. In the reference model, the peak is located at 110 nm.

Figure 5.11b) shows the normalized concentrations of the p- and n-type dopants as a function of the x-position with respect to the waveguide center. The solid lines represent the acceptors while the dashed lines represent the donors. The relation is plotted for different widths w_i of the intrinsic region between

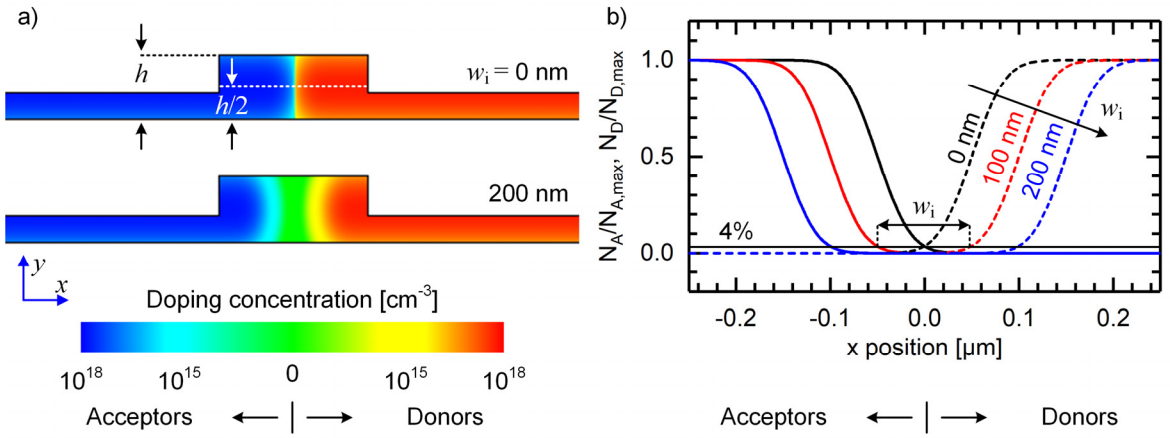

Figure 5.11: Simulation model of the depletion-type pn-phase shifter. a) Structural geometry and doping profile for the intrinsic region widths of 0 nm and 200 nm. The left side is implanted with acceptors while the right side is populated with donors. b) Normalized concentrations of the p- and n-type dopants at the height h/2 as a function of the x-position with respect to the waveguide center. The boundary from a doped region to the intrinsic region is defined as the x-position, where the dopant concentration is reduced to 4%. The intrinsic region width w_i is given by the distance between the boundaries of the n- and the p-doped region.

the doped regions. The offset in x-direction, where the dopant concentration is reduced to 4% is defined as the boundary between the intrinsic and the respective doped region. The width w_i is given by the distance between the two boundaries. The relation is also indicated in the diagram. For $w_i = 0$, the boundaries of the doped regions converge at $x = 0$.

The influence of both the junction offset and the width of the intrinsic region are studied separately in simulations as introduced in section 5.1. In Figure 5.12, the simulation results of the influence of the junction offset on the modulation properties are presented. Figure 5.12a) compares the effective refractive index change Δn_{eff} due to an applied reverse voltage to the pn-junction as a function of the junction offset from the waveguide center. Δn_{eff} is defined with respect to 0 V. At 5 V, which is the highest voltage applied in this study, the dependency of the device performance on the junction alignment becomes most obvious. A shift in the positive x-direction represents a displacement towards the n-doped region. In this case, the deterioration of the device performance is stronger compared to a displacement towards the p-doped region.

In order to compare the simulation result with measurement data, the phase shift of a 3 mm long device is calculated from Δn_{eff} using equation (5.2). The result is presented in Figure 5.12b). The diagram shows the calculated phase shift as a function of the bias voltage. Each curve in the array represents a different lateral junction offset from 0 nm to ±150 nm in steps of 50 nm. Solid lines and symbols represent a shift towards the n-region (+x-direction, $d_m > 0$) and the dashed lines with the half-right solid symbols indicate a shift towards the p-region (−x-direction, $d_m < 0$). The black curve tracing the open squares represents the case, where $d_m = 0$. Additionally, the experimentally obtained steady-state modulation efficiency of the modulator which the simulation model is based on is included by the orange rhombs. Each curve is normalized to the respective phase at 0 V.

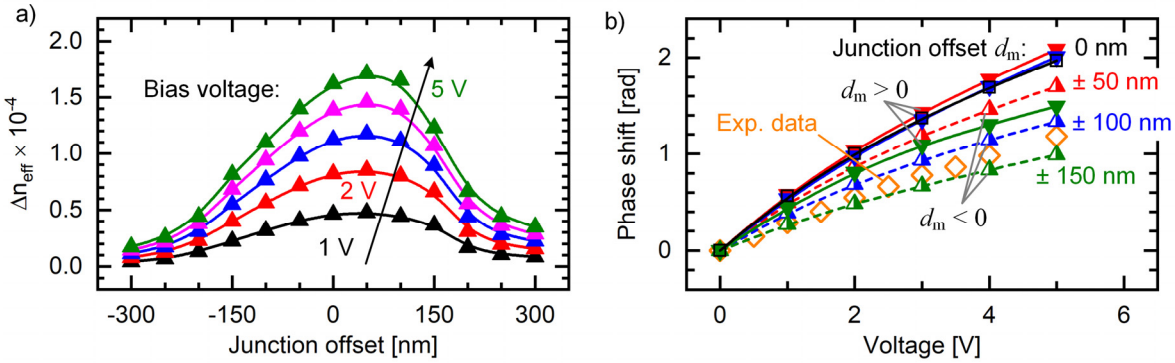

Figure 5.12: Result of the simulation study on the pn-junction displacement. a) Change of the effective refractive index Δn_{eff} in a waveguide incorporating a horizontal pn-junction as a function of the lateral junction displacement from the waveguide center for different bias voltages. b) Calculated phase shift aggregated over an interaction length of 3 mm as a function of the bias voltage for different lateral junction offsets d_m. The experimentally obtained steady-state modulation efficiency of the modelled device is included by the orange rhombs.

The influence of the width of the intrinsic region on the device performance is summarized in Figure 5.13. Figure 5.13a) shows the change of the refractive index Δn_{eff} in the strip-loaded waveguide as a function of the intrinsic region width w_i for different bias voltages. The solid triangles represent the simulated data points, which are connected by the solid lines. The width w_i is varied from 0 nm to 300 nm in steps of 50 nm by equally receding the doped regions' boundaries from the center of the waveguide. At all considered bias voltages, a non-linear decrease of Δn_{eff} for increasing w_i is observed. Similar to the previous study, the resulting phase shift of a 3 mm device is calculated from the simulation data. Again, the result is compared to the measured steady-state modulation efficiency of the real device. The result is shown in Figure 5.13b), where the phase shift as a function of the reverse bias voltage is shown for different intrinsic region widths w_i. Following the mapping of Figure 5.12b), triangular solid

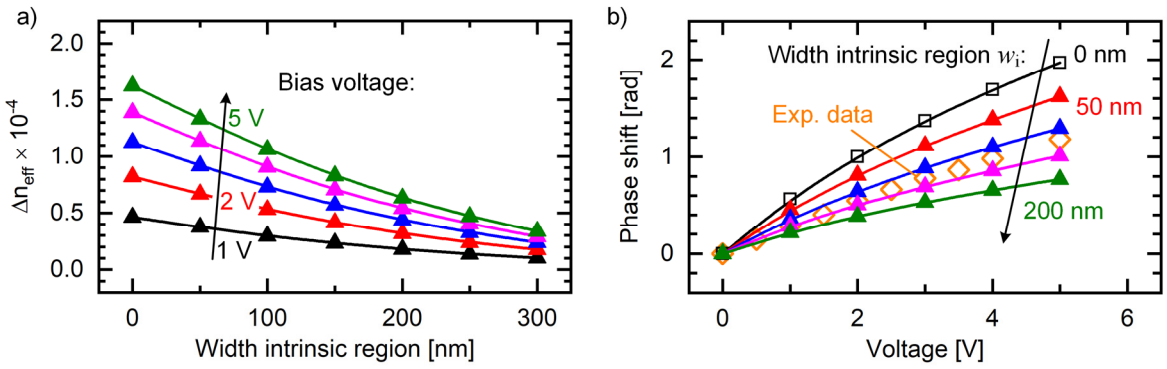

Figure 5.13: Simulation result of the influence of the intrinsic region width w_i on the modulation efficiency. a) Change of the refractive index Δn_{eff} in the strip-loaded waveguide as a function of the intrinsic region width w_i for different bias voltages. b) Calculated phase shift aggregated over an interaction length of 3 mm as a function of the reverse bias voltage for different widths of the intrinsic region. The measured steady-state modulation efficiency of the modelled device is included by the orange rhombs.

symbols represent the simulated phase shift for the given w_i, while the open rectangular symbols show the case $w_i = 0$. The data points from the experiment are included by orange rhombs.

Both studies show, that the alignment of the pn-junction has a strong influence on the change of the effective refractive index Δn_{eff} and thus on the modulation efficiency. Especially the junction displacement offers the potential for optimization: uneven concentrations of p- and n-type dopants such as specified for the reference device yield a displacement of the depletion zone center at thermal equilibrium. The result is a reduced overlap of the optical mode with the active region, which could be compensated by adjusting the displacement d_m. It manifests is Figure 5.12a), where an offset of the doped regions' interface towards the +x-direction ($d_m > 0$) yields an improved Δn_{eff}. On the other hand, an alignment of the interface that does not match the proportion between the dopant concentrations has a negative effect on the device performance.

The effect of an intrinsic region between the doped regions is dependent on its width in relation to the waveguide dimensions. A relatively large section yields a small change of free charge carriers in the proximity of the mode's intensity maximum, which again impairs the overlap between the mode and the active region. According to Figure 5.13, Δn_{eff} diminishes with increasing w_i and thus the modulation efficiency is reduced. The studies on the pn-junction alignment show that the modulation efficiency is governed by the overlap between the optical mode and the depletion zone. To be more specific, the effective refractive index change Δn_{eff} is stronger, the more energy of the mode is confined in the area where the gradient of the free carrier concentration is highest. The space charge region is optimally aligned, if it is centered on the mode's intensity maximum. At the same time, the region's extent governed by the doping concentrations is small compared to the waveguide width.

The third important aspect related to dopant implantation is the concentration of n- and p-type dopants. First of all, it governs the extent of the depletion region according to equation (3.4) and thereby relates to the issue of the intrinsic region. On the other hand, the alignment of the pn-junction might be affected, because the location of the space charge region depends on the ratio between the dopant species. Lastly, the modulator loss significantly depends on the dopant concentrations due to free carrier absorption. Therefore, the influence of the doping concentration on the modulator characteristics is studied. For this study, the pn-junction displacement from the waveguide center as well as the width of the intrinsic region are assumed to be zero.

The purpose is to explore the impact of the dopant concentration variations due to process tolerances. Beginning with the nominal concentrations, the steady-state modulation efficiency is analyzed for different combinations of reduced dopant concentrations. The approach is based on the assumption that due to tolerances of the implantation process the achieved doping concentrations are more likely lower than the nominal values than higher. A summary of the investigation is presented in Figure 5.14. The

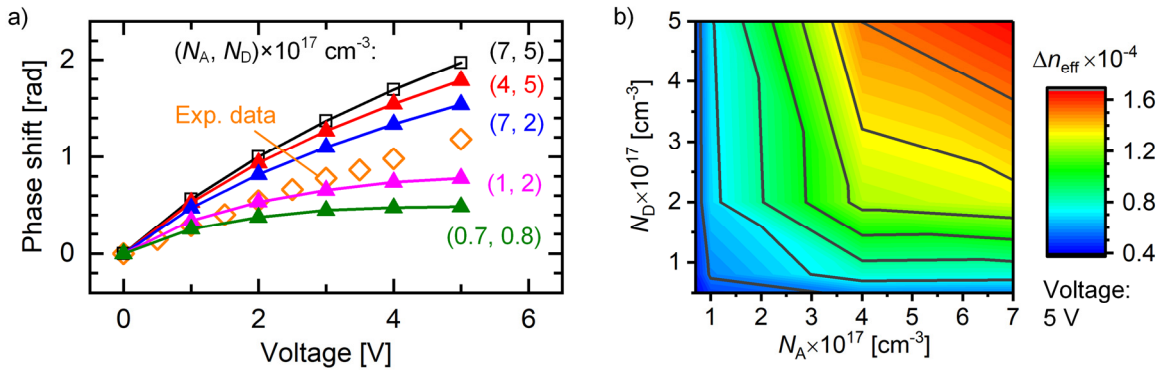

Figure 5.14: Simulation result of the influence of different donor and acceptor concentrations on the steady-state modulation efficiency of a 3 mm long pn-phase shifter. a) Phase shift as a function of the bias voltage for selected combinations of donor and acceptor concentrations. The contour diagram in b) shows the change of the effective refractive index at a bias voltage of 5 V.

phase shift as a function of the bias voltage is shown in Figure 5.14a) for a selection of dopant concentration combinations. The black open symbols connected by the black curve represent the result for the nominal doping concentrations, i.e. 7×10^{17} cm^{-3} of acceptors and 5×10^{17} cm^{-3} of donors. The solid triangular symbols and solid lines show the simulated phase shifts for the reduced concentrations. The experimental data from the real device is also included. The contour diagram in Figure 5.14b) shows the dependency of the refractive index change on both the acceptor and the donor concentration at a bias voltage of 5 V, which is the highest voltage applied in the study.

It is evident from Figure 5.14a) that the doping concentrations have a strong influence on the modulation efficiency. The lower the doping concentrations are, the smaller the phase shift at a given bias voltage becomes. For a pair of high doping concentrations, such as the nominal values, the progression of the phase shift is monotonously rising in the considered voltage range. A similar behavior is observed if the concentrations deviate slightly from this reference. In contrast, a saturation of the phase shift is observed for significantly smaller concentrations. For (N_A, N_D) = (0.7, 0.8)$\times10^{17}$ cm^{-3}, the saturation of the phase shift can be recognized above 3 V.

The correlation stems predominantly from the overlap between the optical mode and the active region. Since the extent of the depletion region is proportional to $\left(N_A^{-1} + N_D^{-1}\right)$ described by equation (3.4), lower concentrations of the dopants result in the depletion of a significant fraction of the waveguide cross section, even if the pn-junction is unbiased. In this case, the change of the free carrier density mostly takes places relatively far away from the intensity maximum, which significantly limits the effective refractive index change Δn_{eff}. Moreover, a further reduction of Δn_{eff} occurs, if the boundaries of the depletion region move beyond the confinement of the waveguide upon increasing the bias voltage. On the other hand, the overlap can be optimized when the doping concentrations are high, because the extent of the depletion region of the unbiased modulator can be minimized. Hence, the change of the free carrier density takes place in the proximity of the intensity maximum and thus Δn_{eff} is significantly increased. Consequently, the modulation efficiency at small bias voltages is improved and a saturation of Δn_{eff} can be avoided. However, high doping concentrations involve significant free carrier absorption, which reduces the device performance in terms of an increased insertion loss.

Another aspect of the selection of the doping profiles is discussed using the contour diagram in Figure 5.14b), where the color encodes the change of the effective refractive index Δn_{eff} at a bias voltage of 5 V. It is evident that Δn_{eff} varies most distinctly, if the ratio between the involved dopants remains same as with the nominal values (N_A, N_D) = (7, 5)$\times10^{17}$ cm^{-3}. Confirming the result deduced from Figure 5.14a), Δn_{eff} decreases, the more the dopant concentrations are reduced. Furthermore, Δn_{eff} diminishes further, the more the ratio of the concentrations deviates from that of the nominal values. This is due to the different extends of the depletion region towards the n- and the p-zone. A change in the ratio therefore results in an altered alignment of the pn-junction in x-direction. Ultimately, this yields a

reduction of the overlap between the optical mode and the depletion zone, unless compensated by a junction interface offset.

In summary, the modulator performance is dependent on its design as well as several aspects related to the fabrication process accuracy. The comparison of the simulation results with the experimental data indicates, that the device performance is not governed by variances of one of the investigated properties alone. Alignment tolerances during the fabrication process as well as the implantation energy and dose govern the alignment of the pn-junction. As discussed above, the concentrations of the dopants not only affects the modulation efficiency by the available free carriers, but also relates to the lateral junction displacement and the intrinsic region. Hence, for an optimum modulator design, the doping concentrations decide about the optimum alignment of the pn-junction. On the other hand, the desired alignment of the pn-junction governs the required doping concentrations. Moreover, an upper boundary of doping concentrations may be given by considering the loss imposed by the excess charge carriers.

5.4.4 Steady-state modulation efficiency

In this section, the steady-state modulation efficiency of silicon depletion-type phase shifters is analyzed in both simulations and experiments. A strip-loaded waveguide fabricated on an SOI wafer with a silicon layer thickness of 250 nm models the devices. The width of the strip waveguide is 500 nm. Depending on the modulator type, the height of the slab region is either 120 nm or 180 nm. The devices are fabricated according to the process described in section 5.2. The purpose of the simulation is to predict the device properties according to specified sets of parameters, such as different doping concentrations or variations of the geometry. On the other hand, deviations of the fabrication processes can be deduced based on the simulation results. In order to facilitate the device characterization, identical phase shifters are inserted into an asymmetric Mach-Zehnder interferometer. Hence, the steady-state modulation efficiency can be measured according to the procedure described in section 5.3.1.

The nominal concentration of donors N_D is 2.5×10^{17} cm^{-3} while it is $N_A = 3.5\times10^{17}$ cm^{-3} for the acceptors. The concentration in the highly-doped zones providing the ohmic contact to the metal vias and electrodes is $10^{19}\mathrm{cm}^{-3}$ for both species. Simulations of the implantation processes conducted by the foundry *IMS-CHIPS* suggest an intrinsic region between the p- and n-doped regions in the active zone with a width of at least 50 nm[1]. The possible junction offset is estimated to be ±50 nm at most to take tolerances of the mask alignment during the implantation process into account.

For the discussion of the following characteristics, it is anticipated that the nominal doping concentrations in the active zone have not been achieved in the fabrication process. Since test structures for measuring the doped silicon conductivity are not included on the photonic chip, an exact determination is not possible. However, a comparison of the measured modulation efficiency with simulations suggests smaller levels for both species. Based on an optimistic approach, which disregards a severe pn-junction misalignment, the maximum concentrations are estimated to be $N_A = 2.0\times10^{17}$ cm^{-3} and $N_D = 1.5\times10^{17}$ cm^{-3}. Furthermore, measurements of the pn-junction breakdown voltage confirm reduced concentrations. According to this method, the dopant concentrations appear to be even smaller by one order of magnitude. Thus, 1.5×10^{16} cm^{-3} is considered the lower boundary for both N_A and N_D. The drawback of this method is, that no distinction between the species can be made. In contrast, no indication is found that the concentration in the highly-doped zones does not match the design values.

The modulation efficiency is analyzed in detail on the basis of a depletion-type pn-modulator with a length of 3 mm and a slab height of 120 nm. The results of other modulator lengths and geometries are discussed later on. The phase shift as a function of the bias voltage in the range of 0 V to 10 V is presented in Figure 5.15. The open triangular symbols represent the relative phase shift at the respective

[1] The result is part of an internal documentation and therefore not publicly available.

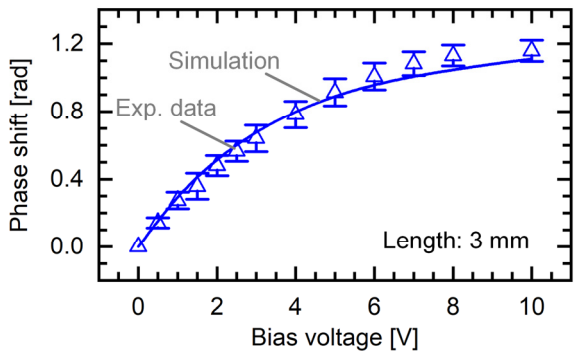

Figure 5.15: Steady-state modulation efficiency of depletion-type pn-modulators with a length of 3 mm. The diagram compares the simulated results (solid line) and experimentally obtained data (open triangular symbols)

bias voltage obtained by the characterization of four samples located in the same region of the wafer. It is normalized to the phase at 0 V. The progression is monotonously rising and asymptotically approaches a maximum close to 1.2 radians corresponding to approximately 0.4π radians. The solid line shows the modulation efficiency predicted by the simulation, which takes into account the reduced doping concentration levels from above. The comparison with the experimental data reveals a very good agreement with the simulation results.

In the bias voltage range of 0 V to 5 V, the phase change is dominated by the increasing extent of the depletion zone close to the energy maximum of the guided mode. With further rising bias voltage, the phase shift per voltage decreases due to the square root dependency of w_{dep} on the bias voltage. Above 5 V, the depletion zone's boundaries overlap with the mode edges away from the propagation axis, where the amount of energy is lower. Therefore, the contribution to the overlap integral likewise becomes smaller which results in a further reduction of the phase shift per voltage. For even higher bias voltages, the phase shift becomes even less effective. Around 10 V the modulation efficiency appears to saturate. This is the operation range, where the depletion region's extent eventually reaches beyond the section where the mode is confined.

According to the previous section, the modulation efficiency and the maximum achievable phase shift is strongly dependent on the profiles and concentration of the dopants. The reason is that the doping governs the extent of the depletion zone and thus the interaction of the refractive index change with the guided mode. This becomes apparent by comparing the steady-state modulation efficiency of the device presented in Figure 5.15 with that of the reference device of section 5.4.2, where the doping concentrations are more than three times higher. It will be shown below, that the geometry of the strip-loaded waveguide has a similar influence on the modulation efficiency.

The analysis of the modulation efficiency is extended to phase shifters with varying lengths from 1 mm to 4 mm in asymmetric Mach-Zehnder configuration. The experimental procedure follows section 5.3.1. The diagram in Figure 5.16a) shows a representative for each modulator length in the bias voltage range of 0 V to 10 V. The solid triangles represent the measured phase shift at the respective bias voltage. The solid line traces the progression of a fit curve according to

$$\Delta\varphi(V) = a\left(1 - \mathrm{e}^{-bV}\right), \tag{5.9}$$

with a and b being real constants. Although the phase shift $\Delta\varphi$ is dependent on $\mathrm{w}_{\mathrm{dep}}$, also the overlap between the optical mode and the depletion region has a strong impact. This is taken into account by the exponential term. In fact, the overlap appears to dominate the modulation efficiency of the modulators at hand, because the saturation at high bias voltages is also accounted for. Against this backdrop, equation (5.9) describes the modulation efficiency more accurately than using a square root dependency according to equation (3.4).

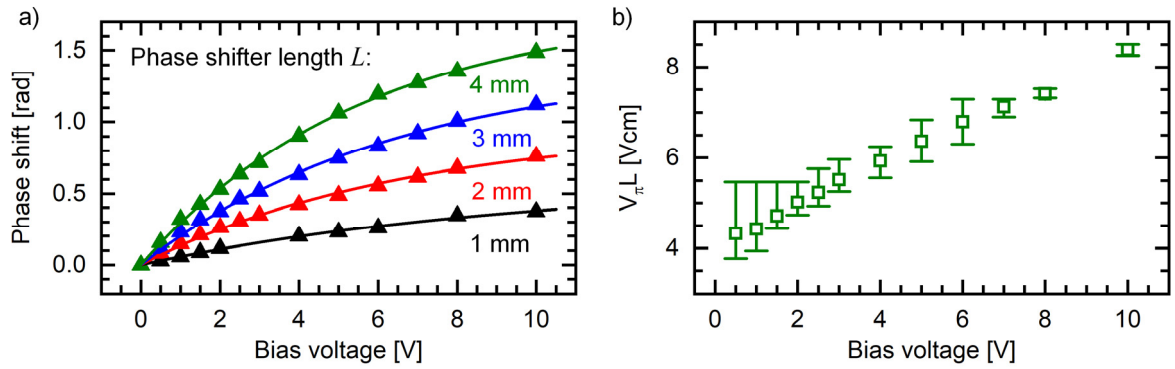

Figure 5.16: Steady-state characterization results of depletion-type pn-modulators of different lengths from 1 mm to 4 mm. a) Representative modulation efficiency of each modulator length in the bias voltage range of 0 V to 10 V. The triangular symbols represent the relative phase shift values obtained by experimental characterization while the solid lines are associated fit curves. b) Voltage-length product $V_\pi L$ obtained by the average over all device lengths from 1 mm to 4 mm.

Similar to Figure 5.15, the phase shift increases monotonously and appears to advance towards a saturation value. This becomes most apparent at the curve of the 4 mm device. Due to the reduced dopant concentrations, a π-shift is not achieved for the given voltage range.

The voltage length product $V_\pi L$ according to equation (5.6) is visualized in Figure 5.16b) as a function of the bias voltage. The symbols represent the average $V_\pi L$ over all device lengths from 1 mm to 4 mm and the solid line connecting the data points is included to guide the eye. The error bars represent the maximum deviation of individual specimens from the average. Because the modulation efficiency of the 1 mm device is represented by less data points than all the other devices, the three missing values are interpolated to be available for the averaging.

According to Figure 5.16b), the voltage length product increases with rising bias voltage. This is expected, because the modulation efficiency generally decreases. In the bias voltage range up to 2 V, a significant deviation of $V_\pi L$ from the average towards higher values is observed. The reason is the small modulation efficiency of the 1 mm devices in this voltage range. For higher bias voltages, the steady-state performances of devices with different lengths converge, which results in smaller error bars. Above 2 V, the progression approaches an almost linear relation, which reflects the tendency towards saturation. Based on the described analysis, a $V_\pi L$ of 4.4 Vcm at a bias voltage of 1 V is determined. This result is exceptionally high compared to state-of-the-art modulators and is explained by the relatively small doping concentrations that constitute the pn-junction.

After the discussion of the steady-state modulation efficiency of depletion-type pn-modulators with a slab height of 120 nm, the study is extended to devices with a 180 nm slab. With that slab height, only MZM with 3 mm phase shifters are available on the test chip. Therefore, a comparison can be made only for this device length. Figure 5.17 visualizes the influence of the slab height and thus the waveguide geometry on the efficiency of the phase modulator. Figure 5.17a) compares the modulation efficiency of depletion-type pn-modulators with a slab height of 120 nm and 180 nm. The values of measured phase shifts are marked by the triangular open symbols. The solid lines show the result of comparative simulations using the model described in section 5.4.2.

The result of the device with the 120 nm slab is taken from the evaluation presented in Figure 5.15. The continuously accumulating phase shift with increasing bias voltage is recognized as well as the saturation tendency. Increasing the slab height to 180 nm distinctly alters the modulation efficiency, although the trend is maintained. This becomes obvious by comparing the characteristics of both devices in Figure 5.17a). In the bias voltage range of 0 V to 8 V, the slope associated to the 180 nm slab modulator is smaller and the phase shift remains below the value obtained for the 120 nm slab device. At 8 V both curves approach each other and eventually intersect, because the phase shift of the 120 nm device saturates while that of the 180 nm sample continues to rise. Upon a further increase of the bias

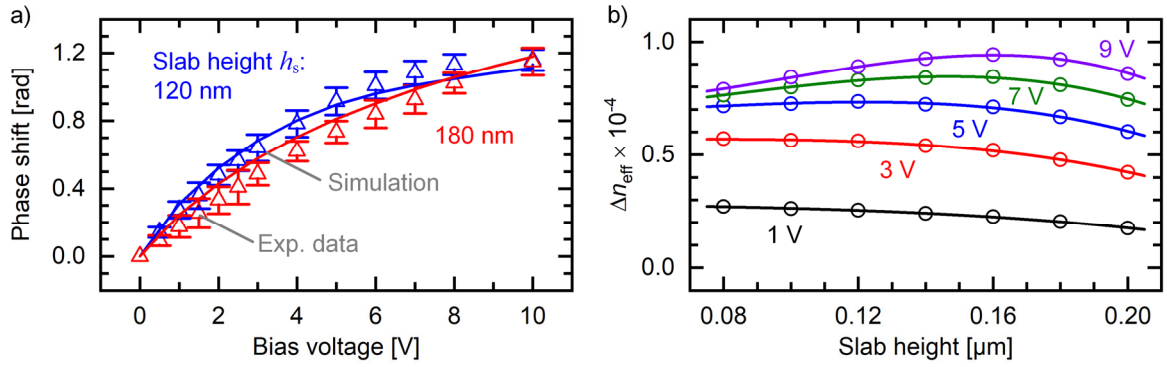

Figure 5.17: Influence of the slab height on the efficiency of a phase modulator. a) Phase shift of a 3 mm long depletion-type pn-modulator as a function of the bias voltage for the slab heights 120 nm and 180 nm obtained by experiments (triangular symbols) as well as by simulations (solid lines). b) Simulated steady-state change of the effective refractive index Δn_{eff} as a function of the slab height at different voltages. The solid lines are fit curves, which trace the simulation results represented by the circles.

voltage, the phase shift of the 180 nm slab device increases while the other one appears to remain at the saturation value. Thus, the maximum accumulated phase shift is higher compared to that of the 120 nm slab device. Although the simulation predicts an intersection of the curves at a lower bias voltage than the experimental data show, the measured values are in good agreement.

In order to analyze the relation between the phase shift and the slab height, Figure 5.17b) is considered. The diagram shows the simulated change of the effective refractive index Δn_{eff} as a function of the slab height for different bias voltages from 1 V to 9 V. The circles represent the simulation results, while the solid lines are polynomial fit curves. Only the curves for odd values of the bias voltage are shown for clarity. All curves show a general tendency of a decreasing Δn_{eff} for increasing the slab height from 80 nm to 200 nm. However, above 5 V, the progression forms a ridge in the proximity of 160 nm slab height, which eventually masks the trend. The reason for this behavior is the relation between the mode confinement due to the waveguide dimensions and the distribution of charge carriers due to the extent of the depletion zone. Thus, the slab height directly relates to the refractive index change.

At a small bias voltage, the extent of the region is small and a strong mode confinement results in a strong overlap. With growing slab height, the confinement of the mode reduces. Therefore, its energy distributes over a larger cross section and the change of the depletion region has less effect. For a bias voltage higher than 5 V, the situation changes to the opposite. Due to the larger extent of the depletion zone, the interaction with a strongly confined mode is no longer pronounced. In fact, the mode confinement weakens if the slab height is increased, but this yields to a stronger overlap with the depletion zone. Consequently, Δn_{eff} increases for higher slabs, until an optimum is reached which expresses itself by the ridge in the progression. Increasing the slab height further again yields a reduction of Δn_{eff}. The energy of the mode is distributed across a larger cross section, which is accompanied by a flattened spatial distribution and reduced peak intensity. Thus, the effect of the interaction with the depletion region is significantly reduced.

Taking the example of the slab heights 80 nm, 120 nm and 180 nm, the impact of the slab height on the phase shifter characteristic is discussed. The strip section has a width of 500 nm and a height of 250 nm. Figure 5.18 illustrates the waveguide geometries and the normalized electric field of the guided mode in the upper row. In the lower row, the associated change of the effective refractive index Δn_{eff} as a function of the bias voltage is shown. In Figure 5.18a) the slab height of 80 nm is assumed. The guided mode is strongly confined and most of the energy is concentrated at the waveguide's central axis. A small change of the bias voltage therefore results in a distinct raise of Δn_{eff}. On the other hand, the Δn_{eff} tends to saturate already in the range of 5 V, because the depletion region's extent exceeds that of the mode. In a waveguide with a slab height of 120 nm as shown in Figure 5.18b), the mode confinement is not as strong as it is with 80 nm. Yet, the slope of Δn_{eff} does not change significantly below 5 V.

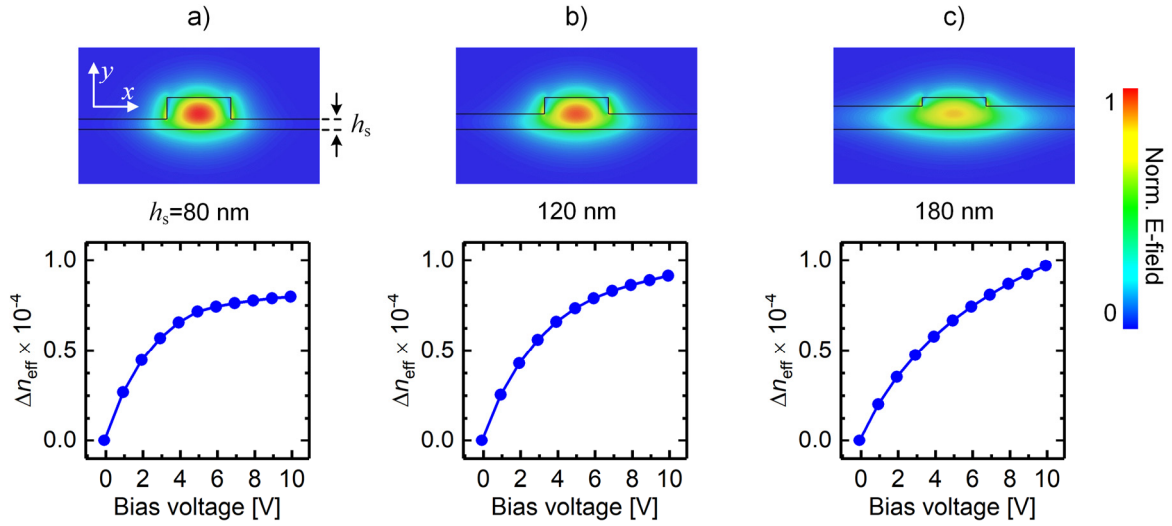

Figure 5.18: Analysis of the effect of the modulator's slab waveguide height h_s on the modulation efficiency for a) h_s=80 nm, b) 120 nm and c) 180 nm. Upper row: mode field distribution in the strip-loaded waveguide. Lower row: associated steady-state change of the effective refractive index Δn_{eff} as a function of the bias voltage.

However, due to the improved overlap of the depletion region and the mode at higher bias voltages, the total accumulated change of the refractive index is higher and the tendency towards saturation is considerably less pronounced. In Figure 5.18c) the situation in a waveguide with a slab height of 180 nm is presented. The mode confinement is even weaker and the distribution's tails protrude deeply into the slab. In contrast, the maximum electric field at the waveguide axis is accordingly smaller. As expected, the raise of Δn_{eff} below 5 V is smallest compared to the previous examples. An optimum overlap of the depletion region and the guided mode is reached only at a considerably higher voltage compared to the situation with stronger mode confinements. Therefore, the maximum change of the effective refractive index at 10 V is highest, and a saturation is not observed within the given voltage range.

These findings verify the results presented in Figure 5.17a). By again comparing the phase shift of the devices with the slab heights of 120 nm and 180 nm, a change of the characteristics as discussed above is recognized. For lower bias voltages, the change of the effective refractive index is stronger for the device with 120 nm slab. On the other hand, a saturation of the phase shift at a high bias voltage is not observed for the device with the 180 nm slab. Thus, a higher accumulated phase shift is achieved. The dominating source of uncertainty in the experimental analysis is the lack of the exact knowledge of the etch depth for which the means are not available in this study.

5.4.5 Small-signal characteristics

The electro-optic small-signal response of MZM in push-pull operation is characterized using a vector network analyzer (VNA) according to the experimental setup presented in Figure 5.4. Similar to the steady-state characterization, the phase shifter lengths of 1 mm to 4 mm are considered in the study. The phase shifters of the MZM are equally reverse-biased. In contrast to a single-ended operation, the spectrum does not shift upon changing the bias voltage. Thus, a fixed operating point can be selected, where the frequency responses at all bias voltages can be characterized. The operating point is derived from the steady-state transmission spectrum similar to Figure 5.2a) on page 45. In order to achieve maximum modulation depth, the wavelength is selected as such the transmission is attenuated by 3 dB with respect to the maximum. The amplitude of the electrical driving signal is 0.32 V, corresponding to an average electrical power of 0 dBm at 50 Ω load resistance. The optical power at the modulator input is adjusted for each specimen to maintain an optical input power at the photodetector of -0.5 dBm. According to the data sheet, the detector sensitivity at 1550 nm is 0.36 A/W.

Typical frequency responses of the modulators with a slab height of 120 nm are presented in Figure 5.19a). The diagram shows the normalized EOE responses of asymmetric MZM with depletion-type pn-

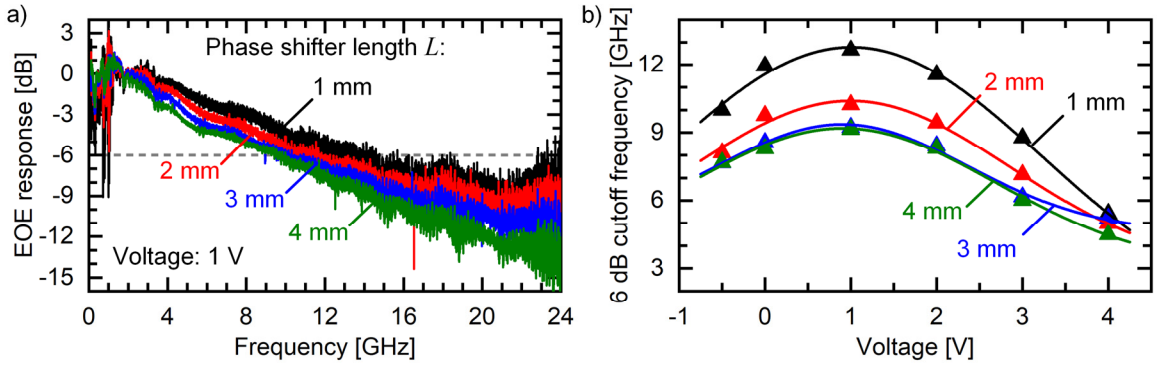

Figure 5.19: Small-signal characterization results of depletion-type pn-modulators in MZM configuration with a length from 1 mm to 4 mm. a) Measured EOE responses at 1 V bias voltage, b) 6 dB cutoff frequency as a function of the bias voltage for each modulator length.

modulators. The lengths of the phase shifters are 1 mm to 4 mm and they are equally reverse-biased at a voltage of 1 V. In the range between DC and 2 GHz, the characteristics of all modulators rise by approximately 3 dB. Furthermore, the responses of the 1 mm (black) and 2 mm (red) devices exhibit overshoots in the range around 1 GHz. Above 2 GHz the responses drop monotonously with frequency, which resembles a linear progression with respect to the logarithmic scale. The horizontal grey dashed line indicates the -6 dB cutoff level. The frequency, at which the response traverses this level, is defined as the 6 dB cutoff frequency of the EOE response.

In Figure 5.19b), the 6 dB cutoff frequencies as a function of the bias voltage for the modulator lengths 1 mm to 4 mm obtained from the measurement data is presented. Beginning with 0.5 V in forward direction, each of the curves increases with rising bias voltage and reaches its maximum at approximately 1.0 V in reverse direction. Evidently, a further increase of the voltage magnitude results in diminishing the cutoff frequency again. Above 4 V, the cutoff can no longer be determined, because the EOE responses of all modulators decrease very sharply even at low frequencies. Another property of the results is the similarity of the cutoff frequency progressions. Except for the absolute value, which is dependent on the modulator length, the dependencies on the bias voltage are the same within the measurement accuracy. All curves resemble a Gaussian distribution. This is indicated by the fit functions represented by the solid lines in the diagram.

The EOE response at 1 V represents the typical behavior of the modulators at a favorable operating point. The ascending tendency of the response between DC and 2 GHz is attributed to the photodetector transfer characteristic. The origin of the overshoots is electromagnetic interference due to an imperfect shielding of photodetector RF-output. Both symptoms are observed regardless of the considered specimen or operating point throughout the entire study and are therefore considered a systematic error. The electrical 6 dB cutoff frequency, which is identical to the frequency at the optical 3 dB cutoff, is comparatively low. Even the 1 mm device achieves only 12.6 GHz at a bias voltage of 1 V. This performance limitation can be explained by the doping profile constituting the pn-junction. As elaborated in the steady-state analysis in the previous section, the doping concentrations achieved in the fabrication process are lower than intended. The consequence is a reduced conductivity of the neutral regions in the strip waveguide as well as in the slab. Thus, the time constant represented by the product of the resistances and the capacity in equation (3.5) becomes larger, which diminishes the cutoff frequency.

In order to analyze the relation between the dynamic behavior of the modulators and the bias voltage, the electro-optic response is compared to the electrical scattering parameters of the devices, which are determined experimentally using the setup presented in Figure 5.5. Selected results are summarized in Figure 5.20. In Figure 5.20a), the magnitude of the S_{21} parameters of the Mach-Zehnder modulators with a phase shifter length from 1 mm to 4 mm is shown. The bias voltage is 1 V. Since the results are not normalized, the actual cutoff is extracted at the frequency, where the response drops to -3 dB with

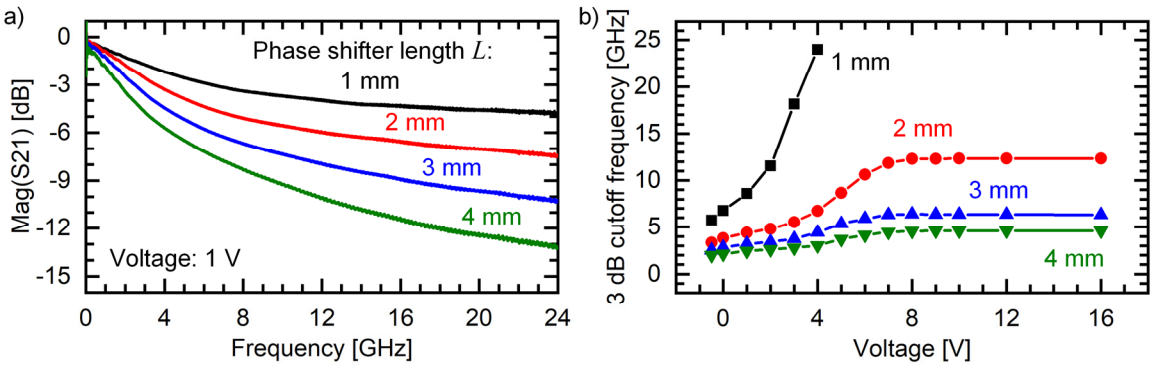

Figure 5.20: Result of the scattering parameter characterization of depletion-type pn-modulators in MZM configuration with a length from 1 mm to 4 mm. a) Magnitude of the S_{21} parameters as a function of the RF frequency at a bias voltage of 1 V in reverse direction. b) 3 dB cutoff frequency of each modulator as a function of the bias voltage. The curve of the 1 mm device is interrupted at 4 V due to limitation of measurement range.

respect to the low-frequency level. All curves in the diagram resemble a low-pass characteristic, of which the slope gradually decreases for increasing frequency. On the other hand, the curves generally become steeper with the modulator length, which results in a reduction of the cutoff frequency.

The cutoff frequency of the MZM as a function of the bias voltage for the phase shifter lengths of 1 mm to 4 mm is shown in the diagram in Figure 5.20b). The solid symbols represent the cutoff frequency extracted from the S_{21} parameters. The lines are included to guide the eye. In the range between 0.5 V in forward direction and 3 V in reverse direction, the cutoff frequency increases approximately proportional to the square root of the bias voltage. This resembles the change of the depletion region width, which is governing the capacity of the pn-junction. With further rising voltage, a stronger increase of the cutoff frequency is observed, which turns into saturation above 8 V. Despite the length, each modulator shows the same behavior. Although the curve for the 1 mm device is interrupted at 4 V due to the limitation of the measurement range, the S_{21} parameters likewise saturate with increasing bias voltage. By means of extrapolating the measured spectra linearly with respect to the logarithmic magnitude, the cutoff frequency at saturation is estimated to be 45 GHz.

The measured S_{21} parameter represents the residual amplitude of the RF signal after the propagation along the transmission line of the modulator electrodes. A fraction of the energy is reflected at the input port of the modulator electrodes, while another is expended for the modulation of the carrier distribution. Furthermore, energy dissipation due to parasitic elements must also be considered. Typically, the cutoff frequency of a depletion-type pn-modulator would increase proportional to the square root of the bias voltage. The reason is the dependency of the depletion region's width on the bias voltage as described by equation (3.4), which in turn dominates the pn-junction capacity.

The modulators at hand, however, exhibit this relation only for small bias voltages. The strong increase of the cutoff frequency above 3 V indicates that the interaction between the electrical wave and the pn-junction becomes increasingly obstructed. This hypothesis may be confirmed by a comparison with the EOE response. The significant reduction of the 6 dB cutoff frequency with the bias voltage can be attributed to the frustrated interaction between the electrical wave and the pn-junction. Simultaneously, the steady-state modulation efficiency is not affected (see Figure 5.16). Therefore, a possible explanation is the existence of a frequency-dependent series resistance, which is approximated by a series inductivity. It can either be assigned to the neutral zones of the pn-junction, the transmission line or the vias. However, on the basis of the experimental data, it is not possible to determine its dependency on the bias voltage. A further increase of that impedance results in a progressive isolation of the pn-junction from the feeds. The effect can no longer be traced in the EOE response, because the RF signal extracted from the photodetector practically vanishes above a bias voltage of 4 V.

In contrast, the response of the S_{21} parameters seem to confirm the tendency. Once the series impedance is sufficiently high to achieve a total isolation of the pn-junction, the residual effective

capacity of the transmission line becomes independent of the voltage. This can be observed for bias voltages larger than 8 V. From there, the 3 dB cutoff frequency remains constant upon a further voltage increase. This result suggests that the capacity is governed by the transmission line, which consists of the metal electrodes on top of the SiO_2 cladding and the vias.

In an attempt to confirm this assumption, the scattering parameters of the metal electrodes are experimentally determined. The photonic chip contains test structures of just the modulator electrodes associated to corresponding device lengths of 1 mm to 4 mm. The S_{21} parameters for each electrode length as a function of the frequency is shown in the diagram in Figure 5.21a). The results reflect the transmission line losses of the coplanar waveguide. Figure 5.21b) summarizes the dependence of the 3 dB cutoff frequency on the electrode length. The solid triangular symbols represent the results obtained by the analysis of S_{21}. Due to the limited measurement range, the cutoff frequency of the 1 mm electrode cannot be determined. Therefore, a comparative simulation using CST *Microwave Studio* is conducted. The results are included in the diagram by the open triangular symbols. Where experimentally obtained values are available, they show excellent agreement with the simulations. Thus, the result for the 1 mm electrode is considered reliable. A fit curve indicating a dependency proportional to an exponential decay is also shown in the diagram. In the range, where both experimental and simulation results concur, it is represented by the solid line. Beyond that range, the line is dashed in order to emphasize its predictive nature.

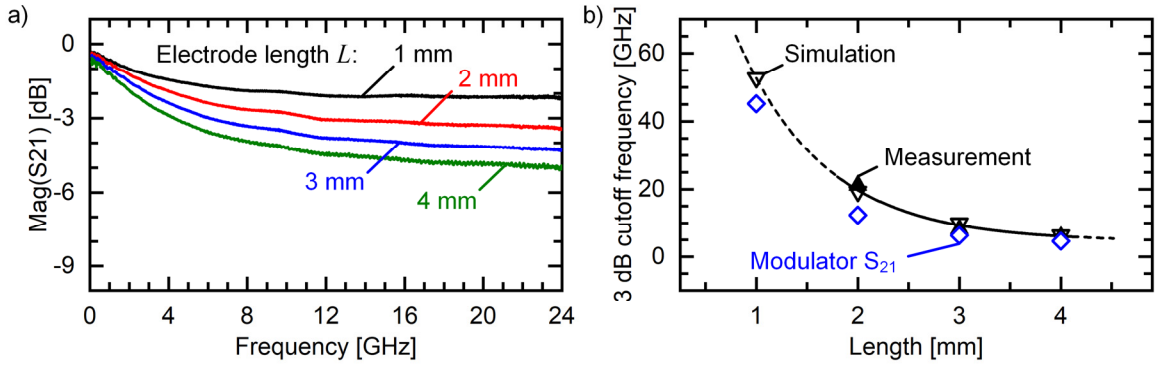

Figure 5.21: Scattering parameters of the electrodes without the modulators. a) Magnitude of the S_{21} parameter. b) 3 dB cutoff frequency as a function of the electrode length. Solid symbols represent experimental values, while the black open symbols reflect the simulation results. The line traces a fit curve. Beyond the range of the measured results, it is dashed in order to emphasize its predictive nature. The blue open symbols are the 3 dB cutoff frequency at maximum bias voltage extracted from the modulator scattering parameters presented in Figure 5.20b).

To facilitate a comparison between the modulators and the electrodes alone, the 3 dB cutoff frequency of each modulator length at maximum bias voltage is included. The results are extracted from the data presented in Figure 5.20b) at 16 V. The values are smaller than those representing just the electrodes, but likewise resemble an exponential decay.

Assuming even a strong isolation of the pn-junction from the feeds, the transmission line of the modulators does not only include the electrodes, but also the vias extending down to the silicon slab. In contrast, the reference electrodes only consist of the deposited metal layer on top of the SiO_2 cladding. This difference affects the transmission line characteristic and can explain the deviation of the results in Figure 5.21b). Still, it appears to be confirmed that the electrical properties of the pn-phase shifter at high bias voltages are dominated by the metal elements. Furthermore, since the dynamic modulation becomes less effective for increasing bias voltages, the increasing isolation of the pn-phase shifter from the feeds proofs to be a reasonable explanation.

The electro-optic small-signal response of MZM in push-pull operation with pn-phase shifters exhibiting a slab height of 180 nm is also characterized. The MZM are symmetrically biased and the measurements are again conducted using a vector network analyzer (VNA) according to Figure 5.4. Since MZM with phase shifters of that slab height are only available with a length of 3 mm on the test

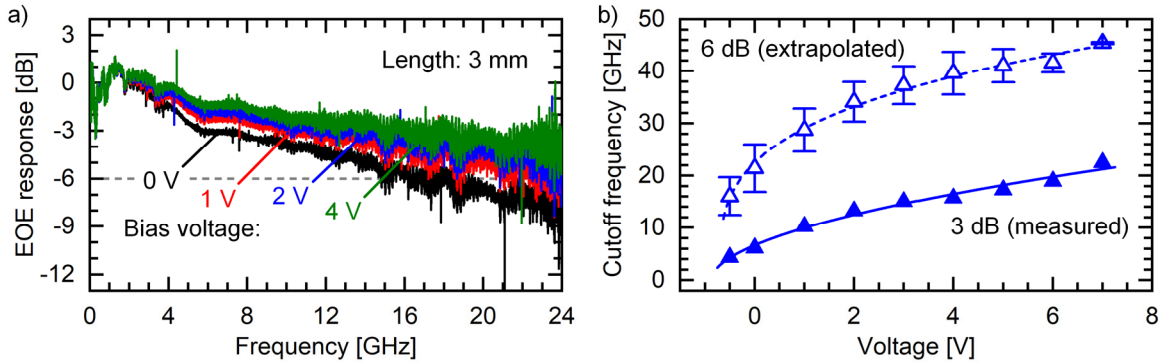

Figure 5.22: Small-signal characterization results of a depletion-type pn-modulator in MZM configuration with a length of 3 mm and a slab height of 180 nm. a) Measured EOE responses at 0 V, 1 V, 2 V and 4 V bias voltage, b) measured 3 dB cutoff frequency and extrapolated 6 dB cutoff frequency as a function of the bias voltage.

chip, the study is limited to this length. The normalized EOE frequency responses for bias voltages from 0 V to 4 V are presented in Figure 5.22a). Similar to previous measurements, the 3 dB notch between DC and 2 GHz caused by the photodetector is recognized. Above 2 GHz, a low-pass characteristic is observed for all bias voltages. Above 6 GHz, it turns into a linear progression with respect to the logarithmic scale. The slopes of the responses decrease for increasing bias voltage. The -6 dB cutoff level is indicated by the horizontal grey dashed line. The cutoff frequency is given by the frequency, at which the EOE response falls below this level.

It is evident from the diagram, that the 6 dB cutoff frequency cannot be determined for all bias voltages, because the measurement range is limited to a maximum of 24 GHz. Therefore, an extrapolation is required for the evaluation: at first, the EOE response is extrapolated linearly with respect to the logarithmic frequency scale. Secondly, the 3 dB cutoff frequency is determined from both the original response and the extrapolation. The discrepancy between the results is used to estimate the error of the extrapolation. Finally, the 6 dB cutoff frequency is calculated from the extrapolation function. The results using this method are summarized in Figure 5.22b). The solid triangular symbols represent the 3 dB cutoff frequency extracted from the measured EOE response as a function of the bias voltage. The open triangular symbols show the 6 dB cutoff frequency based on the extrapolation. The error bars reflect the estimated discrepancy between the results. The solid line as well as the dashed line represent fit curves, which are proportional to the square root of the bias voltage.

Despite the notch below 2 GHz, the EOE responses represent a behavior typical for a depletion-type pn-modulator. Each of the curves traces a linear progression, which reflects a first-order low pass characteristic dominated by the feed resistance and the depletion region capacitance. The latter reduces with increasing bias voltage due to the growing extent of the depletion region. Thus, the slope of the response reduces and the cutoff frequency is enhanced. The relation can be recognized in the diagram in Figure 5.22b): according to equation (3.7), the pn-junction capacitance C_{dep} is inversely proportional to the depletion region width w_{dep}. Using equation (3.5), the relation between the cutoff frequency and w_{dep} is linear. Moreover, as w_{dep} increases with the square root of the bias voltage as expressed in equation (3.4), the cutoff frequency eventually grows at the same rate.

As shown above, the small-signal modulation efficiency of the standard etch depth modulators significantly diminishes with increasing bias voltage. Against this backdrop, the issue is addressed once more by measuring the electrical scattering parameters of the modulators with a slab height of 180 nm. The magnitude of the S_{21} parameter as a function of the frequency is presented in Figure 5.23a) for the bias voltages from 0 V to 4 V. Each curve resembles the characteristic of a multi-stage low-pass, of which the 3 dB cutoff frequency rises with increasing bias voltage. This relation is emphasized by the diagram in Figure 5.23b), where the 3 dB cutoff frequency is shown as a function of the bias voltage in

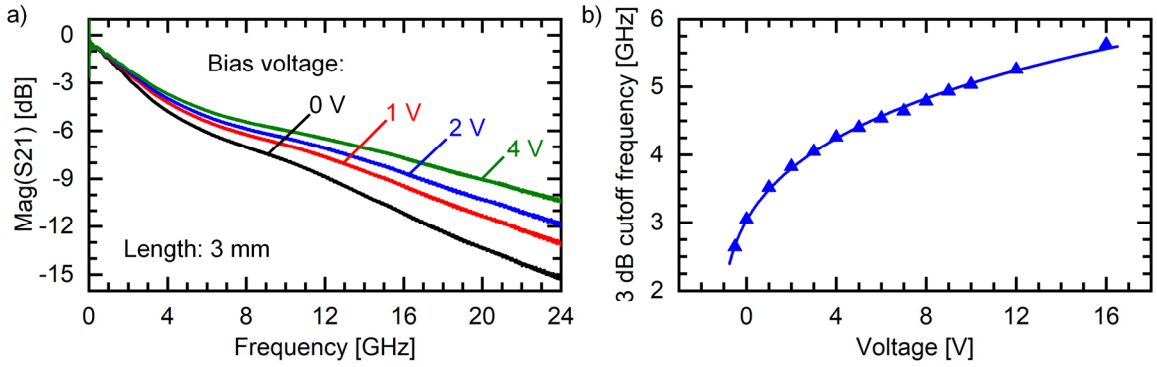

Figure 5.23: Scattering parameter characterization of a Mach-Zehnder modulator. The phase shifters have a length of 3 mm and the slab height is 180 nm. a) Magnitude of the S_{21} parameters as a function of the RF frequency for the bias voltages 0 V to 4 V. b) The 3 dB cutoff frequency of S_{21} as a function of the bias voltage.

the range from 0 V to 16 V. The symbols mark the values extracted from the S_{21} measurement. The solid line is a fit curve growing with the square root of the bias voltage.

Apparently, the variation of the S_{21} parameters with increasing bias voltage implies that the dynamic behavior of the pn-junction is dominated by the depletion region capacity. Similar to the EOE response, the relation manifests in the dependency of the 3 dB cutoff frequency on square root of the bias voltage. The significantly lower values of the cutoff frequency originate from a strong attenuation of the RF wave upon propagation along the transmission line, because the major part of its energy is expended in the electro-optic conversion.

Unlike the modulator type with 180 nm slab height, the device with the standard slab height appears to be subject to severe parasitic effects, which become more effective with increasing bias voltage. They cannot be attributed to the sole difference between the slab heights, although this property has an influence on both the steady-state and the dynamic characteristics. Instead, the reason for the wide variance most likely originates from the fabrication process. Two fabrication steps are identified, which are at least indirectly affected by the modulator slab height. The vias are defined by etching windows into the SiO_2 cladding and the slots are filled by metal deposition across the entire wafer. The formation of the metal electrodes is subsequently achieved by optical lithography and etching of the metal. The associated process parameters are etching duration and the metal deposition rate and duration. If the etching process is optimized for a slab height of 180 nm, the contact windows for the 120 nm slabs might not be homogeneously etched down to the slab surface. Consequently, the desired contact cross section is not achieved, which results in an increased contact resistance and a non-negligible inductance.

Based on these considerations, an imperfect transition between the metal vias and the highly-doped slab regions of the strip-loaded waveguide is considered to be the source of impairment of the dynamic modulator characteristics. A simplified equivalent circuit as presented in Figure 5.24 consisting of the transmission line and the depletion-type pn-phase shifter can be assembled. Figure 5.24a) shows the cross-section of the modulator, which also includes the SiO_2 cladding, the vias and the metal electrodes. The schematic indicates the relevant contributions to the total device impedance. The depletion region of the pn-junction is modeled by the series capacitance C_{dep}. The resistances $R_{\mathrm{s,p}}$ and $R_{\mathrm{s,n}}$ represent the series resistances of the p- and the n-regions, respectively. The parallel circuit of C_{el} and C_{via} models the capacitances of the electrodes and the metal vias. Finally, $L_{\mathrm{via,p}}$ and $L_{\mathrm{via,n}}$ represent the inductances of the vias connecting the electrodes and the slab. The resistance of the electrodes and the vias are not considered.

In Figure 5.24b), the equivalent circuit is shown. For clarity, components that are assigned to the p- or the n-region are combined to a single component. Furthermore, the termination resistance is also included. It can be deduced from the circuit, that the inductivity L_{via} acts as barrier for non-DC signals,

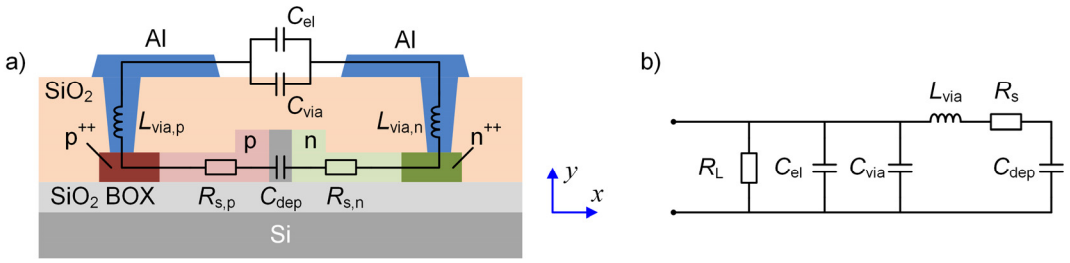

Figure 5.24: Assembly of an equivalent circuit of a depletion-type pn-modulator and the associated transmission line. a) Cross-section of the modulator, which indicates the relevant contributions to the total impedance. b) Equivalent circuit of the modulator and the transmission line.

which eventually isolates the pn-junction modelled by R_s and C_{dep} from the electrodes. In this particular case, the characteristics are then governed by the electrodes and vias.

5.4.6 Data transmission experiment

After the analysis of the fundamental device properties in the previous sections, the qualities of digital signals encoded by MZM with the different types of depletion-type phase shifters are assessed. The experimental setup is presented and described in Figure 5.8 on page 50. The driving signal from the FPGA board is an 11.3 Gbit/s NRZ-OOK PRBS with a length of $2^7 - 1$. According to the small-signal characterizations, the phase shifters with a slab height of 120 nm achieve the highest cutoff frequency at a bias voltage of approximately 1 V. To maintain an optimum operating point of the driver amplifiers, the minimum peak-to-peak voltage to drive the modulator is 2.9 V. Hence, the bias voltage for the phase shifters is set to 1.5 V in order to prevent a forward biasing of the pn-junction. Although this is not the optimum operating point, the diminution of the cutoff frequency is negligible. The phase shifters are equally biased and the MZM is driven in push-pull operation. For all measurements, a preemphasis is applied to the driving signal. The sensitivity of the SFP+ receiver at 11.3 Gbit/s is specified for a PRBS with a length of $2^{31} - 1$ by -15 dBm. The actual receiver input power is adjusted to 0 dBm by tuning the EDFA pump current.

Additional to recording eye patterns of the received signal, the associated BER is measured. Using the presented experimental setup, burst errors occur randomly, which are most likely triggered by electromagnetic interference. The measurements are interrupted and started over after the occurrence of error bursts until at least 10^{12} bits are evaluated. Consequently, the measurement duration does not reach the required time for statistical certainty [169], but provides for a qualified BER estimation. Eventually, a number of evaluated bits between 3.2×10^{12} and 1.1×10^{13} is reached.

In Figure 5.25a) to d), the eye patterns along with the measured BER are presented for asymmetric MZM incorporating phase shifters with a slab height of 120 nm and a length from 1 mm to 4 mm. Evidently, the eyes are clearly open for each device. Except for the 4 mm device, the BER is in the range of 10^{-12} or below. The eye pattern of the 1 mm device in Figure 5.25a) shows an increased amount of noise compared to the other results. The reason is the comparatively small modulation efficiency, which yields a reduced modulation depth. For the devices with a length of 2 mm and 3 mm, of which the eye patterns are shown in Figure 5.25b) and c), the highest signal quality is observed. In contrast, a slightly increased jitter of the eye pattern transitions and a higher BER is recognized in the received signal from the 4 mm device presented in Figure 5.25d). Possibly, the increased rise and fall times of the signal are indications of a larger capacity due to the modulator length. Yet, the performance is comparable to those of the other specimens.

For comparison, the quality of the received signal from an MZM with phase shifters exhibiting a length of 3 mm and slab height of 180 nm is evaluated. In contrast to the devices with the 120 nm slab, this device is not subject to the restrictions on the operating point. Hence, the bias voltage on both phase shifters is 2.5 V in reverse direction in order to increase the margin to a pn-junction forward biasing. The eye pattern and the measured BER of the received signal are presented in Figure 5.26. The eye is

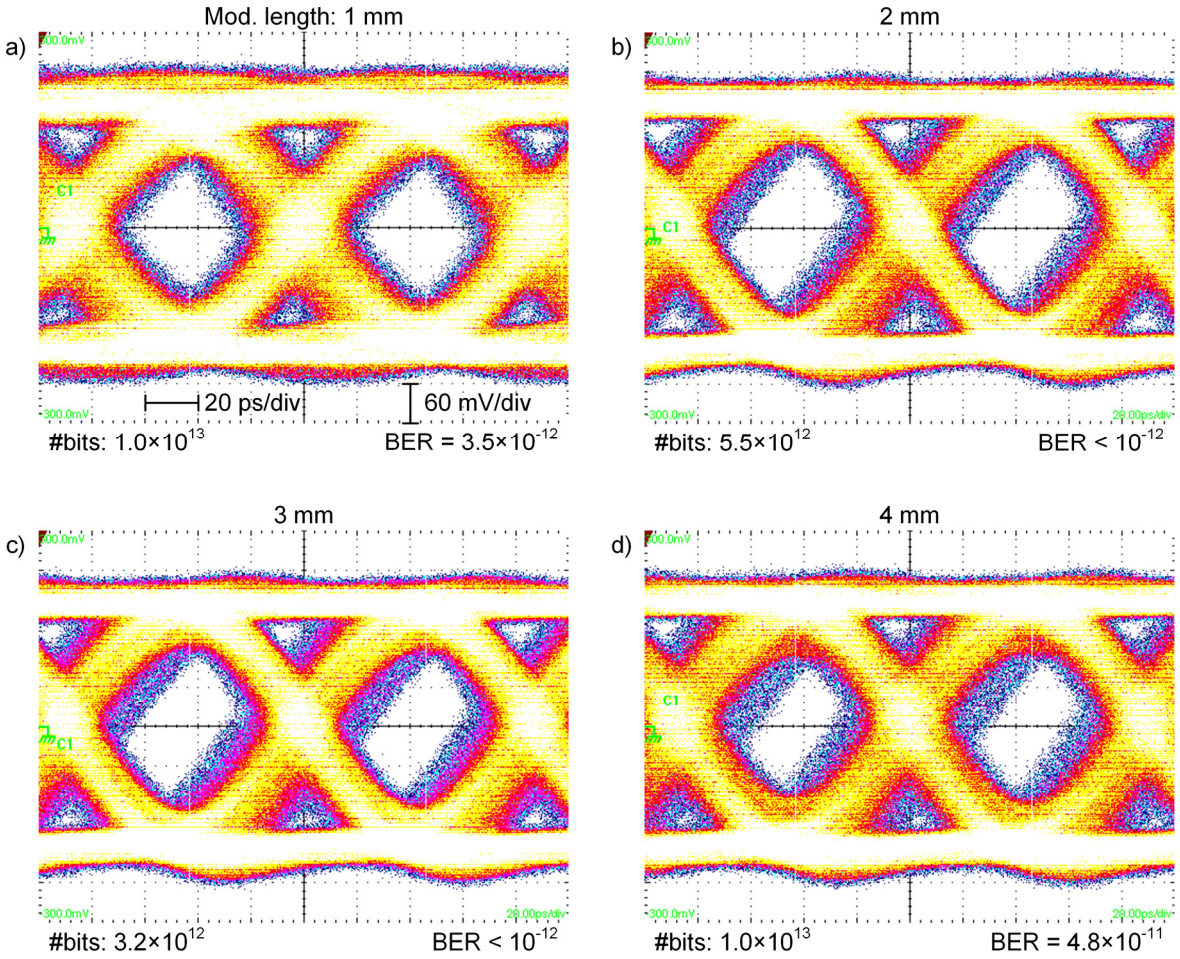

Figure 5.25: Eye patterns and measured BER of MZM in push-pull operation with depletion-type pn-phase shifters with a length of 1…4 mm (a) to d)) and a slab height of 120 nm operating at 11.3 Gbit/s NRZ-OOK.

clearly open and the BER is smaller than 10^{-12}. While almost twice the number of bits are evaluated, the eye opening appears to be slightly wider compared to the 120 nm device. The reason is the significantly higher cutoff frequency associated to this operating point. On the other hand, the curvature of the steady-state modulation efficiency diminishes with increasing bias voltage. Thus, the improvement is limited, because the higher bias voltage yields a reduced modulation depth.

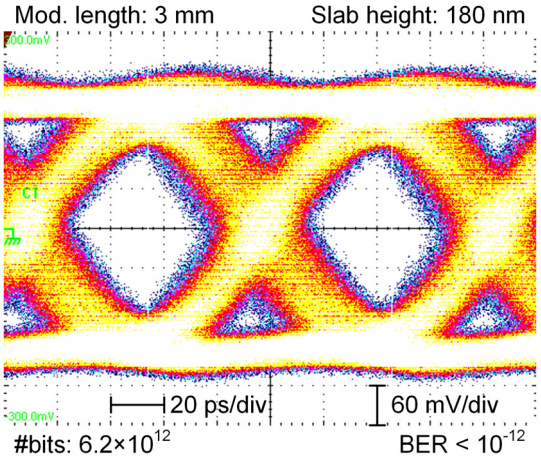

Figure 5.26: Eye pattern and measured BER of an 11.3 Gbit/s NRZ-OOK signal encoded by an MZM with 3 mm depletion-type pn-phase shifters with a length of 3 mm and a slab height of 180 nm in push-pull operation.

5.4.7 Outlook: Additional dopant implantation

As already discussed in section 5.4.4, difficulties in the fabrication process of the photonic chip resulted in dopant concentrations which are smaller than the targeted nominal values. Consequently, the depletion-type pn-modulators exhibit a relatively small modulation efficiency. Shortly before the completion of this thesis, IMS-CHIPS was able to deliver a new batch of chips, which have been exposed to a second dopant implantation. Although a detailed characterization of the devices is clearly beyond the scope, an analysis of the steady-state modulation efficiency according to section 5.3.1 is performed. Similar to the analysis of the first batch, the devices under test are asymmetric MZM with phase shifters with a slab height of 120 nm and a length of 1 mm to 4 mm. One device of each length is considered for this characterization. The result is summarized in Figure 5.27.

The diagram in Figure 5.27a) shows the relative phase shift as a function of the bias voltage in reverse direction for each phase shifter length. Solid triangles represent the measured relative phase shift at the respective bias voltage while the progression of the fit curves according to equation (5.9) is included by the solid lines. Each of the curves increases monotonously and exhibits a tendency toward saturation. This characteristic has already been observed in the results of the modulators that have been exposed to a single dopant implantation only. The performance improvement becomes apparent in the absolute values of the modulation efficiencies. A comparison of the diagram in Figure 5.27a) with that presented in Figure 5.16a) reveals, that the modulation efficiency of every modulator length is increased by 33% in average.

The diagram in Figure 5.27b) shows the calculated voltage-length product as a function of the bias voltage averaged over all device lengths from 1 mm to 4 mm. The open blue rhombs represent the results of the modulators that stem from the process including the second implantation procedure. For comparison, the results of the modulators from the first batch are included by the green squares. Evidently, $V_\pi L$ is significantly reduced as a consequence of the additional dopant implantation. An average reduction of approximately 25% for all phase shifter lengths is found. At 1 V, $V_\pi L$ is found to be 3.4 Vcm. Based on the comparison of the experimental results with existing simulation data, the doping concentrations after the additional implantation are estimated to be increased by approximately 50% to 60% of the initial values.

5.4.8 Thermal studies

As mentioned previously in chapter 4, the front-end electronics of a detector system requires operating reliably over a wide temperature range, which even might exceed Telcordia standards. In order to obtain an understanding of the response on environmental conditions, this section is dedicated to the experimental characterization of one of the essential components for a photonic transmitter: the Mach-

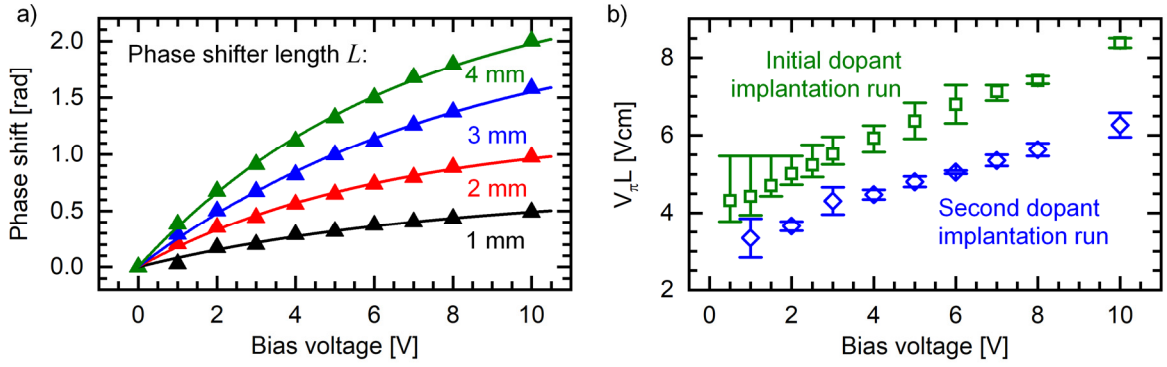

Figure 5.27: Steady-state characterization results of depletion-type pn-modulators of different lengths from 1 mm to 4 mm after a second dopant implantation. a) Modulation efficiency of each modulator length in the bias voltage range of 0 V to 10 V. The triangular symbols represent the relative phase shift values obtained by experimental characterization while the solid lines are associated fit curves. b) Voltage-length product $V_\pi L$ averaged over all device lengths. The open blue rhombs represent the results of the modulators after the second implantation. The green squares are the values associated to the first batch and are included for comparison.

Zehnder modulators (MZM). The analysis of the grating-based (de-)multiplexers is discussed in section 5.6. To get the full picture, the stability of the fiber-to-chip coupling arrangement for the optical transmitter is investigated separately in chapter 6.

The experimental setup for the thermal studies is similar to that described in section 5.3.1 except for a specially designed sampler holder with water-cooled, stacked Peltier elements. A sketch of the setup and photographs of the sample holder are shown in Figure 5.28. In principle, the sample holder is an isolated trough with a copper base plate. The Peltier elements are mounted to the bottom side. The device under test (DUT) is fixed on the base plate by a clamp in order to establish thermal contact. Active components are contacted to a source measure unit (SMU) with appropriate electrical probes. Optionally, an RF-signal can be applied using a bias-tee. To prevent short circuits due to condensing humidity upon cooling, the sample holder can be flooded with a dielectric fluid (*3M Novec* 7500).

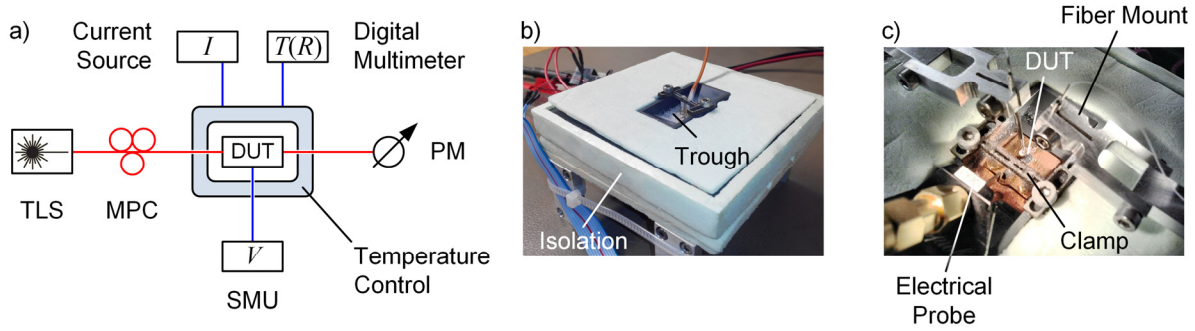

Figure 5.28: Experimental setup for the temperature characterization of photonic components. a) Setup sketch, b) photograph of the sample holder, c) close-up photograph of the trough for the dielectric fluid.

Cleaved standard single-mode fibers are used to optically probe the DUT. The polarization is adjusted to match the grating couplers of the photonic chip by using a manual polarization controller (MPC). The temperature is monitored by measuring the resistance of a Pt100 sensor set into the base plate with a digital multimeter. The steady-state modulation efficiency is analyzed by measuring the MZM transmission spectra at different bias voltages using a tunable laser source (TLS) and a power meter (PM).

The DUT is an asymmetric Mach-Zehnder modulator with 3 mm long depletion-type phase shifters. The device is part of a photonic chip fabricated in a multi-project wafer process run and based on a commercially available design provided by the *OpSIS* project [160]. The physical length difference of the two arms is 30 µm. In this study, the non-elongated MZI arm is provided with a bias voltage between 0 V up to 16 V. The ambient temperature varies between -28 °C and 57 °C.

Figure 5.29 presents excerpts of the normalized fit curves of one modulator's measured transmission spectra. The diagram in Figure 5.29a) shows the spectra for different bias voltages at a chip temperature of 40 °C. Noticeably, applying a bias voltage results is a blue shift. In Figure 5.29b), the transmission spectra at a bias voltage of 0 V for changing temperature is shown. A red-shift is recognized for increasing temperature.

The experimental results reveal two effects. The application of a bias voltage increases the effective refractive index in the waveguide and thereby retards the propagating mode. Since the non-elongated arm of the MZI contains the active phase shifter, the delay between the co-propagating modes in the two arms at a fixed wavelength decreases. On the other hand, the effective refractive index increases with raising temperature due to the thermo-optic effect. In contrast to applying a voltage to one arm, the temperature-induced change affects the entire device. In good approximation, the refractive index change in the phase-shifting elements is identical and their contribution on the relative phase of the two arms cancels out. The remaining variable is the difference of the optical path lengths due to the

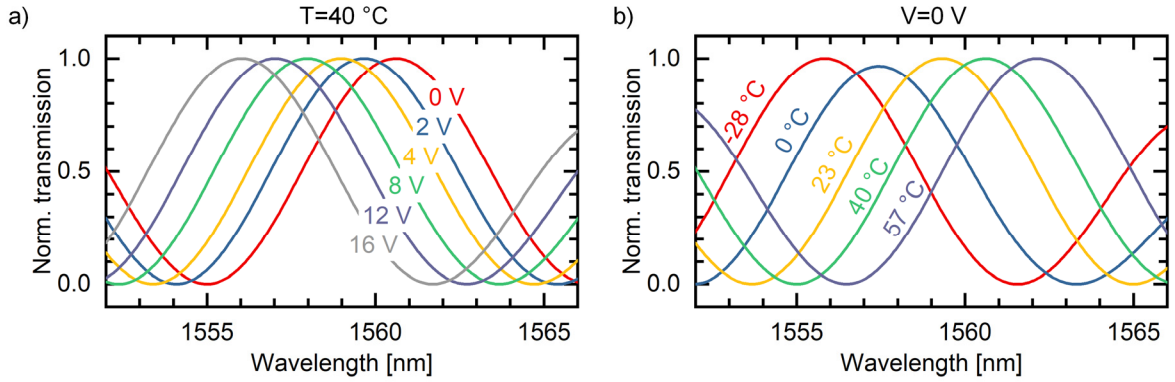

Figure 5.29: Fit curves of the measured spectra of a Mach-Zehnder modulator based on depletion-type phase shifters of 3 mm length. a) Excerpt of the normalized transmission spectra of the modulator for different bias voltages from 0 V to 16 V at 40 °C. b) Excerpt of the normalized transmission spectra of the same modulator at a bias voltage of 0 V for different temperatures from -28 °C to 57 °C.

asymmetric MZI geometry. In fact, a thermally induced refractive index change yields a stronger enhancement of the optical path length of the elongated waveguide. Hence, the delay between the two arms at a fixed wavelength increases.

According to equation (5.5), the steady-state modulation efficiency is calculated. To maintain consistency, a positive phase shift corresponds to a blue-shift in Figure 5.29. The relative phase shift as a function of the bias voltage for different temperatures between -28 °C to 57 °C is presented in Figure 5.30a). The symbols represent the calculated phase obtained from the measured transmission spectra and the solid lines are corresponding fit curves proportional to the square root of the bias voltage. All values are normalized to the phase at 23 °C and 0 V. The temperature variation yields a phase shift of less than 0.05 K^{-1} while the modulation characteristic and efficiency remains unchanged. Hence, an adjustment of the modulator bias voltage can easily compensate for the temperature-induced shift of the operating point without affecting the signal quality. A similar results has been published in [135].

Furthermore, the dynamic behavior of the modulator at changing temperature is characterized using the experimental setup described in section 5.3. Figure 5.30b) shows the normalized measured electrical-optical-electrical (EOE) response of the modulator in the temperature range between -13 °C to 57 °C at a bias voltage of 0 V. The equivalent power of the electrical signal driving the modulator is 10 dBm and the average optical input power on the photodetector is -6 dBm. The diagram is a representative of all considered operating points. For reasons of clarity and comprehensibility, the curves are smoothed by averaging over 50 data points corresponding to a frequency interval of 50 MHz. Similar to the small-signal characterization studies presented in 5.4.5, the wavelength is selected according to the steady-

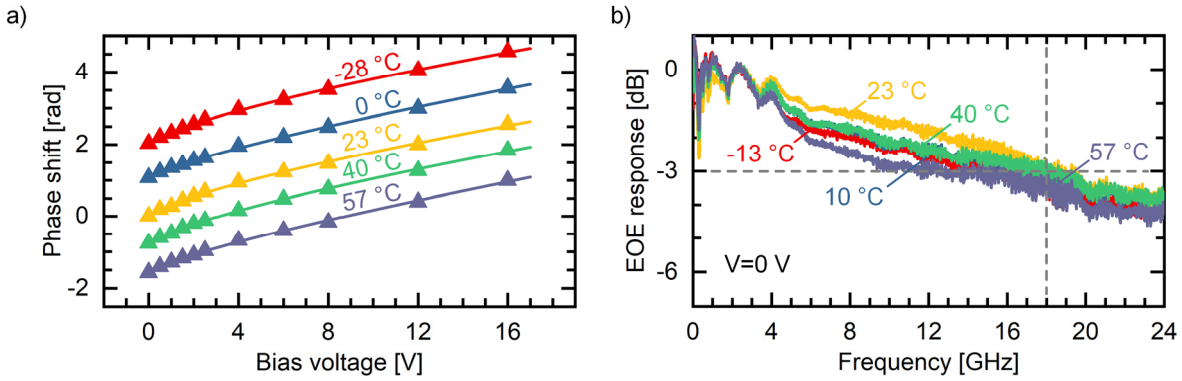

Figure 5.30: Thermal characterization of a depletion-type pn-modulator of 3 mm length. a) Relative phase shift as a function of the bias voltage at different temperatures. The values are normalized to the phase at 0 V and 23 °C. b) Normalized EOE response of the modulator at different temperatures at a bias voltage of 0 V.

state transmission spectrum at the respective temperature as such the transmission is 3 dB lower than the maximum.

The notches in the range between DC and approximately 4 GHz stem from the photodetector transfer characteristic. Above 4 GHz, the spectra resemble a low-pass characteristic. The 6 dB cutoff frequency cannot be derived from the diagram due to the limitations of the measurement range. However, a 3 dB bandwidth of 18 GHz is recognized. A change of the temperature neither affects the frequency response nor the cutoff frequency significantly.

5.4.9 Summary

In this section, the concept and the design as well as simulations and experiments on the steady-state and dynamic characteristics of depletion-type pn-modulators nested in Mach-Zehnder interferometers are presented. The development of a simulation model and the determination of its parameters is discussed. The most important properties affecting the modulation efficiency are the width of an intrinsic region separating the n- and the p-doped region, the alignment accuracy of the pn-junction and the doping concentration.

The steady-state modulation efficiencies are experimentally determined for phase shifter lengths of 1 mm to 4 mm. The target doping concentrations have not been achieved in the fabrication process. Consequently, the devices show a reduced modulation efficiency and a full π-shift is not realized. Still, the simulations show very good agreement with the experimental results, if a reduced doping concentration is assumed. The voltage length-product $V_\pi L$ of this modulator type at a bias voltage of 1 V is found to be 4.4 Vcm.

The influence of the slab height of the phase shifter on the modulation efficiency is investigated by simulations and experiments. The slab height is an important property to adjust in order to improve the modulator's radiation hardness. A small slab height yields a strong change of the effective refractive index Δn_{eff} at low bias voltages, at the cost of a reduced maximum Δn_{eff}. In contrast, a high slab results in a reduced Δn_{eff} with increasing bias voltage, but allows for an improved maximum effective refractive index shift.

For all available lengths of phase shifters with a slab height of 120 nm, the small-signal characteristics of the modulators are investigated experimentally. The 6 dB cutoff frequency of the 1 mm device is 12.7 GHz at a bias voltage of 1 V, while it is 9.3 GHz at a length of 3 mm. It is notable that the cutoff frequency decreases for increasing bias voltages higher than 1 V. Moreover, the study reveals a considerable deviation of the properties between the devices with a slab height of 120 nm and 180 nm. The 6 dB bandwidth of the 3 mm modulator with 180 nm slab height is 28.7 GHz at the same bias voltage. Additionally, the cutoff frequency increases continuously with rising bias voltage. Although the slab height has an influence on both the steady-state and the dynamic characteristics, it cannot explain the wide variance. The imperfect formation of metal vias for the 120 nm slab due to tolerances in the fabrication process is identified to be the most plausible reason.

An error-free transmission of an 11.3 Gbit/s NRZ-OOK is demonstrated for asymmetric MZM incorporating phase shifters with different lengths and a slab heights. Despite the generally low modulation efficiency and the uncommon dynamic characteristics of the phase shifters with the 120 nm slab, the BER of the received signal even from the 1 mm device is in the range of 10^{-12}. The best signal quality is obtained for the devices with a slab height of 180 nm.

The thermal studies of depletion-type pn-modulators reveal a temperature dependency of the steady-state modulation efficiency. Due to the finite FSR of the asymmetric MZM, a temperature change yields a steady-state phase shift and thus a change of the operating point. According to the EOE frequency response, the dynamic characteristics remain unchanged.

5.5 Thermo-optic modulators

In this section, the modulation efficiency of thermo-optic phase shifters in MZM configuration is investigated. The purpose of the devices is the application as supplementary phase shifters in one or both arms of an MZM for the operating point adjustment. Two device variants are realized and experimentally characterized.

5.5.1 Schematic and geometries

In Figure 5.31 two concepts of a thermal modulator are sketched. Both are based on a strip-loaded waveguide with a strip width of 0.5 µm and a length of 100 µm. Instead of the additional deposition of metal in order to form resistances, the heaters are realized by selectively doping the structures. Thus, the devices can be fabricated with the available processing steps as discussed in section 5.2. A p-type doping is selected, due to the lower absorption compared to an n-type dopant. Since the bandwidth of thermal modulators is generally limited below the Megahertz-range, lumped electrodes can be used.

According to the fabrication process specifications, the nominal concentration of the light acceptor concentration N_A is 3.5×10^{17} cm^{-3}. However, according to the reasoning in section 5.4.4, the effective concentrations achieved in the process are considerably lower and are estimated to be 2.0×10^{17} cm^{-3} at most. The schematic of a conventional design is depicted in Figure 5.31a). Since the current flows

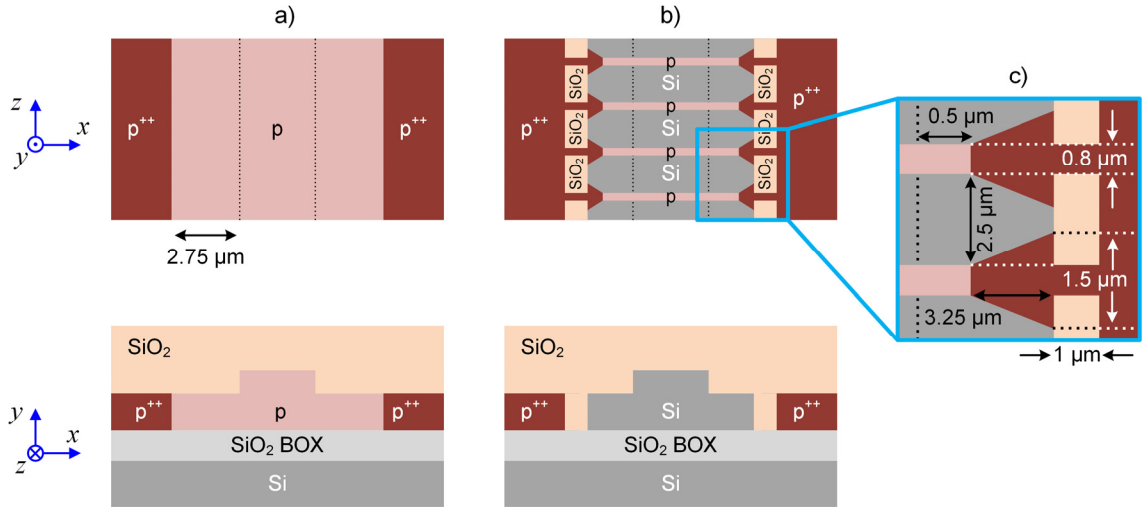

Figure 5.31: Top views and cross-sections of two different thermo-optic modulator designs. a) Conventional design referred to as "bulk heater". b) Advanced design [170] with localized heaters. c) Detailed view of the localized heater structure with the relevant dimensions. The sketches are not to scale.

laterally across the entire length of the waveguide, it is referred to as "bulk heater". The p-doped heater overlaps with the strip waveguide region. The regions located at the edges of the slab are highly p-doped to provide an ohmic contact to the metal vias and electrodes. The slab width is 20 µm and the distance between the p^{++} region and the strip is 2.75 µm. The geometry provides for homogenous current flow across the strip waveguide while avoiding high absorption due to free charge carriers is the p-doped silicon.

The device design presented in Figure 5.31b) is inspired by the geometry proposed in [170]. Similar to the conventional design, it also relies on current flow transversal to the propagation direction of the optical mode. However, unlike using the entire length waveguide as a resistor, localized transverse heaters are aligned periodically along the waveguide by p-doping selected regions to obtain conductive channels. The remainder of the strip waveguide and its proximity remains undoped silicon. The heaters have a width in z-direction of 0.8 µm and the spacing between consecutive elements is 2.5 µm. Furthermore, silicon dioxide barriers are introduced at the transition from the p^{++} to the p region. Their dimensions are 1 µm × 2.5 µm. Due to the significantly smaller thermal conductivity of silicon dioxide (3.2×10^{-3} W/(cm K)) compared to silicon (1.5 W/(cm K)) [171], they prevent heat dissipation from the

p-doped channels to the slab. Between the barriers, tapered segments protrude from the highly-doped regions to establish the electrical contact to the heaters. At the resulting junctions, the distance between the p^{++} region and the strip is 0.5 µm.

Despite the small dimensions of the localized heaters, the total resistances due to the lightly p-doped silicon are designed to be approximately the same for both device geometries at room temperature. However, an improved modulation efficiency due to the heat barriers compared to the bulk heater is expected. Furthermore, the insertion loss can be reduced, because the greater proportion of the waveguide remains undoped.

5.5.2 Experimental characterization

The thermo-optic phase shifters are embedded in asymmetric Mach-Zehnder interferometers. Thus, the steady-state characterization can be performed by measuring transmission spectra according to the procedure described in section 5.3.1. The small-signal characteristics are measured using a setup similar to Figure 5.4a). The RF source is the low-frequency signal generator of a *Rohde&Schwarz* SMB100A microwave signal generator. It covers the frequency range from 1 Hz to 1 MHz. This is adequate for the characterization of thermal modulators and does not require a termination of the circuit. The RF analyzer unit is a *Rohde&Schwarz* FSW43 signal and spectrum analyzer. The essential steady-state and dynamic characteristics of both modulator types are summarized in Figure 5.32.

In Figure 5.32a) a comparison of the steady-state modulation efficiencies between both modulator types is presented. The diagram shows the relative phase shift of the optical wave as a function of the electrical power expended for heating. The open symbols mark the measured values, while the solid straight lines represent fit curves reflecting the linear dependency of the effective refractive index change Δn_{eff}. The power value P_π is defined as the electrical power, which is required to achieve a π-shift and is calculated from the fit curves. The π shift is highlighted by the horizontal dashed line. Employing the bulk heater yields a P_π of (33.8±1.3) mW. In contrast, P_π is determined to be (20.3±0.8) mW for the device utilizing the localized heaters.

The small-signal characterization results of both modulator types is presented in Figure 5.32b). The diagram shows the EOE response as a function of the modulation frequency. To facilitate the distinction between the plots, a logarithmic frequency axis is used. The smallest frequency, at which a response can be determined is 20 kHz due to the bias-tee's frequency response. The progressions appear to decrease monotonously according to an exponential decay. The 6 dB cutoff frequency of the bulk heater device is 59 kHz. For the modulator with the localized heaters, it is found to be 82 kHz.

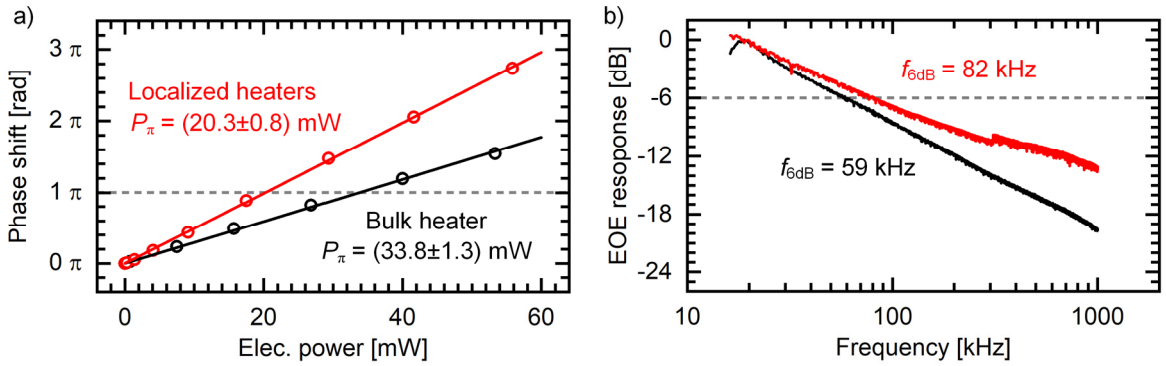

Figure 5.32: Electro-optic characterization results of thermal modulators with a length of 100 µm according to the two different design approaches. a) Steady-state modulation efficiency as a function of the electrical power for the heating. b) Small-signal EOE response as a function of the modulation frequency.

From Figure 5.32a) it is apparent, that both modulator designs achieve a phase shift well beyond π within the electrical power range of 0 mW to 60 mW. However, the modulator with the localized heaters yields an improved modulation efficiency compared to the device utilizing the bulk heater. Partially, the

improvement can be attributed to the reduced heat dissipation to the slab as a result of the oxide barriers. On the other hand, it is a consequence of the different geometries and volumes of the resistive regions. The dynamic characteristics are primarily governed by the duration of the resistor temperature change. Typically, the cooling takes longer than the warming and thus the modulation bandwidth is dominated by the cooling time constant [172]. The difference between the cutoff frequencies of both modulator variants is attributed to the different total heater volumes. The significantly lower volume of the localized heaters yields a reduced time constant and thus a larger bandwidth. This increase, however, is still limited: it has already been shown, that the improved modulation efficiency due to thermal insulation of the heaters from the substrate comes at the expense of longer heating and cooling durations [173].

In order to analyze the difference, the electrical properties of both devices are compared in Figure 5.33. The diagram in Figure 5.33a) shows the total resistance as a function of the injection current. It is calculated using the measured voltage drop across the heaters. The symbols represent the calculated resistances, which are connected by solid lines. The resistances increase with rising injection current. Up to 0.4 mA, the rate is similar for both devices. Above 0.5 mA the resistance of the bulk heater increases with a bigger rate before it appears to saturate at 13 kΩ towards 2 mA. In contrast, the resistance of the device with localized heaters increases at an unchanged rate and saturates approximately at 1 mA.

Basically, the reason for the resistance increase is the heating of the solid due to the injection current. The resistance of a semiconductor is governed by the charge carrier mobility. An applied electric field accelerates the carriers and results in a drift in the direction of the field. The motion is disturbed by scattering processes due to collisions with lattice vibrations (phonon scattering) and ionized donors or acceptors (impurity scattering). Therefore, the mobility is dependent on both the doping concentrations and the temperature. Generally, impurity scattering is relevant in highly-doped semiconductors at low temperatures. Phonon scattering becomes the dominating effect for increasing temperature, because the carrier velocity increases and the lattice vibrations intensify [174].

In case of the bulk heater, the current flows homogeneously across the full length of the modulator and causes the heating. The resulting increase of the material resistivity affects the entire volume and the absolute change of the resistance manifests in the progression shown in Figure 5.33a). Apart from the waveguide cross section, where the optical mode interacts with the local change of the effective refractive index Δn_{eff}, parts of the lightly doped area extends to the slab. Thus, a fraction of the heating power dissipates in that region and therefore cannot contribute to the modulation effect. However, the expended electrical power does contribute to the power budget and therefore diminishes the modulator's efficiency.

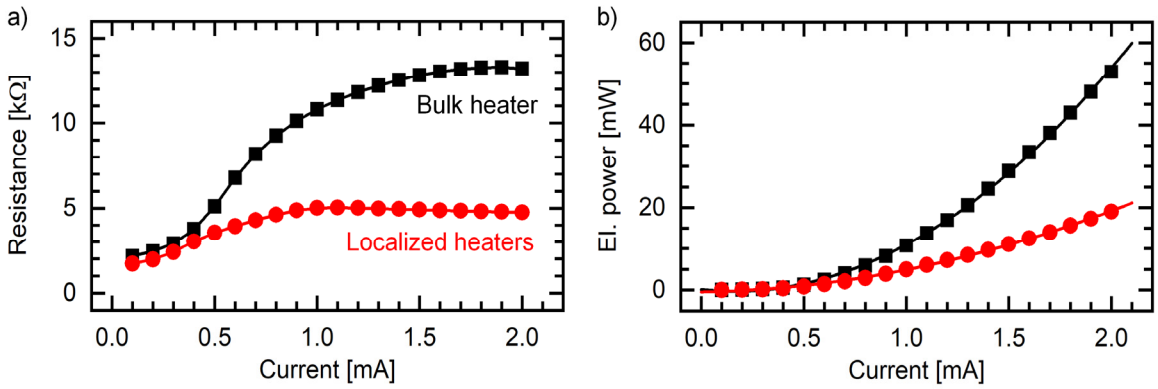

Figure 5.33: Comparison of electrical characteristics between both modulator types. a) Steady-state resistance of the heaters and b) resulting electrical power as a function of the injected current.

In contrast, the total volume of the localized heaters is considerably smaller compared to the bulk and the resistance of the modulator is given by the parallel circuit of all heater elements. Hence, the accumulated resistance due to the increasing resistivity of the material with temperature is smaller. At

the same time, the conductive channels sustain a significantly higher current density, which locally results in a strongly increased temperature. Moreover, due to the thermal barriers even the heat released outside the waveguide boundaries can contribute to the modulation effect. In essence, using localized heaters achieves an improved modulation efficiency while significantly reducing the modulator resistance.

The implication is illustrated in Figure 5.33b), where the resulting electrical power is shown as function of the injection current for both modulator variants. The values obtained by the product of the injection current and the voltage drop are included by the symbols. Due to the higher resistance of the bulk heater, the dissipated electrical power increases stronger with rising injection current. Despite the non-linear relation between the resistance and the current, the progression of the electrical power describes a parabola. This is indicated by the fit curve included in the diagram by the solid lines.

5.5.3 Summary

In this section, two variants of thermal modulators based on strip-loaded waveguides are presented. The devices can be fabricated in a standard SOI process and do not require metallic heaters. Instead, the resistances are realized by lightly doping the silicon. The first proposed design relies on the homogeneous doping of the strip and its proximity, while the second uses localized heating channels. The required electrical power to achieve a π-shift are 33.8 mW and 20.3 mW, respectively and the modulation bandwidths are found to be 59 kHz. and 82 kHz. Although the designs may not be fully optimized, both devices exhibit a satisfactory performance.

Beyond the geometry and extent of the active region, several differences in the device geometry affect the resistance of the modulator device. Therefore, the improved efficiency of the localized heaters should not be compared directly to that of the bulk heater. However, it is shown, that a very efficient modulator can be built based on localized heaters. An optimized bulk heater might achieve a comparable efficiency. Similar restrictions apply for the comparison of the modulation bandwidths, not least because the impact of the thermal insulation of the heater from the substrate is not considered separately. However, since the envisioned application for the devices is the operating point adjustment, the absolute bandwidth of the thermal modulators is of minor importance.

5.6 Grating-based (de-)multiplexers

The (de-)multiplexers are implemented as planar concave grating (PCG) spectrographs, which are based on the Rowland mounting introduced in section 2.1.6. Figure 5.34 shows a sketch of the device layout including typical device dimensions. The grating is composed of a fully-etched Bragg reflector array with a grating period of 320 nm. The width of the individual Brag reflector gratings varies between 2 µm and 10 µm. In this section, the spectrograph is regarded as a demultiplexer, where the common port is used as the input. An optical field incident from the common waveguide port propagates in z-direction along the free propagation region (FPR), which is a silicon slab waveguide of finite width. The wave fronts diverge in x-direction before they hit the curved grating where they are reflected. According to the wavelength, the image of the optical field is focused on one of the output ports. The areas beyond the boundaries of the FPR are heavily n-doped. This enables the absorption of unwanted scattered light in order to reduce crosstalk between the (de-)multiplexer channels.

5.6.1 Device generation and selected parameters

A set of algorithms [12] implemented in MATLAB generates the layouts of PCG devices according to given parameters: The refractive indices n_i $(i = 1, 2, 3)$ of the wafer substrate, silicon layer and cladding yield the effective refractive index n_{eff} of the slab waveguide. The highest and lowest transmission window's peak wavelengths λ_{max} and λ_{min} and the number of channels N define the channel spacing

$$\Delta\lambda = \frac{\lambda_{\mathrm{max}} - \lambda_{\mathrm{min}}}{N - 1}. \tag{5.10}$$

To maintain compatibility to commercially available telecommunication equipment, the (de-)multiplexer channels should match the specifications for DWDM systems according to ITU-T G.694.1 [175]. If applicable, the generation routines are capable of adjusting given input values to the grid. The geometry of the grating is derived from the radius r of the Rowland circle and the grating

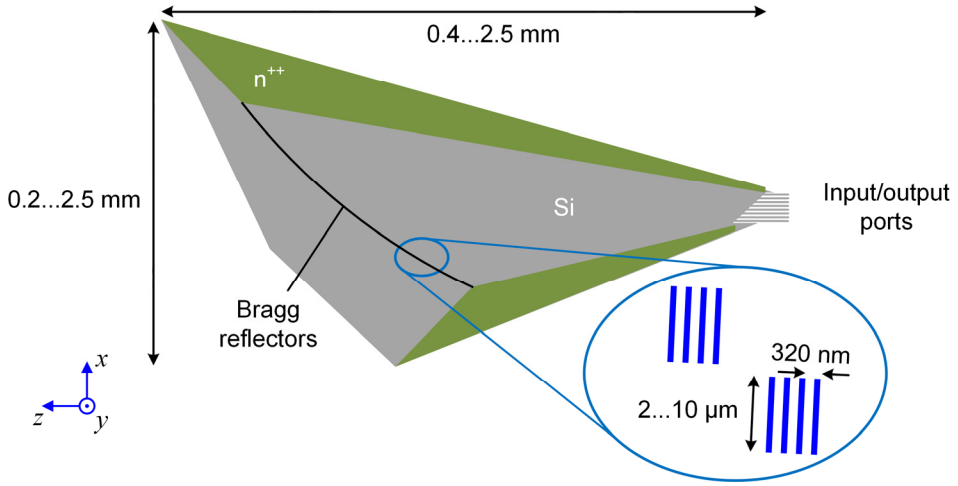

Figure 5.34: Schematic of a PCG (de-)multiplexer and typical dimensions. The inset shows a close-up of the Bragg reflectors which in case of a Rowland mounting are aligned along a circle. Typical device dimensions are a length of 0.4…2.5 mm and width of 0.2…2.5 mm.

length l. The angles θ_{i} and θ_{o}, which determine the position of the input and output waveguides on the Rowland circle and the diffraction order m of the grating also have to be provided.

5.6.2 Simulation

The PCG devices are simulated using COMSOL Multiphysics after importing the layout via MATLAB LiveLink. The finite-elements method is used for the numerical calculations in the frequency domain. The analysis of two different PCG (de-)multiplexers is presented as representation of an entire study on the variation of device generation parameters. The designs are distinguished by a consecutive numbering. Table 2 lists the parameters that define the two specimens. Alongside λ_{max}, λ_{max}, and N, the angles of the input and output waveguide alignment θ_{i} and θ_{o} are specified as well as the radius of the Rowland circle r, the reflector length l and the diffraction order m.

Table 2: List of parameters which define the PCG (de-)multiplexers discussed in this section. These devices are selected representatives of an entire study on the variation of device generation parameters.

ID	λ_{max}	λ_{min}	N	θ_{i}	θ_{o}	r	l	m
GM-04	1592.10 nm	1514.87 nm	13	46.0°	41.5°	320 µm	250 µm	9
GM-01	1555.75 nm	1536.61 nm	7	47.0°	45.0°	600 µm	540 µm	9

GM-04 is a 13-channel (de-)multiplexer with a footprint of 0.26 mm^2. The design center wavelength is 1552.52 nm and the channel spacing is 6.4 nm. That implies that several channels are spectrally located beyond the boundaries of the C-band and might therefore not be available for a comparative

measurement. This, however, has been designed deliberately, because it introduces a certain margin in case that the channels are spectrally shifted due to variances of the effective refractive index. Those may result from potential variations of the silicon layer thickness due to fabrication tolerances. Figure 5.35 summarizes the simulation results.

In Figure 5.35a) the transmission spectra of the device are presented. The channels 1 to 12 are located distinctly within the spectral boundaries of the simulation. Channel 13, however, is not covered entirely by the range, which is why the descending part of the simulated curve can only suggest the location and shape of the associated transmission window. Each spectrum is approximated by a Gaussian-shaped fit curve, which is not shown in the diagram for clarity.

The maximum crosstalk of adjacent channels is -26 dB. Every channel of the device exhibits an insertion loss in the range of 10 dB, which is considerably higher than one might expect and what comparative measurements show. The most plausible reason is the limitation of the simulated area in favor of reduced computation time. Because one boundary is located directly at the slab waveguide's edge and heads from the input waveguide to the reflector array, a fraction of the input power is absorbed there and lost for the spectrograph. Hence, this has no physical meaning in the real device. Furthermore, the loss is uniform across all simulations, which qualifies as a systematic error. Hence, a comparison between the results of different PCG geometries is still possible.

Figure 5.35b) shows the wavelength of peak transmission for each channel as a function of the channel number and Figure 5.35c) shows the bandwidth of each channel expressed by its full width at half maximum (FWHM). The values for peak wavelength and FWHM are obtained by parameter extraction from the fit curves and are included in Figure 5.35b) and c) by symbols. Since the results obtained for channels of which the transmission windows exceed the simulation range, they can only be considered qualified estimates. Therefore, the respective data points are marked by open symbols. The solid straight line in Figure 5.35b) represents the linear relation between the peak transmission wavelength and the channel number. Its slope equals the channel spacing $\Delta\lambda$ and is determined to be (6.4±0.14) nm. The average FWHM of (2.6±0.2) nm is marked in Figure 5.35c) by the dashed line.

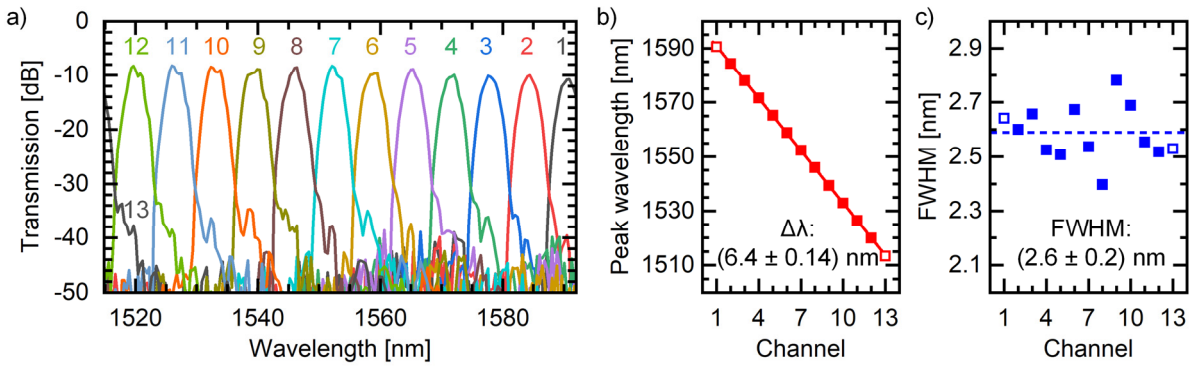

Figure 5.35: Simulation result of the 13-channel PCG (de-)multiplexer GM-04. a) Transmission spectrum, b) wavelength of peak transmission and c) FWHM bandwidth of the individual channels.

GM-01 is the layout of the device, which is actually included in the four-channel transmitter described in section 4.4.2 as WDM (de-)multiplexer. In contrast to GM-04, distinct requirements on the filter characteristics as well as spatial constraints apply. For one, the channel bandwidth should be in the range of 1 nm to meet DWDM specifications and to obviate crosstalk between adjacent channels. On the other hand, the transmitter only supports four WDM channels, so the requirements on the channel spacing can be relaxed. Thus, a 7-channel (de-)multiplexer design is chosen, of which only every second channel is used. That implies that a dark "guard-channel" separates adjacent channels, which is additionally beneficial on the device crosstalk. The targeted channel spacing is 3.2 nm.

To accommodate the aforementioned properties in a PCG design, a reduced channel spacing and an enhanced grating resolution compared to GM-04 is required. A larger Rowland radius achieves the former while the latter stems either from reducing the grating period or by increasing the diffraction order. On the other hand, the diffraction order and the length of the grating governs the resulting width of the device. In the particular case of GM-01, especially the width is restricted to the available distance between the outermost edges of two adjacent modulators (see Figure 4.7 on page 39). Eventually, GM-01 has a Rowland radius and grating length, which are considerably larger compared to those of a compact structure such as GM-04. The resulting footprint is 0.75 mm^2.

The larger footprint imposes a severe limitation to the device simulation, because the memory capacity requirements and the computation time increase significantly. Therefore, the numerical calculation of discrete transmission spectra becomes impractical. A way to circumvent this restriction is to conduct the simulation for a given device only for the center wavelength λ_0 and the minimum and maximum wavelengths λ_{max} and λ_{min}. This allows for a test if a reflected optical field at a wavelength associated to a specific output channel is concentrated to the respective output waveguide aperture.

Figure 5.36 shows the pseudo-color images of the optical field distribution in GM-01 calculated for the wavelengths λ_{max}, λ_0 and λ_{min}. The respective wavelength, frequency and the ITU channel are indicated. The pictures only show the region in the proximity of the common port (COM) and the output ports and therefore omits most of the FPR for clarity. The reflected fields are concentrated correctly on the designed output ports. Only in the case of output channel 1, a slight deviation of the focal point from the port center position is recognized and the wave fronts hit the boundary of the slab. The reflections disperse in the slab waveguide and are lost for the output port. A possible explanation for the deviation is the inaccurate positioning of the output waveguides. It is calculated by a linear dispersion equation [12] based on the effective refractive index n_{eff} of a slab waveguide and therefore might yield an uncertainty on the waveguide positions on the Rowland circle. In contrast to GM-04, where the spectral location of the transmission windows are predicted correctly by theory, the larger dimensions of GM-01 might cause a more pronounced impact. However, the simulation result indicates a very good agreement with the predefined characteristics.

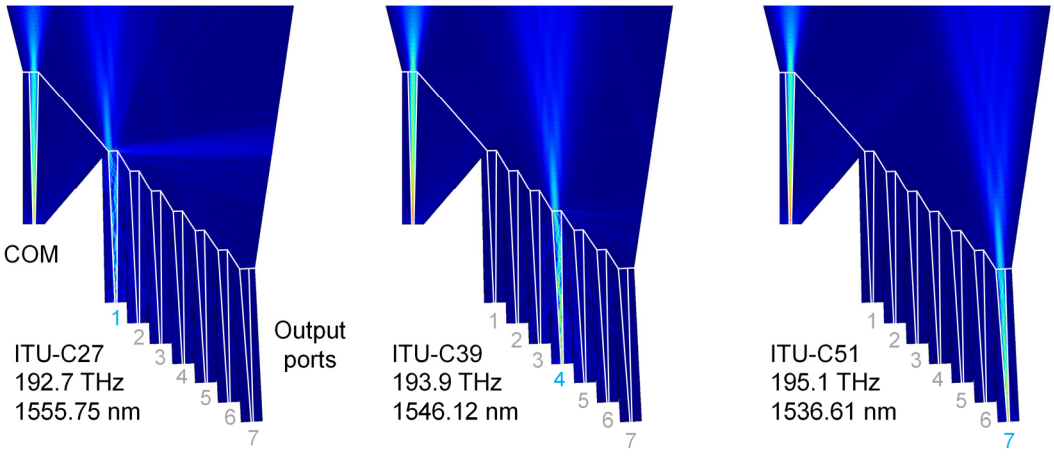

Figure 5.36: Simulated optical field distributions of the 7-channel PCG (de-)multiplexer GM-01. The wavelengths of the incident fields at the common port (COM) are chosen as such that the output signal is concentrated on the first channel (1), the center channel (4) or the last channel (7), respectively. The (DE-)MUX channel number, its target frequency and wavelength as well as the associated ITU channel number are reported in the picture.

5.6.3 Experimental characterization

The transmission of GM-01 is also analyzed experimentally. The device is fabricated on an SOI substrate with a silicon thickness of 250 nm on 3 µm of buried oxide. The process is described in section 5.2. The experimental setup introduced in section 5.3.1 is used for the study. The input and output ports are probed by cleaved single-mode fibers. The transmission spectrum from the common port to every output

port is measured consecutively. In Figure 5.37, the results of the characterization are presented. Figure 5.37a) shows the transmission spectra of all (de-)multiplexer channels. The measured values are compensated for the grating couplers' transfer functions. Parameters are extracted by approximating the spectra with a Gaussian function in the proximity of the main lobes. The corresponding curves are not included in the diagram.

The central wavelength at the transmission maximum of channel 4 is 1539.9 nm. The average insertion loss across all channels is 3.6 dB and the maximum crosstalk from one channel to another adjacent is -12.3 dB. These properties are comparable to results found in the literature [176]. The wavelength of peak transmission of each channel as a function of the channel number is shown in Figure 5.37b). The symbols represent the values obtained by parameter extraction. The linear progression of $\Delta\lambda$ is emphasized by the straight solid line. Its derivative corresponds to the channel spacing of 3 nm. Finally, the FWHM bandwidth of each channel is shown in Figure 5.37c). Again, the symbols show the values extracted from the fit functions. The dashed line marks the average across all channels.

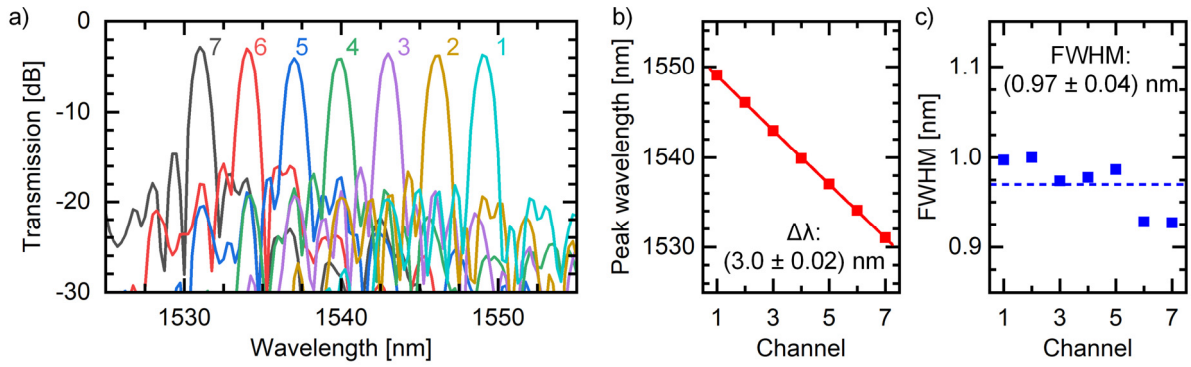

Figure 5.37: Experimental characterization results of the 7-channel PCG (de-)multiplexer GM-01. a) Transmission spectrum, b) wavelength of peak transmission and c) FWHM bandwidth of the individual channels.

The measurement results show the satisfactory operation of the device. It exhibits a low insertion loss and the channel spacing is in good agreement with the design value. However, the absolute spectral locations of the transmission windows deviate considerably. For the center wavelength, the offset amounts to 6.2 nm. For one, this can be attributed to the layout generation. As already stated before, the effective refractive index n_{eff} is determined in the course of calculating the relevant parameters and might induce an inaccuracy. On the other hand, the thickness of the silicon layer on an SOI wafer is subject to uncertainties across the wafer, which in turn affects n_{eff}. The same applies for variances in the thickness and compound of the cladding layer. Hence, fluctuation of the wafer properties and variances in the process yield a deviation of the device from design characteristics. This becomes even more intense, the larger the device dimensions are.

5.6.4 Thermal study

Due to the relatively large thermo-optic coefficient (see section 3.4.2), the performance of silicon photonic devices significantly depends on the temperature. A temperature-induced shift of the refractive index directly translates to a shift of the filter characteristic of a grating-based (de-)multiplexer, because it changes the angular dispersion in the grating equation (2.7). In this section, the influence of the ambient temperature on the (de-)multiplexer performance is investigated.

The device under test (DUT) is 9-channel PCG-(de-)multiplexer, which is fabricated on an SOI substrate with a silicon thickness of 250 nm on 3 µm of buried oxide [154] and covers an area of 0.2 mm^2. The design parameters are listed in Table 3. The experimental setup for this study is similar to section 5.4.7. A clamp on the base plate of the isolated trough fixes the DUT, whose input and output ports are probed by cleaved single-mode fibers. In contrast to the thermal studies of the depletion-type pn-modulators, no voltage supply and thus no dielectric fluid is required. The transmission spectrum is

characterized by providing the input signal to the common channel and measuring the intensity consecutively at each of the output channels. The procedure is repeated for all channels within the measurement range at different temperatures between 8 °C and 80 °C.

Table 3: List of parameters of the PCG analyzed in the temperature study.

ID	λ_{max}	λ_{min}	N	θ_i	θ_o	r	l	m
GM-11	1524 nm	1576 nm	9	45.0°	40.0°	200 µm	200 µm	30

Figure 5.38 summarizes a selection of representative results. In Figure 5.38a) the normalized transmission spectrum of a single channel (#2) is shown for different ambient temperatures. The open symbols show the measured values while the solid lines are fit curves, which represent a modified Gaussian function. To reveal the spectral shift with the temperature, the transmission is expressed on a linear scale. Upon increasing the temperature, the transmission window shifts towards longer wavelengths, while the bandwidth remains unchanged. Figure 5.38b) shows the progression of the wavelength at which the transmission is maximum as a function of the temperature for the DEMUX channels 2, 3 and 4. The open circles represent the wavelength values extracted from the fit functions in Figure 5.38a). The fit curves expressed by the solid lines indicate the linear relation between the transmission peak wavelength and the temperature.

The shift of the transmission window directly relates to the grating equation (2.7). The parameters, i.e. the angles of the input and output waveguides as well as the grating period and the diffraction order are defined by the device design and therefore are considered constants. Rearranging the equation yields

$$\lambda = \frac{\Lambda}{m}[\sin(\theta_i) + \sin(\theta_m)] \cdot n\,, \tag{5.11}$$

which means that the wavelength is proportional to the refractive index n. Since the thermo-optic coefficient is positive, an increasing temperature yields an enhanced effective refractive index. Hence, the center wavelength of the transmission window is red-shifted upon a temperature increase. A comparison of the results of the different channels in Figure 5.38b) shows that the slope of the progressions increases with rising channel index, which corresponds to a decreasing center wavelength. The reason also becomes apparent in equation (5.11), because the relation between λ and n is weighted by both the input waveguide alignment angle θ_i and the diffraction angle θ_m. In order to clarify the influence of the output waveguide position on the wavelength shift, equation (5.11) is differentiated and the diffraction angle θ_m is expressed by the angular position θ_o of the output waveguide. Taking opposite signs of θ_m and θ_o into account, the following expression is obtained:

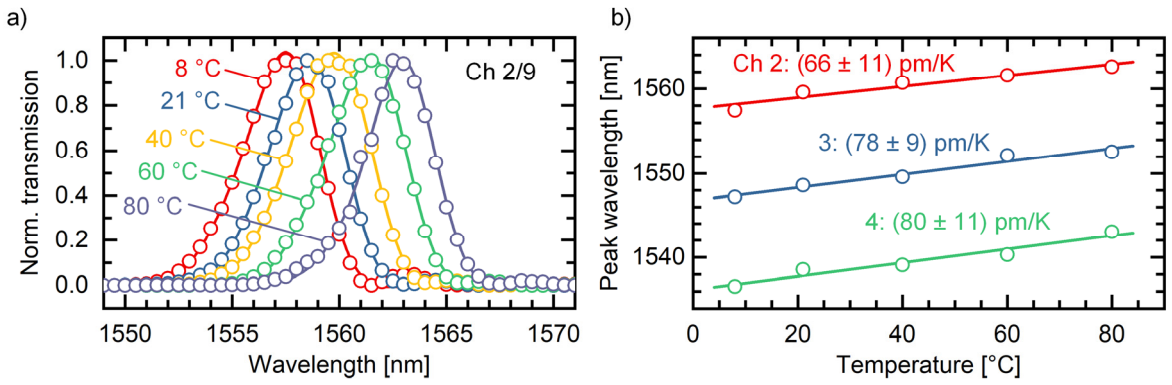

Figure 5.38: Response of the filter characteristic of the 9-channel PCG (de-)multiplexer GM-11 upon a variation of the temperature. a) Normalized transmission spectra of a single channel at different temperatures between 8 °C and 80 °C. The symbols represent measured values, while the solid lines are fit functions. b) Wavelengths of the transmission maxima of the three adjacent channels 2, 3 and 4 as a function of the temperature. Here, the symbols represent the respective center wavelength derived from the fit functions.

$$\frac{\Delta\lambda}{\Delta n} = \frac{\Lambda}{m}[\sin(\theta_\mathrm{i}) - \sin(\theta_\mathrm{o})]\,. \tag{5.12}$$

Since the input waveguide port as well as the output waveguide ports are located in the right half-plane on the Rowland circle (see Figure 2.7), the angles θ_m and θ_o can only take values between zero and $\pi/2$ and $\sin(\theta_\mathrm{i})$ and $\sin(\theta_\mathrm{o})$ are between 0 and 1. Furthermore, θ_i is constant for a specific geometry. According to equation (5.12), the wavelength shift becomes more pronounced, the smaller θ_o becomes. In turn, a smaller θ_o is associated to a shorter wavelength. Thus, the impact of a temperature-induced change of the refractive index is stronger, the smaller the center wavelength of the considered (de-)multiplexer channel is. This appears to confirm the observation in Figure 5.38b), where the rate of the wavelength shift increases for decreasing channel center wavelength.

5.6.5 Summary

The design, simulation and the experimental characterization of PCG (de-)multiplexers on the SOI platform is presented by reference to selected device geometries, which are defined by a set of parameters. The numerically calculated transmission spectra of a 13-channel device is presented and discussed in detail. By reference to a 7-channel device, the agreement between the simulation and the experimental characterization is evaluated. However, due to the comparatively large radius of the Rowland circle, a simulation of continuous transmission spectra is impractical. Still, the design is verified by simulating the device only for few selected wavelengths. The experimental characterization reveals good agreement of the channel spacing, while the absolute spectral alignment of the channels deviates considerably by 6.2 nm. Most likely, this can be attributed to fabrication tolerances. The average insertion loss is found to be 3.6 dB. Finally, the evolution of the filter characteristic of an SOI PCG (de-)multiplexer with changing ambient temperature is investigated. The transmission windows of the considered channels shift with changing temperature by 66 pm/K to 80 pm/K. Apparently, the specific rate depends on the output waveguide's position and thereby on the wavelength.

5.7 Multi-mode interferometers

Self-imaging in a multi-mode waveguide can be made use of in order to construct passive waveguide couplers. For using Multi-mode interferometers (MMI) for splitting and combining optical signals in a Mach-Zehnder modulator (MZM), the goal of the device design is to achieve parity of the optical intensities at both output channels when a signal is applied to one input channel. On the other hand, acting as an MZM output combiner, the MMI images the signals from its two input ports preferably to one of the output ports exclusively. Ideally, the transmission characteristics are only weakly dependent on the wavelength. Primarily, the impact of the MMI length and width on the splitting ratio and the phase is investigated. A 2×2-configuration is chosen to facilitate the device characterization. The feed waveguides are tapered to enable an adiabatic mode size enlargement before the wave enters the multi-mode section. This is useful to reduce propagation losses at the abrupt transition. The design schematic including the dimensions is presented in Figure 5.39. Except for the MMI length and width, the geometrical properties are kept fixed throughout the study.

5.7.1 Simulation and determination of MMI geometry

In order to find an optimized MMI geometry, the transmission characteristics of the device are analyzed using the transient solver of CST MICROWAVE STUDIO (see section 5.1). The 2×2-configuration

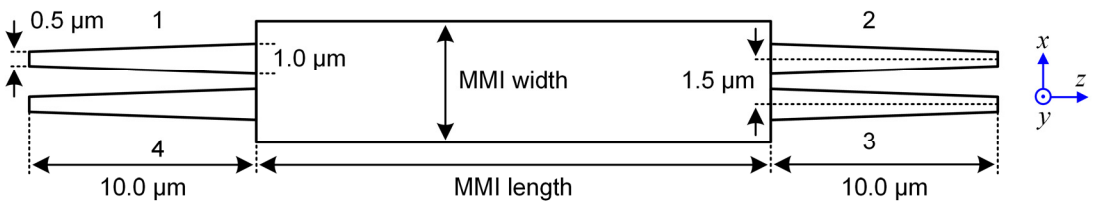

Figure 5.39: Schematic of a 2×2-MMI including the device dimensions and port numbering.

constitutes a 4-port network and thus the device can be evaluated by analyzing the associated scatter parameters. A guided mode is launched at the input port (port 1 in Figure 5.39). From there, it propagates along the waveguide taper towards the multimode waveguide. The transmission from the input port to the two output ports is expressed by the scatter parameters S_{21} and S_{31}, respectively, while S_{11} represents the return loss and S_{41} the crosstalk to the open port adjacent to the input. The model is based on an SOI wafer with a silicon layer of 250 nm height on 3 µm buried oxide. The cladding material is silicon dioxide.

In this study, primarily the magnitude of the scatter parameters is considered, because parity between both output signal intensities is aimed for. The phase of the output signals with respect to the input is of minor importance. In contrast, the phase relation between the output ports 2 and 3 is of particular interest. Acting as a splitter or combiner in an interferometer, it directly affects the relative phase between the two arms. A guided mode's phase is obtained by calculating the 1D field amplitude along the propagation axis in the respective port waveguide and extracting the absolute phase. The propagation axis is oriented in z-direction and originates in the center of the rectangular waveguide. The phase relation is determined by the difference of the absolute phases of the modes co-propagating in adjacent feed waveguides.

The two degrees of freedom considered in this study are the length and the width of the multi-mode waveguide. All other geometrical properties remain constant at the values summarized in Figure 5.39. For the specification of a range of reasonable results, different well-known material definitions for the Si layer and the SiO_2 cladding and substrate are taken as basis for the evaluation. In the following, they are summarized as material sets 1 and 2. In set 1, the refractive indices of Si and SiO_2 is defined according to [177] and [178], while set 2 refers to [179] and [180]. The former is part of the simulation software's database, while the latter is provided by a publicly available database [153].

5.7.2 Simulation results

Figure 5.40 shows a representative pseudo-color image of the optical field distribution in a 2×2-MMI with a length of 23.3 µm and a width of 4.5 µm at a wavelength of 1550 nm. Port 1 is the input, where a guided mode is launched at the narrow end of the taper. At the abrupt transition from the tapered single-mode waveguide to the multi-mode waveguide, several higher-order modes are excited. Since each of them has a different propagation constant, interference patterns emerge along the z-direction. At the far end of the multi-mode waveguide the interference yields two intensity maxima that coincide with the locations of the output waveguides.

Figure 5.41a) shows the transmission spectrum from the input port to the output ports expressed by the magnitude of the scattering parameters for the MMI width 4.5 µm and selected lengths between 23.1 µm and 23.5 µm. The device is modelled using material set 1. Solid lines represent $|S_{21}|$ and the dashed lines $|S_{31}|$. Globally, the transmission losses of both output channels decrease for longer wavelengths until a maximum of approximately -5 dB is reached. Above the respective wavelength of maximum transmission, $|S_{31}|$ decreases stronger than $|S_{21}|$. Between 1460 nm and 1600 nm, the curves proceed almost in parallel. Although the absolute values differ slightly for the different device lengths, all $|S_{21}|$ and $|S_{31}|$ curves have a similar characteristic. The average return loss at 1550 nm is -32 dB and the crosstalk to port 4 -57 dB. Taking into account an attenuation of 3 dB per channel due to the splitting

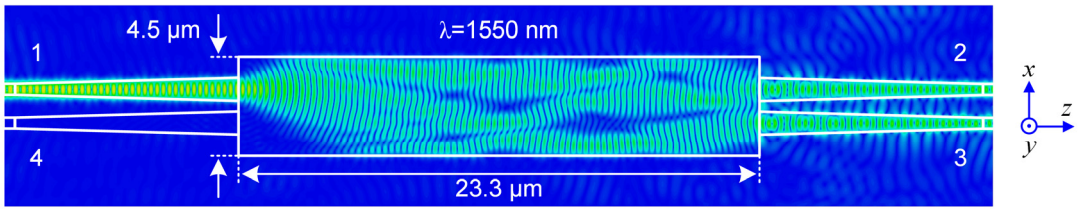

Figure 5.40: Simulated optical field distribution of a 2×2 MMI with a width of 4.5 µm and a length of 23.3 µm. The wavelength is 1550 nm.

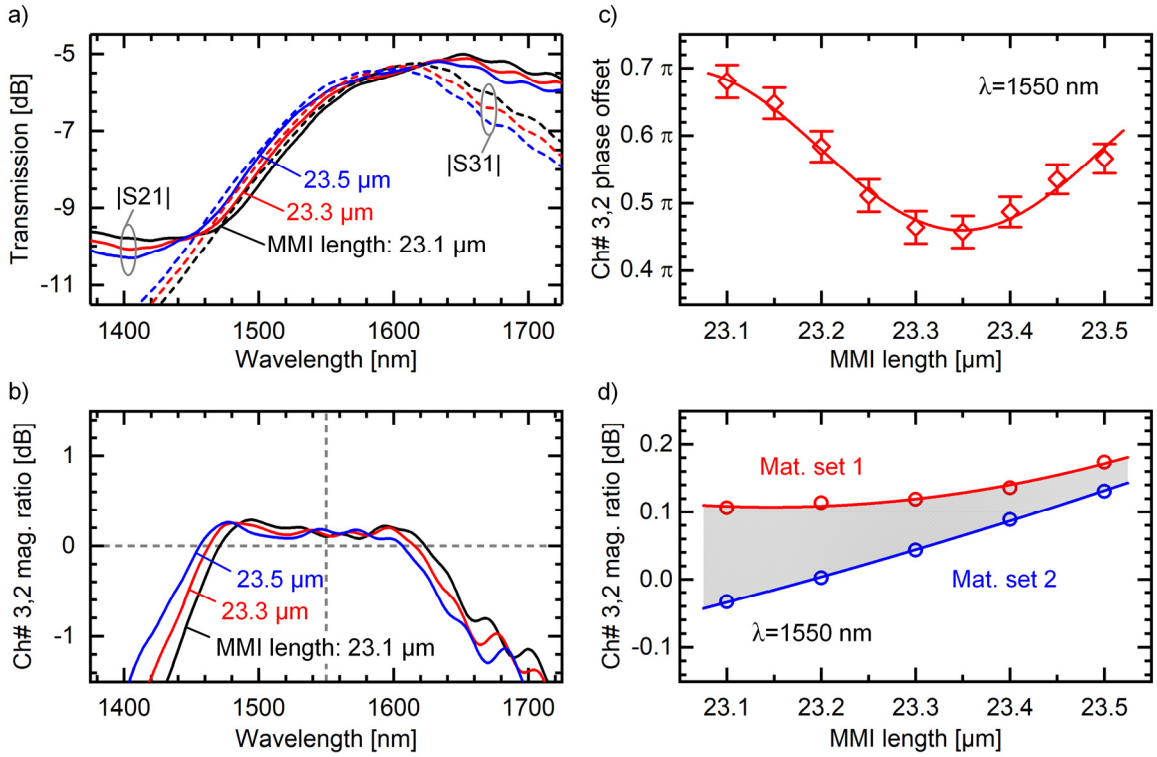

Figure 5.41: Simulated characteristics of a 2×2 MMI with a width of 4.5 µm and a length from 23.1 µm to 23.5 µm. a) Transmission spectrum from port 1 to port 2 and 3 expressed in S-parameter magnitudes for different MMI lengths. Solid lines represent S_{21} and dashed lines S_{31}. b) Ratio of the magnitudes at port 3 and 2 for different MMI lengths as a function of the transmission wavelength. c) Phase relation of the output fields at port 2 and 3 as a function of the device length. d) Comparison of the channel magnitude ratio at 1550 nm as a function of the device length for two different sets of material definitions for silicon and silicon dioxide.

ratio, the insertion loss of the device in the wavelength range of interest is in the range of 3 dB. As will be shown by the experimental characterization, the simulation overestimates the insertion loss. This is most likely due to the definition of the boundaries of the calculation domain: at each MMI port, an area is defined which can stimulate or absorb energy exchanged with the simulated structure. These areas are referred to as waveguide ports. In order to prevent the overlap of adjacent waveguide ports, the extent in x-direction has to be constrained. Consequently, the waveguide ports reflect a fraction of energy, which therefore is not exchanged with the simulated structure.

In order to determine the ratio between the magnitudes of the output signals, $|S_{31}|/|S_{21}|$ is calculated and plotted in Figure 5.41b). Again, the resulting curves represent the device width 4.5 µm and three different lengths 23.1…23.5 µm. The parallel progression of $|S_{21}|$ and $|S_{31}|$ between 1460 nm and 1600 nm finds expression in a plateau. Within this wavelength range, the ratio remains almost constant and close to 0 dB, which indicates only a slight deviation of the optical power of the two output channels. The phase relation between the output signals is presented in Figure 5.41c). The open rhomb symbols represent the simulated phase offset between port 3 and 2 as a function of the MMI length while the solid line is a fit curve. The error bars represent the uncertainty from the parameter extraction for each result. For a device length of 23.1 µm, the phase difference of the output waveguide modes is approximately 0.7×π. It diminishes with increasing length to a minimum of 0.46×π at 23.35 µm before rising again. The progression resembles a sinusoidal, which is emphasized by the fit curve.

According to the simulation results, similarity of the output signals can be achieved with respect to the intensity. The device length has only a minor influence on the splitting ratio. However, the phase offset between the two output signals can only be minimized to a residual value in the range of 0.5×π. Both an even splitting ratio and a minimum phase offset are favorable for the application as power splitter and combiners. Thus the optimum device length appears to be 23.35 µm.

Finally, the magnitude ratio between channel 3 and channel 2 as a function of the MMI length for the two different material sets is shown in Figure 5.41d). The open symbols represent the simulation results at the wavelength 1550 nm for both sets. The solid lines show the progression of the respective polynomial fit function. The ratio $|S_{31}|/|S_{21}|$ is always larger for material set 1 compared to material set 2. Yielding a larger effective refractive index, the results based on material set 1 therefore constitute the upper boundary, while material set 2 is considered the lower boundary. The grey area in between represents the range of reasonable results for the channel ratio. However, at 1550 nm and in the observed range of device lengths, the different material definitions only have a minor influence on the device characteristics. The maximum ratio between the two results in Figure 5.41d) is 0.14 dB and becomes well below 0.1 dB for increasing device length. Hence, the simulation accuracy is not affected by the material set selection.

5.7.3 Experimental characterization

In order to verify the MMI design, a series of 2×2 MMI devices is experimentally characterized. Corresponding to the simulated geometries, devices with a width of 4.5 µm and a length between 23.1 µm and 23.5 µm are considered. The experiments are carried out using the steady-state measurement setup introduced in section 5.3.1. The optical signal is coupled to both the ports 1 and 4 and the transmission spectra are measured at both output ports consecutively. Thus, all transmission paths from left to right are analyzed. The measurement is repeated for one single device as well as three and five concatenated devices, respectively. The transfer functions of the grating couplers are compensated for by the transmission spectrum measurement of a reference structure. The significant results are the splitting ratio between the two output channels and the insertion loss of the device. Based on the simulation results presented in the previous section, the MMI utilized as MZM splitters and combiners have the dimensions 23.3 µm×4.5 µm. Consequently, the experimental characterization results of devices with that geometry are discussed in detail as representative for the study. Figure 5.42 shows a summary of the characterization.

In Figure 5.42a) the measured transmission spectra from the input port 4 to the output ports 2 and 3 of a single MMI are presented. It is recognizable, that the optical power at both ports is weakly modulated with the wavelength. Port 2 has an average transmission of -3.8 dB while it is -3.9 dB for port 3. The ratio between the optical powers of port 3 and 2 as a function of the wavelength is shown in Figure 5.42b). The curve resembles a plateau, despite the slight modulation around the average value of -0.2 dB. Additionally, a comparison of the transmission spectra after one, three and five MMI is plotted in Figure 5.42c). The respective output port is chosen as such all signals have the identical phase. The supplemental triangular symbols highlight local maxima of the transfer characteristics. The wavelengths of maximum transmission are obtained by fitting a Gaussian to the local maxima. Since the experimental data is discretized by a wavelength interval of 0.5 nm, the actual transmission value is obtained at the data point that is nearest to the maximum of the fit function. First of all, the diagram

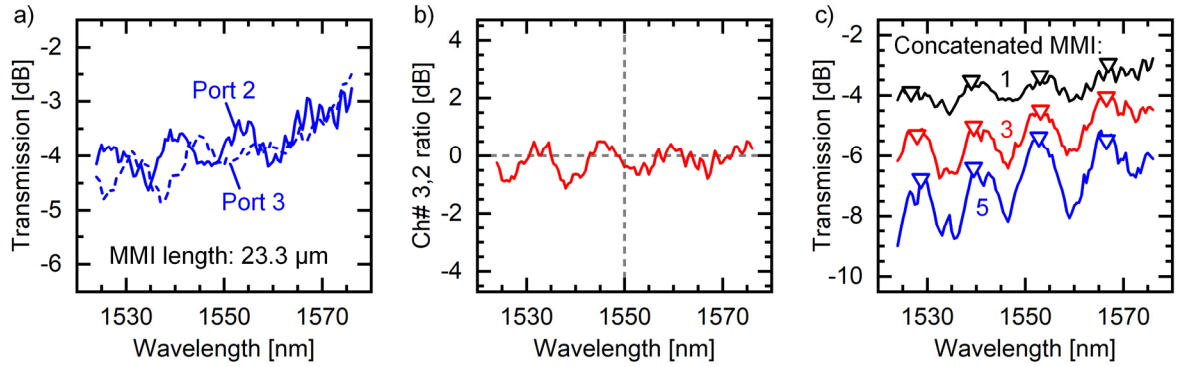

Figure 5.42: Characterization result of a 2×2 MMI with a length of 23.3 µm and a width of 4.5 µm. a) Measured transmission spectra from port 4 to port 2 and 3, b) transmission magnitude ratio between port 3 and port 2 as a function of the wavelength, c) transmission spectra of equal phase measured after 1, 3 and 5 concatenated MMI.

shows that the attenuation increases the more devices are concatenated. On the other hand, the modulation of the spectra evolves to more distinct notches. A general tendency of higher attenuation for shorter wavelengths is also observed.

Acting as a symmetric splitter, both ports ideally receive half the total injected optical power. That explains a 3 dB proportion of the attenuation in Figure 5.42a). Residual reduction of the optical power is attributed to imbalance, material loss and scattering loss. The modulation of the transmission with the wavelength is due to the wavelength-dependent formation of interference patterns in the multi-mode section of the MMI. The propagation constants of the excited modes vary with their wavelength. Thus, the interference patterns shift along the z-direction and therefore the position of the resulting maxima change. Consequently, they may no longer coincide with the output waveguide apertures, which in turn reduces the available optical power at the output ports. The modulation further yields a slight imbalance of the device. This manifests in the diagram in Figure 5.42b), where the power ratio oscillates around 0 dB.

By reference to Figure 5.42c), a filter characteristic of the MMI due to the wavelength dependency becomes apparent. It becomes more explicit if identical MMI are concatenated, because the formation of periodic notches in the transmission spectra is observed. Moreover, the total attenuation of the signal grows with the number of concatenated MMI due to the accumulated insertion loss. The splitting ratio can be disregarded here, because every MMI with even count compensates the phase relation and splitting ratio of the preceding device with an odd count. Therefore, no power is lost for the analysis to an open port. For determining the insertion loss of a single MMI, the local maxima of the transmission spectra are used to calculate the differential attenuation. The insertion loss is eventually obtained by the average, which is found to be (0.64±0.03) dB.

5.7.4 Summary

In this section, the impact of the geometry on the splitting ratio and the phase relation between the output signals of 2×2 MMI is explored. The dimensions required to achieve an even splitting ratio are determined. In particular, MMI with various combinations of width and length of the multimode waveguide section are simulated based on current material definitions. A splitting ratio close to parity is found for a width of 4.5 µm and a length of 23.3 µm, which is confirmed by experimental characterizations. By means of measuring the transmission of concatenated MMI, the insertion loss per device is found to be 0.64 dB.

5.8 Grating couplers

To enable the coupling of single-mode fibers to the sub-micrometer waveguides on the silicon photonic the test chip, shallowly-etched focusing grating couplers as described in section 2.2.3 are implemented. A model template of the grating coupler is included in the general silicon photonic design kit [181] provided by the *University of British Columbia* in Vancouver (Canada) and the design method is described in [182]. Based on calculations according to equation (2.15), simulations are conducted to determine the grating period as a function of the coupling angle for an optical field at a given wavelength.

5.8.1 Simulation and determination of GC parameters

Figure 5.43a) shows a picture of the simulation model. It is essentially a corrugated silicon waveguide on a BOX layer. A straight uniform grating consisting of 20 segments with the grating period Λ approximates the grating coupler. The width of the structure is 10 µm, which is similar to the dimension at the wide end of the waveguide taper. According to the process description in section 5.2, the waveguide height of the model is 250 nm and the etch depth of the grating trenches is 70 nm. The transient solver of CST MICROWAVE STUDIO and far-field calculation is used for the analysis. The optical signal is launched to the silicon waveguide and disperses at the grating. The simulation calculates the far-field of the scattered wave and the distribution of the intensity as a function of the propagation

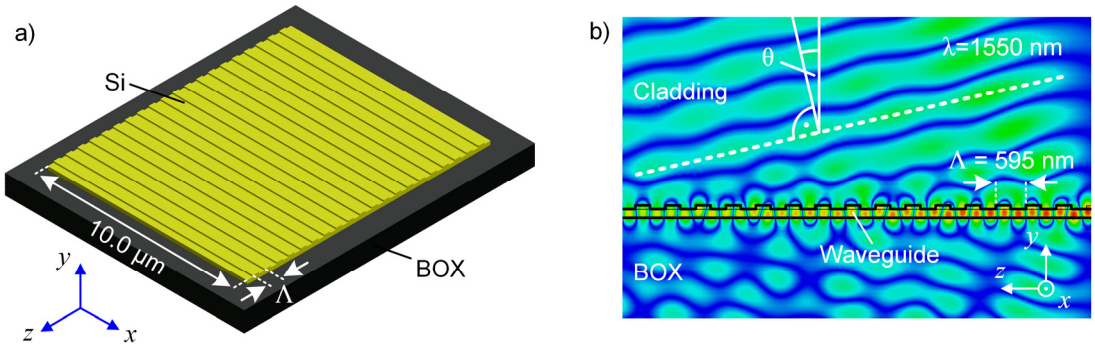

Figure 5.43: Simulation of a straight uniform grating in order to approximate a grating coupler. a) Simulation model with the relevant dimensions. b) Distribution of an optical field at 1550 nm that propagates in +z-direction and scatters at the waveguide grating with a period of 595 nm.

angle. The insertion loss is calculated by the ratio between the power radiated towards the cladding and the power of the excitation wave.

In Figure 5.43b), the distribution of an optical field that propagates along the waveguide in +z-direction is presented. The wavelength is 1550 nm and the grating period Λ is 595 nm. Obviously, scattering occurs at the grating segments and the field disperses towards the cladding as well as towards the substrate. The angle θ with respect to the surface normal defines the direction of the propagation vector of the field that is scattered towards the cladding.

In order to take variations of the effective refractive index into account, two different sets of material definitions for Si and SiO_2 are considered. Similar to the study of MMI in the previous section, a range of possible results is thereby specified. The simulation results are presented in Figure 5.44a) and b). Figure 5.44a) shows the normalized coupling efficiency at 1550 nm as a function of the angle to the surface normal for different grating periods. These results are obtained using material set 1. Within the spectral range of interest, each curve resembles a Gaussian function with the center located at maximum transmission. The coupling angle is defined as the angle with respect to the surface normal, at which the far-field intensity at a given wavelength is maximum. It is extracted from a fit curve. In Figure 5.44b) the dependency of the coupling angle on the grating period for the two different sets of materials is shown. The open symbols show the simulation results and the solid lines trace linear fit curves. The grey area enveloped by the two curves is considered the range of possible results with a variance of 1.6°.

The dependency of the coupling efficiency on the coupling angle is eventually identical to the problem of an angular misalignment of two waveguides. According to equation (2.14), the relation

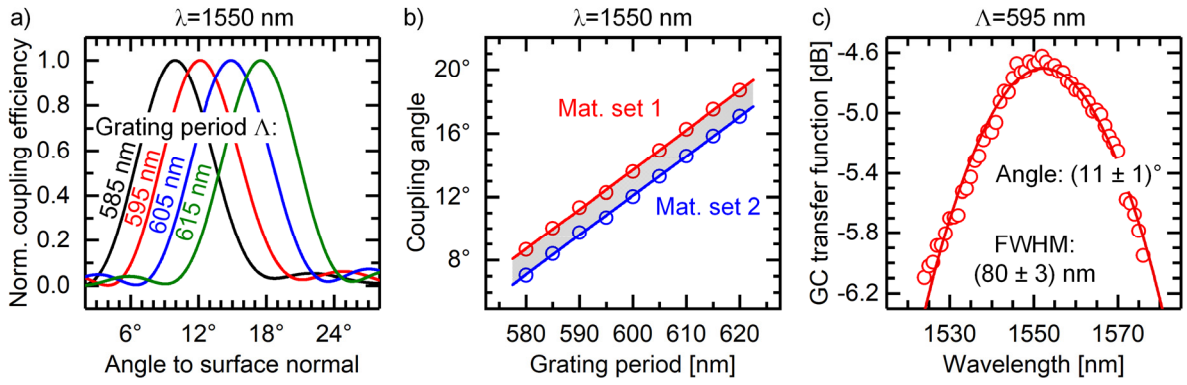

Figure 5.44: Summary of the study on grating couplers for the photonic test chip. a) Normalized coupling efficiency obtained by the simulation of a shallowly-etched straight uniform grating at 1550 nm as a function of the angle to the surface normal for different grating periods Λ . b) The coupling angle as a function of the grating period for two different sets of material definitions. c) Measured transmission spectrum of a grating coupler with a grating period of 595 nm at a coupling angle of 11°.

conforms to a Gaussian distribution, which manifests in Figure 5.44a). Although equation (2.15) yields a non-linear dependency of the coupling angle θ on the grating period Λ, it can be approximated by a linear relation for small variations of θ. Hence, the change of the coupling angle with the grating period $\mathrm{d}\theta/\mathrm{d}\Lambda$ is constant for both material definitions and the linear approximation of the progressions in Figure 5.44b) is justified. The insertion loss at maximum coupling efficiency is estimated by the simulations to be 3.4 dB.

A grating period of 595 nm is predefined for the process layout. Based on the simulation results a coupling angle of 12° at most is expected. The grating coupler devices are part of the photonic test chip fabricated according to section 5.2. Specimens of the focusing grating couplers are experimentally characterized. The coupling angle is set by adjusting the tilt of the optical fibers manually. In order to obtain the transfer functions, the transmission spectra of test waveguides connecting two identical grating couplers are measured. The results are extracted after compensating for the waveguide losses. Figure 5.44c) shows the measured transmission spectrum of a focusing grating coupler with a grating period Λ of 595 nm at a coupling angle of (11±1)°. The measurement equipment (see section 5.3.1) limits the wavelength range from 1524 nm to 1576 nm. The open symbols represent the experimentally obtained transmission values and the solid line is a Gaussian-shaped fit curve. Despite the limited accuracy of determining the coupling angle, this result indicates a very good agreement between the simulation and the real device. The insertion loss deduced from peak transmission at 1552.4 nm is 4.6 dB. Based on the measured wavelength range, a bandwidth (FWHM) of (80±3) nm is estimated. Grating couplers identical to this specimen are used for the integrated transmitter unit and all supplemental components fabricated on the photonic chip.

5.8.2 Summary

This section discusses the adaption of a grating coupler design to a fabrication process and the wafer geometry. In particular, the relation between the fiber coupling angle and the associated grating period is investigated by simulations and a grating period of 595 nm is predefined for the process layout. A coupling angle of (11±1)° is experimentally determined. Within the scope of the measurement accuracy, this is in very good agreement with the simulation results.

5.9 Four-channel silicon photonic transmitter

The monolithically integrated four-channel transmitter design is assembled from the photonic components presented in the previous sections. The schematic is described in section 4.4 and an excerpt of the process layout showing the transmitter design is presented in Figure 4.7 on page 39. As already stated, two transmitter variants utilizing different (de-)multiplexer designs are implemented on the test chip. The MZM consist of a phase shifter with a length of 3 mm in each interferometer arm.

In contrast to the modulators discussed above, the geometric length of the interferometer arms are equal. Assuming uniformity of the wafer, this results in uniform optical path lengths. Hence, they are referred to as symmetric MZM. The reason for utilizing symmetric MZM is the attempt to decouple the operating point from the wavelength, because the assignment of the carrier wavelength to the transmitter channels is predefined by the (de-)multiplexer transmission window. Moreover, the dependency of the phase relation on the temperature reduces significantly compared to an asymmetric MZM. The drawback, however, is that restrictions apply on the operating point adjustment, because it exclusively relies on the selection of an appropriate bias voltage of the phase shifters. Even so, this limitation can be mitigated by introducing additional phase shifters in the interferometer arms.

5.9.1 Experimental characterization

The steady-state transmission of the four-channel transmitter is characterized using the setup presented in Figure 5.3 on page 46. The study aims to quantify the spectral separation of the transmitter channels, the modulator characteristics and the unit's insertion loss. The DUT of which the results are discussed below, is a transmitter equipped with 7-channel (de-)multiplexers. The characteristics of a reference

(de-)multiplexer are presented in section 5.6.3. The DUT is optically probed via the common ports of the input demultiplexer and the output multiplexer, respectively. The modulators remain unbiased. The transfer function of the grating couplers is compensated in the course of evaluation. The results are presented in Figure 5.45.

The complete transmission spectrum is shown in Figure 5.45a). Four distinct transmission maxima can be recognized, which are identified as the transmission windows. They are numbered in the diagram according to the (de-)multiplexer channel indices. The insertion loss varies between 10.9 dB and 16.6 dB across the four channels. In Figure 5.45b), the peak transmission wavelength is shown as a function of the channel index and Figure 5.45c) provides an overview of the FWHM bandwidth variance. In each of the diagrams, the solid symbols represent values that are extracted from Gaussian functions that approximate the transmission windows. From the dependency of the peak wavelength on the channel index, a nominal channel spacing $\Delta\lambda$ of 3.1 nm is determined. However, since only the odd channels are used, the effective spectral spacing of the transmitter channels is 6.2 nm. A red-shift of the transmission maxima by 2.1 nm in average compared to the reference device is recognized. The average FWHM of the transmission windows is 0.67 nm, which is a reduction to 69% of the reference bandwidth.

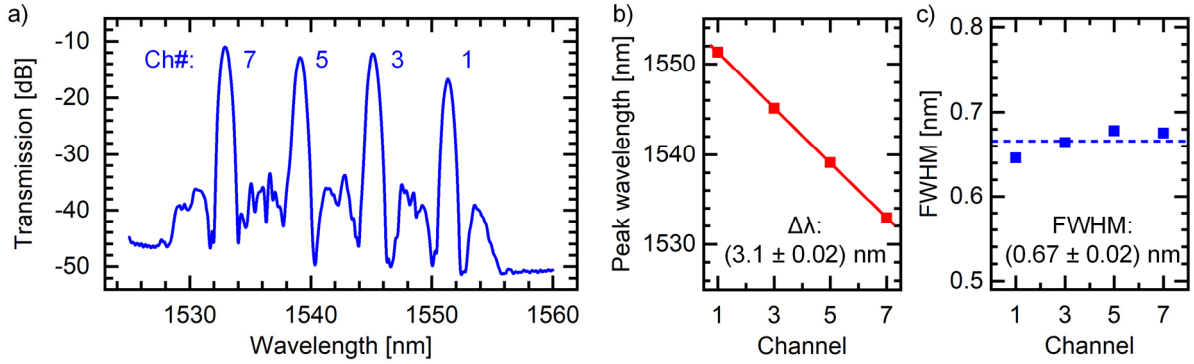

Figure 5.45: Steady-state transmission spectrum and characteristics of the four-channel transmitter. a) Measured transmission spectrum, b) wavelength of peak transmission and c) FWHM bandwidth of the individual channels. The channel numbering follows the (de-)multiplexer port indices.

The insertion loss of each transmitter channel is composed of the (de-)multiplexer losses and the loss of the modulator as well as the attenuation of the power couplers and the waveguides. The characterization of the reference device yields an average insertion loss of 3.6 dB and only minor fluctuations across the different channels. Furthermore, the losses of the MMI and the modulators are only weakly wavelength-dependent. Thus, the insertion loss variance across the transmitter channels is attributed to attenuation due to the operating points of the unbiased modulators. Their characteristics are elaborated below and the phase offset fluctuations between the interferometer arms due to fabrication tolerances are discussed in detail.

The reason for the transmission window shift and the reduction of the associated bandwidth are the consequence of a variation of the effective refractive index n_{eff} across the wafer. Typically, fabrication tolerances, and in particular the thickness of the wafer layers are the reason for n_{eff} depending on the location. The angular dispersion of the (de-)multiplexer reflector grating relates to n_{eff} and thus a variation results in a shift of the transmission spectrum. Furthermore, both the input demultiplexer and the output multiplexer are equally affected. Therefore, the transmission spectra become less uniform and the overlap of the transmission windows is reduced. Since the total transmission spectrum of the transmitter is dominated by the two concatenated devices, this results in an increased insertion loss of the channels and a reduced bandwidth.

After the discussion of the channel separation, the steady-state characteristics of the four MZM are evaluated. The MZM transfer function is measured using the experimental setup depicted in Figure 5.3. At a fixed wavelength, the transmission is measured while varying the bias voltage applied to the phase shifter in one arm of the interferometer. The phase shifter in the other arm is biased at 0 V. The procedure

is repeated for both arms. Results are normalized to the maximum of both measurements in order to facilitate a comparison of the phase relations between the different modulators.

A representative result of the steady-state characteristics of the four MZM within a transmitter unit is presented in in Figure 5.46a). The diagram shows the normalized transmission of each MZM as a function of the reverse bias voltage applied either to the upper (V_{B1}) or the lower (V_{B2}) interferometer arm. The wavelength is selected according to the respective (de-)multiplexer transmission window. The relation between the transmission and the bias voltage V_{B1} is shown by the up-pointing triangular symbols. The down-pointing triangular symbols represent the dependency on the voltage V_{B2}. Both progressions resemble damped cosine functions. In particular, they are proportional to a squared cosine, which stems from the MZM intensity transfer function according to equation (3.1). The damping factor takes the diminishing modulation efficiency of the depletion-type pn-phase shifters with increasing bias voltage into account. Thus, the transfer functions can be approximated by

$$T(V_{Bi}) = A(V_{Bi}) \cdot \cos^2[\Delta\varphi(V_{Bi}) - \varphi_0], \quad (i = 1, 2)\,. \tag{5.13}$$

It is fundamentally dependent on the phase shift $\Delta\varphi$, which in turn depends on the bias voltage V_{Bi} applied to the respective interferometer arm. The value φ_0 takes a potential phase offset into account. The factor $A(V_{Bi})$ expresses the damping that becomes more pronounced with rising bias voltage V_{Bi}. The lines in Figure 5.46a) trace curves according to equation (5.13). The solid lines are associated to the upper arm biased at V_{B1}, while the dashed lines describe the relation when biasing the lower arm at V_{B2}.

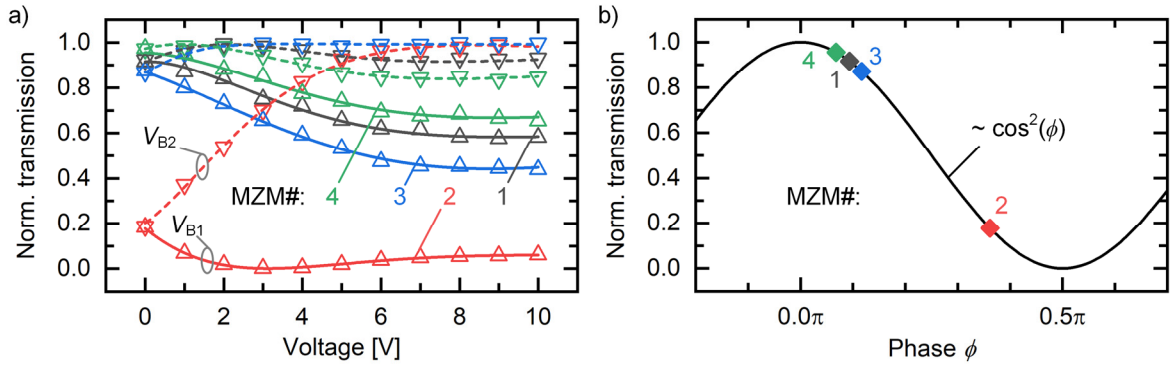

Figure 5.46: Steady-state transfer functions of all four MZM the transmitter unit consists of. a) Normalized transmission of each MZM as a function of the bias voltage. The two interferometer arms are biased independently and successively, i.e. while biasing one phase shifter, the other one is kept at 0 V. b) Theoretical MZM transfer function and estimated operating point of the modulators at 0 V.

The transfer functions compiled in Figure 5.46a) show that the MZM operate successfully as intensity modulators. Upon biasing the phase shifter in the lower interferometer arm, the relative phase between both arms becomes smaller. Consequently, the output intensity increases. On the other hand, a phase shift in the upper arm yields an increased phase difference, which results in an intensity reduction. However, all specimens appear to be subject to an imbalance between the interferometer arms. This results in a non-zero relative phase at 0 V, which manifests in a transmission of less than maximum. It becomes most apparent in the transfer function of MZM 2: the transmission at 0 V is distinctly attenuated but increases towards maximum with rising bias voltage V_{B2} applied to the lower arm. Furthermore, biasing the upper arm with V_{B1} up to 3 V results in further suppression of the output signal. Above 3 V, the intensity of the output signal grows again, although at a significantly reduced rate due to the progressive reduction of the phase shifter modulation efficiency.

The phase offset φ_0 is estimated using equation (5.13). At $V_{Bi} = 0$ V, both the damping factor $A(V_{Bi})$ and the voltage-induced phase shift $\Delta\varphi(V_{Bi})$ can be neglected and φ_0 can directly by determined. The results are assembled in Figure 5.46b) in relation to a calculated transfer function of an MZM as a function of the total phase ϕ between the interferometer arms. According to equation (3.1), it is

proportional to the squared cosine of ϕ. By highlighting the pairs of values $T(0\,\mathrm{V})$ and φ_0 on the ideal transfer function, the locations of the MZM operating points at 0 V extracted from Figure 5.46a) can be visualized. The condensed results in Figure 5.46b) show a significant variance of the MZM steady-state characteristics even of the specimens that constitute a single transmitter unit. A comparison between different transmitter units reveals an almost random distribution of the absolute phase offsets. The reason is an uncertainty of the effective refractive index Δn_{eff} either due to variances of the silicon layer thickness or fabrication process tolerances, although the modulators are nominally identical by design.

The variances may have a considerable impact on the signal performance. As discussed in the characterization results of individual MZM in section 5.4, the nominal concentrations of both donors and acceptors are not achieved in the course of the fabrication process. Thus, the efficiency of the depletion-type pn-phase shifters is limited, which is characterized by a $V_\pi L$ of 4.4 Vcm at 1 V bias voltage. Against this backdrop, the variances of the steady-state characteristic can impair the performance of some of the MZM because they limit the range of possible operating points. Consequently, the signal quality may suffer either from strong attenuation, a small extinction ratio or non-linear distortions. The former is caused by an operating point in the proximity of a transmission minimum. This, however, can be mitigated by the supply of sufficient power of the optical carrier to compensate for the insertion loss or an increased receiver sensitivity. The reason for an insufficient extinction ratio is the dependency of the modulation efficiency of a depletion-type phase shifter on the bias voltage. According to equation (3.4), it is approximately proportional to the square root of the bias voltage. Thus, a large bias voltage required to adjust the MZM to a favorable operating point opposes the phase shifter to operate efficiently. Lastly, non-linear distortions may noticeably impair the quality of the amplitude-modulated signal, if the MZM operates far away from the quadrature point. Eventually, they add up to those induced by the non-linear characteristic of the modulation efficiency.

Using the experimental setup presented in Figure 5.4b) on page 47, the electro-optic small signal response of the symmetric MZM is characterized. Unless the phase offset φ_0 at zero bias voltage results in strong attenuation of the optical output, the phase shifters are equally reverse-biased. Alternatively, the voltages are adjusted individually, i.e. one of the phase shifters is biased as such the mean transmission is increased to a suitable level for the characterization procedure. Since the phase shift per voltage of a depletion-type pn-modulator decreases with rising bias voltage, the resulting modulation depth of the MZM is reduced compared to push-pull operation. This affects the amplitude of the RF signal at the photodetector, but has no further impact on the MZM small-signal characteristics.

The small-signal characteristics of a single transmitter modulator are shown in Figure 5.47 as a representative result. The phase shifters of this device are equally reverse-biased. The normalized EOE responses at bias voltages of 1 V to 4 V are presented in the diagram in Figure 5.47a). According to the small-signal analysis presented in section 5.4.5, the notch close to DC and the ascent of the responses

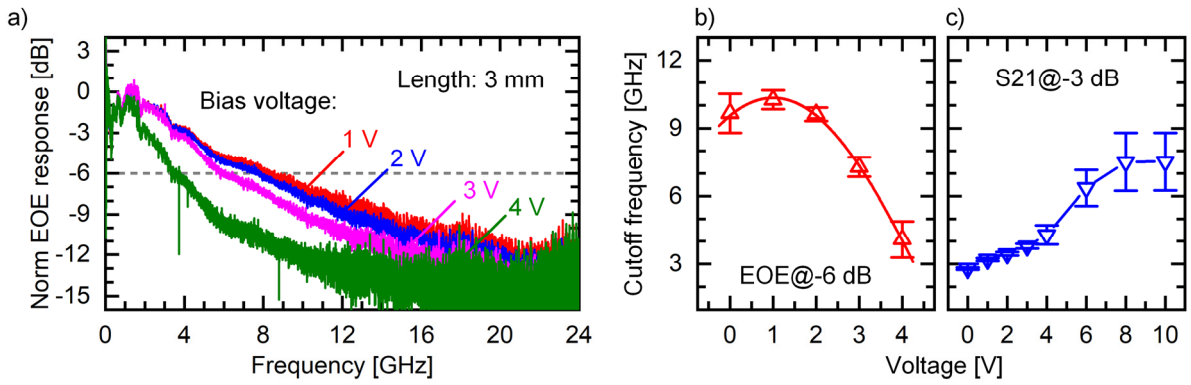

Figure 5.47: Small signal characteristic of the transmitter modulators. a) Measured EOE responses of one of the transmitter modulators at the bias voltages 1 V to 4 V, b) average 6 dB cutoff frequency of the EOE response as a function of the bias voltage, c) average 3 dB cutoff frequency of the S_{21} parameter as a function of the bias voltage.

up to approximately 2 GHz occur due to the frequency response of the photodetector. For frequencies higher than 2 GHz, all EOE responses resemble a low-pass characteristic. Noticeably, the bandwidth decreases with increasing bias voltage. This is most apparent at a bias voltage of 4 V, because the EOE response exhibits a sharp decline even for low frequencies compared to 3 V.

The evolution of the 6 dB cutoff frequency of the EOE response as a function of the bias voltage is presented in Figure 5.47b). The diagram shows the average of all four modulators of a transmitter unit. The error bars represent the maximum deviation from the average. The cutoff frequency is 9.7 GHz at 0 V and increases to 10.2 GHz at 1 V, which apparently is the maximum. Beyond 1 V, the cutoff frequency decreases again with rising bias voltage up to 4 V. For even higher bias voltages, it can no longer be determined due to the sharp decline of the response even at low frequencies.

A similar behavior is also observed in the analysis of asymmetric MZM with depletion-type phase shifters, which is discussed in section 5.4.5. By reference to the asymmetric MZM with 3 mm phase shifters, the cutoff frequencies of both device variants are as well comparable. That apparently is expected, because the modulators only differ in the MZI properties but utilize identical phase shifter designs.

The relation of the cutoff frequency on the bias voltage is extensively discussed section 5.4.5 in the context of the asymmetric MZM. It is found that the imperfect realization of the metal vias causes the isolation of the pn-junction from the travelling-wave electrodes. The effect appears to be progressively dependent on the bias voltage. It is also shown that the effect can be observed in the evolution of the S_{21} parameters. Similar to section 5.4.5, the scattering parameters of the symmetric MZM are experimentally determined. In particular, the absolute values of the S_{21} parameters are analyzed and the 3 dB cutoff frequencies are determined. The results are summarized in Figure 5.47c), which shows the average 3 dB cutoff frequency of all four transmitter MZM as a function of the bias voltage. The symbols represent the values extracted from the measured S_{21} parameters. Similar to the analysis of the EOE response, the scattering of the results is taken into account by the error bars. The cutoff frequency increases approximately proportionally to the square root of the bias voltage between 0 V and 3 V. Above 3 V, it increases at a higher rate and appears to saturate at 8 V. Again, the results are in agreement with the characteristics of the asymmetric MZM. With increasing bias voltage, the interaction between the electrical and the optical wave that co-propagate along the modulator is progressively frustrated. Consequently, the fraction of energy expended to the electro-optic conversion is minimized, while the greater part is dissipated in the transmission line termination. Hence, the bandwidth of the electro-optic conversion is maximum at a small bias voltage and drops significantly for increasing bias voltage.

In order to complete the picture of the transmitter performance, the quality of an 11.3 Gbit/s NRZ-OOK signal encoded by one of the transmitter MZM is assessed. The utilized experimental setup is presented in Figure 5.8 on page 50. Unlike the demonstration using asymmetric MZM, the operating point is selected exclusively by the bias voltage of the phase shifters. The DUT for this experiment is MZM 2 of the transmitter unit already considered in the steady-state characterization. Due to the imbalanced dependency of the MZM transfer function on the bias voltages $V_{\mathrm{B}i}$ $(i = 1, 2)$, the DUT is not symmetrically biased. Instead, V_{B1} is set to 1.5 V, and V_{B2} is 6 V. At this operating point, optimum signal quality is reached, because high transmission is achieved while maintaining an acceptable modulation depth. Similar to the investigation of the asymmetric MZM, a preemphasis is applied to the driving signal. The eye pattern and the measured BER of the received signal are presented in Figure 5.48.

Although the eye is clearly open, the signal quality appears to be slightly diminished compared to using the asymmetric MZM with the 3 mm phase shifters as presented in Figure 5.25c). This manifests in a higher measured BER of 7.2×10^{-11} and a more pronounced jitter, which is recognized at the falling signal edges. Since both MZM variants are identical except for the ratio between the optical path lengths, a similar device performance is expected. Therefore, any residual difference between the signal qualities must be originated in the device characteristics governed by the operating point.

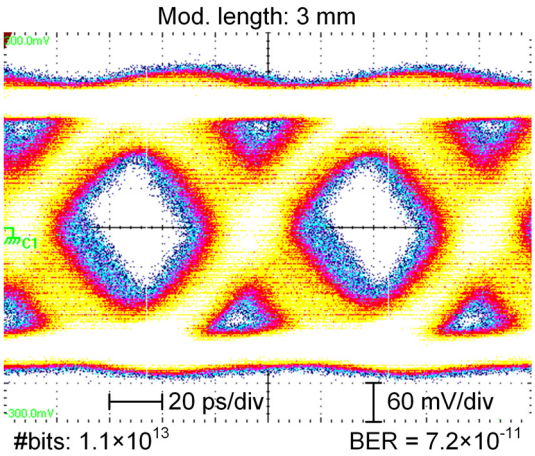

Figure 5.48: Eye pattern and measured BER of an 11.3 Gbit/s NRZ-OOK signal encoded by one of the transmitter unit's symmetric MZM with 3 mm depletion-type pn-phase shifters in push-pull operation.

In contrast to asymmetric MZM, where the operating point can be chosen by the wavelength, its selection in the symmetric MZM exclusively relies on biasing the phase shifters. As elaborated in the context of the device characterization results in this section, the range of possible operating points is limited. This becomes all the more pronounced considering the variances of the steady-state characteristic in Figure 5.46. Hence, the signal quality can only be improved, if the range of possible operating points will be enhanced.

5.9.2 Summary

In this section, the steady-state and dynamic characteristics of the monolithically integrated four-channel transmitter are measured and evaluated. The photonic circuit is based on depletion-type pn-modulators in MZM configuration, MMI and PCG (de-)multiplexers.

The transfer function of the two concatenated (de-)multiplexers is obtained by measuring the transmission spectrum of the entire transmitter while leaving each modulator unbiased. Compared to the reference (de-)multiplexer, the transmission spectrum is red-shifted by 2.1 nm and the FWHM bandwidth of the transmission windows is reduced 69%. The reason is the detuning of the transmission spectra of the input demultiplexer and the output multiplexer due to process tolerances. The impact on the channel spacing, however, is beyond the resolution of the measurement. The insertion loss of the concatenated devices is not evaluated, because the attenuation of the unbiased modulators cannot be separated. The steady-state characteristics of the individual MZM are evaluated based on the normalized transmission as a function of the bias voltage. It is shown that despite the interferometers are designed symmetrically, the MZM geometries are subject to significant variances, which manifest as arbitrary phase offset at 0 V. Given a limited modulation efficiency in consequence of dopant concentrations smaller than targeted in the fabrication process, this restricts the range of operating points and thus impairs the signal quality.

The small-signal characteristics of the transmitter modulator specimens resemble those of the asymmetric MZM with a slab height of 120 nm. This is expected, since they are identical by design except for the difference of the optical path lengths between the two interferometer arms. Consequently, a similar atypical relation between the modulation bandwidth and the bias voltage is observed: the bandwidth is maximum at a bias voltage of 1 V and decreases for higher voltages. Following the reasoning from before, the imperfect realization of metal vias for the 120 nm slab due to fabrication tolerances is most likely the cause for the limitation. Completing the study of the integrated transmitter unit, the back-to-back transmission of an 11.3 Gbit/s NRZ-OOK with one of the symmetric MZM is demonstrated. The device performance appears to be comparable to the asymmetric MZM that utilize the identical 3 mm phase shifters. A measured BER of 7.2×10^{-11} is achieved at the best possible operating point of this device.

6 Packaging and fiber-to-chip coupling

In this chapter, the design approach, the implementation and the characterization of a fiber-to-chip coupling arrangement for grating-coupled SOI waveguides are discussed. Fibers and supporting structures are fastened with UV-curing adhesive bonding. Two different adhesive joint designs are compared by means of evaluating an arrangement using aluminum sockets for a conventional out-of-plane coupling. The evaluation involves the coupling stability of the arrangement over time and the displacement due to changes in the environmental conditions such as ambient temperature and humidity. From this investigation, design rules for subsequent designs of a coupling arrangement are derived.

The construction of a size-reduced coupling arrangement using angle-polished optical fibers is pursued. A process for grinding and polishing standard single-mode fibers for prototypes and small quantities is developed and optimized. The alignment tolerances are studied experimentally and in simulations, and the coupling stability over time is evaluated in a long-term measurement. Finally, the penalty on the coupling efficiency due to changes in environmental conditions are evaluated by measurements in a climate testing cabinet.

6.1 Out-of-plane fiber-to-chip coupling assembly

6.1.1 Joint design

Despite the availability of adhesives with minimum shrinkage and hygroscopic expansion, the design of the adhesive joint has a significant influence on the stability of the fiber-to-chip coupling arrangement. Figure 6.1 represents the schematics of two different realizations. Figure 6.1a) shows a conventional joint, where a component is bonded to the substrate with an adhesive layer as homogeneous as possible. The component has no direct contact to the substrate, that is, beyond adhesion, the layer acts as a separator. Therefore, shrinkage of the adhesive directly translates to a relative displacement of the component. Another approach depicted in Figure 6.1b) involves the structuring of the bottom side of the component, which forms a regular pattern of notches. The adhesive is applied to the corners of the remaining teeth and the substrate. That enables a curing with UV-radiation, even if both the component and the substrate are opaque. After curing, the bond is established around the sides of the teeth, while their bottoms remain in direct contact to the substrate. Thus, the expansion or contraction of the adhesive volume occurs equally at every bonding spot of the arrangement. As the result, a global displacement is avoided, because the contributions of all spots cancel out.

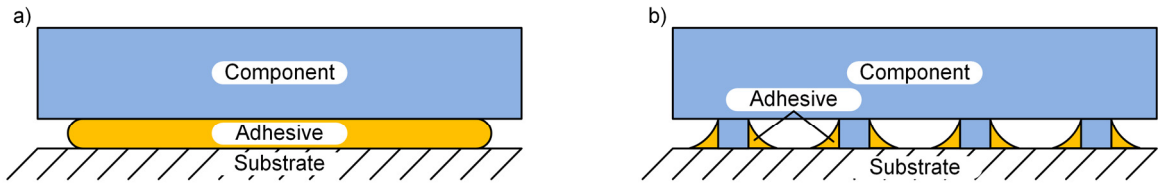

Figure 6.1: Two different concepts for the adhesive bonding of a component on a substrate. In a), a homogeneous separation layer is formed by the adhesive, while in b) the adhesive is applied to the corners of elevation sockets and the substrate.

6.1.2 Fiber socket design

In order to facilitate the positioning and fixation at a given orientation, a socket is required to mount an optical fiber on and to manipulate its position by precision alignment equipment. Since the coupling to a grating coupler is considered, the fiber is aligned at a small angle with respect to the grating normal. The finite bending radius of the fiber and the operability of the socket positioning govern the minimum size of the arrangement. In addition, the distance between the fiber facet and the grating must be variable to some extent. Finally, if the coupling of more than one fiber is required, the sockets must not obstruct each other. The actual concept is designed in order to establish the permanent coupling of a silicon electro-optic modulator, which requires an input and an output optical fiber.

In Figure 6.2a), a model of an out-of-plane fiber-to-chip coupling arrangement is depicted. The photonic chip is bonded to the substrate with a thermally curing adhesive. The optical fibers are suspended in metal ferrules, which rest in a groove of the respective socket. That way, the alignment of the fibers in z-direction remains adjustable, until fastening in the ferrule. The grooves are located at the side of the sockets, which avoids visual obstruction of the fiber tips upon alignment. The front side of the socket is milled at the appropriate angle matching the coupling angle of the involved grating couplers on the photonic chip. The bottom side of the sockets is structured as suggested above. Figure 6.2b) reveals the regular pattern of the notches and teeth along the socket's rim. In Figure 6.2c), an isometric view is presented including the essential dimensions. The sockets are manufactured from an AlMg3 aluminum alloy. Their relatively large size compared to the photonic chip is chosen to facilitate the handling and positioning with an alignment stage using vacuum plates. The substrate for the assembly is a *CeramTec Rubalit* alumina ceramic tile with a linear coefficient of thermal expansion (CTE) of 6.8×10^{-6} K^{-1}.

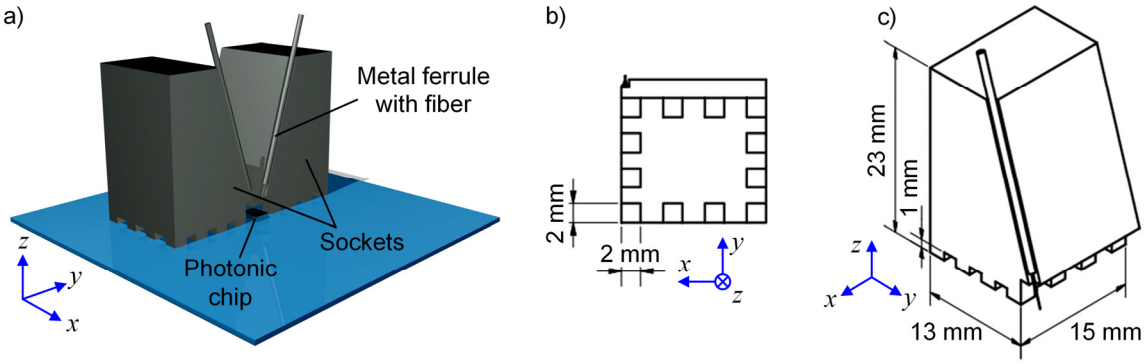

Figure 6.2: Overview of the concept for an out-of-plane fiber-to-chip coupling arrangement. a) An optical fiber is mounted on each of the two sockets, which are aligned to achieve optimum coupling efficiency. b) Bottom view of one of the mounting sockets, revealing the pattern and dimensions of the notches along its rim. c) Isometric view of one of the sockets including dimensions.

A second set of sockets similar to those in Figure 6.2 is manufactured. In contrast to the initial design, the bottom surface is flat-polished, to provide for a homogenous adhesion layer between the sockets and the substrate. An overview including an excerpt of the technical drawing is presented in Figure 6.3. The assembly of the coupling arrangement as shown in Figure 6.3a) is identical to the initial design in Figure 6.2a). However, as indicated in Figure 6.3b), the dimensions of the sockets are slightly reduced. A glass tile is used as a substrate for the coupling arrangement for several reasons: for one, the glass tile provides sufficient rigidity for a stable arrangement and can be bonded reliably with most of the commercially available adhesives. Secondly, similar to alumina, glass has a small CTE in the range of 9×10^{-6} K^{-1}, which limits the susceptibility of the assembly to thermal stress of the substrate. Lastly, glass is

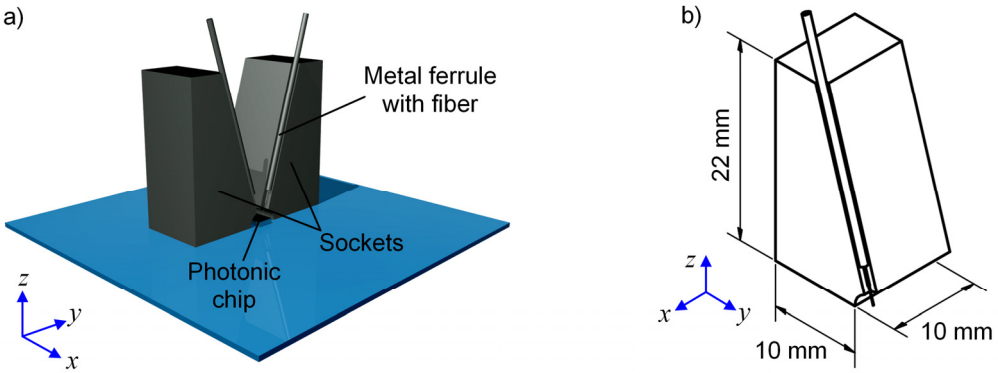

Figure 6.3: Overview of an alternative design of a socket for an out-of-plane fiber-to-chip coupling arrangement. The assembly of the arrangement a) is identical to the initial design presented in Figure 6.2. b) Excerpt of the technical drawing of a socket with flat-polished bottom surface.

transparent for UV-radiation. This allows for curing the adhesive by irradiating the substrate from the bottom during the assembly process. Hence, the photonic chip can be bonded to the substrate using the same adhesive as for the fixation of the sockets.

6.1.3 Alignment and assembly procedure

A photograph of the alignment setup is presented in Figure 6.4. The sample holder, which essentially is a vacuum plate, holds the substrate tile carrying the photonic test chip. To each of the sockets, a ferrule with an optical fiber is bonded. The fiber sockets are temporarily adhered to handling stages by specially designed vacuum plates to facilitate the manipulation of the position in x- and y-direction. The stages, which are not shown in the photograph, consist of stepper motors (*Newport* MFA Series) and piezo-driven handling stages (*PI* NanoCube). A camera with a magnifying lens is used to enable a side view of the area where the fibers and the test chip surface meet. That simplifies the minimization of the gap between the fiber facet and the chip surface during the alignment process. The assembly relies on active alignment, that is, the optical power coupled to and from the test chip is monitored continuously during the process. For the measurement, an *Agilent* 81689A tunable laser source, a manual polarization controller, and an optical head and interface (*Agilent* 81623B and 81618A) are used.

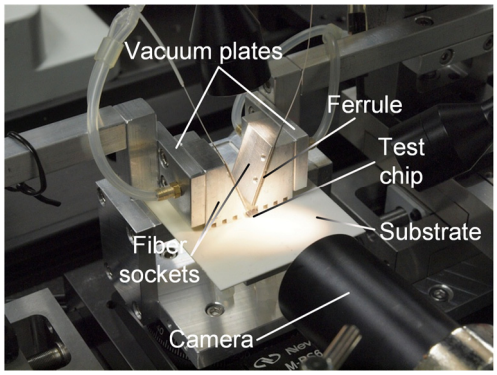

Figure 6.4: Photograph of the alignment setup used for the out-of-plane fiber-to-chip coupling arrangement. The essential components required for the procedure are indicated.

A multi-component photonic test chip [183] is used for the assembly. Its non-uniform focusing grating couplers [20] have a coupling angle of 17° at the central wavelength 1550 nm. Since all coupling arrangements are assembled with the same test chip, the front side of both the regularly-notched and flat sockets are milled according to that angle.

At first, the photonic chip is bonded to the substrate. The adhesive is chosen depending on the used material. In case of the glass substrate, an UV-curing adhesive identical to that used for the fixation of the fiber sockets is used. In contrast, a thermally curing adhesive is for bonding the test chip on the alumina ceramic, because the adhesion layer interface cannot be UV-irradiated. The second step is the insertion of the optical fibers in the ferrules and the cleaving of the facets. The ferrules are bonded to the grooves in the fiber sockets with the same UV-curing adhesive used subsequently in the process. The assembly of the coupling arrangement with regularly-notched and flat sockets are almost identical.

Prior to the actual alignment of the regularly-notched sockets, they are positioned coarsely. In the case of the regularly-notched sockets, this is useful to prevent the adhesive from getting under the teeth during the motion of the sockets in the course of the fine alignment. Then, the adhesive is applied to the contact spots for the bonding in the corners between the teeth and the substrate. If the flat sockets are used, the adhesive is applied to the flatly-polished bottom of the coupling sockets before the coarse alignment. The actual positioning in the chip plane (x- and y-direction) is carried out using the positioning stages. The vertical z-axis of the alignment stages is used to bring the vacuum plates to the same level of the coupling sockets.

The distance between the fiber facet and the grating is adjusted manually and examined using the side-view camera. The highest coupling efficiency is achieved for a minimum clearance between the fiber facet and the grating coupler. Once the position of the socket is optimized to maximum coupling efficiency, the adhesive is cured by irradiating the bonding spots with an UV-light source (*Dymax* BlueWave 50). The regularly-notched adhesion interface can be irradiated from all sides while the flat polished structure has to be irradiated from the bottom through the transparent glass substrate.

6.1.4 Fiber displacement tolerance

The displacement may be quantified by analyzing the coupling efficiency of an SMF and the grating coupler as a function of the fiber position. To maintain consistency to the following analysis, the same photonic test chip is used. Two SMF are positioned for optimum coupling of a test waveguide on the photonic chip. While one of the fibers is deliberately displaced in discrete steps of the piezo actuator, the other one is optimized in every iteration. The piezo controller unit measures the moving distance. The characterization is repeated consecutively for the displacement lateral and parallel to the waveguide propagation direction. The results are presented in Figure 6.5, which shows the normalized coupling efficiency as a function of the fiber displacement from the optimum position. Open symbols represent the measured coupling efficiency and the solid lines are Gaussian-shaped fit curves.

Figure 6.5a) shows the dependency of the coupling efficiency on a lateral displacement. The fit curve excellently agrees with the data points. In Figure 6.5b) the impact of a parallel fiber displacement is shown. A displacement in negative direction corresponds to a forward motion of the fiber from the optimum towards the waveguide. The progression of the data points likewise resembles for the most part a Gaussian, with a slightly larger width compared to Figure 6.5a). At a displacement beyond +5 µm, the efficiency tends to decrease less intensely than the Gaussian dictates. In essence, the diagrams reflect the overlap between the fundamental mode of the fiber and the mode of the grating coupler. The lateral displacement characteristic suggests conformity between both modes. The utilization of a non-uniform grating appears to achieve a good matching of the mode shapes also in the parallel orientation. However, the focusing properties of the grating coupler slightly enhances the extent of the grating coupler mode towards the outermost grating tooth. A displacement of 4.5 µm lateral or 5.5 µm parallel to the on-chip waveguide propagation direction yields a penalty of 3 dB. Using these relations of fiber displacement and the associated attenuation, the actual offset from optimum can be estimated based on the measured coupling efficiency.

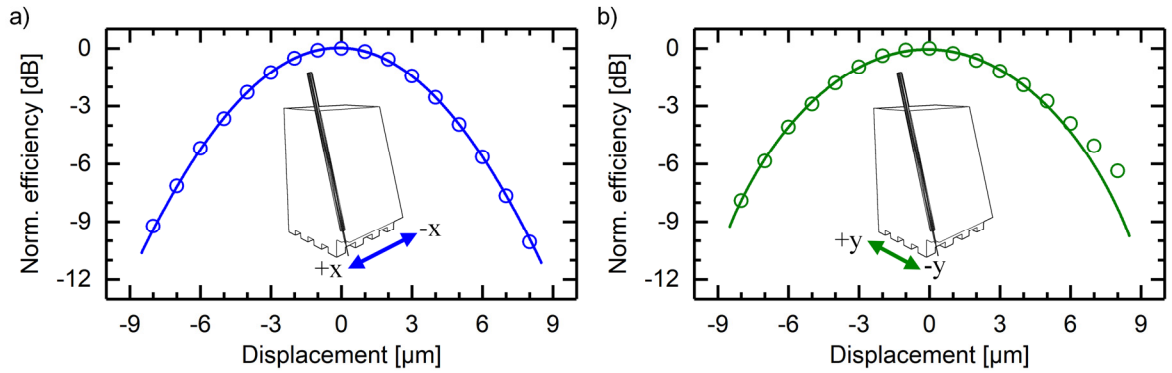

Figure 6.5: Normalized coupling efficiency as a function of the fiber displacement a) lateral and b) parallel to the on-chip waveguide propagation direction from the optimum position.

6.1.5 Joint design evaluation

In order to evaluate the suitability of the joint designs to guarantee a stable fiber-to-chip coupling arrangement, the coupling efficiency over time from the moment of curing the adhesive is observed. The total insertion loss of the grating-coupled test structure on the photonic chip is 16 dB. Due to the potential shrinkage of the adhesive during and after the curing procedure, a displacement of the fiber

sockets and thus a deterioration of the coupling efficiency may occur. For the evaluation, a coupling arrangement with two fibers and a photonic test chip is assembled. Consequently, no distinction is made from which of the two coupling sockets a potential displacement stems from.

The duration of the measurements is given by the time, at which an unambiguous tendency of the coupling efficiency is observed. Thus, the durations of the individual measurements may differ considerably. The coupling efficiency is normalized to the maximum measured transmission, which is typically achieved at the beginning of the measurement.

To suppress potential additional displacement due to a change in ambient conditions, the coupling assemblies are transferred to a climate testing cabinet (*Weiss* Type WK3-340/40) for the measurement to ensure stabilized temperature and humidity. Both are chosen so that the ambient conditions in the testing cabinet are similar to those during the assembly. Thus, the samples do not suffer an abrupt change, which may compromise the alignment accuracy.

At first, the stability of the fiber-to-chip coupling assembly with the regularly-notched sockets and the alumina substrate is analyzed in the climate testing cabinet. The utilized adhesives are two variants of *Dymax Multi-Cure* 921. According to the product specifications, the uncured properties are similar except for the viscosity (921-VT: 7.5×10^2 cP, 921-GEL: 2.5×10^4 cP). The adhesives are applied to the bonding spots in the corners between the teeth and the substrate. The coupling penalty after the curing is 1.5 dB. The subsequent measurement of the coupling efficiency begins immediately after assembly, curing and the transfer to the climate testing cabinet. In Figure 6.6, the results for both adhesives are presented. They are representative also for assemblies using other adhesive specimens.

Figure 6.6a) shows the normalized coupling efficiency as a function of the duration since the assembly using the adhesive 921-VT. A maximum occurs after approximately 10 hours after which the assembly appears to be steadying. However, after 24 hours, a continuous decrease of the efficiency is observed. The experiment is aborted after 96 hours, where the penalty on the coupling efficiency is 1.3 dB. Assuming an even displacement of both coupling sockets and equal impact of the x- and y-direction, the offset per socket is estimated to 1.6 µm in each direction according to the considerations above. The kink of the efficiency after 68 hours occurs due to a manual adjustment of the polarization of the field incident to the input grating coupler.

In Figure 6.6b), the progression of the normalized coupling efficiency since the assembly using the adhesive 921-GEL is shown. The coupling efficiency decreases strongly right from the beginning of the measurement. Therefore, the experiment is terminated after 18 hours, with a penalty on the coupling of

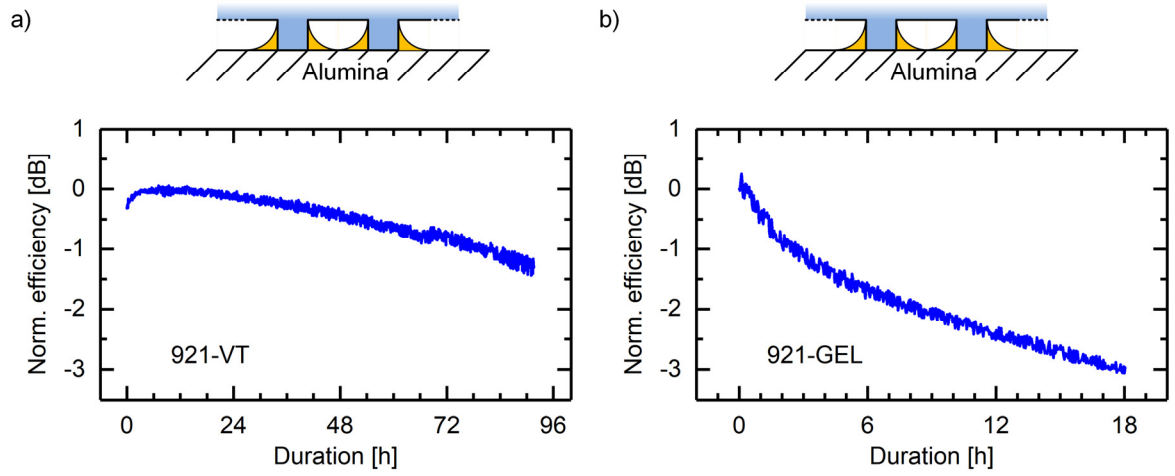

Figure 6.6: Evaluation of a fiber-to-chip coupling assemblies using aluminum sockets with a structured bottom surface. The adhesive is applied to the corners between structured teeth and the substrate. The diagrams show the progression of the coupling efficiency over time immediately after assembly for two variants of Dymax 921 with different viscosities. a) Dymax Multi-Cure 921-VT (7.5×10^2 cP), b) Dymax Multi-Cure 921-GEL (2.5×10^4 cP).

3 dB. Under the assumption of an even displacement in both directions, this corresponds to an offset per socket of 2.4 µm in x-direction and 2.6 µm in y-direction.

Although the results are not shown here, the experiments are repeated using other adhesives. Among others, these are *Dymax Multi-Cure* 6-621-GEL and *Panacol Vitralit* 4731-VT. While maintaining the assembly procedure, no correlation between the type of adhesive and the stability of the coupling can be determined. Thus, the process is modified iteratively. The most important changes are summarized in the following.

With a non-negligible probability, any of the adhesives can get under the teeth of the regularly-notched sockets. Since both the coupling sockets and the alumina substrate are opaque to UV-radiation, this fraction will not cure upon irradiation. Hence, it remains in an unknown state exhibiting non-predictable properties. Consequently, the above assembly is repeated using a glass substrate, which allows for the complete curing of the adhesive at any location at the assembly. Furthermore, the photonic test chip can be fastened with the same adhesive. No significant change of the stability is observed after the modification. However, glass substrates are used subsequently to eliminate the aforementioned issue to compromise the stability of the assemblies. Moreover, they are a prerequisite for the flat socket assembly.

Apparently, the displacement of the assembly components occurs dominantly due to a volume change of the adhesive. Therefore, a reduction of the applied amount is expected to yield a diminished displacement after curing. Moreover, the displacement upon curing due to shrinkage is presumed to reduce likewise. On the other hand, a minimum amount of adhesive is required to maintain mechanical stability.

To allow for a comparison, the coupling arrangement with the regularly-notched sockets is assembled using the adhesive 921-VT. In contrast to the initial assembly (see Figure 6.6a)), the amount of adhesive is reduced significantly. Since no suitable dispenser is available for the study, a minimum amount is applied manually. The coupling penalty after curing reduces to 0.5 dB. A representative result of the subsequent measurement of the coupling stability is shown in Figure 6.7a). The diagram shows the measured coupling efficiency over time since the assembly. Over the duration of almost 96 hours, a decrease of the coupling efficiency is still observed. However, the rate is significantly smaller compared to the original assembly. Moreover, the result can be reproduced for the other adhesives. In summary, the reduced deterioration of the coupling efficiency over time implies a reduced displacement of the fibers. Therefore, the hypothesis, after which a minimization of the amount of adhesive reduces the

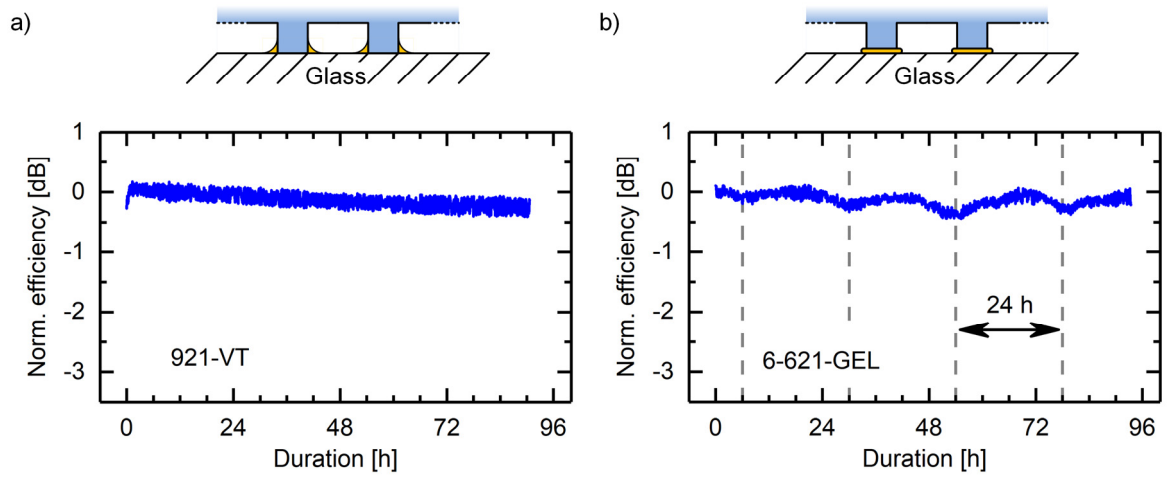

Figure 6.7: Evaluation of fiber-to-chip coupling assemblies using aluminum sockets with a structured bottom surface and a significantly reduced amount of adhesive. Coupling efficiency over time directly after the assembly, if the adhesive is applied a) to the corners between structured teeth and the substrate or b) between bottom faces of the teeth and the substrate. A periodicity with a period of 24 hours is indicated by the vertical dashed lines.

displacement, appears to be verified. However, a residual non-negligible degradation of the coupling efficiency over time remains.

Since the assembly is based on a glass substrate, any adhesive applied between the bottom of the coupling sockets and the substrate can be cured by UV-irradiation. In order to estimate the suitability of a joint design utilizing a flat adhesion interface, the adhesive is applied deliberately only at the teeth surfaces. The schematic is shown in Figure 6.7b). Curing is possible by the irradiation of the interfaces from the bottom side of the glass substrate. Because of the limited availability of the climate testing cabinet, the measurement of the coupling stability is conducted in non-stabilized environment. The result is also presented in the diagram in Figure 6.7b), which shows the coupling efficiency as a function of the duration since the assembly. Despite a fluctuation of the coupling efficiency, no significant change is observed during the period of almost four days. Apparently, the fluctuation follows a periodicity of 24 hours. Therefore, and by taking the hygroscopic properties of acrylate-based adhesives into account, it is attributed to the change of ambient conditions in the course of the days. Despite the periodic fluctuation of the coupling efficiency, this assembly appears to have the best stability compared to the other designs discussed above. Therefore, a further improvement is expected by extending the flat adhesion interfaces to the entire bottom surface of the socket. Hence, an assembly using the flat sockets is favored for the continuing study.

Finally, coupling assemblies that rely on flatly-polished sockets are analyzed. Compared to using regularly-notched sockets (Figure 6.7b)), the applied amount of any adhesive can be reduced further. At the same time, the stability of the assembly is significantly improved. Primarily due to the availability and additional slight benefits considering linear shrinkage and water absorption, the adhesive *Dymax* 921-VT is omitted in favor of *Panacol Vitralit* 4731-VT. The latter is also used for the study on the impact of ambient conditions during the assembly validation discussed in section 6.1.6, which is why the coupling efficiency since the assembly using this adhesive is presented here in order to get a complete picture. However, the difference of the properties does not have a severe impact on the coupling stability. The penalty on the coupling efficiency upon the curing procedure due to adhesive shrinkage can be reduced to 0.2 dB for the entire assembly. Figure 6.8 shows representative results of the coupling efficiency as a function of the duration since the assembly for the adhesives 4731-VT and 6-621-GEL. Both assemblies do not exhibit a significant degradation of the coupling efficiency over a duration of four days. The results can be reproduced for assemblies where the other adhesives are applied.

In summary, a fiber-to-chip coupling assembly with regularly-notched coupling sockets does not provide a satisfying stability. No evidence is found that the sum of local expansion or contraction of the adhesive at the numerous bonding spots is capable of counteracting a global displacement. The dominant

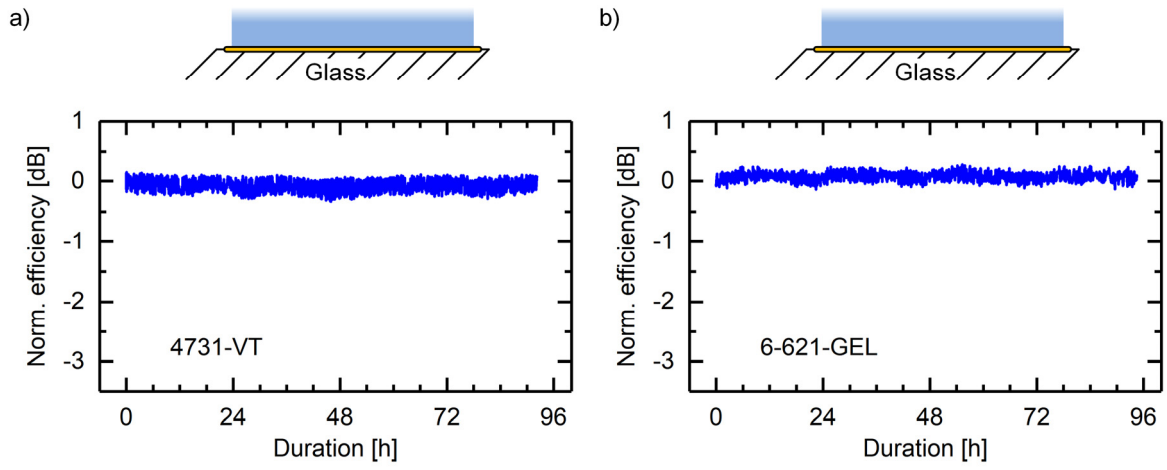

Figure 6.8: Evaluation of a fiber-to-chip coupling arrangement using aluminum sockets with a flatly-polished bottom surface. The diagrams show the progression of the coupling efficiency over time for two different adhesives directly after assembly. a) Panacol Vitralit 4731-VT, b) Dymax Multi-Cure 6-621-GEL.

reason appears to be the relatively large amount of adhesive material required for this method and the uneven distribution among the bonding spots. Moreover, the direct accessibility of the bonding spots for the UV-radiation does not provide a significant simplification of the process. In contrast, using flatly-polished sockets appears to yield a stable coupling arrangement. This is mainly due to the homogenous interface and the minimized amount of adhesive. Furthermore, the effective area of the adhesion interface is significantly larger compared to the regularly-notched structure, which eventually yields an improved stability of the assembly. Hence, the fiber-to-chip coupling assembly with flatly-polished coupling sockets based on a glass substrate is considered the final out-of-plane assembly. A photograph of the complete assembly is presented in Figure 6.9. In order to verify its reliability, the sensitivity of the coupling efficiency upon a variation of ambient conditions is investigated in the next section.

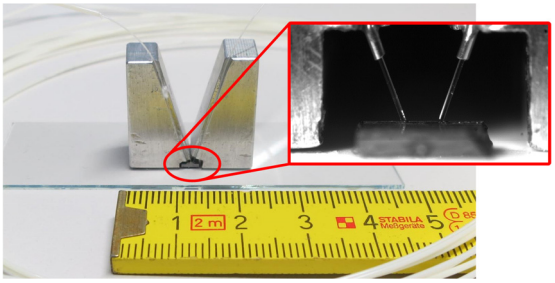

Figure 6.9: Photograph of the complete fiber-to-chip coupling assembly using aluminum sockets with a flat-polished bottom surface. The inset shows a close-up of the fibers aligned to the photonic test chip.

6.1.6 Assembly validation

In this section, the impact of ambient conditions on the stability of the fiber-to-chip coupling assembly with flatly-polished coupling sockets based on a glass substrate is investigated. In order to assess the influence, studies of the coupling stability with respect to ambient temperature and humidity are performed. Furthermore, the long-term stability is evaluated. In part, the results have already been published in [135].

The impacts of changing ambient temperature and humidity can be investigated separately using the climate testing cabinet. As indicated above, humidity is a critical parameter, since acrylate-based adhesives tend to behave hygroscopically. Consequently, the adhesive and thus the bonding interface changes in volume, which may result in a fiber displacement and thus in increased coupling loss. In contrast, a temperature change causes thermal expansion or contraction of the involved components. Due to different CTE, this may induce strain to the assembly, which likewise results in a displacement of the fiber alignment.

The measurements of the coupling efficiency with respect to ambient temperature and humidity are carried out with a grating-coupled test structure on a test chip similar to the previous studies. The applied adhesive is *Panacol Vitralit* 4731-VT. Figure 6.10a) shows a representative result of the coupling efficiency as a function of the relative humidity (RH) in the range of 30%, which is similar to the humidity during assembly, to 80% RH. The ambient temperature is 20 °C. The humidity is increased or decreased at a rate of 2% RH per hour. Thus, the assembly is given ample time to adapt and stabilize. The black curve in the diagram shows the progressions of the coupling efficiency for increasing the humidity, while the red curve represents the measurement for decreasing humidity. The accordingly colored arrows emphasize the mapping. The efficiency is normalized to the measured value at the beginning of the measurement at 30% RH. This is considered the optimum alignment. With rising humidity, a decrease of the coupling efficiency is observed, which saturates at 60% RH. Above 70% RH, the decrease continues. The maximum penalty on the coupling efficiency is 0.2 dB at 80% RH. The progression is almost reproduced for decreasing humidity from 80% RH back to 30% RH. Consequently, the fiber displacement is considered fully reversible.

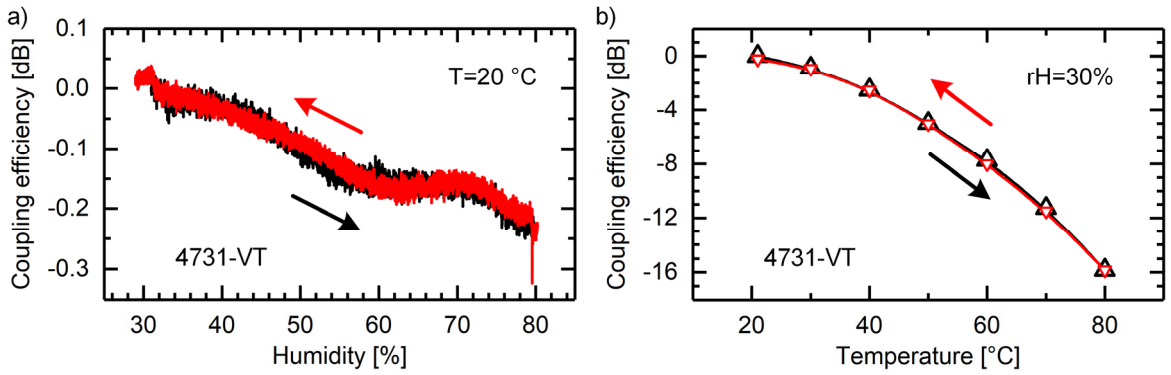

Figure 6.10: Impact of ambient conditions on a fiber-to-chip coupling assembly using aluminum sockets with a flatly-polished bottom surface. Coupling efficiency as a function of a) relative humidity and b) ambient temperature. The applied adhesive is Panacol Vitralit 4731-VT. The black curves represent the coupling efficiency during the increase of humidity and temperature, respectively, while the red curves show the progress during the subsequent decrease.

In Figure 6.10b), the dependency of the coupling efficiency on ambient temperature from approximately 20 °C to 80 °C at a relative humidity of 30% is shown. The efficiency is measured at each temperature increment only after it has stabilized. The triangular symbols represent the measured values, which are connected by solid lines. The coupling efficiency is normalized to the initial value around 20°C. In a first approximation, the progression resembles a Gaussian shape, which again reveals the mode field of the grating coupler upon displacement. A maximum loss of 16 dB at 80 °C compared to the optimum is recognized. Similar to changing humidity, the displacement due to temperature drift is fully reversible.

The study shows, that the coupling efficiency of the fiber-to-chip coupling assembly shifts upon a change in ambient conditions. Apparently, it is only weakly dependent on the humidity, since the degradation is significantly smaller than 1 dB within the measured humidity range. In contrast, the impact of a temperature shift is severe. However, considering the CTE of aluminum alloys in the range of 23×10^{-6} K^{-1}, this is attributed to the thermal expansion of the aluminum sockets, which eventually masks any change related to the adhesive. Hence, a comprehensive assessment of the impact of temperature on the adhesive is not possible.

In order to investigate the long-term stability of the fiber-to-chip coupling assembly, the coupling efficiency in non-stabilized environment is observed over a period of more than two years. In uneven intervals, the coupling efficiency is measured over a duration of several hours. Consequently, the measurement takes into account potential fluctuation during the course of a day. The result is presented in Figure 6.11. The diagram shows the coupling efficiency normalized to the highest measured value as a function of the elapsed time since the assembly. The open symbols represent the mean values of the measured coupling efficiency.

Since the data is not acquired continuously, the fibers are connected to the laser source and power meter and the polarization is adjusted before each measurement. This is the dominating source of uncertainty. The residual scattering of the data points is due to fluctuations of ambient conditions. The ratio between the highest and the lowest value is 1.4 dB. No significant deterioration of the coupling efficiency is observed over the entire duration. Therefore, the assembly is considered long-term stable. In conclusion, the flatly-polished adhesion interface is the reliable joint design, which is a finding congruent with the literature [184].

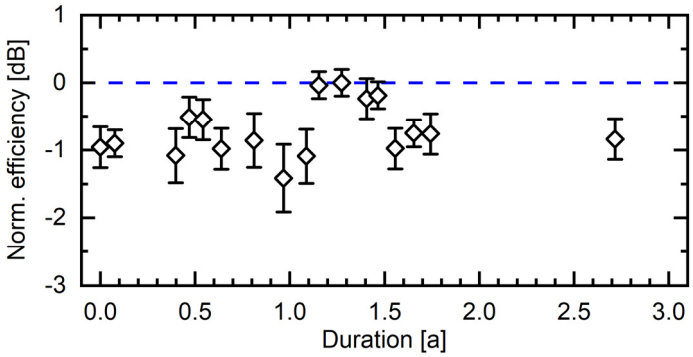

Figure 6.11: Result of the long-term investigation of the fiber-to-chip coupling arrangement using aluminum sockets with a flat-polished bottom surface. The diagram shows the coupling efficiency normalized to the highest measured value over a period of more than two years.

6.2 In-plane fiber-to-chip coupling with angle-polished fibers

As discussed in the previous section, an out-of-plane vertical fiber-to-chip coupling assembly provides reliable coupling stability. However, due to the large footprint, it is impractical to build compact devices and therefore cannot be considered part of a packaging process. Therefore, the development of a low-profile approach using angle-polished optical fibers as described in section 3.7.2 is presented and its reliability evaluated.

A schematic of the assembly showing a photonic chip and one optical fiber is presented in Figure 6.12. An optical fiber is mounted on a standard glass v-groove chip. A matching glass lid fastens the fiber in the groove through adhesive bonding. The fiber facet protrudes from the v-groove chip's front, so that it can reach the targeted grating coupler on the photonic chip. The primary fiber coating and the buffer layer are removed in order to fit the fiber into the v-groove and to reduce the amount of material that may deform upon temperature and humidity change.

Based on the results of the successful out-of-plane fiber-to-chip coupling assembly, all components are fixed with the UV-curing adhesive *Panacol Vitralit* 4731-VT. The description of the fabrication and the assembly as well as the results of the assembly validation are published in [185].

6.2.1 Fabrication and assembly procedure

This section is devoted to the fabrication of the angle-polished fibers, the mounting to v-groove chips and the complete assembly of the fiber-to-chip coupling arrangement.

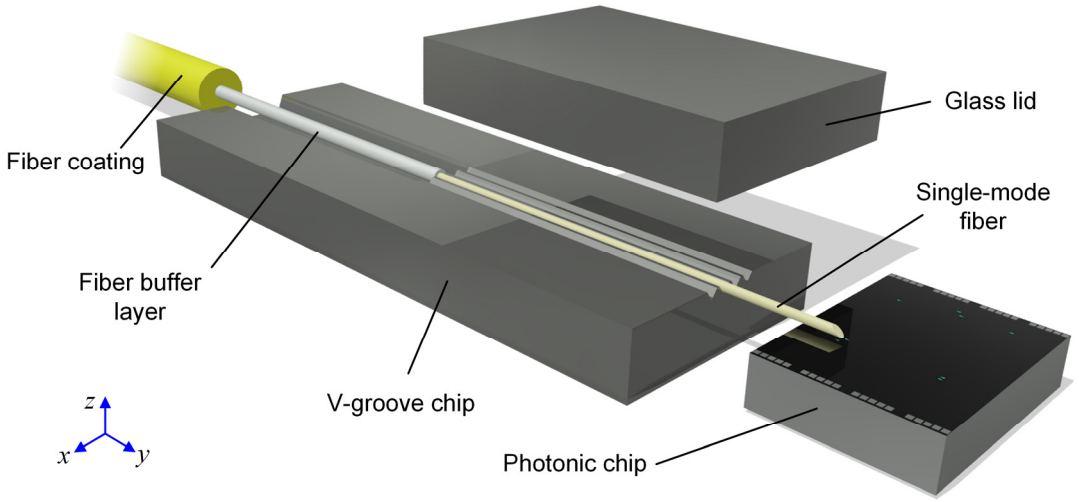

Figure 6.12: Three-dimensional schematic of an angle-polished single-mode fiber mounted on a v-groove chip.

The polishing angle is calculated using the equations (3.8) and (3.9). The refractive index n_1 of the fiber cladding is obtained from the fiber data sheet [15] and is 1.44681. The surrounding medium is air and thus $n_2 = 1$. The photonic test chip is another specimen of the multi-component chip [183] used for the out-of-plane assembly. The focusing non-uniform grating couplers [20] have a coupling angle of 17° at the central wavelength 1550 nm. The equations thus yield a grinding angle θ of 39.2°. The statistical evaluation of grinded and polished fibers yields a systematic error of -1.5° due to alignment tolerances, by which the grinding angle is adjusted.

A rotating grinding machine (*Struers LaboPo*l-5) is utilized for grinding and polishing the fiber facets. A specially designed fiber holder produced by a *Makerbot* 3D-printer enables the handling of up to four fibers for the grinding procedure. A photograph is shown in Figure 6.13a). The device consists of a stainless steel base plate, an exchangeable socket, a handle and an adjustable cantilever. The cantilever carries a ceramic tile, where the fibers are fixed by a solvent adhesive in v-grooves to provide for a stable mounting. The ceramic tile is fastened on the cantilever with a clamp and thus is easily exchangeable. A close-up photograph is presented in Figure 6.13b). The fiber holder is placed at the edge of the polishing wheel. Upon starting the process, the cantilever is lowered, so that only the fiber tips touch the grinding surface. The cantilever is mounted on the long side of the triangular socket by a hinge. The socket serves as a gauge to set the polishing angle and is selected according to requirements. The handle facilitates the manual positioning of the device. The base plate provides for mass and stability.

The quality of the polished fiber's end face is largely dependent on the selection of the abrasives. At the beginning of the process, the fiber end face is coarsely shaped by equipping the polishing wheel with abrasive paper with a grit size of 3200. Subsequently, the residual surface roughness is smoothed incrementally by applying diamond suspensions to the polishing wheel with a grain size of 9 µm, 3 µm and 1 µm. Optimum results are obtained for a polishing duration of 8 minutes per step at a rotation speed of 175 to 200 rounds per minute.

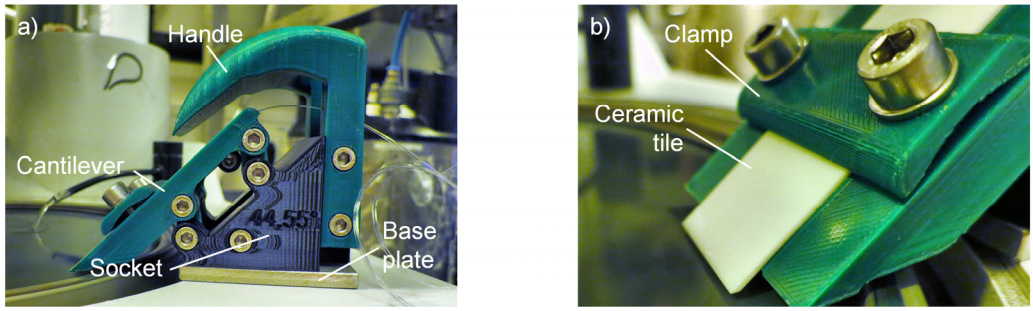

Figure 6.13: Specially designed holder for grinding and polishing up to four fiber specimens. a) Side view with emphasize on the exchangeable socket to select the polishing angle. b) Detail photograph of the cantilever with mounted ceramic tile carrying the fibers.

Prior to mounting the fibers on the v-groove chips, the rotation with respect to the fiber axis (rotation angle θ_{rot}, see section 3.7.4) is optimized. The elevation angle θ_{elev} is already taken into account by optimizing the polishing angle θ of the fiber. The supplemental azimuthal tilt θ_{azim} is optimized at later stage of the assembly. The absolute azimuthal tilt is of minor importance due to the alignment tolerances provided by using the grating couplers. However, it does affect the polarization alignment of the optical field with respect to the grating coupler.

The fiber rotation is optimized for maximum coupling efficiency using the reference to a grating-coupled test waveguide at the target wavelength of 1550 nm. The fiber rotation is manipulated using a customized mechanical fiber rotator, of which a photograph is shown in Figure 6.14a). The accuracy requirements allow for a manual adjustment with a micrometer screw. A ridge that is level with the axis

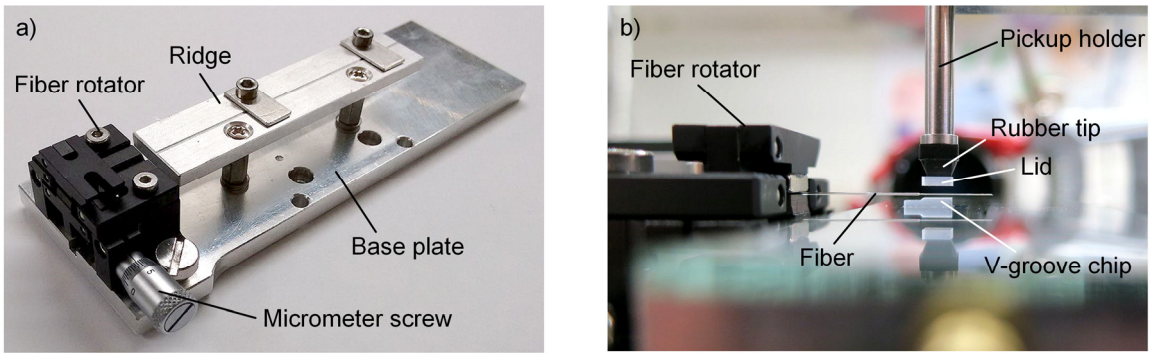

Figure 6.14: a) Manual handling stage to adjust the rotation of an optical fiber with respect to its axis. b) Detail photograph of the fiber alignment setup, showing the fiber rotator, the vacuum gripper and the v-groove chip.

of the rotator supports the fiber upon the alignment. Both the rotator and the ridge are mounted to a stabilizing base plate. The entire assembly is mounted on a xyz-translation stage.

Subsequently to the rotation adjustment, the fiber is fastened on the v-groove chip. The situation is visualized in the photograph in Figure 6.14b). At first, the chip is positioned manually under the fiber, which then is lowered until it rests in the targeted groove. After that, the adhesive is applied to the spot. The glass lid is attached on top of the v-groove chip using an alignment setup with a vacuum pickup holder and a rubber tip matching the dimensions of the lid. The setup is also used for the final assembly and is described in detail in the following paragraph. Finally, the adhesive is cured by UV-irradiation and the fiber, the v-groove chip and the lid constitute a building block.

In order to demonstrate the feasibility of the permanent coupling using angle-polished fibers, a fiber-to-chip coupling assembly for an electro-optic modulator embedded on the photonic chip used during the process development is presented. Photographs of the alignment setup are shown in Figure 6.15. The setup has already been used in part for the fastening of an optical fiber on the v-groove chip, as described above. It is based on the same equipment used for the analysis of the joint design in section 6.1. A photograph of one of the utilized translation stages consisting of stepper motors (Newport MFA Series) for the coarse alignment and a piezo-driven handling stage (*PI* NanoCube) is presented in Figure 6.15a). A vacuum pick-up holder facilitates the handling of the fibers. As shown in Figure 6.15b), it is mounted on a customized cantilever and connected to a vacuum hose with a PVC fitting. A detailed view of the pickup holder is shown in Figure 6.15c). It is a custom-built model of the vendor *MicroMechanics*. Automated pick-and-place machines for microelectronics use similar components. The rubber tip is chosen according to the dimensions of the handled component and enables the contact to the pickup holder.

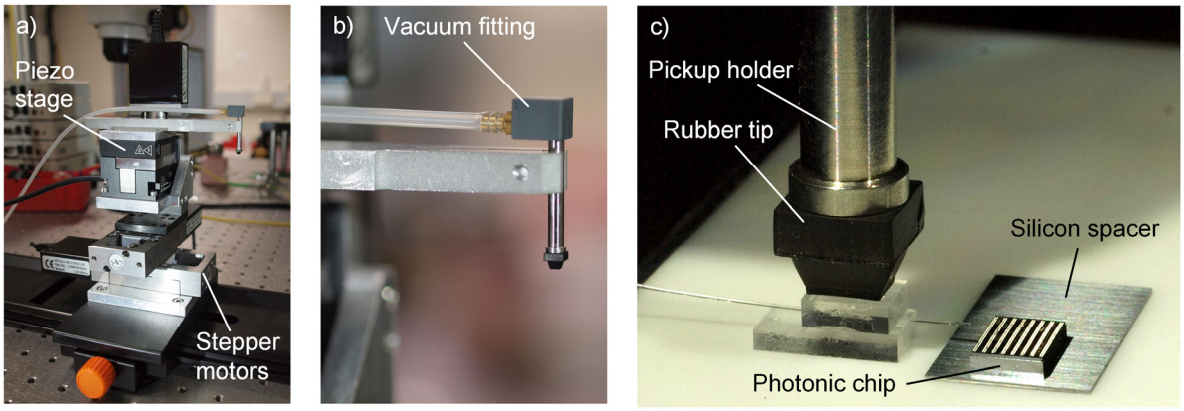

Figure 6.15: Positioning equipment for the alignment process. a) Positioning stage consisting of stepper motors and piezo-driven handling stages. b) Detail picture of the cantilever tip with a customized vacuum pick-up holder. c) Close-up photograph of the pick-up holder that is equipped with an appropriate rubber tip.

The steps of the assembly are described chronologically below. At first, the photonic chip is bonded to the substrate. In order to minimize the clearance between the fiber cladding and the surface of the photonic chip, a spacer is required in most cases. This is equivalent to the minimization of the gap size w_g according to Figure 3.5 on page 27. In the present study, the distance between the photonic chip surface and the fiber cladding is approximately 210 µm. That makes a net distance from the fiber core to the grating coupler of approximately 270 µm. According to equation (2.12), this yields a penalty on the coupling efficiency of 8.3 dB. Therefore, the chip is elevated by a silicon spacer in order to minimize w_g. The spacer is a tile of a silicon wafer, which is ground to the appropriate thickness. Being opaque for UV-radiation, the photonic chip is bonded to the top of the spacer with a heat-curing adhesive. In this study, *SPI Supplies Crystal Bond* 509 is used. The adhesive for bonding the spacer can be selected according to the substrate. Here, a glass substrate is used, which allows for using the same UV-curing adhesive as for bonding the v-groove chips The situation is also shown in Figure 6.15c).

In the next step, the v-groove chips carrying the optical fibers are coarsely aligned and a small amount of adhesive is applied to the interface between their bottom and the substrate. Once the alignment is optimized to maximum coupling efficiency, the adhesive at the respective interface is cured by irradiation with a *Dymax BlueWave* 50 UV light source from above through the transparent v-groove chips. A penalty on the coupling efficiency due to contraction of the adhesive during the curing process is not observed. The mechanical stability of the assembly is improved by also bonding the fibers to the chip surface. The current assembly allows for adhesion spots sufficiently far away from the grating couplers. Thus, no adhesive gets between the fiber cladding and the grating coupler, which otherwise would change the coupling angle due to a different refractive index.

Finally, a ceramic conductor board is manufactured by silk-screening in order to provide electrical access to the modulator. The contact pads on the photonic chip are connected to the conductor board by wire bonds. Wire strands are soldered to the adapted contacts on the board. Thus, a bias voltage can be applied for characterization purposes without the necessity for electrical probes. The final assembly is presented in the photograph in Figure 6.16a). Figure 6.16b) and c) show top view and the side view of one of the angle-polished fibers. In Figure 6.16d), a close-up photograph of the fiber alignment on the chip surface is shown.

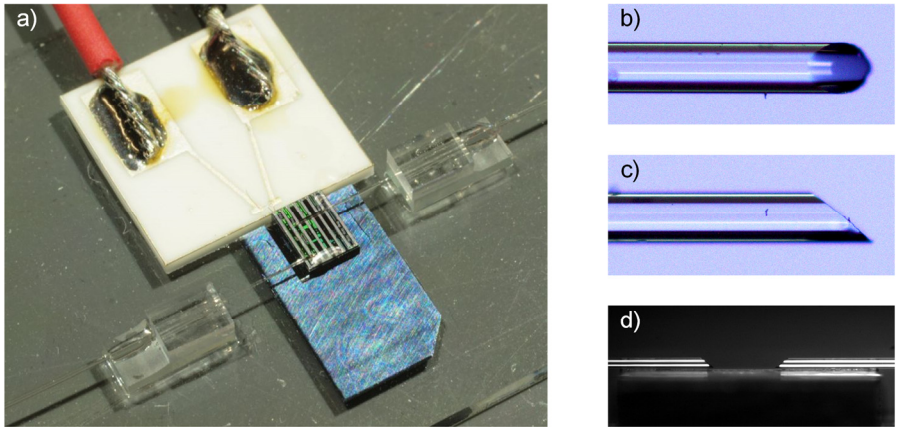

Figure 6.16: a) Close-up photograph of the permanent fiber-to-chip coupling and electrical contacting of an electro-optic modulator on a multi-component photonic chip. b) Top view and c) side view of an angle-polished fiber. d) Side view of the coupling arrangement.

6.2.2 Assembly validation

The fiber-to-chip coupling arrangement is validated upon each stage towards the complete assembly. For one, the alignment tolerances are studied by both simulations and experiments. After the assembly, the sensitivity towards ambient conditions and the long-term stability in a non-stabilized environment is investigated.

The simulations are conducted using the software package *Zemax OpticStudio* utilizing the physical optics propagation method (POP). A cylindrical lens models the optical fiber, since the optical field passes the fiber's cladding radially with respect to the fiber axis. The lens radius equals half the fiber diameter of 125 µm. Due to the small difference of less than 1% of the refractive indices between the fiber core and the cladding, a change of the angle of refraction is neglected at the boundary.

The simulations consider the fundamental mode propagating along the fiber axis. Therefore, the field has a Gaussian energy distribution, which is maintained after being totally reflected at the polished facets. Hence, a Gaussian-shaped field source is located at the lens axis. The mode accepted by the grating coupler is assumed to have a Gaussian shape, too. This is a suitable approach, since the design of the utilized grating couplers attempt to maximize the overlap between the mode of the fiber and the coupler [80], [84]. Furthermore, the mode-size of the coupler is assumed to match that of the fiber. Again, this is justified by taking an optimized coupler design for granted. Thus, the grating coupler is modelled by a Gaussian-shaped fundamental mode with a radius matching that of the optical fiber. The design coupling angle is taken into account by tilting the propagation vector of the coupler's mode field accordingly. A graphical representation of the simulation model is shown in Figure 6.17.

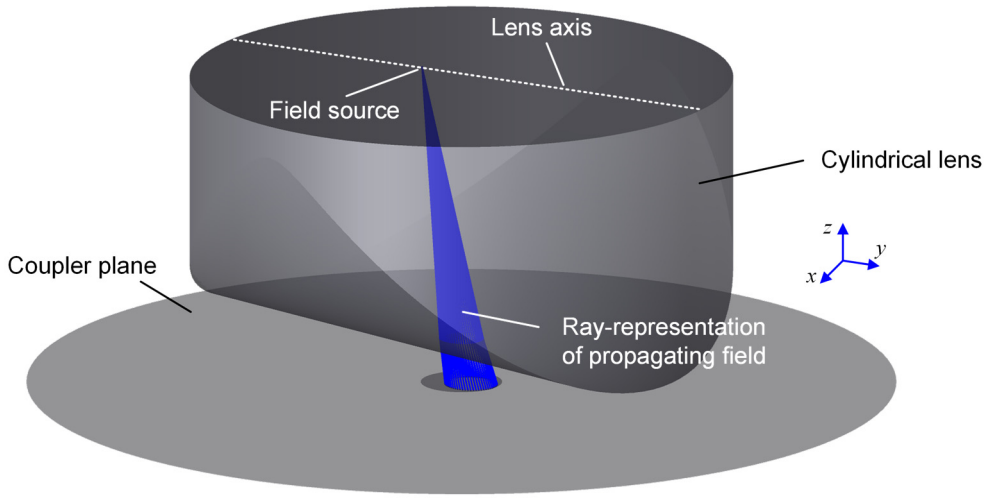

Figure 6.17: Graphical representation of the Zemax OpticStudio simulation model. A cylindrical lens represents the optical fiber. The optical field couples radially with respect to the fiber axis.

The simulator calculates the propagation of the field through the lens. The coupling efficiency is obtained by calculating the overlap integral between the involved modes at the location of the grating coupler. With this model, the coupling efficiency as a function of spatial displacement from the optimum alignment between the fiber and the grating coupler is obtained. That includes the offset in the chip surface plane lateral (x-direction, see Figure 3.5) and parallel (y-direction) to the fiber axis as well as the gap between the fiber cladding and the grating coupler (z-direction). The impact of a misalignment of the fiber rotation is analyzed, too.

Except for the rotation angle, the dependency of the coupling efficiency on the displacement is also determined experimentally. The method is similar to the previous section, where the displacement of an out-of-plane fiber-to-chip coupling assembly is analyzed. An angle-polished single-mode fiber is positioned to achieve optimum coupling to a grating-coupled test waveguide. A cleaved single-mode fiber probes the output grating coupler. While the alignment of the angle-polished fiber is iteratively displaced in discrete steps, the cleaved fiber's alignment is continuously optimized. That way, the impact of displacing the angle-polished fiber in x-, y- and z-direction on the coupling efficiency can be analyzed. Since the means for an exact determination of the fiber rotation angle are not available, the rotational misalignment is not considered.

The results of both the simulations and the experiments, where applicable, are presented in Figure 6.18. The solid lines represent the simulation results while the dashed lines are connections of data points

obtained by measurements. Figure 6.18a) and b) show the normalized coupling efficiency as a function of the areal displacement in the plane of the photonic chip surface. In both diagrams, the simulation results resemble a Gaussian shape. An alignment error of 5.0 µm lateral or 4.5 µm parallel to the fiber axis yields a penalty of 3 dB. Although the measured efficiency in x-direction in Figure 6.18a) has a slightly reduced width, an excellent agreement of the experimental results with the simulation is noted for the areal displacement. Nevertheless, the comparison of the simulation and the experimental result of the parallel displacement in Figure 6.18b) reveals a deviation in $+y$-direction. Obviously, the coupling efficiency decreases stronger for $0 < y \leq 6$ µm than the simulation predicts. On the other hand, at an offset greater than 6 µm, the decrease of the efficiency diminishes. This confirms that the mode of the real grating coupler in y-direction differs from the Gaussian shape, which is not taken into account in the simulation. As already elaborated in section 6.1.4 on page 98, the mode deformation is attributed to the focusing properties of the grating coupler.

The coupling efficiency of the in-plane design is equally dependent on lateral displacement as the out-of-plane design shown in Figure 6.5a). Thus, an average margin for a 3 dB penalty of 4.5 µm is observed. Apparently, the focusing effect of the fiber cladding acting as a cylindrical lens is negligible. In contrast, the in-plane assembly is more sensitive to a parallel displacement. The 3 dB margin is reduced by more than 1 µm to 4.1 µm. A possible explanation is a deformation of the mode in y-direction. Due to the coupling angle and the distance between the fiber axis and the grating coupler, the extent of the mode radiated from the fiber core via the reflection at the polished facet is asymmetrically enhanced in y-direction. This adds to the mode mismatch between the fiber and the grating coupler and therefore constricts the alignment tolerance.

The impact of the gap size w_g between the fiber cladding and the grating coupler is visualized in Figure 6.18c). The diagram shows the normalized coupling efficiency as a function of the gap size. Since the coupling angle θ with respect to the chip surface normal is non-zero, a change of w_g also involves a

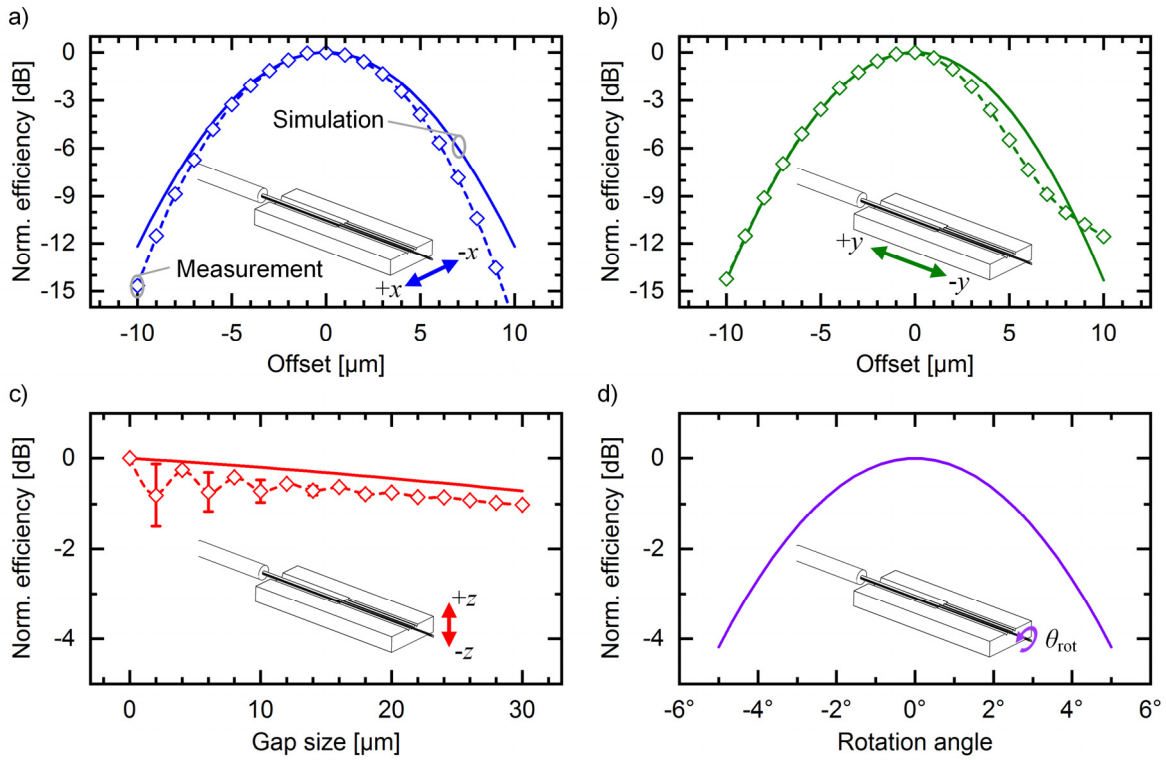

Figure 6.18: Coupling efficiency as a function of the spatial displacement of an angle-polished fiber from the optimum position. Solid lines show simulation results while the data points connected by dashed lines are obtained by experiments. Impact of a) lateral and b) parallel offset with respect to the fiber axis, c) gap size w_g between the cladding of the fiber and the grating coupler and d) rotation angle of the fiber.

displacement in y-direction. For a proper assessment of the dependency of the coupling efficiency on w_g, that displacement is compensated by adjusting the fiber position in y-direction. The simulated coupling efficiency shows a monotonously decreasing progress. The experimental result is quite similar, although the efficiency oscillates around a mean value with increasing w_g. The reason is a superposition of reflections that occur between the fiber cladding and the grating coupler. However, the experiment and the simulation are in very good agreement and show a high tolerance of the coupling efficiency against the gap size w_g. Even at 30 µm, the measured penalty is only 1 dB.

Finally, the simulation result of the rotational misalignment is presented in Figure 6.18d). The diagram shows the normalized coupling efficiency as a function of the rotation angle compared to optimum alignment. The progression also resembles a Gaussian shape, because the rotational misalignment is essentially equivalent to a lateral displacement accompanied by an asymmetric defocusing.

After the successful completion of the fiber-to-chip coupling assembly, the coupling stability at changing ambient conditions is studied. Similar to the out-of-plane design, a change of the adhesive properties due to temperature and humidity might involve a volume change. In turn, this may result in a displacement of the fiber alignment and thus in an increased penalty on the coupling efficiency. In order to achieve a separation of the effects, all measurements are carried out using a climate testing cabinet. The procedure is identical to section 6.1.6. Since it is already shown, that the displacements are fully reversible, the measurements are not replicated for decrementing humidity and temperature. The results of the study are summarized in Figure 6.19.

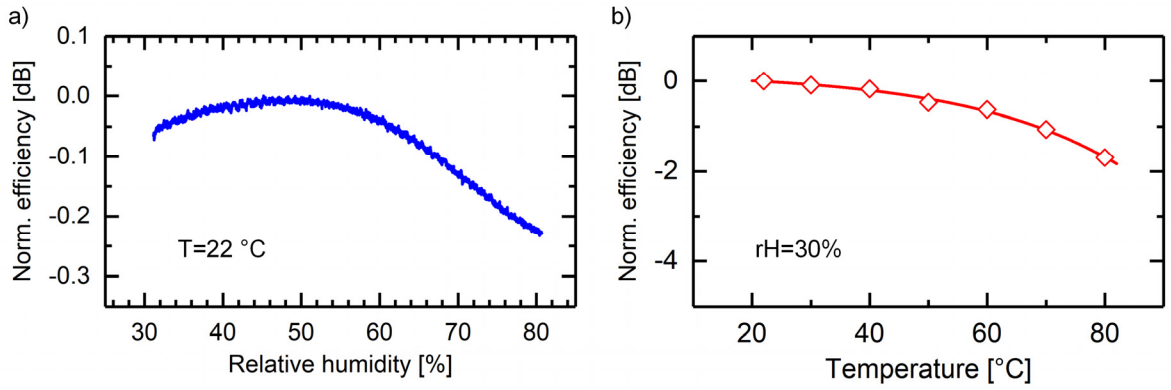

Figure 6.19: Response of the coupling efficiency of the fiber-to-chip coupling arrangement using angle-polished fibers and glass v-groove chips upon changes in ambient conditions. Relative coupling efficiency normalized to the maximum value at optimum coupling as a function of a) the ambient humidity at a temperature of 22 °C in the range of 30% RH to 80% RH and as function of b) the ambient temperature at 30% RH relative humidity in the range of 22 °C to 80 °C.

In Figure 6.19a), the dependency of the coupling efficiency on the relative humidity in the range of 30% RH to 80% RH at an ambient temperature of 22 °C is shown. The values are normalized to the maximum value. Obviously, the coupling efficiency improves upon increasing humidity from 30% RH towards 50% RH. That indicates an initial displacement of the assembly, which is compensated at 50% RH. Still, the maximum penalty on the coupling due to displacement within the given range of humidity is 0.2 dB. Figure 6.19b) shows the measured and normalized coupling efficiency as a function of the ambient temperature in the range of 22 °C to 80 °C. The maximum efficiency is observed at 22 °C, which is also the temperature during the assembly. With rising temperature, a misalignment of the fiber manifests by the increase of the coupling loss. The maximum penalty at 80 °C compared to 22 °C is less than 2 dB.

The impact of the ambient humidity on the fiber-to-chip coupling assembly using angle-polished fibers appears to be comparable to that relying on the vertical alignment. Both assemblies use a flat adhesion interface for the bonding of the fiber sockets to the substrate. However, due to the higher

sensitivity of angle-polished fibers to displacement in y-direction, the penalty due to a change of the relative humidity has a stronger impact on the coupling efficiency. In contrast, the impact of a change of ambient temperature is significantly reduced. Mainly, this improvement is achieved by replacing the metal sockets with the glass v-groove chips with a CTE smaller by one order of magnitude. The result is a reduced impact of thermal expansion or contraction of the sockets on the coupling. The residual penalty observed in Figure 6.19b) is attributed to the thermal expansion or contraction of the adhesive.

Similar to the analysis of the out-of-plane design, the long-term stability of the fiber-to-chip coupling assembly using angle-polished fibers is investigated. The observation period to date is just above three years. In uneven intervals, the coupling efficiency is determined by measuring the transmission of the permanently-coupled electro-optic modulator at the wavelength of its maximum transmission around 1.54 µm. The data is not acquired continuously. Instead, the assembly is connected to the laser source and the power meter each time the measurement is initiated. This also involves a polarization adjustment. Figure 6.20 shows the coupling efficiency normalized to the highest measured value as a function of the elapsed time since the assembly. The open symbols represent the measured values. The re-plugging and the polarization adjustment are identified as sources of uncertainty. Fluctuations of ambient conditions provoke supplemental scattering of the data points. Apart from that, the evaluation of the data does not reveal a significant coupling penalty over the elapsing time. The ratio between the highest and the lowest value is 1.1 dB.

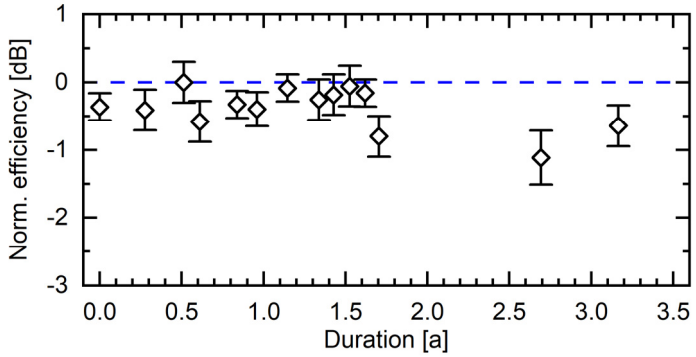

Figure 6.20: Long-term stability of the fiber-to-chip coupling arrangement using angle-polished fibers and v-groove chips. The picture shows the normalized coupling efficiency over the elapsed time since the assembly.

6.2.3 Comparison of coupling designs

Finally, a comparison between the two coupling designs is made. It has already been shown, that the spatial requirements of the in-plane assembly are significantly reduced compared to the out-of-plane alignment. In contrast, the alignment tolerance of the angle-polished fibers appear to be smaller compared to cleaved fibers. Furthermore, the fabrication of the former requires several polishing steps while that of the latter relies only on fiber cleaving. On account of minimized hygroscopic expansion of the utilized adhesive, both assemblies exhibit only a small sensitivity to changes of the relative humidity. The tremendously higher impact of the ambient temperature on the out-of-plane assembly is due to the thermal expansion of the aluminum sockets and therefore cannot be attributed to the fiber orientation.

Lastly, the absolute coupling efficiencies of both fiber alignments are addressed. Generally, the permanent coupling of SMF does not yield a penalty compared to using fiber alignment stages. However, due to the larger distance between the fiber core and the grating coupler, a slight increase of the coupling loss using angle-polished fibers is expected. The schematics of both fiber alignments are shown in Figure 6.21. Even for a zero clearance between the fiber cladding and the chip surface as shown in Figure 6.21a), the perpendicular minimum distance from the fiber axis to the coupler is given by half the SMF diameter d_{SMF}. In case of the cleaved SMF aligned at the coupling angle θ according

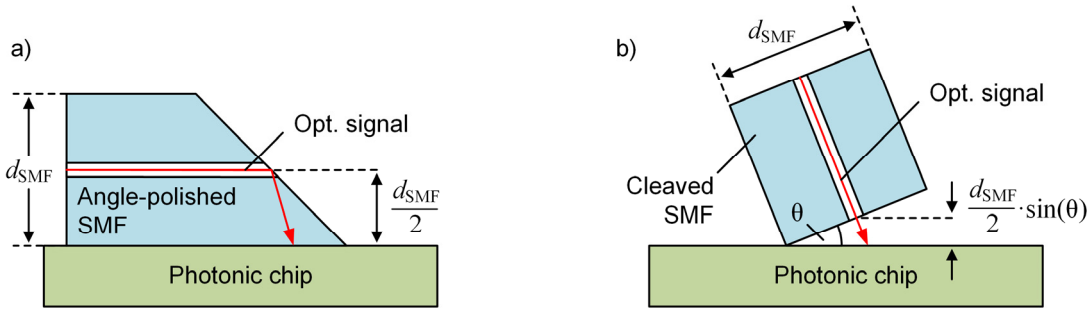

Figure 6.21: Schematics of fiber-to-chip coupling assemblies to facilitate the derivation of the minimum perpendicular distance from the fiber axis at the facet to a coupler on the photonic chip. a) in-plane alignment with angle-polished fibers, b) out-of-plane alignment with cleaved fibers.

to Figure 6.21b), the distance from the coupler to the fiber axis is proportional to $d_{\mathrm{SMF}}/2 \cdot \sin(\theta)$. Thus, it is always smaller than $d_{\mathrm{SMF}}/2$ which implies a smaller coupling loss.

Against this backdrop, the coupling efficiencies of both fiber alignments are experimentally compared. In order to achieve a representative result, all six combinations of two specimens out of four angle-polished fibers with optimum coupling angle are tested at a grating-coupled test structure. The coupling efficiency for each fiber pair is derived from measured transmission spectra using the experimental setup presented in Figure 5.3 on page 46. The optical input power is 6 dBm. The evaluation is based on the optical power measured at the wavelength of the grating coupler transmission maxima. For comparison, the experiment is repeated with a similar test structure using a pair of vertically aligned cleaved fibers. Here, the coupling angle is optimized by adjusting the fiber mounting angle manually.

Using angle-polished fibers, the average coupling efficiency is -9.4 dB across all specimen combinations, while it is -9.2 dB for the vertically aligned cleaved fibers. Both results include the insertion losses of both the input and the output grating coupler. Similar to preceding experiments, the measured optical power is subject to uncertainties due to the fiber connections and the polarization adjustment. Thus, the result may not qualify for a rigorous comparison due to the limited precision of the measurement. Therefore, the hypothesis of an intrinsically higher coupling loss of angle-polished fibers cannot be confirmed within the scope of this study. However, the precision is considered sufficient to ascertain that the coupling losses of both fiber alignments appear to be comparable and that an in-plane fiber alignment does not impose a significant penalty on the coupling efficiency.

6.3 Summary

In this chapter, the development, the assembly and the evaluation of a fiber-to-chip coupling assembly is discussed. Different vertical arrangements are constructed and characterized in order to find an optimum adhesive joint design for an UV-curing adhesive. The influence of environmental conditions and the long-term stability are extensively studied. An assembly based on aluminum sockets with a flatly-polished adhesion interface is found to be most reliable. However, the high CTE of aluminum results in a high sensitivity of the coupling efficiency on temperature changes.

An advanced concept pursues the permanent coupling with angle-polished single-mode fibers. It enables a substantially reduced footprint, because the fibers are aligned in the plane of the chip surface. A process is developed, which encompasses the fabrication of the polished fibers, the alignment using standard glass v-groove chips and the fixation with an UV-curing adhesive. Since it does not require specialized packaging equipment, it is even suitable for the rapid coupling of prototype components.

Similar to the out-of-plane concept, the influences of environmental conditions are studied and the long-term stability is demonstrated. Neither the strong variation of the ambient temperature nor humidity causes a significant deterioration of the coupling efficiency. The substantial reduction of the sensitivity to ambient temperature change is mainly achieved by replacing the metal sockets with glass v-groove chips. Lastly, both assemblies are compared and the respective advantages and disadvantages are

emphasized. Although a higher coupling loss is expected using angle-polished fibers, a significant difference between the coupling efficiencies cannot be determined experimentally.

7 System demonstrator

In this chapter, the experimental setup is described, which is used to demonstrate the functionality of the WDM-based optical link for detector data read-out applications. The system aims for the demonstration of a data transmission over all four channels of the integrated on-detector transmitter. A schematic of the system is presented in Figure 7.1. Apart from the integrated transmitter, the essential components are the laser source, the electrical drivers for the electro-optic modulators and the test unit for the bit error ratio (BER). Further, a DWDM demultiplexer is utilized for the separation of incident optical channels at the BER testing unit.

The laser source generates up to four optical carriers, which are combined and conveyed over a standard single-mode fiber (SMF) to the transmitter input. Since the polarization state of the optical carriers is vital for the coupling efficiency, the downlink should be implemented by a polarization-maintaining fiber.

A pseudo-random bit sequence (PRBS) is generated by a BER testing unit, which essentially consists of a field programmable gate array (FPGA) running on a development board and four SFP+ transceiver modules. The PRBS can be generated individually for each channel. A decorrelation is achieved by internal delay lines or cables of different length. An electrical driver amplifies the signals to a level suitable to drive the electro-optic modulators. Matching the number of channels of the integrated transmitter, the driver is capable to process up to four signals in parallel. All driver channels are powered and operated by a common driver control board (DCB).

The combined optical output signals of the transmitter are separated by a *Fiberstore* 40 channel dual-fiber DWDM (de-)multiplexer. Each optical channel is routed back to an SFP+ module of the BER testing unit. Additionally to the BER measurement, the eye pattern of the received signals can be monitored by a Tektronix CSA8200 communication signal analyzer (CSA) with a Tektronix 80E04 sampling module.

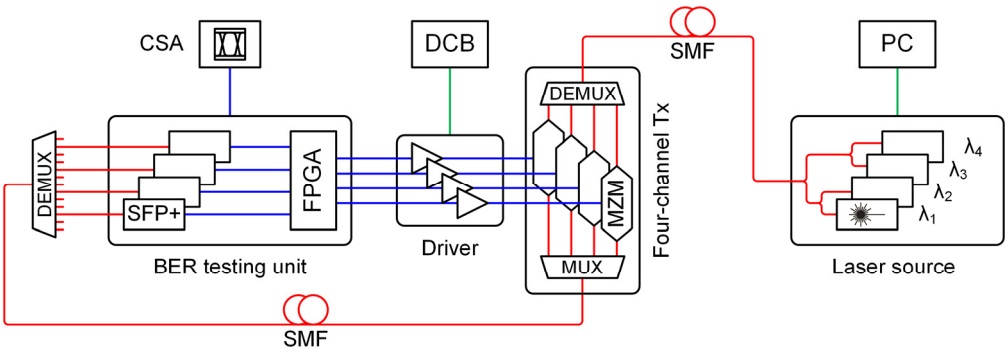

Figure 7.1: Schematic of the system demonstrator operating at up to four optical channels. PRBS generation and BER analysis is implemented on one FPGA development board.

7.1 Laser source

The four-channel laser source is assembled from *Emcore* 1782 *DWDM source laser devices* in pigtailed butterfly packages. The bias current supply and the thermo-electric control (TEC) is achieved using *OptoSci* LDRS-OEM laser drivers which are controlled by a common software tool. Each laser device is equipped with an in-built photodiode for output power monitoring. In order to preserve the polarization state of the individual laser modules, cascaded polarization-maintaining power couplers are utilized instead of a WDM multiplexer for the concentration of optical carriers in the output fiber.

The lasers have a nominal optical output power of up to 40 mW. The design central emission wavelength is selected according to the ITU grid and to match as accurately as possible the transmission windows of the PCG (de-)multiplexers of the four-channel transmitter. If required, the wavelength can be tuned within a limited range by manipulating the laser's operating temperature.

The assembled array is presented in Figure 7.2a). The laser modules are mounted to a base plate along with the power couplers and the common power supply. The base plate is mounted in a *Bopla Intergo* housing. External interfaces are an IEC socket panel mount for the power supply, a USB interface to connect the device to a personal computer and two FC/APC connectors for the optical output. Figure 7.2b) shows one of laser driver modules. The laser diode is soldered to the mount board, which sits on top of the driver board. A heat sink covers the entire surface of the butterfly package.

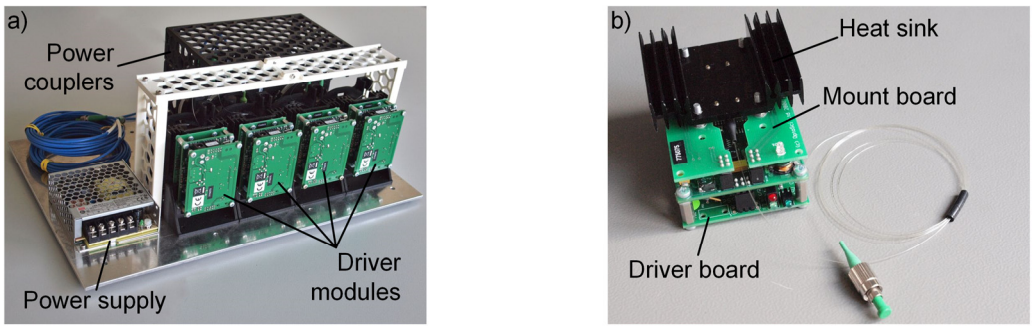

Figure 7.2: Assembly of the four-channel laser source. a) Housing which contains four laser diodes whose outputs are merged to the two fiber connectors on the front plate. b) Photograph of a laser driver module. The laser diode is soldered to the mount board.

7.2 Electrical driver

In this section, the electrical driver circuitry for the Mach-Zehnder modulators is presented. Figure 7.3 shows the schematic of the amplifier chain to drive one transmitter channel. In the link demonstrator system as presented in Figure 7.1, up to four driver units operate in parallel. The electrical driver itself consists of the driver unit, the link board and the termination board. The driver board amplifies the data signal to an amplitude suitable for an electro-optic modulator, while the termination board provides for the bias voltage supply and the transmission line termination. The link board adapts the transmission line of the driver board to dimensions suitable for wire-bonding. The entire driver is powered by a common power supply. All required voltage levels are generated by the driver control board. The electrical driver is designed for supporting a 10 Gbit/s nonreturn-to-zero on/off keying (NRZ-OOK) signal with an 8B/10B coding scheme.

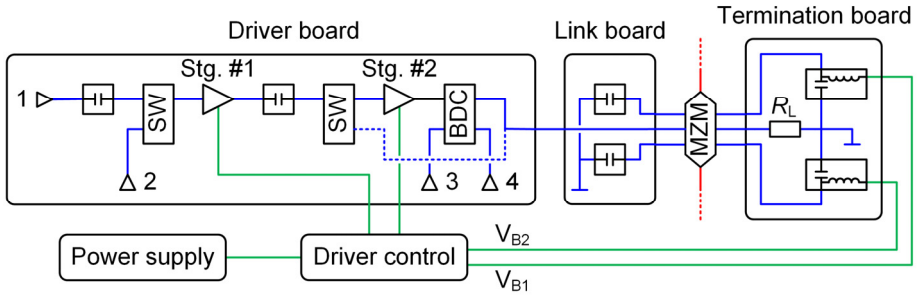

Figure 7.3: Schematic of the HF driver showing the amplifier chain of one transmitter channel. The circuitry consists of three modules. The driver board contains the electrical amplifiers, the link board enables the connection between the photonic chip and the driver and provides for ground isolation between the HF source and the bias supply. The Mach-Zehnder modulator (MZM) is supplied with the bias voltages V_{B1} and V_{B2} using two bias-tees on the termination board, which also contains the termination resistance R_L.

The driver unit contains the actual amplifier chain. It is assembled from discreet components, which are coupled by SMA connectors and semi-rigid cables. Essentially, it consists of two cascaded *Analog Devices* HMC870 distributed amplifiers, of which each is operated on an evaluation board. They offer a gain of 16 dB within a bandwidth of 20 GHz. Due to be more suitable as a pre-amplifier, the first HMC870 in the chain will be replaced by an *Analog Devices* HMC7144 broadband driver amplifier in

a later stage of development. In contrast to the HMC870, it contains a power sensor, which enables the signal monitoring at nominal operation, that is, in the presence of an electrical load.

The amplitude of the input signal at port 1 has a peak-to-peak voltage (V_{pp}) of 0.5 V corresponding to the voltage levels predetermined by the FPGA output. The signal is AC-coupled to the first amplifier stage, where V_{pp} is increased to 1.2 V. Alternatively, the signal of a calibration source connected to port 2 can be DC-coupled to the amplifier. The input can be selected by a switch (SW). The amplifiers are mounted on evaluation boards, which do not exhibit separate connectors for the power supply. Therefore, additional bias-tees are used in the amplifier chain.

The stage 1 output is AC-coupled to stage 2. The intermediate voltage level is required to operate the stage 2 amplifier in its optimum operating point. Behind the stage 2 amplifier, V_{pp} of the signal amplitude is up to 8 V. Due to this relatively large amplitude, the system is even capable to accommodate modulators with a high voltage-length product. By introducing another switch, the stage 1 output signal can be directly routed to the board's output. This feature can be used for probing the amplifier's output while simultaneously decoupling the stage 2 input. On the other hand, this output can be used for modulators which require a smaller modulation amplitude to achieve an adequate extinction ratio.

The last element in the chain is a bi-directional coupler (BDC). It facilitates probing the stage 2 output at nominal operation. The device introduces an additional port both in forward and reverse direction with respect to the transmission line. Thus, by probing the ports 3 and 4, the output of the stage 2 amplifier can be monitored as well as the reflected power from the load. Since the HMC7144 is internally capable of monitoring the output signal, the first stage is not equipped with a BDC.

The main purpose of the link board is to adapt the on-board waveguides to the dimensions of the modulator contact pads. Secondly, the board contains coupling capacitors, which separate the ground potentials of the RF source and the bias power supply. The link board is attached to the driver unit by semi-rigid cables with SMA connectors and the connection to the modulator contact pads is established by wire bonds.

The termination board contains a termination resistance R_{L} for the signal line of each electrical channel. Furthermore, it accommodates two bias-tees to feed the bias voltages V_{B1} and V_{B2} to each of the phase shifters in the MZM. The bias voltage potentials lie on the modulator's ground electrodes, which is why the isolation of the ground potentials between the RF source and the DC source is required. A top-view photograph of the driver electronics module is shown in Figure 7.4. Besides accommodating the driver circuitry, the module servers as the package for the integrated transmitter. The photonic chip is fixed on a submount between the link board and the termination board. The electrical contacts are established by wire bonds. The input and output fibers are coupled to the chip according to the in-plane fiber-to-chip coupling method described in chapter 6.

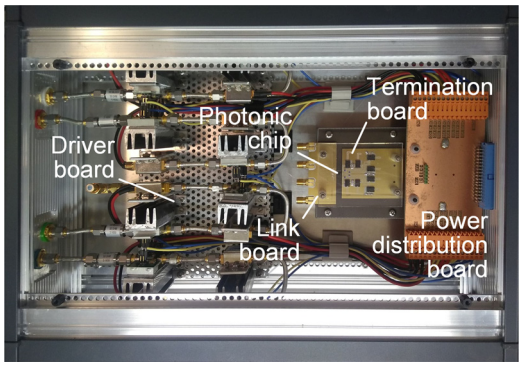

Figure 7.4: Top-view photograph of the driver electronics module with the essential components labelled. The photonic chip carrying the transmitter is mounted between the link board and the termination board according to the method described in chapter 6.

7.3 BER testing unit

A testing unit for evaluating the bit error ratio (BER) of the transmission link is realized on an *Altera* Stratix V GX FPGA running on a *Transceiver Signal Integrity Development Board*. The vendor provides several FPGA configurations and a control application to use various board features. In order to setup the BER testing unit, the board's GXB SMA transceivers are used. This enables the direct routing of each of the PRBS signals to one of the SMA input channels of the electrical driver, where they are amplified to an amplitude appropriate to drive an MZM. The receiver front-ends are implemented by the optical receiver modules of *Fiberstore* SFP-10GER-55 SFP+ transceivers. The SFP+ interfaces are adapted to the GXB transceivers using *Hightech Global* SMA to SFP conversion modules, which provide differential SMA interfaces for the transmitting and receiving direction.

The FPGA generates a PRBS of the length $2^N - 1$ as test signal. It can be routed to a specific transmitter channel. The resulting data rate of the sequence can be selected between 0.6 Gbit/s and 12.5 Gbit/s. The available polynomial orders N are 7, 15, 23 and 31. The analogue front-end of the GXB transceivers allows for the adjustment of various signal parameters. Among others, the most important are the voltage output differential and the pre-emphasis of the transmitter signal, and the gain and equalization of the received signal. Eye diagrams of both the source and the received signals can be monitored using a CSA. The source signal is probed via a supplemental GXB transceiver output. The received signal is accessible at one of the FPGA's monitor outputs or by interrupting one of the differential connections between the SMA to SFP conversion modules and the FPGA board.

7.4 Summary

In this chapter, the demonstrator setup is presented, which is capable to verify the parallel transmission of PRBS encoded on different optical carriers by the integrated WDM transmitter. The system essentially consists of a laser source, an electrical driver and a BER testing unit. The laser source is assembled from commercially available laser diodes whose outputs are concentrated to a single fiber using polarization-maintaining couplers. The electrical driver consists of four parallel amplifier chains, which are operated individually. The housing of the module servers simultaneously as the package for the transmitter unit. The BER testing unit is realized on an FPGA running on a development board. The PRBS signals are amplified by the electrical driver to a level appropriate for the MZM. The optical receivers are implemented by the receiver modules of commercial odd-the-shelf SFP+ transceivers. Once the setup is assembled completely, it will be used to demonstrate the parallel transmission of decorrelated PRBS over all four channels of the transmitter.

8 Conclusion and outlook

8.1 Conclusion

The demands on the resolution refinement of detector systems in various scientific applications increase continuously. In particular experiments in high-energy physics, astroparticle physics or photon science are perpetually subject to technological upgrades allowing for unprecedented spatial, temporal and energy resolution. Besides the ability to push forward the scientific frontiers, this poses tremendous requirements on the technical infrastructure, because the data link between the detector and the counting room progressively becomes the bottleneck of the detector system. In the course of the high-luminosity LHC upgrade phases 1 and 2, optical links based on directly modulated laser diodes are deployed enabling an upstream data rate per fiber of 10 Gbit/s. A promising solution for further increasing the per-fiber data rate is a WDM-based optical link. Besides satisfying the demand for a large data rate, it also reduces the number of cables between the detector barrel and the counting room. In photon science, this yields a reduction of cables in the vacuum-air feed-through and thus improves the sealing of the experimental chamber. In a HEP experiment, this decreases the volume and mass of the detector front-end and thus is advantageous to avoid multiple scattering. The silicon-on-insulator technology is identified to be the ideal platform for the realization of the on-detector components. Energy-efficient modulators optimized to be resilient to the harsh environment in the detector chamber can be built as well as WDM (de-)multiplexers with a small footprint. The optical link relies on a silicon-photonic on-detector multi-channel transmitter, which requires only a single standard single-mode fiber for each the input and the output, regardless of the number of WDM channels. The on-detector transmitter consists of depletion-type pn-modulators in MZM configuration and PCG (de-)multiplexers. The modulators are found to be most feasible for an application in optical transmitters in harsh environments. Although other technologies might be at an advantage considering properties such as linearity or energy-efficiency, depletion-type pn-modulators are unrivalled in terms of miniaturization and process maturity. Furthermore, the modulators exhibit an intrinsic resilience to radiation, and methods for further improvement have already been proposed and studied.

This thesis presents the essential milestones along the path towards the realization of a WDM-based optical transmission system for detector instrumentation. The achievements provide the basis for the assembly of the link demonstrator as presented in chapter 7. At the current stage, the driver circuitry is relatively bulky and requires the manual adjustment of the amplifier operating points. The modulator operating points are likewise controlled manually. Even considering revisions of the link components, such as the miniaturization of the driver or the integration of thermal modulators in the transmitter MZM, the link could be installed within the next two to three years. The first application would be a detector in photon science, where spatial constraints are of minor importance. The link could replace conventional read-out infrastructures and demonstrate the feasibility of the system. As described in chapter 4, a research group at CERN is also working on optical links for detector instrumentation. However, current developments such as the VL project rely on directly modulated laser diodes. Activities targeting the high-luminosity LHC concentrate on the optimization of silicon photonic modulators for harsh environments. Thus, the presented link architecture is unique in the world of particle physics, which makes the project and its achievements unprecedented.

Two major topics are addressed in this work: the integrated transmitter is developed based on the study of its individual components. Simulations are carried out in order to find optimized designs of modulators, (de-)multiplexers and power couplers. Furthermore, a comprehensive method is established to generate the layouts for the CMOS foundry. Secondly, an in-plane fiber-to-chip coupling arrangement is studied, in order to attach angle-polished optical fibers to grating-coupled waveguides. A process for a permanent coupling is established, which exclusively makes use of technical equipment any research facility has at its disposal. The achievements in the specific sub-topics are summarized below.

The characteristics of depletion-type pn-modulators are studied. Five designs with varying length and slab height are developed. The steady-state device performance is predicted accurately using an efficient simulation method established for design specification. The nominal doping concentrations according to the process specification have not been achieved in the fabrication process. Consequently, a relatively high voltage-length product $V_\pi L$ of 4.4 Vcm at 1 V bias voltage is found and a full π-shift is not realized. Modulators that have been exposed to a second dopant implantation exhibit an improved modulation efficiency by 33%. The voltage-length product at 1 V is reduced by approximately 25% to 3.4 Vcm. In contrast to modulators with a slab height of 180 nm, an unusual dependency of the modulation bandwidth on the bias voltage of devices with a 120 nm slab is found. The imperfect formation of metal vias of the latter is the most plausible explanation. Yet, a bandwidth of 28.7 GHz at a bias voltage of 1 V is determined upon the characterization of a 3 mm modulator with a slab height of 180 nm. Despite the restrictions on the modulation efficiency and the bandwidth of some of the phase shifters, the encoding of an 11.3 Gbit/s NRZ-OOK PRBS with excellent signal quality is demonstrated for every modulator type. Based on the modulation bandwidth obtained from the characterization of the 180 nm slab device, the modulator design is expected to support a data rate in the range 40 Gbit/s even at a length of 3 mm. In addition, the improvement of the modulation efficiency after the additional dopant implantation process gives reason to expect a performance, which competes state-of-the-art devices. Auxiliary components, such as MMI utilized as power couplers to assemble MZM are carefully designed. The measured insertion loss of a 2×2 MMI achieving an even splitting ratio is 0.64 dB.

PCG (de-)multiplexer designs are analyzed both by simulations and in experiments. It is shown that PCG multiplexers are attractive for the utilization in the transmitter, because efficient devices can be fabricated with a small footprint. Taking the example of two PCG specimens, simulation results are presented. Where applicable, the characteristics are compared with experiments. In particular, the 7-channel design, which is utilized in the transmitter layout is discussed in detail. Its average insertion loss is 3.6 dB and the maximum crosstalk -12.3 dB. A channel spacing of 3 nm is found which is in good agreement with the theoretical value of 2.7 nm. On the other hand, the measured transmission spectra are blue-shifted by 6.2 nm compared to the theoretical transmission window peaks. Apart from potential fabrication tolerances, the deviation is attributed to inaccuracies due to approximations in the calculation of the PCG parameters.

For the first time, an integrated four-channel transmitter comprising of four depletion-type pn-modulators, an input demultiplexer and an output multiplexer based on PCG spectrographs is designed and fabricated. Although specimens of all building blocks are included on the photonic chip, the steady-state and dynamic characteristics of the entire unit are evaluated in a separate study. Despite the symmetric design, the MZM are subject to significant variances. This is determined by an arbitrary phase offset at zero bias voltage. The small-signal characteristics are identical to those found upon the characterization of individual MZM utilizing phase shifters with a slab height of 120 nm. Likewise, the error-free encoding of an 11.3 Gbit/s NRZ-OOK signal can be demonstrated. The transmission spectrum of the concatenated PCG (de-)multiplexers is red-shifted by 2.1 nm compared to the reference device and the bandwidth is reduced to 69%. The reason is a detuning of the transmission spectra due to process tolerances.

Thermal modulators for the MZM operating point adjustment are successfully demonstrated. The efficiencies of two different approaches are studied. They do not require metallic heaters because the formation of resistances is achieved by lightly doping the silicon waveguide. Therefore, both designs can be fabricated in a standard CMOS process, which allows for a smooth integration in existing Mach-Zehnder modulator designs. An advanced thermal modulator design based on localized heaters and thermal insulation of the waveguide achieves a π-shift at an electrical power of 20.3 mW. The modulation bandwidth of the device is 82 kHz. A conventional design based on a bulk heater integrated in the waveguide achieves the π-shift at 33.8 mW and has a bandwidth of 59 kHz. Especially the advanced design is promising: although not entirely optimized, both the modulation efficiency and the

bandwidth of the device can undoubtedly compete with state-of-the art devices, among which some require fabrication steps beyond standard CMOS processes.

Packaging and in particular fiber-to-chip coupling is essential for the application of photonic components. A coupling process for attaching standard single-mode fibers to grating-coupled silicon photonic integrated circuits using angle-polished fibers is presented. Bonding of the fibers is achieved using an UV-curing adhesive. The major steps towards the final assembly are the fabrication of angle-polished fibers and their mounting on standard glass v-groove chips as well as the precise alignment and the adhesive bonding. Since no specialized packaging equipment is required, the process is even suitable for rapid prototyping in a laboratory environment. The bonds are carefully designed and evaluated with aluminum-based test structures. The alignment tolerances are studied by both simulations and experiments. Misalignments of 5.0 µm lateral and 4.5 µm parallel to the fiber axis can be tolerated for a 3 dB penalty on the coupling efficiency. The fiber rotation angle may deviate by ±4.2°. In contrast, the coupling efficiency is only weakly dependent on the clearance between the fiber cladding and the grating coupler. Up to a gap size of 30 µm, the measured penalty does not exceed 1 dB. The reliability of the assembly is demonstrated successfully: the fiber displacement due to a temperature variation of nearly 60 K degrades the coupling efficiency by less than 2 dB, while a sweep of the relative humidity results in a penalty of 0.2 dB. Finally, it is shown that the coupling efficiency does not deteriorate over a period of more than three years. In addition to the small footprint, the minimum coupling penalty and the reliability of the assembly, the major achievement in this research field is the establishment of a permanent coupling assembly process that can be implemented without any specialized packaging equipment.

8.2 Outlook

Against the backdrop of the modulator characterization results, the fabrication of the devices should be repeated according to recommendations addressing the process imperfections. In particular, the formation of vias of modulators based on a strip-loaded waveguide with a slab height of 120 nm should be optimized. Furthermore, the modulation efficiency should be fundamentally improved. Above all, this can be achieved by increasing the doping concentrations. Indeed, the characterization of modulators that were exposed to an additional dopant implantation reveals a higher efficiency. Further improvement will be achieved by adjusting the pn-junction alignment according to the waveguide geometry and the doping concentrations in order to maximize the overlap between the optical mode and the depletion region. Apart from the fabrication process optimization, the research should focus on the resilience of photonic components to performance degradation due to radiation exposure, because this is a key property for detector components in high-energy physics. At first, the influence of the slab height can be investigated on the basis of comparing the modulator with a slab height of 120 nm to that with a slab height of 180 nm. Specimens of both variants are included in the photonic chip the experimental work of this thesis is based on. Making use of the fiber-to-chip coupling process presented in chapter 6, even in-situ radiation experiments become possible. Moreover, the approach of partly removing the oxide surrounding the strip-loaded waveguide can be further pursued. Using the simulation method presented in chapter 5 will path the way to a thorough understanding of the underlying processes.

Based on the experimental characterization of PCG (de-)multiplexers, the generation of the layouts should be refined. This encompasses the minimization of calculation uncertainties due to approximations as well as the adaption of foundry-specific wafer and process properties. Apart from the process optimization discussed above, potential enhancements of the integrated transmitter are identified. A future variant should include thermo-optic modulators for the operating point adjustment of the MZM. In combination with a control circuit, an automated operating point adjustment could be realized. The optimization of the thermo-optic modulators with respect to a further reduction of the power dissipation should also be pursued. In order to introduce a downlink for the transmission of control signals from the counting room to the detector, the functionality should be extended to turn the unit into a transceiver. This can either be accomplished by adding dedicated downlink channels that are

terminated by a photo receiver. On the other hand, a reconfigurable architecture is conceivable, where a photo receiver is attached to an auxiliary port of the output power coupler of one or several modulators. The respective MZM can be biased as such a downlink signal is directly routed to the photo receiver. Furthermore, other modulator concepts can be utilized. For instance, using resonant ring modulators for the multi-channel transmitter results in a substantially reduced footprint as well as a voltage-length product decreased by an order of magnitude compared to phase shifters in MZM configuration. In addition, the transmitter design could potentially relinquish the input demultiplexer and the output multiplexer. Because each ring can be designed to produce a filter notch at a desired wavelength, several modulators can be cascaded on a common bus waveguide. However, this comes at the cost of a heavy dependency of the operating point on the ambient temperature and therefore requires an additional temperature control.

The research in the field of fiber-to-chip coupling should focus on the utilization of polarization-maintaining fibers. Since the grating couplers of the silicon PIC are polarization sensitive, a polarization controller is required for each input channel. Because of the stringent spatial requirements at the detector front-end, the polarization controller has to be directly installed at the laser source outside the experimental cavern. In order to stabilize the optical mode's polarization upon propagating along the fiber, polarization-maintaining fibers are required. This imposes the rotation of the fiber with respect to its axis as a degree of freedom in both the fabrication and the assembly process.

The next steps towards the implementation of the link in a detector environment are dedicated to the miniaturization of the driver electronics. For one, this involves an electronic assembly based on die components on a dedicated circuit board. Next, an appropriate wire bonding process is required, which not only comprises the bond design in terms of short wires, straight wire trajectories and a low attenuation, but also to find a circuit board fabrication process that supports small feature sizes matching the pitch of the photonic chip's bonding pads. The ultimate goal is the integration of the entire driver in an ASIC, because only then the stringent spatial requirements that may apply for the detector front-end can be fulfilled.

9 Bibliography

[1] G. T. Reed and A. P. Knights, *Silicon photonics: an introduction*. Wiley, 2004.

[2] T. W. Ang, G. T. Reed, A. Vonsovici, A. G. R. Evans, P. R. Routley, and M. R. Josey, "0.15 dB/cm loss in Unibond SOI waveguides," *Electronics Letters*, vol. 35, no. 12, pp. 977–978, Jun. 1999, doi: 10.1049/el:19990689.

[3] M. Bruel, "Silicon on insulator material technology," *Electronics Letters*, vol. 31, no. 14, pp. 1201–1202, Jul. 1995, doi: 10.1049/el:19950805.

[4] B. E. A. Saleh and M. C. Teich, *Fundamentals of photonics*, 2nd ed. Hoboken, N.J.: Wiley, 2007.

[5] G. Grau and W. Freude, *Optische Nachrichtentechnik: Eine Einführung*, 3rd ed. Berlin: Springer, 1991.

[6] H. Fouckhardt, *Photonik: eine Einführung in die integrierte Optoelektronik und technische Optik*. Stuttgart: Teubner, 1994.

[7] K. S. Chiang, "Analysis of optical fibers by the effective-index method," *Appl. Opt., AO*, vol. 25, no. 3, pp. 348–354, Feb. 1986, doi: 10.1364/AO.25.000348.

[8] L. B. Soldano and E. C. M. Pennings, "Optical multi-mode interference devices based on self-imaging: principles and applications," *Journal of Lightwave Technology*, vol. 13, no. 4, pp. 615–627, Apr. 1995, doi: 10.1109/50.372474.

[9] M. Bachmann, P. A. Besse, and H. Melchior, "General self-imaging properties in N × N multimode interference couplers including phase relations," *Appl. Opt., AO*, vol. 33, no. 18, pp. 3905–3911, Jun. 1994, doi: 10.1364/AO.33.003905.

[10] H. A. Rowland, "LXI. Preliminary notice of the results accomplished in the manufacture and theory of gratings for optical purposes," *Philosophical Magazine Series 5*, vol. 13, no. 84, pp. 469–474, Jan. 1882, doi: 10.1080/14786448208627217.

[11] H. A. Rowland, "XXIX. On concave gratings for optical purposes," *Philosophical Magazine Series 5*, vol. 16, no. 99, pp. 197–210, Sep. 1883, doi: 10.1080/14786448308627419.

[12] R. J. Lycett, D. F. G. Gallagher, and V. J. Brulis, "Perfect Chirped Echelle Grating Wavelength Multiplexor: Design and Optimization," *IEEE Photonics Journal*, vol. 5, no. 2, pp. 2400123–2400123, Apr. 2013, doi: 10.1109/JPHOT.2013.2251874.

[13] J. Brouckaert, W. Bogaerts, P. Dumon, D. V. Thourhout, and R. Baets, "Planar Concave Grating Demultiplexer Fabricated on a Nanophotonic Silicon-on-Insulator Platform," *Journal of Lightwave Technology*, vol. 25, no. 5, pp. 1269–1275, May 2007, doi: 10.1109/JLT.2007.893025.

[14] R. März, *Integrated optics : design and modeling*. Boston: Artech House, 1995.

[15] "Corning® SMF-28^{TM} Optical Fiber." Product Information, Jun-2013.

[16] Y. Fu, T. Ye, W. Tang, and T. Chu, "Efficient adiabatic silicon-on-insulator waveguide taper," *Photon. Res., PRJ*, vol. 2, no. 3, pp. A41–A44, Jun. 2014, doi: 10.1364/PRJ.2.000A41.

[17] T. Shoji, T. Tsuchizawa, T. Watanabe, K. Yamada, and H. Morita, "Low loss mode size converter from 0.3 μm square Si wire waveguides to singlemode fibres," *Electronics Letters*, vol. 38, no. 25, pp. 1669–1670, Dec. 2002, doi: 10.1049/el:20021185.

[18] Y. Ding, H. Ou, and C. Peucheret, "Ultrahigh-efficiency apodized grating coupler using fully etched photonic crystals," *Opt. Lett., OL*, vol. 38, no. 15, pp. 2732–2734, Aug. 2013, doi: 10.1364/OL.38.002732.

[19] F. Van Laere *et al.*, "Compact Focusing Grating Couplers for Silicon-on-Insulator Integrated Circuits," *IEEE Photonics Technology Letters*, vol. 19, no. 23, pp. 1919–1921, Dec. 2007, doi: 10.1109/LPT.2007.908762.

[20] L. He *et al.*, "A High-Efficiency Nonuniform Grating Coupler Realized With 248-nm Optical Lithography," *IEEE Photonics Technology Letters*, vol. 25, no. 14, pp. 1358–1361, Jul. 2013, doi: 10.1109/LPT.2013.2265911.

[21] Y. Wang, H. Yun, Z. Lu, N. A. F. Jaeger, and L. Chrostowski, "State-of-the-art sub-wavelength grating couplers for silicon-on-insulator platform," in *2016 IEEE Canadian Conference on Electrical and Computer Engineering (CCECE)*, 2016, pp. 1–4, doi: 10.1109/CCECE.2016.7726633.

[22] M. Antelius, K. B. Gylfason, and H. Sohlström, "An apodized SOI waveguide-to-fiber surface grating coupler for single lithography silicon photonics," *Opt. Express, OE*, vol. 19, no. 4, pp. 3592–3598, Feb. 2011, doi: 10.1364/OE.19.003592.

[23] A. Mekis *et al.*, "A Grating-Coupler-Enabled CMOS Photonics Platform," *IEEE Journal of Selected Topics in Quantum Electronics*, vol. 17, no. 3, pp. 597–608, May 2011, doi: 10.1109/JSTQE.2010.2086049.

[24] D. Vermeulen *et al.*, "Reflectionless grating couplers for Silicon-on-Insulator photonic integrated circuits," *Opt. Express, OE*, vol. 20, no. 20, pp. 22278–22283, Sep. 2012, doi: 10.1364/OE.20.022278.

[25] R. A. Larrea, A. M. Gutiérrez, J. Hurtado, J. M. Ramírez, B. Garrido, and P. Sanchis, "Compact focusing grating couplers for silicon horizontal slot waveguides," *Opt. Lett., OL*, vol. 42, no. 3, pp. 490–493, Feb. 2017, doi: 10.1364/OL.42.000490.

[26] G. P. Agrawal, *Fiber-optic communication systems*, 3rd ed. New York: Wiley-Interscience, 2002.

[27] H. Kanamori *et al.*, "Transmission characteristics and reliability of pure-silica-core single-mode fibers," *J. Lightwave Technol.*, vol. 4, no. 8, pp. 1144–1150, Aug. 1986, doi: 10.1109/JLT.1986.1074837.

[28] A. H. Gnauck and P. J. Winzer, "Optical phase-shift-keyed transmission," *Journal of Lightwave Technology*, vol. 23, no. 1, pp. 115–130, Jan. 2005, doi: 10.1109/JLT.2004.840357.

[29] E. Agrell *et al.*, "Roadmap of optical communications," *J. Opt.*, vol. 18, no. 6, p. 063002, 2016, doi: 10.1088/2040-8978/18/6/063002.

[30] J.-X. Cai, "Advanced Technologies for High Capacity Transoceanic Distance Transmission Systems," in *Proceedings Optical Fiber Communication Conference*, 2017, doi: 10.1364/OFC.2017.Th4D.3.

[31] A. Ghazisaeidi *et al.*, "65Tb/s Transoceanic Transmission Using Probabilistically-Shaped PDM-64QAM," in *Proceedings European Conference on Optical Communication*, 2016.

[32] S. Zhang *et al.*, "Capacity-approaching transmission over 6375 km at spectral efficiency of 8.3 bit/s/Hz," in *Proceedings Optical Fiber Communication Conference*, 2016, doi: 10.1364/OFC.2016.Th5C.2.

[33] J. A. Tatum *et al.*, "VCSEL-Based Interconnects for Current and Future Data Centers," *J. Lightwave Technol., JLT*, vol. 33, no. 4, pp. 727–732, Feb. 2015.

[34] "fs.com - Data Center & Cloud Computing Infrastructure Solutions." [Online]. Available: https://www.fs.com/. [Accessed: 25-Oct-2017].

[35] A. V. Krishnamoorthy *et al.*, "Computer Systems Based on Silicon Photonic Interconnects," *Proceedings of the IEEE*, vol. 97, no. 7, pp. 1337–1361, Jul. 2009, doi: 10.1109/JPROC.2009.2020712.

[36] Y. Arakawa, T. Nakamura, Y. Urino, and T. Fujita, "Silicon photonics for next generation system integration platform," *IEEE Communications Magazine*, vol. 51, no. 3, pp. 72–77, Mar. 2013, doi: 10.1109/MCOM.2013.6476868.

[37] H. Venghaus and N. Grote, Eds., *Fibre Optic Communication: Key Devices*, 2nd ed. Cham: Springer, 2017.

[38] R. W. Boyd, *Nonlinear optics*, 3rd ed. Amsterdam: Elsevier, Academic Press, 2008.

[39] A. Yariv and P. Yeh, *Photonics: optical electronics in modern communications*, 6th ed. New York, NY: Oxford University Press, 2007.

[40] W. Bogaerts *et al.*, "Silicon microring resonators," *Laser & Photonics Reviews*, vol. 6, no. 1, pp. 47–73, 2012, doi: http://dx.doi.org/10.1002/lpor.201100017.

[41] D. Thomson *et al.*, "Roadmap on silicon photonics," *J. Opt.*, vol. 18, no. 7, p. 073003, 2016, doi: 10.1088/2040-8978/18/7/073003.

[42] J. Leuthold *et al.*, "Silicon Organic Hybrid Technology—A Platform for Practical Nonlinear Optics," *Proceedings of the IEEE*, vol. 97, no. 7, pp. 1304–1316, Jul. 2009, doi: 10.1109/JPROC.2009.2016849.

[43] J. A. Schuller, E. S. Barnard, W. Cai, Y. C. Jun, J. S. White, and M. L. Brongersma, "Plasmonics for extreme light concentration and manipulation," *Nature Materials*, vol. 9, no. 3, pp. 193–204, Mar. 2010, doi: 10.1038/nmat2630.

[44] D. J. Thomson *et al.*, "High Performance Mach–Zehnder-Based Silicon Optical Modulators," *IEEE Journal of Selected Topics in Quantum Electronics*, vol. 19, no. 6, pp. 85–94, Nov. 2013, doi: 10.1109/JSTQE.2013.2264799.

[45] G. T. Reed, D. J. Thomson, F. Y. Gardes, Y. Hu, J.-M. Fedeli, and G. Z. Mashanovich, "High-speed carrier-depletion silicon Mach-Zehnder optical modulators with lateral PN junctions," *Front. Phys.*, vol. 2, 2014, doi: 10.3389/fphy.2014.00077.

[46] R. Spickermann, S. Sakamoto, and N. Dagli, "GaAs/AlGaAs traveling-wave electro-optic modulators," in *Optoelectronic Integrated Circuits*, 1997, vol. 3006, pp. 272–280, doi: 10.1117/12.264228.

[47] R. Soref and B. Bennett, "Electrooptical effects in silicon," *IEEE Journal of Quantum Electronics*, vol. 23, no. 1, pp. 123–129, Jan. 1987, doi: 10.1109/JQE.1987.1073206.

[48] R. Gross and A. Marx, *Festkörperphysik*. München: Oldenbourg, 2012.

[49] H. Jayatilleka, W. D. Sacher, and J. K. S. Poon, "Analytical Model and Fringing-Field Parasitics of Carrier-Depletion Silicon-on-Insulator Optical Modulation Diodes," *IEEE Photonics Journal*, vol. 5, no. 1, pp. 2200211–2200211, Feb. 2013, doi: 10.1109/JPHOT.2013.2240381.

[50] G. Cocorullo, F. G. Della Corte, I. Rendina, and P. M. Sarro, "Thermo-optic effect exploitation in silicon microstructures," *Sensors and Actuators A: Physical*, vol. 71, no. 1, pp. 19–26, Nov. 1998, doi: 10.1016/S0924-4247(98)00168-X.

[51] Y. Okada and Y. Tokumaru, "Precise determination of lattice parameter and thermal expansion coefficient of silicon between 300 and 1500 K," *Journal of Applied Physics*, vol. 56, no. 2, pp. 314–320, Jul. 1984, doi: 10.1063/1.333965.

[52] M. Jacques, A. Samani, E. El-Fiky, D. Patel, Z. Xing, and D. V. Plant, "Optimization of thermo-optic phase-shifter design and mitigation of thermal crosstalk on the SOI platform," *Opt. Express, OE*, vol. 27, no. 8, pp. 10456–10471, Apr. 2019, doi: 10.1364/OE.27.010456.

[53] M. B. Reid and M. Ozcan, "Temperature dependence of fiber optic Bragg gratings at low temperatures," *OE, OPEGAR*, vol. 37, no. 1, pp. 237–241, Jan. 1998, doi: 10.1117/1.601610.

[54] B. Jalali and S. Fathpour, "Silicon Photonics," *J. Lightwave Technol., JLT*, vol. 24, no. 12, pp. 4600–4615, Dec. 2006.

[55] J. E. Bowers *et al.*, "Recent advances in silicon photonic integrated circuits," presented at the Next-Generation Optical Communication: Components, Sub-Systems, and Systems V, 2016, vol. 9774, p. 977402, doi: 10.1117/12.2221943.

[56] Y. Wan *et al.*, "Optically pumped 1.3 μm room-temperature InAs quantum-dot micro-disk lasers directly grown on (001) silicon," *Opt. Lett., OL*, vol. 41, no. 7, pp. 1664–1667, Apr. 2016, doi: 10.1364/OL.41.001664.

[57] J. Klamkin, "3D Hybrid Integration for Silicon Photonics," in *Frontiers in Optics 2016 (2016), paper FF5F.1*, 2016, p. FF5F.1, doi: 10.1364/FIO.2016.FF5F.1.

[58] E. L. Wooten *et al.*, "A review of lithium niobate modulators for fiber-optic communications systems," *IEEE Journal of Selected Topics in Quantum Electronics*, vol. 6, no. 1, pp. 69–82, Jan. 2000, doi: 10.1109/2944.826874.

[59] C. Wang, M. Zhang, B. Stern, M. Lipson, and M. Loncar, "Nanophotonic Lithium Niobate Electro-optic Modulators," *arXiv:1701.06470 [cond-mat, physics:physics]*, Jan. 2017.

[60] R. G. Walker, N. I. Cameron, Y. Zhou, and S. J. Clements, "Optimized Gallium Arsenide Modulators for Advanced Modulation Formats," *IEEE Journal of Selected Topics in Quantum Electronics*, vol. 19, no. 6, pp. 138–149, Nov. 2013, doi: 10.1109/JSTQE.2013.2266321.

[61] R. Spickermann and N. Dagli, "Experimental analysis of millimeter wave coplanar waveguide slow wave structures on GaAs," *IEEE Transactions on Microwave Theory and Techniques*, vol. 42, no. 10, pp. 1918–1924, Oct. 1994, doi: 10.1109/22.320774.

[62] H. R. Khazaei, R. James, E. Berolo, F. Rahmatian, N. A. F. Jaeger, and F. Ghannouchi, "Novel coplanar-strip slow-wave structure for ultrawide-bandwidth electro-optic modulators," *Microwave and Optical Technology Letters*, vol. 15, no. 5, pp. 303–305, 1997, doi: 10.1002/(SICI)1098-2760(19970805)15:5<303::AID-MOP10>3.0.CO;2-6.

[63] H. R. Khazaei, E. Berolo, and F. Ghannouchi, "High-speed slow-wave coplanar strip GaAs/AlGaAs electro-optic laser modulator," *Microwave and Optical Technology Letters*, vol. 19, no. 3, pp. 184–186, 1998, doi: 10.1002/(SICI)1098-2760(19981020)19:3<184::AID-MOP3>3.0.CO;2-H.

[64] C. R. Doerr, "Silicon photonic integration in telecommunications," *Frontiers in Physics*, vol. 3, Aug. 2015, doi: 10.3389/fphy.2015.00037.

[65] S. Chandrasekhar, X. Liu, P. J. Winzer, J. E. Simsarian, and R. A. Griffin, "Small-form-factor all-InP integrated laser vector modulator enables the generation and transmission of 256-Gb/s PDM-16QAM Modulation Format," in *2013 Optical Fiber Communication Conference and Exposition and the National Fiber Optic Engineers Conference (OFC/NFOEC)*, 2013, pp. 1–3.

[66] C. R. Doerr, "Metro Silicon Photonics Market Watch: PIC vs. Silicon Photonics: Hype or Reality?," presented at the Optical Fiber Communications Conference and Exhibition (OFC), 2014, San Francisco, CA, USA, 09-Mar-2014.

[67] T. Tekin, "Review of Packaging of Optoelectronic, Photonic, and MEMS Components," *IEEE Journal of Selected Topics in Quantum Electronics*, vol. 17, no. 3, pp. 704–719, May 2011, doi: 10.1109/JSTQE.2011.2113171.

[68] H.-M. Yang, S.-Y. Huang, C.-W. Lee, T.-S. Lay, and W.-H. Cheng, "High-Coupling Tapered Hyperbolic Fiber Microlens and Taper Asymmetry Effect," *J. Lightwave Technol., JLT*, vol. 22, no. 5, p. 1395, May 2004.

[69] M. Fritze *et al.*, "Fabrication of three-dimensional mode converters for silicon-based integrated optics," *Journal of Vacuum Science & Technology B: Microelectronics and Nanometer Structures Processing, Measurement, and Phenomena*, vol. 21, no. 6, pp. 2897–2902, Nov. 2003, doi: 10.1116/1.1625967.

[70] A. Khilo, M. A. Popović, M. Araghchini, and F. X. Kärtner, "Efficient planar fiber-to-chip coupler based on two-stage adiabatic evolution," *Opt. Express, OE*, vol. 18, no. 15, pp. 15790–15806, Jul. 2010, doi: 10.1364/OE.18.015790.

[71] H. Park, S. Kim, J. Park, J. Joo, and G. Kim, "A fiber-to-chip coupler based on Si/SiON cascaded tapers for Si photonic chips," *Opt Express*, vol. 21, no. 24, pp. 29313–29319, Dec. 2013.

[72] P. Markov, J. G. Valentine, and S. M. Weiss, "Fiber-to-chip coupler designed using an optical transformation," *Opt. Express, OE*, vol. 20, no. 13, pp. 14705–14713, Jun. 2012, doi: 10.1364/OE.20.014705.

[73] V. R. Almeida, R. R. Panepucci, and M. Lipson, "Nanotaper for compact mode conversion," *Opt. Lett., OL*, vol. 28, no. 15, pp. 1302–1304, Aug. 2003, doi: 10.1364/OL.28.001302.

[74] C. Kopp *et al.*, "Silicon Photonic Circuits: On-CMOS Integration, Fiber Optical Coupling, and Packaging," *IEEE Journal of Selected Topics in Quantum Electronics*, vol. 17, no. 3, pp. 498–509, May 2011, doi: 10.1109/JSTQE.2010.2071855.

[75] M. Papes *et al.*, "Fiber-chip edge coupler with large mode size for silicon photonic wire waveguides," presented at the Integrated Optics: Physics and Simulations II, 2015, vol. 9516, p. 95160K, doi: 10.1117/12.2181547.

[76] J. V. Galan *et al.*, "CMOS compatible silicon etched V-grooves integrated with a SOI fiber coupling technique for enhancing fiber-to-chip alignment," in *Group IV Photonics, 2009. GFP '09. 6th IEEE International Conference on*, 2009, pp. 148–150, doi: 10.1109/GROUP4.2009.5338334.

[77] D. Taillaert *et al.*, "Grating Couplers for Coupling between Optical Fibers and Nanophotonic Waveguides," *Jpn. J. Appl. Phys.*, vol. 45, no. 8A, pp. 6071–6077, Aug. 2006, doi: 10.1143/JJAP.45.6071.

[78] F. Van Laere *et al.*, "Compact and Highly Efficient Grating Couplers Between Optical Fiber and Nanophotonic Waveguides," *Journal of Lightwave Technology*, vol. 25, no. 1, pp. 151–156, Jan. 2007, doi: 10.1109/JLT.2006.888164.

[79] Y. Ding, C. Peucheret, H. Ou, and K. Yvind, "Fully etched apodized grating coupler on the SOI platform with −0.58 dB coupling efficiency," *Opt. Lett., OL*, vol. 39, no. 18, pp. 5348–5350, Sep. 2014, doi: 10.1364/OL.39.005348.

[80] D. Vermeulen *et al.*, "High-efficiency fiber-to-chip grating couplers realized using an advanced CMOS-compatible Silicon-On-Insulator platform," *Opt. Express, OE*, vol. 18, no. 17, pp. 18278–18283, Aug. 2010, doi: 10.1364/OE.18.018278.

[81] J. Notaros *et al.*, "Ultra-Efficient CMOS Fiber-to-Chip Grating Couplers," in *Optical Fiber Communication Conference (2016), paper M2I.5*, 2016, p. M2I.5, doi: 10.1364/OFC.2016.M2I.5.

[82] B. Snyder, B. Corbett, and P. O'Brien, "Hybrid Integration of the Wavelength-Tunable Laser With a Silicon Photonic Integrated Circuit," *Journal of Lightwave Technology*, vol. 31, no. 24, pp. 3934–3942, Dec. 2013, doi: 10.1109/JLT.2013.2276740.

[83] "Corning® SMF-28™ Ultra Optical Fiber." Product Information, Nov-2014.

[84] B. Snyder and P. O'Brien, "Packaging Process for Grating-Coupled Silicon Photonic Waveguides Using Angle-Polished Fibers," *IEEE Transactions on Components, Packaging and Manufacturing Technology*, vol. 3, no. 6, pp. 954–959, Jun. 2013, doi: 10.1109/TCPMT.2012.2237052.

[85] D. Hartman, M. Grace, and F. Richard, "An effective lateral fiber-optic electronic coupling and packaging technique suitable for VHSIC applications," *Journal of Lightwave Technology*, vol. 4, no. 1, pp. 73–82, Jan. 1986, doi: 10.1109/JLT.1986.1074630.

[86] K. P. Jackson, A. J. Moll, E. B. Flint, and M. F. Cina, "Optical Fiber Coupling Approaches For Multi-Channel Laser And Detector Arrays," presented at the Optoelectronic Materials, Devices, Packaging, and Interconnects II, 1989, vol. 0994, pp. 40–50, doi: 10.1117/12.960108.

[87] I. Ladany, "Laser to single-mode fiber coupling in the laboratory," *Appl. Opt., AO*, vol. 32, no. 18, pp. 3233–3236, Jun. 1993, doi: 10.1364/AO.32.003233.

[88] Y. Oikawa, H. Kuwatsuka, T. Yamamoto, T. Ihara, H. Hamano, and T. Minami, "Packaging technology for a 10-Gb/s photoreceiver module," *Journal of Lightwave Technology*, vol. 12, no. 2, pp. 343–352, Feb. 1994, doi: 10.1109/50.350587.

[89] C. Li, K. S. Chee, J. Tao, H. Zhang, M. Yu, and G. Q. Lo, "Silicon photonics packaging with lateral fiber coupling to apodized grating coupler embedded circuit," *Opt. Express, OE*, vol. 22, no. 20, pp. 24235–24240, Oct. 2014, doi: 10.1364/OE.22.024235.

[90] U. H. P. Fischer-Hirchert, *Photonic Packaging Sourcebook : Fiber-Chip Coupling for Optical Components, Basic Calculations, Modules*. Berlin, Heidelberg: Springer, 2015.

[91] A. Rogner, W. Ehrfeld, D. Munchmeyer, P. Bley, C. Burbaum, and J. Mohr, "LIGA-based flexible microstructures for fiber-chip coupling," *J. Micromech. Microeng.*, vol. 1, no. 3, p. 167, 1991, doi: 10.1088/0960-1317/1/3/007.

[92] T. Paatzsch *et al.*, "Very low-loss passive fiber-to-chip coupling with tapered fibers," *Appl. Opt., AO*, vol. 36, no. 21, pp. 5129–5133, Jul. 1997, doi: 10.1364/AO.36.005129.

[93] G. Böttger, H. Schröder, and R. Jordan, "Active or passive fiber-chip-alignment: approaches to efficient solutions," presented at the Optoelectronic Interconnects XIII, 2013, vol. 8630, p. 863006, doi: 10.1117/12.2014176.

[94] I. M. Soganci, A. L. Porta, and B. J. Offrein, "Flip-chip optical couplers with scalable I/O count for silicon photonics," *Opt. Express, OE*, vol. 21, no. 13, pp. 16075–16085, Jul. 2013, doi: 10.1364/OE.21.016075.

[95] N. Boyer *et al.*, "Novel, High-Throughput, Fiber-to-Chip Assembly Employing Only Off-the-Shelf Components," in *2017 IEEE 67th Electronic Components and Technology Conference (ECTC)*, 2017, pp. 1632–1639, doi: 10.1109/ECTC.2017.185.

[96] K. S. Prabhu, T. L. Schmitz, P. G. Ifju, and J. G. Daly, "A survey of technical literature on adhesive applications for optics," 2007, p. 666507, doi: 10.1117/12.735948.

[97] K. T. Rohdes, "Aerobic adhesives VII: a new high-performance bonding option for optical assembly," presented at the Integrated Optics Devices IV, 2000, vol. 3936, pp. 172–184, doi: 10.1117/12.379964.

[98] A. Bachmann, "Advances in light curing adhesives," presented at the Optomechanical Design and Engineering 2001, 2001, vol. 4444, pp. 185–196, doi: 10.1117/12.447301.

[99] L. Evans and P. Bryant, "LHC Machine," *J. Inst.*, vol. 3, no. 08, p. S08001, 2008, doi: 10.1088/1748-0221/3/08/S08001.

[100] P. Lujan, "CMS Luminosity - Public Results." [Online]. Available: https://twiki.cern.ch/twiki/bin/view/CMSPublic/LumiPublicResults#LHC_and_CMS_luminosity_records. [Accessed: 23-Oct-2017].

[101] L. Rossi and O. Brüning, "Introduction to the HL-LHC Project," *Adv. Ser. Dir. High Energy Phys.*, 2015, doi: 10.1142/9789814675475_0001, 10.1142/9789814675475_0001.

[102] The ATLAS Collaboration, "The ATLAS Experiment at the CERN Large Hadron Collider," *Journal of Instrumentation*, vol. 3, no. 08, p. S08003, 2008.

[103] The CMS Collaboration *et al.*, "The CMS experiment at the CERN LHC," *J. Inst.*, vol. 3, no. 08, p. S08004, 2008, doi: 10.1088/1748-0221/3/08/S08004.

[104] The TOTEM Collaboration *et al.*, "The TOTEM Experiment at the CERN Large Hadron Collider," *J. Inst.*, vol. 3, no. 08, p. S08007, 2008, doi: 10.1088/1748-0221/3/08/S08007.

[105] The LHCf Collaboration *et al.*, "The LHCf detector at the CERN Large Hadron Collider," *J. Inst.*, vol. 3, no. 08, p. S08006, 2008, doi: 10.1088/1748-0221/3/08/S08006.

[106] The ALICE Collaboration *et al.*, "The ALICE experiment at the CERN LHC," *J. Inst.*, vol. 3, no. 08, p. S08002, 2008, doi: 10.1088/1748-0221/3/08/S08002.
[107] The LHCb Collaboration *et al.*, "The LHCb Detector at the LHC," *J. Inst.*, vol. 3, no. 08, p. S08005, 2008, doi: 10.1088/1748-0221/3/08/S08005.
[108] J. L. Pinfold, "The MoEDAL experiment at the LHC. Searching beyond the standard model," *EPJ Web Conf.*, vol. 126, p. 02024, Nov. 2016, doi: 10.1051/epjconf/201612602024.
[109] "Schematic of CMS-Detector," *CMS Experiment*. [Online]. Available: https://cms.cern/detector. [Accessed: 10-Oct-2017].
[110] CMS Collaboration, "The CMS electromagnetic calorimeter project," Technical Design Report CERN-LHCC-97-033; CMS-TDR-4, 1997.
[111] CMS Collaboration, "The CMS hadron calorimeter project," Technical Design Report CERN-LHCC-97-031; CMS-TDR-2, 1997.
[112] CMS Collaboration, "The CMS muon project," Technical Design Report CERN-LHCC-97-032; CMS-TDR-3, 1997.
[113] S. R. Davis, "CMS slice image view (transverse/longitudinal/3-D)," *CERN Document Server*, 03-Aug-2016. [Online]. Available: http://cds.cern.ch/record/2204863. [Accessed: 10-Oct-2017].
[114] S. Dasu *et al.*, "The TriDAS project: The trigger systems," Technical Design Report Volume 1, 2000.
[115] P. L. Rocca and F. Riggi, "The upgrade programme of the major experiments at the Large Hadron Collider," *J. Phys.: Conf. Ser.*, vol. 515, no. 1, p. 012012, 2014, doi: 10.1088/1742-6596/515/1/012012.
[116] CMS Collaboration, "Technical proposal for the upgrade of the CMS detector through 2020," Jun. 2011.
[117] J. Butler, D. Contardo, M. Klute, J. Mans, and L. Silvestris, "Technical Proposal for the Phase-II Upgrade of the CMS Detector," Geneva, CERN-LHCC-2015-010. LHCC-P-008. CMS-TDR-15-02, Jun. 2015.
[118] J. Troska *et al.*, "Optical readout and control systems for the CMS tracker," *IEEE Transactions on Nuclear Science*, vol. 50, no. 4, pp. 1067–1072, Aug. 2003, doi: 10.1109/TNS.2003.815124.
[119] J. Troska *et al.*, "Radiation-hard optoelectronic data readout for the ATLAS SCT," presented at the Photonics for Space Environments VII, 2000, vol. 4134, pp. 214–222, doi: 10.1117/12.405346.
[120] K. Gill *et al.*, "High Statistics Testing of Radiation Hardness and Reliability of Lasers and Photodiodes," presented at the 10th Workshop on Electronics for LHC and Future Experiments, Boston, MA, USA, 2004, pp. 153–157, doi: 10.5170/CERN-2004-010.153.
[121] J. Troska *et al.*, "Radiation Damage Studies of Lasers and Photodiodes for Use in Multi-Gb/s Optical Data Links," *IEEE Transactions on Nuclear Science*, vol. 58, no. 6, pp. 3103–3110, Dec. 2011, doi: 10.1109/TNS.2011.2172633.
[122] L. Amaral *et al.*, "The versatile link, a common project for super-LHC," *Journal of Instrumentation*, vol. 4, no. 12, p. P12003, 2009, doi: 10.1088/1748-0221/4/12/P12003.
[123] P. Moreira, K. Kloukinas, and A. Marchioro, "The GBT: A proposed architecture for multi-Gb/s data transmission in high energy physics," in *Proceedings Topical Workshop on Electronics for Particle Physics*, Prague, Czech Republic, 2007, pp. 332–336, doi: 10.5170/CERN-2007-007.332.
[124] P. Moreira *et al.*, "The GBT Project," in *Proceedings Topical Workshop on Electronics for Particle Physics*, Paris, France, 2009, pp. 342–346, doi: 10.5170/09-006.34CERN-202.
[125] F. Vasey *et al.*, "The Versatile Link common project: feasibility report," *Journal of Instrumentation*, vol. 7, no. 01, p. C01075, 2012.
[126] J. Troska *et al.*, "Laser and photodiode environmental evaluation for the Versatile Link project," *J. Inst.*, vol. 8, no. 02, p. C02053, 2013, doi: 10.1088/1748-0221/8/02/C02053.
[127] F. Vasey *et al.*, "The Versatile Link Application Note, Version 2.2." 30-Sep-2013.
[128] P. Moreira, "The LpGBT: Project Status and Overview," presented at the Common ATLAS CMS ElectronicS Workshop for HL-LHC (ACES), Zurich, Switzerland, 08-Mar-2016.
[129] C. Soós *et al.*, "Versatile Link PLUS transceiver development," *J. Inst.*, vol. 12, no. 03, p. C03068, 2017, doi: 10.1088/1748-0221/12/03/C03068.

[130] T. Zhang, S. Kulis, P. Gui, F. Tavernier, and P. Moreira, "GBLD10+: a compact low-power 10 Gb/s VCSEL driver," *J. Inst.*, vol. 11, no. 01, p. C01015, 2016, doi: 10.1088/1748-0221/11/01/C01015.

[131] D. Guo *et al.*, "Developments of two 4 × 10 Gb/s VCSEL array drivers in 65 nm CMOS for HEP experiments," *J. Inst.*, vol. 12, no. 02, p. C02065, 2017, doi: 10.1088/1748-0221/12/02/C02065.

[132] Z. Zeng, T. Zhang, G. Wang, P. Gui, S. Kulis, and P. Moreira, "LDQ10: a compact ultra low-power radiation-hard 4 × 10 Gb/s driver array," *J. Inst.*, vol. 12, no. 02, p. P02020, 2017, doi: 10.1088/1748-0221/12/02/P02020.

[133] Y. A. Vlasov, "Silicon CMOS-integrated nano-photonics for computer and data communications beyond 100G," *IEEE Communications Magazine*, vol. 50, no. 2, pp. s67–s72, Feb. 2012, doi: 10.1109/MCOM.2012.6146487.

[134] Telcordia Technologies, Inc., "NEBS(TM) Requirements: Physical Protection," *Telcordia Technologies Generic Requirements*, vol. GR-63, no. 3, 2006.

[135] D. Karnick, P. Skwierawski, M. Schneider, L. Eisenblätter, and M. Weber, "Optical links for detector instrumentation: on-detector multi-wavelength silicon photonic transmitters," *J. Inst.*, vol. 12, no. 03, p. C03078, 2017, doi: 10.1088/1748-0221/12/03/C03078.

[136] B. Henrich *et al.*, "The adaptive gain integrating pixel detector AGIPD a detector for the European XFEL," *Nuclear Instruments and Methods in Physics Research Section A: Accelerators, Spectrometers, Detectors and Associated Equipment*, vol. 633, pp. S11–S14, May 2011, doi: 10.1016/j.nima.2010.06.107.

[137] J. Becker *et al.*, "High speed cameras for X-rays: AGIPD and others," *J. Inst.*, vol. 8, no. 01, p. C01042, 2013, doi: 10.1088/1748-0221/8/01/C01042.

[138] P. Skwierawski, M. Schneider, D. Karnick, L. Eisenblätter, and M. Weber, "A silicon photonic wavelength division multiplex system for high-speed data transmission in detector instrumentation," *J. Inst.*, vol. 11, no. 01, p. C01045, 2016, doi: 10.1088/1748-0221/11/01/C01045.

[139] A. Alduino, "Demonstration of a high speed 4-channel integrated silicon photonics WDM link with hybrid silicon lasers," in *2010 IEEE Hot Chips 22 Symposium (HCS)*, 2010, pp. 1–29, doi: 10.1109/HOTCHIPS.2010.7480075.

[140] X. Zheng *et al.*, "Ultralow Power 80 Gb/s Arrayed CMOS Silicon Photonic Transceivers for WDM Optical Links," *J. Lightwave Technol., JLT*, vol. 30, no. 4, pp. 641–650, Feb. 2012.

[141] Y. Liu *et al.*, "Silicon Mod-MUX-Ring transmitter with 4 channels at 40 Gb/s," *Opt. Express, OE*, vol. 22, no. 13, pp. 16431–16438, Jun. 2014, doi: 10.1364/OE.22.016431.

[142] H. D. Thacker *et al.*, "An all-solid-state, WDM silicon photonic digital link for chip-to-chip communications," *Opt. Express, OE*, vol. 23, no. 10, pp. 12808–12822, May 2015, doi: 10.1364/OE.23.012808.

[143] A. Ramaswamy *et al.*, "A WDM 4×28Gbps Integrated Silicon Photonic Transmitter driven by 32nm CMOS driver ICs," in *Optical Fiber Communication Conference Post Deadline Papers (2015), paper Th5B.5*, 2015, p. Th5B.5, doi: 10.1364/OFC.2015.Th5B.5.

[144] P. Dong *et al.*, "Four-Channel 100-Gb/s per Channel Discrete Multi-Tone Modulation Using Silicon Photonic Integrated Circuits," in *Optical Fiber Communication Conference Post Deadline Papers (2015), paper Th5B.4*, 2015, p. Th5B.4, doi: 10.1364/OFC.2015.Th5B.4.

[145] E. El-Fiky *et al.*, "First demonstration of a 400 Gb/s 4λ CWDM TOSA for datacenter optical interconnects," *Opt. Express, OE*, vol. 26, no. 16, pp. 19742–19749, Aug. 2018, doi: 10.1364/OE.26.019742.

[146] E. El-Fiky, A. Samani, D. Patel, M. Jacques, M. Sowailem, and D. V. Plant, "400 Gb/s O-band silicon photonic transmitter for intra-datacenter optical interconnects," *Opt. Express, OE*, vol. 27, no. 7, pp. 10258–10268, Apr. 2019, doi: 10.1364/OE.27.010258.

[147] T. R. Oldham and F. B. McLean, "Total ionizing dose effects in MOS oxides and devices," *IEEE Transactions on Nuclear Science*, vol. 50, no. 3, pp. 483–499, Jun. 2003, doi: 10.1109/TNS.2003.812927.

[148] J. Zhang, E. Fretwurst, R. Klanner, I. Pintilie, J. Schwandt, and M. Turcato, "Investigation of X-ray induced radiation damage at the Si-SiO 2 interface of silicon sensors for the European XFEL," *J. Inst.*, vol. 7, no. 12, p. C12012, 2012, doi: 10.1088/1748-0221/7/12/C12012.

[149] S. Seif El Nasr-Storey *et al.*, "Effect of Radiation on a Mach–Zehnder Interferometer Silicon Modulator for HL-LHC Data Transmission Applications," *IEEE Transactions on Nuclear Science*, vol. 62, no. 1, pp. 329–335, Feb. 2015, doi: 10.1109/TNS.2015.2388546.
[150] S. Seif El Nasr-Storey *et al.*, "Neutron and X-ray irradiation of silicon based Mach-Zehnder modulators," *J. Inst.*, vol. 10, no. 03, p. C03040, 2015, doi: 10.1088/1748-0221/10/03/C03040.
[151] S. Seif El Nasr-Storey *et al.*, "Modeling TID Effects in Mach-Zehnder Interferometer Silicon Modulator for HL-LHC Data Transmission Applications," *IEEE Transactions on Nuclear Science*, vol. 62, no. 6, pp. 2971–2978, Dec. 2015, doi: 10.1109/TNS.2015.2499041.
[152] CST AG, "CST STUDIO SUITE® Help Documentation." 2016.
[153] M. N. Polyanskiy, "Refractive index database." [Online]. Available: https://refractiveindex.info. [Accessed: 01-Dec-2017].
[154] M. Kaschel, F. Letzkus, J. Butschke, P. Skwierawski, M. Schneider, and M. Weber, "Echelle grating for silicon photonics applications: integration of electron beam lithography in the process flow and first results," in *Silicon Photonics and Photonic Integrated Circuits V*, 2016, vol. 9891, p. 98911V, doi: 10.1117/12.2228817.
[155] H. Yu *et al.*, "Performance tradeoff between lateral and interdigitated doping patterns for high speed carrier-depletion based silicon modulators," *Opt. Express, OE*, vol. 20, no. 12, pp. 12926–12938, Jun. 2012, doi: 10.1364/OE.20.012926.
[156] M. Kaschel, "Silicon photonic layout and process description." Institut für Mikroelektronik, Stuttgart, 01-Feb-2018.
[157] M. Uenuma and T. Motooka, "Temperature-independent silicon waveguide optical filter," *Opt. Lett., OL*, vol. 34, no. 5, pp. 599–601, Mar. 2009, doi: 10.1364/OL.34.000599.
[158] G. Rasigade, D. Marris-Morini, M. Ziebell, E. Cassan, and L. Vivien, "Analytical model for depletion-based silicon modulator simulation," *Opt. Express, OE*, vol. 19, no. 5, pp. 3919–3924, Feb. 2011, doi: 10.1364/OE.19.003919.
[159] Synopsys, "Sentaurus^{TM} Mesh User Guide." 2016.
[160] T. Baehr-Jones *et al.*, "Ultralow drive voltage silicon traveling-wave modulator," *Opt. Express, OE*, vol. 20, no. 11, pp. 12014–12020, May 2012, doi: 10.1364/OE.20.012014.
[161] T. Cao, Y. Fei, L. Zhang, Y. Cao, and S. Chen, "Design of a silicon Mach-Zehnder modulator with a U-type PN junction," *Appl. Opt., AO*, vol. 52, no. 24, pp. 5941–5948, Aug. 2013, doi: 10.1364/AO.52.005941.
[162] Z. Yong *et al.*, "Efficient single-drive push-pull silicon Mach-Zehnder modulators with U-shaped PN junctions for the O-band," in *2017 Optical Fiber Communications Conference and Exhibition (OFC)*, 2017, pp. 1–3.
[163] Y. Liu, S. Dunham, T. Baehr-Jones, A. E. Lim, G. Lo, and M. Hochberg, "Ultra-Responsive Phase Shifters for Depletion Mode Silicon Modulators," *Journal of Lightwave Technology*, vol. 31, no. 23, pp. 3787–3793, Dec. 2013, doi: 10.1109/JLT.2013.2287697.
[164] X. Xiao *et al.*, "44-Gb/s Silicon Microring Modulators Based on Zigzag PN Junctions," *IEEE Photonics Technology Letters*, vol. 24, no. 19, pp. 1712–1714, Oct. 2012, doi: 10.1109/LPT.2012.2213244.
[165] Z.-Y. Li *et al.*, "Silicon waveguide modulator based on carrier depletion in periodically interleaved PN junctions," *Opt. Express, OE*, vol. 17, no. 18, pp. 15947–15958, Aug. 2009, doi: 10.1364/OE.17.015947.
[166] H. Xu *et al.*, "High speed silicon Mach-Zehnder modulator based on interleaved PN junctions," *Opt. Express, OE*, vol. 20, no. 14, pp. 15093–15099, Jul. 2012, doi: 10.1364/OE.20.015093.
[167] F. Y. Gardes *et al.*, "High-speed modulation of a compact silicon ring resonator based on a reverse-biased pn diode," *Opt. Express, OE*, vol. 17, no. 24, pp. 21986–21991, Nov. 2009, doi: 10.1364/OE.17.021986.
[168] D. Pérez-Galacho *et al.*, "Simplified modeling and optimization of silicon modulators based on free-carrier plasma dispersion effect," *Opt. Express, OE*, vol. 24, no. 23, pp. 26332–26337, Nov. 2016, doi: 10.1364/OE.24.026332.
[169] W. Freude *et al.*, "Quality metrics for optical signals: Eye diagram, Q-factor, OSNR, EVM and BER," in *2012 14th International Conference on Transparent Optical Networks (ICTON)*, 2012, pp. 1–4, doi: 10.1109/ICTON.2012.6254380.
[170] N. C. Harris *et al.*, "Efficient, compact and low loss thermo-optic phase shifter in silicon," *Opt. Express, OE*, vol. 22, no. 9, pp. 10487–10493, May 2014, doi: 10.1364/OE.22.010487.

[171] B. El-Kareh and L. N. Hutter, *Fundamentals of Semiconductor Processing Technology*. Springer US, 1995.
[172] F. G. Della Corte, M. Merenda, G. Cocorullo, M. Iodice, I. Rendina, and P. M. Sarro, "Modulation speed improvement in a Fabry-Perot thermo-optical modulator through a driving signal optimization technique," *OE*, vol. 48, no. 7, p. 074601, Jul. 2009, doi: 10.1117/1.3183913.
[173] A. Masood *et al.*, "Comparison of heater architectures for thermal control of silicon photonic circuits," in *10th International Conference on Group IV Photonics*, 2013, pp. 83–84, doi: 10.1109/Group4.2013.6644437.
[174] E. M. Conwell, "Properties of Silicon and Germanium," *Proceedings of the IRE*, vol. 40, no. 11, pp. 1327–1337, Nov. 1952, doi: 10.1109/JRPROC.1952.273956.
[175] International Telecommunication Union, "Spectral grids for WDM applications: DWDM frequency grid," *Recommendation G.694.1*, Feb. 2012.
[176] X. Pommarede *et al.*, "16×100 GHz Echelle Grating-Based Wavelength Multiplexer on Silicon-on-Insulator Platform," *IEEE Photonics Technology Letters*, vol. 29, no. 6, pp. 493–495, Mar. 2017, doi: 10.1109/LPT.2017.2660546.
[177] E. D. Palik, *Handbook of Optical Constants of Solids*, vol. 1. Elsevier, 1985.
[178] G. Ghosh, "Dispersion-equation coefficients for the refractive index and birefringence of calcite and quartz crystals," *Optics Communications*, vol. 163, no. 1, pp. 95–102, May 1999, doi: 10.1016/S0030-4018(99)00091-7.
[179] H. H. Li, "Refractive index of silicon and germanium and its wavelength and temperature derivatives," *Journal of Physical and Chemical Reference Data*, vol. 9, no. 3, pp. 561–658, Jul. 1980, doi: 10.1063/1.555624.
[180] I. H. Malitson, "Interspecimen Comparison of the Refractive Index of Fused Silica," *J. Opt. Soc. Am., JOSA*, vol. 55, no. 10, pp. 1205–1209, Oct. 1965, doi: 10.1364/JOSA.55.001205.
[181] L. Chrostowski *et al.*, "Design methodologies for silicon photonic integrated circuits," in *Smart Photonic and Optoelectronic Integrated Circuits XVI*, 2014, vol. 8989, p. 89890G, doi: 10.1117/12.2047359.
[182] Y. Wang, J. Flueckiger, C. Lin, and L. Chrostowski, "Universal grating coupler design," in *Photonics North 2013*, 2013, vol. 8915, p. 89150Y, doi: 10.1117/12.2042185.
[183] T. Baehr-Jones *et al.*, "A 25 Gb/s Silicon Photonics Platform," *arXiv:1203.0767 [physics]*, Mar. 2012.
[184] Y. Lin, W. Liu, and F. G. Shi, "Adhesive joint design for minimizing fiber alignment shift during UV curing," *IEEE Transactions on Advanced Packaging*, vol. 29, no. 3, pp. 520–524, Aug. 2006, doi: 10.1109/TADVP.2005.850505.
[185] D. Karnick, N. Bauditsch, L. Eisenblätter, T. Kühner, M. Schneider, and M. Weber, "Efficient, Easy-to-Use, Planar Fiber-to-Chip Coupling Process with Angle-Polished Fibers," in *2017 IEEE 67th Electronic Components and Technology Conference (ECTC)*, 2017, pp. 1627–1632, doi: 10.1109/ECTC.2017.245.

A Mathematical relations

A.1 The Gaussian beam

The Gaussian beam describes the propagation of a monochromatic optical field in paraxial approximation with a transversal Gaussian shape in free space. It applies for both one- and two-dimensional fields, because each dimension can be considered separately. It is characterized by its waist w_0 and the wavelength λ of the field. A schematic adopted from [5] taking the example of a slab waveguide is sketched in Figure A.1. The left half plane shows the field distribution $\Psi(y)$ of the mode confined in the slab waveguide. The maximum field amplitude is Ψ_0. The core with the refractive index n_1 extents between $y = \pm h/2$. The surrounding cladding has the refractive index n_2. The right half plane shows the Gaussian beam emerging from the interface between the waveguide and free space. Its waist at $z = 0$ is given by half the guided mode's $1/\mathrm{e}$-width. Upon propagation along the z-axis, the beam diverges and the width is given by

$$w(z) = w_0 \sqrt{1 + \left(\frac{z}{z_\mathrm{R}}\right)^2}, \tag{A.1}$$

where z_R is the Rayleigh length of the beam. z_R indicates the propagation distance of the beam, where the waist is increased by the factor $\sqrt{2}$. For a two-dimensional symmetric beam, this corresponds to a doubling of its cross section. The solid black lines in the right half plane indicate the curves of constant field strength. The dashed lines represent associated asymptotes, which show the approximately linear progression of equation (A.1) in the far field.

The curvature of the spherical phase front evolves upon the propagation of the field along the z-axis. It is expressed by the radius $R = r(z)$. At $z = 0$, the radius is infinite and the phase front is a plane. Upon the propagation along the z-axis, the radius of the phase front curvature reduces until it reaches a minimum at the Rayleigh length before increasing again for $z > z_\mathrm{R}$. The Rayleigh length is directly proportional to the confocal parameter b_c

$$b_\mathrm{c} = 2z_\mathrm{R} = nk_0 w_0^2 = n\frac{2\pi}{\lambda} w_0^2 \tag{A.2}$$

with the vacuum wave number $k_0 = 2\pi/\lambda$ and the refractive index n of the free-space medium.

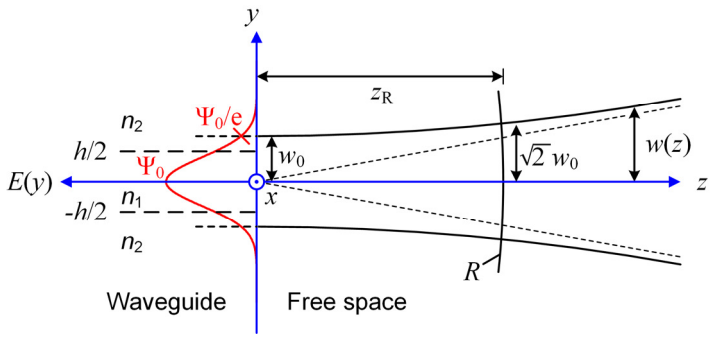

Figure A.1: The fundamental mode of a slab waveguide with the field amplitude $\Psi(y)$ and the maximum amplitude Ψ_0 is radiated into free space in $+z$-direction at $z = 0$. The schematic is adopted from [5].

A.2 Phase matching in grating couplers

The coupling of an optical mode propagating in a waveguide to the cladding eventually equals the problem of resonant mode coupling [39]. The mode in the waveguide has the propagation constant

$$\beta = n_{\text{eff}} k_0 \tag{A.3}$$

and is restricted to the z-direction. The mode coupled to the cladding has the wave vector $\vec{k}_c$. At resonance, phase matching applies for the wave vector components, which both modes have in common. Thus, the y-component of $\vec{k}_c$ is considered, which reads

$$k_{c,y} = n_c k_0 \sin(\theta), \tag{A.4}$$

where θ is the angle at which the monochromatic field oscillating at the wavelength λ_0 in the cladding propagates with respect to the grating normal. The change of the propagation direction is induced by a waveguide perturbation. In a grating coupler, this is a periodic corrugation of the waveguide, which results in a weak modulation of the effective refractive index. This results in a series of possible propagation constants β_m

$$\beta_m = m \frac{2\pi}{\Lambda}, \tag{A.5}$$

where m is an integer representing the diffraction order. The equation, which describes the mode coupling therefore reads

$$n_{\text{eff}} k_0 + n_c k_0 \sin(\theta) = m \frac{2\pi}{\Lambda}, \tag{A.6}$$

which after rearranging yields equation (2.15).

B List of abbreviations

2ASK	Two-level amplitude shift keying
8PSK	8-level phase shift keying
APSK	Amplitude and phase shift keying
AGIPD	Adaptive gain integrated pixel detector
AMPLE	Pyxis Advanced Multi-Purpose Language
ASIC	Application-specific integrated circuit
ATLAS	A Toroidal LHC ApparatuS
BDC	Bi-directional coupler
BER	Bit error ratio
BERT	BER tester
BESOI	Bond and etch-back SOI
BOX	Buried oxide
BP	Bandpass filter
BPSK	Binary phase shift keying
BT	Bias-tee
CCU	Communication and control units
CDI	Coherent diffraction imaging
CMOS	Complementary metal-oxide semiconductor
CMS	Compact muon solenoid
COM	Common port of a (de-)multiplexer
CPW	Coplanar waveguide
CSA	Communication signal analyzer
CTE	Coefficient of thermal expansion
cw	Continuous-wave
DAQ	Data acquisition system
DCB	Driver control board
DEMUX	Demultiplexer
DESY	Deutsches Elektronen-Synchrotron
DFB	Distributed-feedback
DMT	Discrete multi-tone
DOH	Digital opto-hybrid
DSP	Digital signal processing
DTS	Detector technologies and systems
DUT	Device under test
DWDM	Dense WDM
EAM	Electro-absorption modulator
ECAL	Electromagnetic calorimeter
EDFA	Erbium-doped fiber amplifier
EOE	Electrical-optical-electrical

ESA	Electrical spectrum analyzer
Eu-XFEL	European X-Ray Free Electron Laser
FEC	Front-end controller, forward error correction
FED	Front-end driver
FPGA	Field programmable gate array
FPR	Free propagation region
FSR	Free spectral range
FTTH	Fiber-to-the-home
FWHM	Full width at half maximum
GBT	GigaBit Transceiver project
GBTx	GigaBit Transceiver module
HCAL	Hadronic calorimeter
HD-FEC	Hard-decision FEC
HEP	High-energy physics
HL-LHC	High-luminosity LHC project
HLT	High level trigger
IC	Integrated circuit
IM-DD	Intensity modulation and direct detection
IPE	Institute for Data Processing and Electronics
KIT	Karlsruhe Institute of Technology
L1	Level-1 trigger
LDD	Laser diode driver
LHC	Large hadron collider
LHCb	LHC beauty
LHCf	LHC forward
Linac	Linear accelerator
LpGBT	Low-power GBT
LS1…5	Long shutdown 1…5
MMI	Multi-mode interferometer
MoEDAL	Monopole and Exotics Detector at the LHC
MOS	Metal-oxide semiconductor
MPC	Manual polarization controller
MT	Matter and Technology
MUX	Multiplexer
MZI	Mach-Zehnder interferometer
MZM	Mach-Zehnder modulator
NRZ-OOK	Nonreturn-to-zero on/off keying
ONU	Optical network units
PAM	Pulse-amplitude modulation
PCG	Planar concave grating

PD	Photodetector
PIC	Photonic integrated circuit
PM	Power meter
PON	Passive optical network
POP	Physical optics propagation method
PRBS	Pseudo-random bit sequence
PS	Proton synchrotron
PSB	PS booster
QAM	Quadrature amplitude modulation
QCSE	Quantum-confined Stark effect
QPSK	Quadrature phase shift keying
RF-AU	RF analyzer unit
RF-S	RF source
ROC	Read-out chip
Rx	Receiver
SCA	Slow-control adapter
SIMOX	Separation by implanted oxygen
SMF	Single-mode fiber
SMU	Source measure unit
SNR	Signal-to-noise ratio
SOH	Silicon-organic hybrid
SOI	Silicon-on-insulator
SPP	Surface plasmon polariton
SPS	Super proton synchrotron
SW	Switch
TCAD	Technology computer aided design
TEC	Thermo-electric control
TEOS	Thermally oxidized silicon
TIA	Transimpedance amplifier
TLS	Tunable laser source
TOSM	Through-open-short-matched
TOTEM	TOTal Elastic and diffractive cross section Measurement
TTC	Timing, trigger and control
Tx	Transmitter
UV	Ultra-violet
VCSEL	Vertical-cavity surface-emitting laser
VL	Versatile Link
VNA	Vector network analyzer
VTRx	Versatile transceiver module
WDM	Wavelength-division multiplexing

C List of mathematical symbols

Γ	Total coupling efficiency
$\Gamma_{m,s}$	Misalignment-specific coupling efficiency in s-direction, $m = (\mathrm{mm}, \mathrm{l}, \mathrm{t}, \mathrm{a})$, $s = (x, y)$
$\Delta\alpha$	Change of free-carrier absorption, equation (3.3)
$\Delta\alpha_{\mathrm{e,h}}$	Contributions to free-carrier absorption due to change of electron or hole density, equation (3.3)
$\Delta n_{\mathrm{e,h}}$	Change of refractive index due to change of electron or hole density, equation (3.2)
$\Delta\lambda$	Wavelength shift, Figure 5.2
Δn	Change of refractive index, equation (3.2)
$\Delta n(x, y)$	Location-dependent change of the refractive index, equation (5.1)
Δn_{eff}	Change of the effective refractive index, equation (5.1)
$\Delta\varphi$	Phase shift a mode accumulates in a phase modulator, equations (5.2) and (5.5)
Δs	Transversal displacement, equation (2.13)
$\Delta\theta$	Angular offset between coupled waveguides, equation (2.14)
Δz	Gap size between two waveguides upon longitudinal displacement, equation (2.12)
Λ	Grating period, equation (2.9)
ϕ	Generic phase value, equation (5.4)
Ψ	Field of a guided mode, equation (2.6)
Ψ_0	Maximum field amplitude Figure A.1
α_{p}	Angle of SMF polishing, Figure 3.5
β	Propagation constant of a mode in the waveguide, equations (2.5) and (A.3)
β_{B}	Phase constant that complies with the Bragg condition, equation (2.8)
β_m	Propagation constant associated to waveguide grating diffraction order m, equation (A.5)
γ, θ	Angles of the incident and transmitted wave in Snell's law of refraction, Figure 3.5
ϵ_0	Vacuum permittivity, equation (3.4)
ϵ_{r}	Relative permittivity, equation (3.4)
θ	Propagation angle between monochromatic wave and surface normal, equation (2.15)
θ_{azim}	Angle of azimuthal alignment, Figure 3.6
θ_{elev}	Elevation angle of the fiber alignment, Figure 3.6
θ_{i}	Incident angle of a plane wave to the reflector, equation (2.7)
θ_m	Angle at which diffracted waves of m-th order emerge, equation (2.7)
θ_{o}	Alignment angle of PCG output waveguides, Figure 2.8
θ_{rot}	Fiber rotation angle, Figure 3.6
λ	Vacuum wavelength
λ_{B}	Wavelength that complies with the Bragg condition, equation (2.8)
λ_{c}	Wavelength at transmission peak, equation (5.7)
λ_i	Wavelength of the i-th carrier of a WDM system, Figure 3.4
μ_s	Ratio between the mode-field radii r_i $(i = 1, 2)$ in x- or y-direction, equation (2.10)
σ	Conductivity of the majority charge carriers, equation (3.6)
φ	Phase shift of plane wave at the boundary between two media, equation (2.1)

φ_0	Phase offset between the upper and lower arm of the unbiased MZM, equation (5.13)
φ_i	Phase shift in upper ($i = 1$) and lower ($i = 2$) arm of an MZM, equation (3.1)
ψ_i	Field of the i-th mode guided in a multi-mode waveguide, equation (2.6)
ω	Angular frequency given by $\omega = 2\pi f$
A	Generic amplitude, equation (5.4)
$A(V_{\mathrm{B}i})$	Damping factor representing the phase shifter modulation efficiency as a function of the bias voltage, equation (5.13)
$N_{\mathrm{A,D}}$	Acceptor or donor concentration
A_{N}	Numerical aperture, equation (2.3)
B	Normalized propagation constant, equation (2.3)
C_{BT}	Equivalent capacity of the bias-tee, Figure 5.7
C_{dep}	Capacity of the depletion region, equation (3.5)
C_{P}	Blocking capacity integrated in the microwave probe ground lines, Figure 5.7
$\vec{E}(x, y)$	Electrical field vector, equation (5.1)
$E_{\mathrm{in,out}}$	MZM input or output electric field amplitude, equation (3.1)
FSR	Free spectral range, Figure 5.2
I_{p}	Photo current, equation (5.8)
L	Total phase shifter length, equations (3.6), (3.7) and (5.2)
L_{BT}	Equivalent inductivity of the bias-tee, Figure 5.7
M	Number of occurrences of N images
N	Number of self-images
P_{opt}	Optical power, equation (5.8)
P_{el}	Electrical power, equation (5.8)
P_π	Electrical power dissipated in a thermal modulator to achieve a π-shift, Figure 5.32
R	Resistance of a conductor given by the conductivity and the geometry, equation (3.6)
R_{d}	Photodetector responsivity, equation (5.8)
$R_{\mathrm{I}i}$	Internal resistance of the i-th bias voltage supply, Figure 5.7
R_{L}	Load resistance, equation (5.8)
$R_{\mathrm{sn}}, R_{\mathrm{sp}}$	Sum of the series resistances in the slab and the strip region given by the respective majority charge carriers, equation (3.5)
$T(\lambda)$	Gaussian-shaped spectral transfer function of a grating coupler, equation (5.7)
$T(V_{\mathrm{B}i})$	MZM transfer function depending on the phase shifters bias voltage, equation (5.13)
V	Normalized frequency, equation (2.3)
V	Voltage applied to the pn-junction, equation (3.4)
V_0	Built-in potential of the pn-junction, equation (3.4)
$V_{\mathrm{B}i}$	Bias voltage applied to upper ($i = 1$) and lower ($i = 2$) arm of MZM, equation (3.1)
V_{B}	Generic modulator bias voltage, equation (5.6)
$\tilde{V}_{\mathrm{B}i}$	The i-th ideal voltage supply, Figure 5.7
V_i	The i-th modulator bias voltage level, Figure 5.2
V_π	Voltage required to achieve a π-shift, equation (5.6)

a, b	Arbitrary real constants, equations (5.4), (5.7) and (5.9)
b_c	Confocal parameter, equation (A.2)
d	Etch depth of grating teeth, Figure 2.9
d_{SMF}	SMF diameter, Figure 6.21
f_c	Cutoff frequency, equation (3.5)
h	Waveguide height, Figure 2.4, strip waveguide height, Figure 5.9
h_r	Height of resistive region, equation (3.6)
h_s	Height of waveguide slab Figure 5.9
i	Integer index value
$\vec{k}$	Wave vector
k_0	Vacuum wave number given by $k_= = 2\pi/\lambda$
$\vec{k}_c$	Wave vector of a mode that propagates in the waveguide cladding
m	Integer number that represents the order of refraction, equation (2.1)
m	Diffraction order, equation (2.7)
n	Refractive index
$n(x, y)$	Location-dependent refractive index, equation (5.3)
n_c	Refractive index of the cladding material, equation (2.15)
n_{eff}	Effective refractive index, equation (2.5)
n_{gap}	Refractive index of the gap medium between two waveguides, equation (2.14)
p	Integer number that represents the diffraction order of a grating, equation (2.8)
q	Elementary charge, equation (3.4)
r	Radius of the Rowland circle, Figure 2.8
r_i	Mode-field radius of source ($i = 1$) or target ($i = 2$) waveguide, equation (2.10)
s	Cartesian coordinate substitution $s = x, y$, equation (2.10)
u	Transverse phase constant in waveguide core, equation (2.3)
w	Transverse attenuation in the cladding, equation (2.3), width of grating teeth, Figure 2.9, Width of strip waveguide, Figure 5.9
$w(z)$	Width of Gaussian beam as a function of propagation distance along z, equation (A.1)
w_0	Waist of the Gaussian beam, equation (A.1)
w_{dep}	Width of the depletion region, equation (3.4)
w_g	Gap size between the cladding of the angle-polished fiber and the grating coupler
w_n, w_p	Net width of the n- or p-doped region within the strip boundaries, Figure 5.9
w_r	Width of resistive region, equation (3.6)
w_s	Width of waveguide slab, Figure 5.9
$w_{s,n}, w_{s,p}$	Width of n- or the p-region between the heavily doped corners and the strip, Figure 5.9
x, y, z	Cartesian coordinates
z_R	Rayleigh length of the Gaussian beam, equation (A.2)